Measurements of the Electric and Magnetic Form Factors of the Neutron and Their Dependence on Inelastic Modeling

Linda Maureen Stuart

(Ph.D. Thesis)

Manuscript date: June 1992

MASTER

LAWRENCE LIVERMORE NATIONAL LABORATORY ⅃⅃
University of California • Livermore, California • 94551

Measurements of the Electric and Magnetic Form Factors
of the Neutron and Their Dependence on Inelastic Modeling

By

Linda Maureen Stuart
B.A. (Ohio Wesleyan University) 1985
M.S. (University of California, Davis) 1987

DISSERTATION

Submitted in partial satisfaction of the
requirements for the degree of

DOCTOR OF PHILOSOPHY
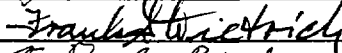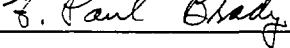
in

Engineering-Applied Science

in the

GRADUATE DIVISION

of the

UNIVERSITY OF CALIFORNIA

DAVIS

Approved:

Committee in Charge

1992

i

ACKNOWLEDGMENTS

This experiment was the result of a collaborative effort from thirteen institutions, and twenty-seven participating physicists, as well as many technicians and support staff. I would like to thank eacn one of these people who made contributions leading to the success of this experiment.

Thanks to my advisor, Frank Dietrich of Lawrence Livermore National Laboratory for his support, encouragement, and time. He provided much help and advice, especially during the thesis writing stage.

A special thanks goes to Peter Bosted of American University who has given me an enormous amount of help during the course of the experiment, the data analysis, and the writing of the thesis. He has taught me a great deal over the years, and all of his efforts are very much appreciated. I would also like to thank the rest of the American University group at SLAC, Steve Rock, Zen Szalata, and Raymond Arnold. They have all been very helpful on numerous occasions.

Finally, I would like to thank my husband, Brent, for his support and understanding, and for putting up with me these last few months, and to my mother, Rose, who has constantly supported and encouraged me from Day 1. Thanks to both of you for being there for me.

Linda Maureen Stuart
May 1992
Engineering-Applied Science

Measurements of the Electric and Magnetic Form Factors

of the Neutron and Their Dependence on Inelastic Modeling

ABSTRACT

The charge and magnetic elastic form factors of the neutron, $G_{En}(Q^2)$ and $G_{Mn}(Q^2)$, have been measured in the four-momentum transfer range $1.75 < Q^2 < 4.00$ $(GeV/c)^2$ using a Rosenbluth separation. These measurements constitute part of experiment NE11 which was performed at the End Station A facilities at the Stanford Linear Accelerator Center in the winter of 1989. The results show that $G_{Mn}(Q^2)/\mu_n/G_D(Q^2)$ is consistent with unity, where μ_n is the neutron anomalous magnetic moment, and $G_D(Q^2) = (1.0 + Q^2/0.71)^{-2}$, is the empirical dipole formula. The results for $(G_{En}(Q^2)/G_D(Q^2))^2$ are consistent with zero within errors.

The extraction of the neutron electromagnetic form factors from deuterium cross sections is a model dependent procedure because of the Fermi momentum of the bound nucleons. In addition to the smeared quasielastic cross section, there is an inelastic tail due to pion production which extends into the quasielastic region. This tail is significant (15% at the largest Q^2 point) and must be subtracted to measure the neutron form factors. An extensive study has been made on the effect of the modeling of this tail on the measured form

iii

factors using different Fermi smearing models, off-mass-shell corrections, and deuteron wave functions. The off-mass-shell-effects were the largest, but still smaller than the experimental error.

Comparisons were made with many theoretical models. There is no single form factor model studied which was able to describe the measured electromagnetic form factors of both the neutron and proton.

Measurements were also obtained of the $\Delta(1232)$ resonance transition form factors in the range $1.6 < Q^2 < 6.75$ $(GeV/c)^2$. These data confirm that the observed fall-off of the transition form factor is faster than that expected from leading order perturbative QCD calculations.

TABLE OF CONTENTS

vi

viii

1. INTRODUCTION

The first studies of the electromagnetic structure of the nucleons using energetic electron beams as probes began in the 1950's with the work by Hofstadter, et al [1][2]. The experimental goal in these early experiments and in those that followed was to understand how the electromagnetic probe interacts with the internal charge and current distributions of the nucleons. The electromagnetic form factors are the embodiment of these interactions. These form factors, $G_E(Q^2)$ and $G_M(Q^2)$, which depend only on the four-momentum transfer squared, are fundamental quantities, and the measured cross section can be directly expressed in terms of them. If a complete theory of hadron structure existed then these quantities could be calculated. Since this is not the case, and may never be, we must rely on experimental measurements and approximate model calculations. The early experiments measured the form factors for the proton in the four-momentum transfer squared range $0.02 < Q^2 < 0.5$ $(GeV/c)^2$ and the neutron form factors in the range $0.02 < Q^2 < 0.3$ $(GeV/c)^2$. These first glimpses into the nucleon structure also indicated that the root-mean-square radius of the nucleons' structure is around 0.80 fm and that the distribution of charge roughly drops off exponentially in the radial direction.

The form factor measurements become increasingly difficult at high Q^2 because the cross section falls as $1/Q^{12}$ at high Q^2 and the counting rates drop correspondingly. Experimental techniques have progressed greatly since the early experiments, however, and success has been made in

extending the Q^2 range of these difficult measurements. Electron-proton elastic cross section measurements [3] have been made out to a Q^2 of 31 $(GeV/c)^2$. However, the cross section depends on both the charge and magnetic form factors, and separate measurements of these quantities have only been made out to a momentum transfer of 3.75 $(GeV/c)^2$ with errors on the order of a few percent [4][5][6][7]. Similarly, the electron-neutron elastic cross sections have been measured [8] out to a Q^2 of 10 $(GeV/c)^2$, while the neutron form factors have only been separately measured out to a momentum transfer of 1.5 $(GeV/c)^2$ with large errors [9][10][11][12][13] The neutron measurement is more difficult due to the lack of free neutron targets. This experiment was designed to make precision measurements of the proton charge and magnetic form factors [14][15] out to a Q^2 of 8.8 $(GeV/c)^2$ and neutron form factors out to a Q^2 of 4.0 $(GeV/c)^2$.
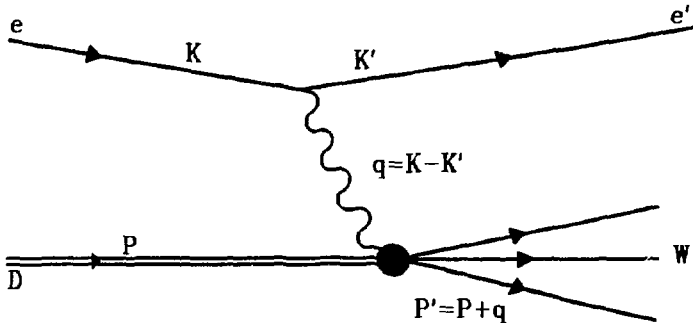
Figure 1.1: Feynman diagram for electron scattering assuming single photon exchange.

The neutron form factors and their dependence on inelastic cross section modeling will be presented here.

Electron-Nucleon Scattering Cross Sections and Form Factors

The lowest order Feynman diagram for the electron-deuteron scattering process is shown in Figure 1.1. It is assumed that $\hbar=c=1$ and the incident and scattered electron are extreme relativistic. If, for the moment, it is also assumed that the hit nucleon was originally at rest, then the four-momentum vectors describing the scattering off of an individual nucleon in the lab frame coordinates are given as:

$$K_\mu = \begin{pmatrix} E_0 \\ 0 \\ 0 \\ E_0 \end{pmatrix}, \ K_\mu' = \begin{pmatrix} E' \\ 0 \\ E'\sin(\theta) \\ E'\cos(\theta) \end{pmatrix}, \ P_\mu = \begin{pmatrix} m_N \\ 0 \\ 0 \\ 0 \end{pmatrix}, \ P_\mu' = \begin{pmatrix} m_N + E_0 - E' \\ 0 \\ -E'\sin(\theta) \\ E_0 - E'\cos(\theta) \end{pmatrix}, \quad (1.1)$$

where E_0 is the incident electron energy, E' is the scattered electron energy, θ is the scattering angle, and m_N is the nucleon mass. This process is characterized by two Lorentz invariant scalars, the four-momentum transfer squared:

$$Q^2 = -q^2 = -(K-K')^2 = 4E_0 E' \sin^2(\tfrac{\theta}{2}), \quad (1.2)$$

assuming that the electron mass can be neglected, and the energy transfer,

$$\nu = \frac{P \cdot q}{m_N} = E_0 - E'. \quad (1.3)$$

The invariant mass of the final hadronic state of the hit nucleon is given by W where

$$W^2 = (P+q)^2 = m_N^2 + 2m_N\nu + q^2. \quad (1.4)$$

In an elastic scattering process from a free nucleon there are no longer two independent variables. By requiring the final state to consist of a single nucleon in its ground state it must be true that $Q^2 \equiv 2m_N\nu$. The differential cross section for the elastic scattering of a spin 1/2 electron off of a spinless point nucleon, including the recoil of the hit nucleon, and assuming single photon exchange is given by the Mott cross section,

$$\left(\frac{d\sigma}{d\Omega}\right)_{MOTT} = \sigma_{MOTT} = \frac{\alpha^2\cos^2(\frac{\theta}{2})}{4E_0^2\sin^4(\frac{\theta}{2})\,[1+\frac{2E_0}{m_N}\sin^2(\frac{\theta}{2})]} \,. \qquad (1.5)$$

Nucleons are not point-like, however, and their structure is described by form factors. The inclusion of this structure results in the Rosenbluth cross section,

$$\left(\frac{d\sigma}{d\Omega}\right)_N = \sigma_{MOTT}\left[\frac{G_{EN}^2(Q^2)+\tau G_{MN}^2(Q^2)}{1+\tau} + 2\tau G_{MN}^2(Q^2)\tan^2(\frac{\theta}{2})\right], \qquad (1.6)$$

where $\tau = Q^2/4M_N^2$, $G_{EN}(Q^2)$ and $G_{MN}(Q^2)$ are the Sachs electric and magnetic form factors, and N is replaced by p for the proton and n for the neutron. The Sachs form factors are often expressed in terms of the Dirac, $F_1(Q^2)$, and the Pauli, $F_2(Q^2)$, form factors

$$G_{MN}(Q^2) = F_{1N}(Q^2) + F_{2N}(Q^2)\,, \qquad (1.7)$$

$$G_{EN}(Q^2) = F_{1N}(Q^2) - \tau F_{2N}(Q^2)\,. \qquad (1.8)$$

In the limit of no nuclear recoil the form factors become the Fourier transforms of the charge and magnetic moment distributions of the nucleons. In the limit of $Q^2 \to 0$ the electric form factors are normalized to the total charge of

the proton and neutron,

$$G_{Ep}(0) = 1, \quad G_{En}(0) = 0, \quad (1.9)$$

and the magnetic form factors are normalized to the anomalous magnetic moments,

$$G_{Mp}(0) = \mu_p = 2.793 \, nm, \quad G_{Mn}(0) = \mu_n = -1.913 \, nm. \quad (1.10)$$

Existing data are consistent with $G_{En}(Q^2) = 0$ and the remaining form factors can be approximated by an empirical dipole formula,

$$G_D(Q^2) = \frac{1}{\left(1 + \dfrac{Q^2}{(0.71)}\right)^2} = G_{Ep}(Q^2) = \frac{G_{Mp}(Q^2)}{|\mu_p|} = \frac{G_{Mn}(Q^2)}{|\mu_n|}, \quad (1.11)$$

where Q^2 must be in units of $(GeV/c)^2$. The Rosenbluth cross section is a function of angle and momentum transfer. By measuring the cross section at different angles and the same Q^2, the individual form factors can be extracted. This is called a "Rosenbluth separation".

If scattering takes place off of a nucleon contained in a deuterium nucleus, the process can no longer be considered elastic because the weak binding of the deuteron (2.225 MeV) generally results in its electrodisintegration. However, since the binding is weak the process is nearly elastic and is called instead "quasielastic". A complication in using a deuterium target is that it is no longer true that the nucleon in the nucleus has no inherent motion. The nucleons are bound together in a confined space and by the uncertainty principle have some nonzero momentum, called the Fermi momentum, distributed between them. This produces a broadening or

smearing of the measured cross sections because the kinematics of the allowed final state depend on this variable quantity. If we want to study scattering from the neutron then there is an additional complication due to the significant contribution to the cross section from quasielastic and inelastic scattering from the proton. In the quasielastic region the deuteron cross section is approximated fairly well by a Plane-Wave Impulse Approximation (PWIA) calculation [16][17]. The inelastic region has contributions due to the production of one or more hadrons, the most dominant contribution in the region of interest being the $\Delta(1236)$ resonance production. The tail of the inelastic region can extend well into the quasielastic region. A careful study and understanding of the cross section modeling of these contributions is vital to correctly extracting the neutron form factors from the measured cross sections. Sample model cross sections for electron-deuterium scattering are shown in Figure 1.2. The total expected cross section, excluding the small elastic electron-deuterium contribution, has been broken into its constituent contributions, the inelastic deuterium and the quasielastic. The electron-proton elastic scattering model cross section is also shown for comparison.

The inelastic electron-deuteron scattering cross section is given by

$$\frac{d^2\sigma}{d\Omega dE'} = \frac{\alpha^2 \cos^2(\frac{\theta}{2})}{4E_0^2 \sin^4(\frac{\theta}{2})} (W_2(x,Q^2) + 2W_1(x,Q^2)\tan^2(\frac{\theta}{2})), \quad (1.12)$$

where $x = Q^2/2m_\nu\nu$ and W_1 and W_2 are the deuteron structure
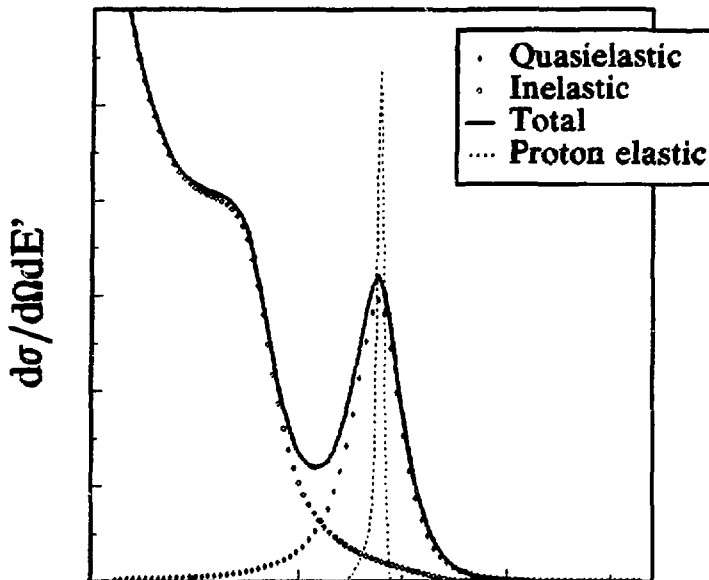
Scattered electron energy, E'

Figure 1.2: Sample electron-deuterium scattering cross section model showing the quasielastic and inelastic contributions. Also shown is the electron-proton elastic scattering cross section for comparison to the quasielastic.

functions. We now define $\tau' = \nu^2/Q^2$ ($\tau' = \tau = Q^2/4m_N^2 =$ previous

definition at the quasielastic peak) and express the structure

functions in terms of the transverse and longitudinal

virtual photoabsorption cross sections σ_T and σ_L:

$$W_1(x,Q^2) = \frac{K}{4\pi^2\alpha}\sigma_T(x,Q^2), \qquad (1.13)$$

$$W_2(x,Q^2) = \frac{K}{4\pi^2\alpha}\left(\frac{\sigma_T(x,Q^2) + \sigma_L(x,Q^2)}{1+\tau'}\right), \qquad (1.14)$$

where, K, the equivalent energy needed for a real photon to produce the same final mass state is given by

$$K = \frac{W^2 - M_n^2}{2M_n} . \tag{1.15}$$

The differential scattering cross section can now be expressed

$$\frac{d^2\sigma}{d\Omega dE'} = \frac{\alpha KE'}{4\pi^2 Q^2 E} \left(\frac{2}{1-\epsilon}\right) \left[\sigma_T(x,Q^2) + \epsilon\sigma_L(x,Q^2)\right], \tag{1.16}$$

where ϵ, the longitudinal polarization of the virtual photon is defined as

$$e = \frac{1}{1 + 2(1+\tau')\tan^2(\frac{\theta}{2})} . \tag{1.17}$$

In the impulse approximation the differential cross section can be expressed in terms of a scaling function, $F(y)$, a phase factor, K_y, and the elastic nucleon cross sections,

$$\frac{d^2\sigma}{d\Omega dE'} = \left[\left(\frac{d\sigma}{d\Omega}\right)_p + \left(\frac{d\sigma}{d\Omega}\right)_n\right] \frac{F(y)}{K_y} . \tag{1.18}$$

The scaling variable, y, is equal in magnitude to the longitudinal momentum of the struck nucleon relative to the virtual photon direction. The total fermi momentum of the struck nucleon, in terms of the longitudinal and transverse components, is given by

$$\vec{P}^2 = \vec{P}_L^2 + \vec{P}_T^2 = y^2 + \vec{P}_T^2 , \tag{1.19}$$

and y is determined from the energy conservation equation

$$E_0 + M_d = E' + \sqrt{M_n^2 + \vec{P}^2} + \sqrt{M_n^2 + (\vec{P} + \vec{q})^2} . \tag{1.20}$$

$F(y)$ is related to the integral over the deuteron wave function. Various proposals have been made as to what is the proper form of K_y, and a study by Petratos [18] compares

these different forms. A comparison of equations 1.16 and 1.18
using equation 1.6 yields the following results valid at the
quasielastic peak,

$$\sigma_T(x, Q^2) = \frac{4\pi^2\alpha}{K} \cdot \frac{F(y)}{K_y} \cdot \tau \left(G_{Mn}^2(Q^2) + G_{Mp}^2(Q^2)\right), \qquad (1.21)$$

$$\sigma_L(x, Q^2) = \frac{4\pi^2\alpha}{K} \cdot \frac{F(y)}{K_y} \left(G_{En}^2(Q^2) + G_{Ep}^2(Q^2)\right). \qquad (1.22)$$

It is convenient for the analysis to define a reduced cross
section given by

$$\sigma_R = \frac{d^2\sigma}{d\Omega dE'} \cdot \frac{4\pi^2 Q^2 E(1-\epsilon)}{2\alpha KE'} = \sigma_T(x, Q^2) + \epsilon\sigma_L(x, Q^2). \qquad (1.23)$$

By plotting σ_R versus ϵ at a given Q^2 it is simple to extract
σ_T and σ_L using a line fit to the data. Then by using values
for $G_{Mp}(Q^2)$ and $G_{Ep}(Q^2)$ which were also measured in this
experiment, and a model for $F(y)/K_y$, $G_{Mn}(Q^2)$ and $G_{En}(Q^2)$ can be
extracted.

Experimental Overview

Inclusive electron-deuteron scattering cross sections
were measured for the kinematic points given in Table 1.1.
Scattered electrons were concurrently measured by two
spectrometers at the Stanford Linear Accelerator Center (SLAC)
End Station A as shown in Figure 1.2. The 1.6 GeV/c
spectrometer was fixed at 90° throughout the experiment and
the 8 GeV/c spectrometer position was varied between 90° and
13°. For the deuterium cross section measurements the Nuclear
Physics Injector (NPI) was used to give an electron beam with
energies between 1.5 and 5.5 GeV and with average currents

1.6 GeV Spectrometer

Toroids

Quadrupole Magnets

Scattering Chamber

Dipole Magnets

-------- **SLAC Electron Beam**

8 GeV Spectrometer
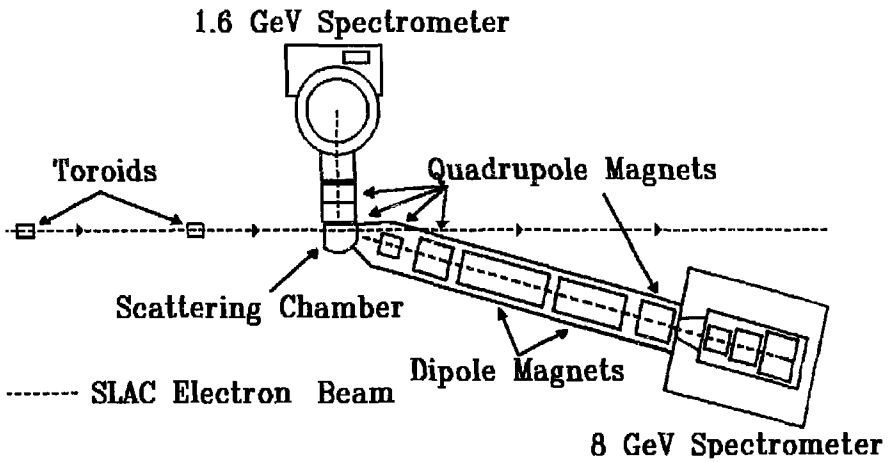
Figure 1.3: End station A experimental facility.

Table 1.1: NE11 deuteron kinematic data points.					
Q^2	E (GeV)	E' (GeV)	θ	ϵ	SPECT
1.75	1.511	0.578	90.0	0.250	8 & 1.6
	1.968	1.035	55.2	0.550	8
	2.407	1.474	41.1	0.704	8
	5.507	4.384	15.2	0.950	8
2.50	1.968	0.635	90.0	0.227	8 & 1.6
	2.407	1.075	58.8	0.479	8
	2.837	1.504	45.0	0.630	8
	5.507	4.167	19.0	0.913	8
3.25	2.407	0.675	90.0	0.206	1.6
	2.837	1.105	61.2	0.426	8
	5.507	3.768	22.8	0.864	8
4.00	2.837	0.705	90.0	0.190	1.6
	5.507	3.223	26.9	0.805	8

between 0.1 and 10 μA. For hydrogen inelastic cross section measurements which will be discussed also, the maximum beam energy used was 9.80 GeV and was attained using the NPI in the short pulse SLED (SLAC Energy Doubler) mode. The solid angle of the 1.6 GeV/c spectrometer was increased to 8 msr for this experiment by the addition of two quadrupole magnets. The detectors and electronics used for this experiment were designed to measure electrons amidst a large background of pions produced in inelastic scattering reactions. These measurements are all part of the SLAC experiment NE11. These data were taken in January and February of 1989.

2. APPARATUS

Electron Beam

Transport System and Energy Measurement

Electron pulses provided by the NPI [19][20] were accelerated through the final 600 meters of the 3000 meter long linear accelerator [21]. The nominal beam rate was 120 pulses per second (pps) with a typical beam pulse width of 1.6 μs and a maximum peak current of around 60 mA. The beam was transported to the experimental area, End Station A (ESA), by the beam switchyard [22][23] via the "A-line", Figure 2.1. The beam was controlled by beam operators at the Main Control Center (MCC) until reaching the final steering magnets, A10-A13, at which point the experimenters assumed control.
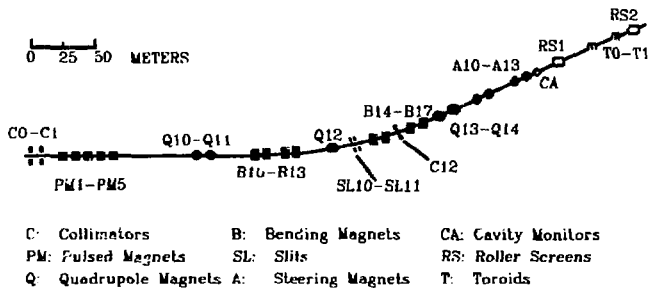
Figure 2.1: Beam transport system to End Station A.

The energy of the beam was defined by bending magnets B10-B17 and was monitored by a rotating flip-coil located in the nominal beam position of a dipole magnet which was nearly identical to the eight bending magnets and was in series with them. A second check on the beam energy was made with a

precision current measuring shunt which was in series with the bending magnets. This second method was somewhat less reliable and was used only as a check. The energy spread was defined by the adjustable slit SL10 and ranged from $\Delta E/E =$ 0.1% to 0.5% for this experiment. The slit designated as SL11 was not used for this experiment.

Beam Steering

The beam position and profile were checked in between data taking runs by the automated insertion of two ZnS fluorescent screens which were viewed by closed-circuit television. During data collection the beam was monitored by two resonant microwave cavities and two sets of secondary emission wire arrays. The microwave cavities, located 52 meters upstream from the target, measured the horizontal and vertical beam offsets by producing an RF resonant signal which was proportional to the distance deviation from the central axis when the beam passes through. One of the wire array sets was located two meters upstream of the target and one was located 0.95 meters downstream. Each set consisted of one horizontal and one vertical plane with twenty-five 0.127 mm thick aluminum wires. The wire spacing was 1.0 mm. The beam monitoring system was controlled via a Digital Microvax II computer. Using the cavities and the upstream wire arrays, the Microvax also controlled small adjustments in the A10-A13 steering magnets in order to keep the beam well-aligned.

The quality of the beam was monitored by two plastic scintillators, each having a phototube. One was mounted along

the beam pipe slightly upstream from the target and was used to measure the beam halo or "bad spill". It was desirable to keep this as small as possible. The other scintillator was mounted about 10 meters from the target and measured the time structure of the beam or "good spill". This structure was kept as close as possible to a square wave. Both systems were displayed via oscilloscopes which could be viewed by both MCC and the experimenters in order to make beam adjustments.

Toroidal Charge Monitors

The total incident charge on the target was measured by two separate and independent ferromagnetic toroidal charge monitors [24][25] located ~10 meters upstream from the target. When a charge pulse passed through the toroid a magnetic field was induced inside the iron which in turn induced a current in a wire which was looped several times around the toroid. The signal was sent to an RC circuit, so with the toroid acting as an inductor, the whole system acted as an RLC circuit producing a resonant signal with an amplitude proportional to the total incident charge. The toroidal charge monitoring system and calibration is discussed in greater detail in appendix A.

Targets

The target assembly system, Figure 2.2, consisted of long and short target cells filled with liquid hydrogen and liquid deuterium and aluminum targets needed for background subtraction. The cell lengths were 15 cm and 4 cm, and all
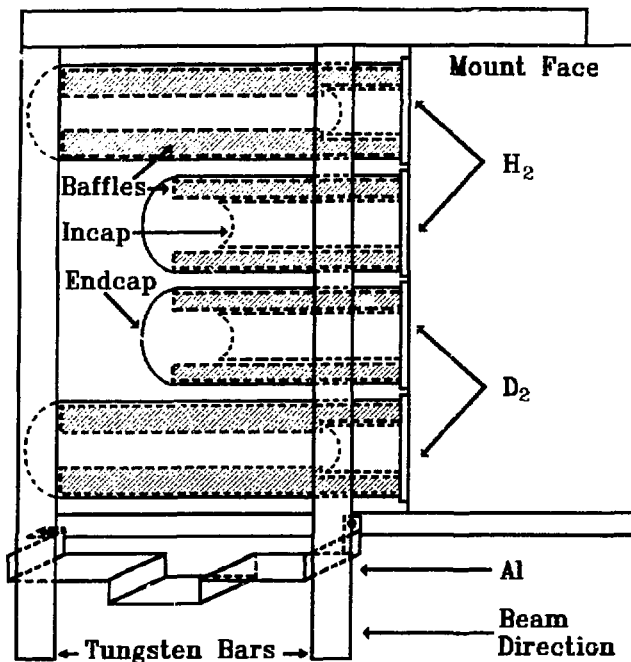
Figure 2.2: Target assembly mount as seen from the 1.6 GeV spectrometer.

the liquid targets had a radius of 3.22 cm. The two aluminum targets were constructed from a single 0.064 mm thick sheet of aluminum as shown in Figure 2.2. This target was mounted at 45° relative to the beamline. The entire assembly mount was remotely controlled by the computer to move up and down inside the scattering chamber so that the desired target was along the beamline. The beam entered the scattering chamber through a 0.0254 cm thick aluminum membrane which separated the beamline vacuum from the scattering chamber vacuum. A detailed

table of target materials seen by the beam and scattered electrons is given in Table 2.1.

The liquid target material was continuously circulated through the targets by fan-like pumps. The circulation over the entire length of the target was aided by the presence of baffle guides. The liquid was at a temperature of 21 K and was pressurized to 2.0 atmospheres. Vapor pressure bulbs and platinum resistors were located near the inlets and outlets of the targets to monitor the target temperature and pressure every 10 seconds. These measurements were converted to density using cryogenic data [26][27] and precision calibration

Table 2.1: Thicknesses of target materials.		
..ame	Material	Thick. (cm)
Materials seen by beam		
Wire arrays	Aluminum	0.00400
Scatt. chamber membrane	Aluminum	0.00254
Incap	Al 5052	0.00762
Long hydrogen	H_2	14.988
Short hydrogen	H_2	3.996
Long deuterium	D_2	14.925
Short deuterium	D_2	4.006
Materials seen by all scattered electrons		
Liquid target	H_2 or D_2	3.1940
Endcap	Al 3004	0.01143
Cell wall	Al 3004	0.01270
Insulation	Mylar	0.00635
Materials seen by electrons scattered into the 8 GeV spectrometer		
Scatt. chamber exit window	Al 6061	0.03048
Air gap	Air	16.00
Quadrupole window	Mylar	0.03048
Materials seen by electrons scattered into the 1.6 GeV spectrometer		
Scatt. chamber exit window	Al 5052	0.00762

measurements relating resistance to temperature. The average densities over the experiment were 0.07055 gm/cm³ for hydrogen and 0.16937 gm/cm³ for deuterium. Comparisons were done on electron and pion counting rates at different beam currents, beam repetition rates, and target circulation rates to study possible local boiling effects. No density fluctuations were observed within the statistical accuracy of the measurements.

8 GeV Spectrometer and Detectors

The 8 GeV spectrometer [28][29], shown in Figure 2.3, consisted of three quadrupole focusing magnets and two bending magnets which each bend 15°. The magnetic fields in the quadrupoles were monitored every ten seconds by Hall probes and the fields in the bending magnets were monitored by nuclear magnetic resonance (NMR) probes. During data runs the NMR's were read in the "out" position, meaning out of the particle acceptance. Between runs the probes were inserted into the uniform field regions and read manually. The spectrometer central momemtum, E', was then calculated from the relation [30]:

$$E'(GeV) = 0.41512 \cdot B + 0.00050, \qquad (2.1)$$

where B is the magnetic field measured by the NMR probes in kG. The offset used in this relation is small and has a comparable error of 0.00037. It accounts for background fields such as the earth's magnetic field. In back of the magnets there was a lead-shielded hut containing the particle detectors. The magnets and the detector package, sat on a

8 GeV Hut Detectors

Quadrupole Magnets

Scattering Chamber

Dipole Magnets
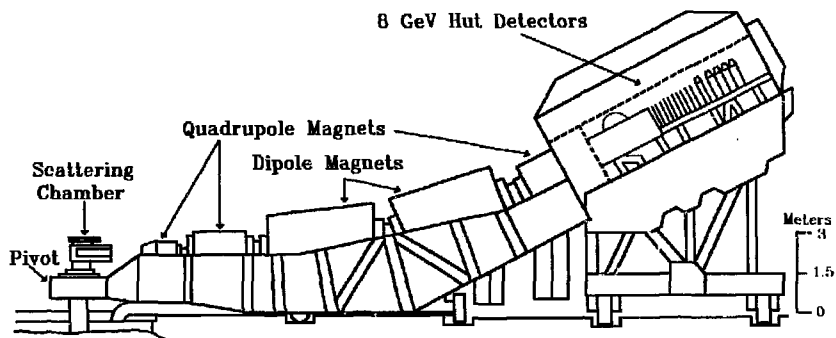
Pivot

Meters
3
1.5
0

Figure 2.3: The 8 GeV spectrometer.

frame which was moveable about the pivot. The motorized movement of the spectrometer was remote-controlled to sit at the desired scattering angle which was known to ± 0.005°. This spectrometer was capable of analyzing particles up to a maximum momentum of 9 GeV/c.

Optical Properties

The 8 GeV/c spectrometer was designed for point-to-point focusing in the vertical or bend plane and for line-to-point focusing in the horizontal or non-bend plane. Point-to-point means that particles scattered in the vertical plane with the same momentum are focused to the same point at the momentum focal plane located in the hut. Line-to-point means that particles scattered in the horizontal plane with the same scattering angle along the length of the target are focused to the same point at the theta focal plane.

The "central ray" of the optics refers to the trajectory of a particle passing through the optical center of the spectrometer magnets. The coordinate system used is relative to this trajectory. The distance measured along the central ray is denoted by Z, while the horizontal and vertical distances measured relative to the central ray are X and Y respectively. The other important coordinate quantities to define are δ which is the percent deviation of a particle's momentum from the spectrometer central momentum, θ which is the horizontal scattering angle at the target, and φ which is the vertical scattering angle at the target. The first order optical properties of the magnets are shown in Figure 2.4 and
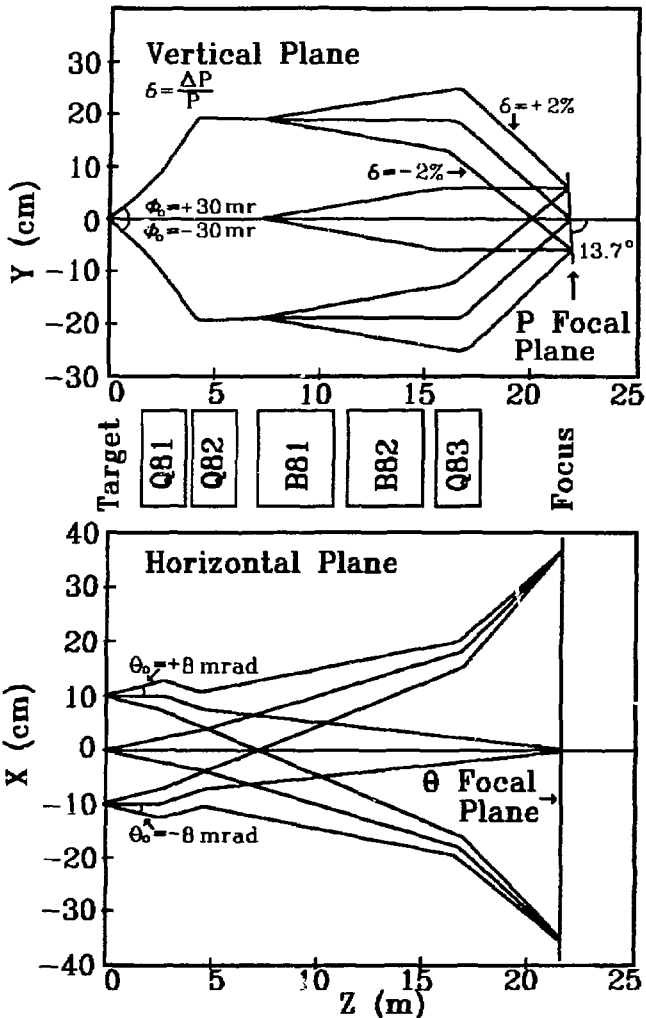
Figure 2.4: First order focal properties of the 8 GeV spectrometer. X and Y are measured horizontally and vertically from the central ray respectively, while Z is the distance along the central ray.
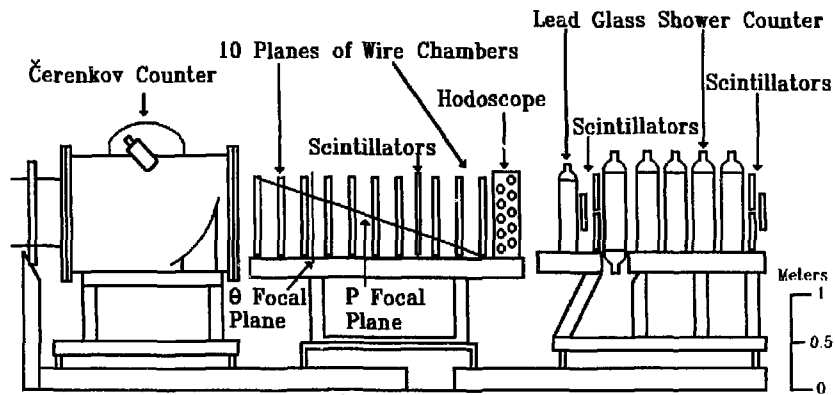
Figure 2.5: The 8 GeV spectrometer hut detectors.

the position and orientation of the focal planes relative to the wire chambers are shown in Figure 2.5. A study of the optical properties of this magnetic spectrometer has been made and the results are recently available [30].

Čerenkov Counter

When a particle passes through a dielectric medium with a velocity exceeding the velocity of light in that medium then Čerenkov radiation is produced. The purpose of the threshold Čerenkov counter is to separate electrons from a background of lower velocity particles (predominantly pions). The Čerenkov counter used in the 8 GeV spectrometer hut was 3.30 meters long and had 0.41 mm thick type 2024 aluminum entrance and exit windows. A spherical mirror, located 3.15 meters from the entrance window, collected Čerenkov light and focused it onto a phototube. The mirror was 6.4 mm thick aluminized lucite with a coating of magnesium fluoride to prevent oxidation and to enhance the reflection of ultraviolet and visible light. The phototube was an RCA 8854 quantacon phototube chosen for its high gain and good efficiency. The phototube was coated with a wavelength shifter to shift the ultraviolet light to the visible range where the photocathode was most sensitive. The gas used was nitrogen at 450 mm of Hg which has an index of refraction of 1.000165 at a temperature of 18° C. This translates to a threshold of 28 MeV/c for electrons and 7.5 GeV for pions. Because the spectrometer momentum was always set lower than 7.5 GeV, pions could only produce signals through the production of "knock-on" electrons in the entrance

plate of the counter. These electrons can produce Čerenkov radiation. The knock-on probability of a pion producing a detectable electron increases with pion momentum and ranged from 0.008% to 0.06% for this experiment.

Wire Chambers

Immediately following the Čerenkov counter were ten planes of multiwire proportional counters [31]. A charged particle passing through a chamber produced ionized atoms and electrons in the gas which, because of the high voltage applied, were accelerated and produced more ionization. The result was an avalanche of particles which collected on the nearest anode wire producing a signal proportional to the original amount of ionization.

The 20 μm anode diameter wires were made of gold plated tungsten and were spaced at 2.0 mm intervals. The active areas of the chambers were 35 cm by 93 cm. The P chambers, which measured the particles' momenta, had 176 anode wires and the T chambers, which measured the scattering angle, had 480 anode wires. Because of the long wire length, a support wire was necessary in each of the P chambers to prevent electrostatic instabilities that could have impaired the performance of the chamber. The support wire was made of teflon coated beryllium and its presence produced a nearby region where the field was depleted. The wires in the T chambers were slanted at a 30° angle relative to the Y direction in the hut. The cathode planes were made of 0.05 mm thick aluminum coated mylar and sat 4.0 mm on either side of
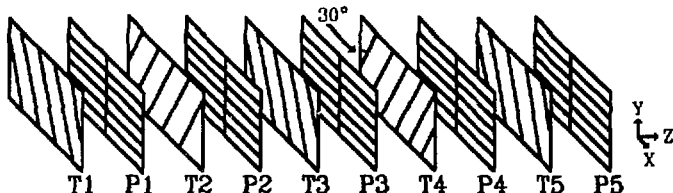
Figure 2.6: 8 GeV wire chambers indicating wire orientation.

the anode wire planes. A high voltage of 3.6 kV was applied for this experiment. The gas used, called "magic gas" was composed of 65.75% argon, 30.00% isobutane ($(CH_3)_2CHCH_3$), 4.00% dimethyl acetal formaldehyde ($CH_2(CH_3)_2$), and 0.25% bromotrifluoromethane ($CBrF_3$). This gas flowed continuously through the chambers at a rate of 5 cc/minute.

Scintillators and Hodoscope

Plastic scintillators [32] are made from polymerized styrene which has been infused with an organic scintillator material such as anthracene or stilbene. A charged particle passing through the material produces ionization which in turn excites molecular states of the scintillator material. De-excitation occurs in the form of fluorescence. It is emitted isotropically about the particle trajectory in just a few nanoseconds. Transparent light guides made of lucite are generally used to couple the scintillator to a phototube.

The positions of the three planes of scintillators and the hodoscope are shown in Figure 2.5. The first plane, SF, consisted of five 15.2 by 22.1 cm long strips which lay

vertically and overlapped partially in the horizontal direction. The SF's had phototubes on the top end. The second plane, SM, and the third plane, SR, consisted of three 16.5 by 114.3 cm long strips which lay horizontally. The SM's and the SR's had phototubes on both ends.

The hodoscope was 15.2 cm thick and was composed of four planes, two segmented vertically and two horizontally. The vertically segmented planes had five left and five right scintillators which were 5.1 by 48.3 cm long and spaced 1.9 cm apart. The planes were aligned so that the gaps in one plane were covered in the other plane. The horizontally segmented planes had eleven scintillators which were 5.1 by 36.2 cm long and spaced 3.8 cm apart. These planes were also aligned so that all gaps were covered. The phototubes used were Hamamatsu R239 phototubes with a high voltage of 1800 Volts.

Lead glass shower counter

The purpose of the lead glass shower counter, shown in Figure 2.7, was to measure the energy deposited by an incident particle and to help in distinguishing between electrons and pions. A highly energetic electron entering the counter will interact with the material and produce both Čerenkov and bremsstrahlung radiation. The bremsstrahlung photons can convert into electron-positron pairs which can also interact with the material producing, after several stages, a shower of Čerenkov photons which are measured by the phototube. Pions entering the counter can only produce an electromagnetic shower by first undergoing a photon producing charge exchange
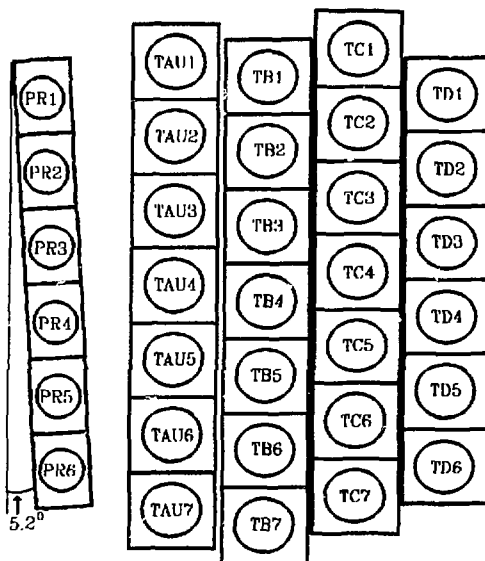
Figure 2.7: Lead glass shower counter as viewed from above.

interaction ($\pi^- p \to \pi^\circ n$, $\pi^\circ \to 2\gamma$). The photons can pair-create to produce the shower. Segmentation of the counter along the direction of the particle path aids in pion discrimination since a shower produced by a pion is more likely to occur farther into the counter than an electron shower.

The 8 GeV spectrometer lead glass shower counter was segmented into five layers with six to seven blocks in each layer. The first layer, called the pre-radiator (PR) since electrons have a high chance of showering here while pions do not, contained six F-2 type Pb-glass blocks, each having a thickness of 10.4 cm (3.22 radiation lengths). These blocks were 32 cm tall, 15.8 cm wide, and had a refractive index of

1.6200. The entire row was rotated 5.2° about the hut vertical axis to suppress the number of particles traveling through the cracks between the blocks. The phototubes used were Amperex XP2041 for all the blocks.

The next four layers of blocks were made of SF-5 type Pb-glass and formed the total absorption counter (TA,TB,TC and TD). This experiment did not use the last layer because the most energetic electrons observed were well stopped by the TC layer. The three rows used each contained seven blocks and had a thickness of 14.6 cm (6.8 radiation lengths). The blocks were 40 cm tall, 14.9 cm wide and had a refractive index of 1.6727. The TA row was the only row to have phototubes placed on the top and bottom of the blocks. This was to maximize the light collection since most of the electron's energy was lost in this layer. For spectrometer momentum settings greater than 4.0 GeV 50 dB attenuators were used on the raw signals for the TA, TB, and TC blocks to keep the signals from saturating the electronics. Detailed information on the shower counter calibration and performance is given in appendix B.

1.6 GeV Spectrometer and Detectors

The 1.6 GeV spectrometer, shown in Figure 2.8, consisted of two 10Q18 quadrupole focusing magnets and one 90° dipole bending magnet. The quadrupoles were 75 cm long each and were mounted on this spectrometer for the first time in this experiment. A fixed slit collimator located 28.8 cm from the target and before the first quadrupole restricted the vertical scattering angle of the electrons to be less than 120 mr
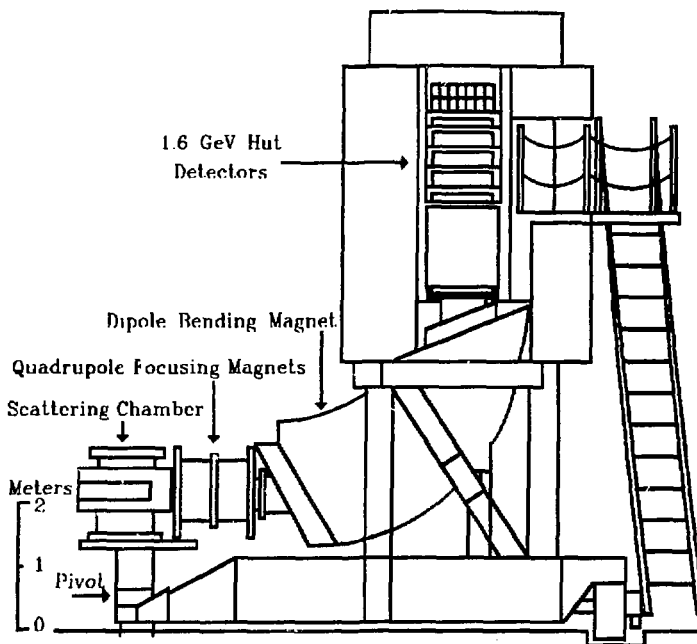
Figure 2.8: The 1.6 GeV spectrometer.

relative to the central angle. The collimator was made from lead and tungsten. The momentum of the dipole was monitored with an NMR probe between all data taking runs. It was inserted into the uniform field region remotely. The spectrometer central momemtum, E′, was then calculated from the relation:

$$E'(GeV) = 0.075 \cdot B \qquad (2.2)$$

where B is the magnetic field measured by the NMR probe in kG. The particle detectors were located in a shielded hut area

above the dipole magnet. This spectrometer sat at a fixed
scattering angle of 90° for the entire experiment.

Optical Properties

With the quadrupole magnets in place, this spectrometer
was capable of analyzing particles up to a maximum momentum of
0.8 GeV/c (with no quads, the maximum momentum is 1.5 GeV/c).
Like the 8 GeV spectrometer, it was designed for point to
point focusing in the bend plane for particles of the same
momentum and for line to point focusing in the non-bend plane
for particles with the same scattering angle [33]. In order to
achieve the line to point focusing the dipole was designed
with slanted entrance and exit pole faces which effectively
produce quadrupole focusing in the horizontal plane. In order
to make the two focal planes coincide in the hut the dipole
was designed with three sextupole regions produced by curved
pole faces. The effect of the quadrupole magnets, whose
magnetic fields were inadvertently set lower than desired, was
to shift the vertical focal plane by three meters. The
coordinate system used for this spectrometer is slightly
different from that of the 8 GeV spectrometer. The distance
measured along the central ray is still denoted by Z, but the
horizontal and vertical coordinates are switched. Y is the
horizontal position relative to the central ray and X is the
vertical position. The coordinate, δ, is still the percent
deviation of a particle's momentum from the spectrometer's
central momentum, and θ and φ are the horizontal and vertical
scattering angles. The optical focusing properties of the
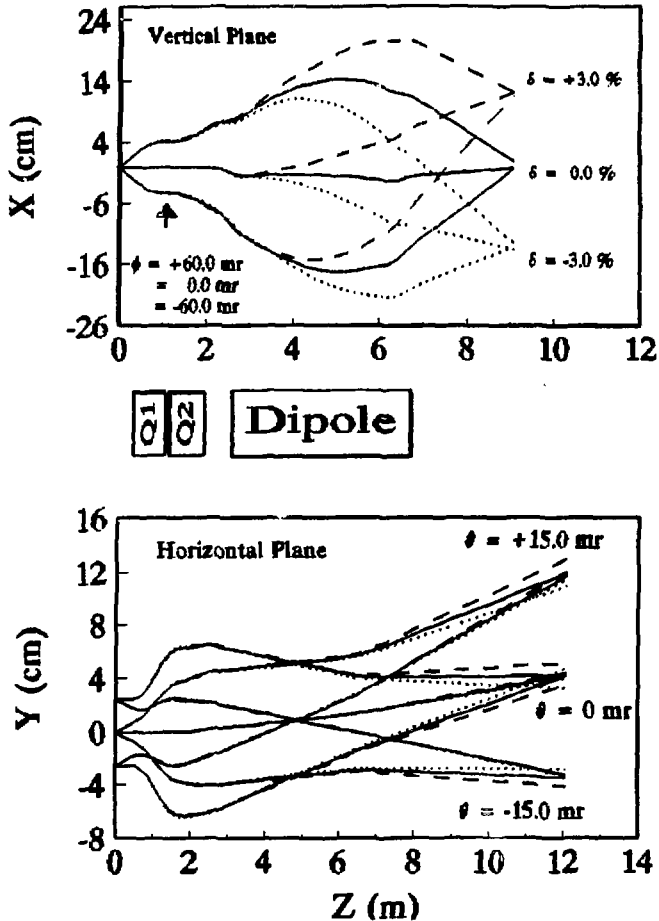
Figure 2.9: Focal properties of the 1.6 GeV spectrometer. The different line types in the horizontal plane figure indicate momentum dispersion. The lines correspond to δ = +2.0% (Dashed), δ = 0.0% (Solid), and δ = -2.0% (Dotted).

magnet are shown in Figure 2.9 and the design focal plane,
located at Z ~ 9 m, relative to the hut detectors is indicated
in Figure 2.10. Note that in Figure 2.9, the horizontal plane
optics are focused at Z ~ 11.5 m instead of the design focal
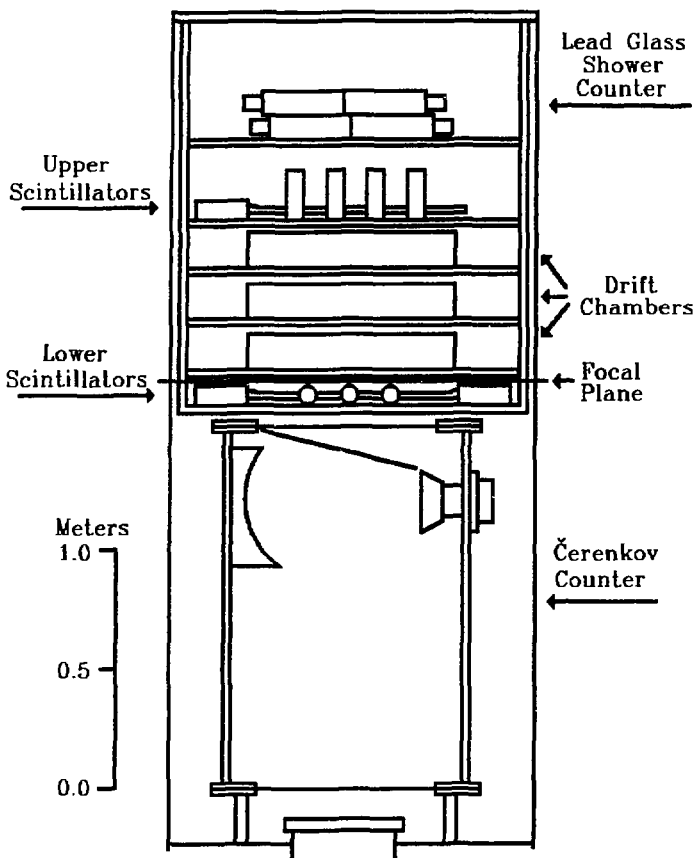
Figure 2.10: The 1.6 GeV spectrometer hut detectors as
seen from the direction of the target.

plane. This is because the quadrupoles fields were inadvertantly set slightly lower than desired during the experiment.

Čerenkov Counter

The Čerenkov counter used in the 1.6 GeV spectrometer was 1.4 meters long, had a diameter of 1.1 meters, and had 0.041 cm thick entrance and exit windows made of 6061 type aluminum. A 0.025 mm thick aluminized mylar mirror sat 1.2 meters from the entrance and was tilted 28° about the X coordinate axis in the hut in order to focus the light onto a spherical mirror. The spherical mirror was made from machined lucite with nickel and aluminum deposited on the surface to form the mirror and a coating of magnesium fluoride to prevent oxidation and improve on ultraviolet light reflection. The spherical mirror was tilted 18° about the X coordinate axis and focused the light onto a five inch diameter RCA 8854 quantacon phototube which had been coated with a wavelength shifter. Mounted around the phototube was a light cone made from aluminized lucite needed to increase the light collection. The cone extended 10.2 cm from the face of the phototube, had an angle of 27°, and increased the area of light collection from a five inch to an eight inch diameter circle. The mirrors were laser aligned before this experiment to optimize the focusing onto the phototube and light cone. The gas used was carbon dioxide (CO_2) at atmospheric pressure which has an index of refraction of 1.00045 at room temperature. This translates to a threshold of 17 MeV/c for electrons and 4.7 GeV/c for pions. A high

voltage of 2650 Volts was applied to the phototube.

Drift Chambers

There were three drift chambers in the 1.6 GeV spectrometer hut. Each drift chamber consisted of two X planes and two Y planes and several layers of foil. A cross section showing the wire configuration in one of the drift chambers is shown in Figure 2.11. The entrance and exit foils in the chambers were made of 0.076 mm thick aluminized mylar. Each plane of wires was sandwiched between foils made of aluminized kapton for a total of five kapton foils in each chamber. Field shaping wires, needed to create a uniform electric field around each anode, alternated every 1.0 cm with the anode wires. The distance between anode wires in each plane was 2.0 cm, but since the planes in a set were only 0.9 cm apart, they were treated as one plane of wires with 1.0 cm wire spacing. Each chamber had 62 X wires and 42 Y wires. A gas composed of 89.06% argon, 9.92% CO_2, and 1.02% methane flowed continuously through the chambers at a rate of 20 cc/minute.

When a charged particle goes through a drift chamber, ionization is produced in the gas. The chambers were designed so that the fields in the vicinity of a given wire are shaped to produce a constant drift velocity for the ionization. Thus, by measuring the drift times for pairs of wires which produce signals the actual position that the particle traversed can be measured. The anode wires were 0.2 mm in diameter and had a high voltage applied of around 1850 Volts. The field shaping wires were at a voltage of -500 Volts and the kapton foils

Field shaping wires   Anode wires
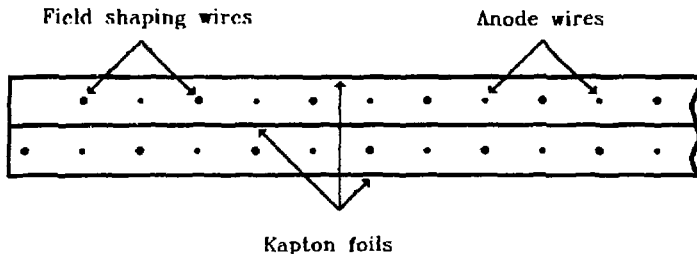
Kapton foils

Figure 2.11: Partial cross sectional view of a set of drift chamber wire planes (either X or Y) indicating anode and field shaping wires and kapton foils. The wire diameters have been exaggerated in this view.

were kept at ground.

Scintillators

There were four planes of scintillators in the 1.6 GeV spectrometer hut. Two of these planes were segmented in X and two were segmented in Y. The scintillators had light guides and phototubes at both ends except for the upper layer of X scintillators which only had phototubes at one end. There were five lower X (XD's), three lower Y (YD's), six upper X (XU's), and four upper Y (YU's) scintillators. The scintillators were 11 cm wide and were mounted to overlap slightly to prevent cracks. The high voltages applied ranged from 1800 to 2200 Volts and RCA 8575 phototubes were used.

Lead Glass Shower Counter

The 1.6 GeV spectrometer lead glass shower counter was segmented into two layers along the direction of particle

traversal with fourteen blocks in each layer. The fourteen blocks were placed in a 7x2 configuration. The first layer was called PA and the second layer was called PB. The blocks were made of SF-6 type Pb-glass which has a refractive index of 1.8052 and measured 10 by 10 by 25 cm. The total radiation length of the counter was 11.9 r.l. The second layer was offset slightly in Y to prevent the particles from traveling entirely through the crack and escaping detection. The phototubes used were three inch Hamamatsu R1911 and the applied voltages ranged from 1400 to 1900 Volts.

Electronics

8 GeV Electronics

The raw signals from the detectors were sent to fast electronics modules located in the ESA counting house via heliax cables for important trigger components and by coaxial cables for other components. The electronics implemented commercially available NIM and CAMAC modules. The raw lead glass phototube signals, PR's and TAD's, and the scintillator phototube signals, SF's and SM's, were fed into separate linear fan-out units which produced input signals for the analog to digital converters (ADC's) and the discriminators. The ADC's recorded pulse height information, and the discriminators provided logic signals for trigger formation, latches, scalers, and time to digital converter (TDC) stop gates. The raw PR and TAD signals were also summed before being sent to a discriminator for use in the trigger electronics. The SF discriminator signals were all sent to the

same logical OR, and the SM discriminator signals were sent to a logic OR after the signals from the same scintillator but different phototubes, had been time averaged. The discriminator settings for signals important to the trigger are given in Table 2.2.

Table 2.2: Discriminator threshold settings.				
Signal	Č	SF	SM	PR	TAD
Disc (mV)	30	40	40	60	60

A simplified schematic drawing of the 8 GeV electronics is shown in Figure 2.12. The trigger was designed to maintain a high electron detection efficiency while giving good background pion rejection. The first level of the trigger had three components, the El-Hi, El-Lo, and PION. El-Hi required three out of the four signals ČK, PRSUM, TADSUM, SM_OR. This combination worked well at higher momenta to detect electrons and discriminate against pions. At lower momenta, when the electron shower can be completely contained in the PR layer, El-Hi loses efficiency. Thus, El-Lo, which always required a ČK signal, was used for increased efficiency at the lower momenta. In addition, El-Lo required two out of the three signals PRSUM, SF_OR, and SM_OR. The PION component required both the SF_OR and the SM_OR signals and was used to monitor the pion background. This trigger was efficient at measuring any charged particle passing through including electrons.

Next, the PION signal was prescaled by a factor which ranged from 2^8 to 2^{11} for this experiment. The prescale factor was chosen so that sufficient pions were detected for analysis
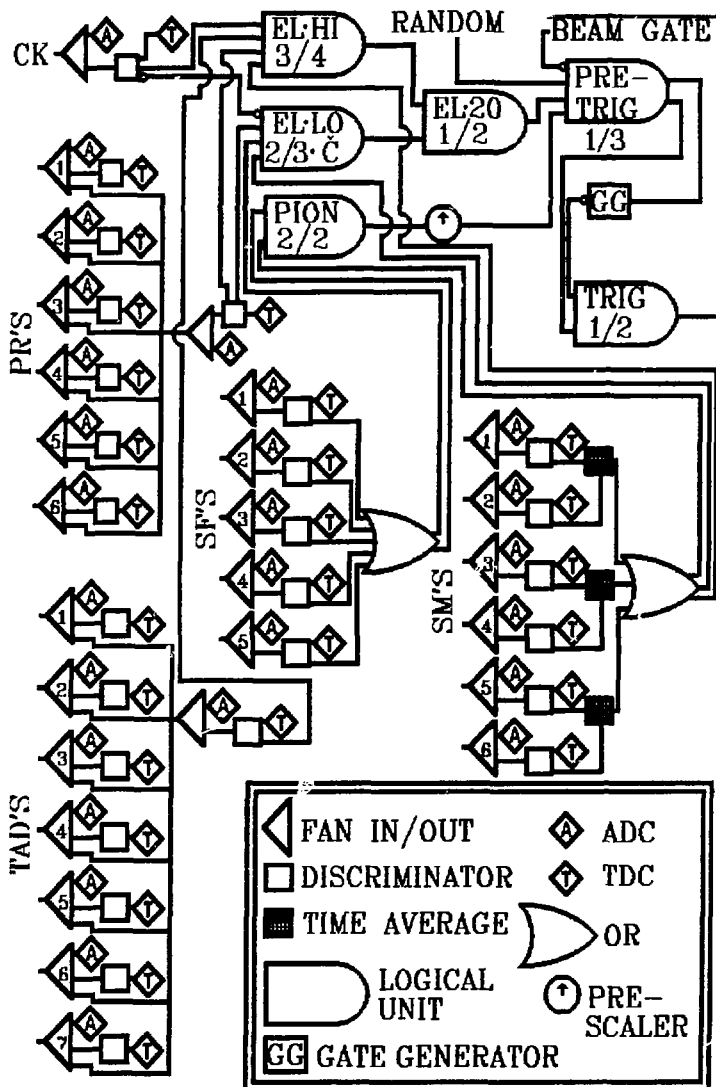
Figure 2.12: 8 GeV spectrometer trigger electronics.

and study of detector performance, but not so many that the electron measurement was hindered. The El-Hi and El-Lo signals entered a logical OR to form the El-20 signal which had a width of 20 ns. Also formed at this stage were El-40, El-60, and El-80 which were the same as El-20, but they had widths of 40, 60 and 80 ns respectively. These electronics were included for measuring electronics deadtime. Additional electronics for the deadtime measurement included the PTC-20, PTC-40, PTC-60, and PTC-80 signals where PTC was a coincidence signal formed from the PR, TAD and Č signals. The number indicates the gate width and the signals are counted by scalers. El-20, and PION_PRESC entered the PRETRIG logical unit along with RANDOM. RANDOM was a random pulse generated approximately every ten seconds to monitor the pedestal levels of the ADC electronics and to examine the noise levels in the multiwire proportional chambers. PRETRIG required one of these three signals along with a beam gate which signaled the presence of the beam. Due to limitations on the rate at which the computer could log event information, it was necessary to restrict the trigger rate to once per beam pulse. This was the purpose of the gate generator located between PRE-TRIG and TRIG. The gate generator allowed only the first PRE-TRIG signal through by creating a gate lasting longer than the beam pulse which masked further PRE-TRIG signals. Once TRIG, the final trigger, was formed it was used to send an interrupt signal to the computer to indicate that the electronics information should be read and logged. TRIG was also used for the TDC start pulses, the gates on the ADC's and the reset signals for the

latches.

There was also additional electronics not shown in Figure 2.12. The multiwire proportional chamber signals were read whenever a TRIG signal was formed. Readout cards were mounted on the chambers themselves. Each card could handle a group of eight wires and contained amplifiers and dual one shot delays for a total delay of 900 ns. These delayed signals were latched if a trigger was formed and were read out serially by a CAMAC wire chamber readout module which processed the data for logging onto magnetic tape. There was a limit of 64 wire groups which could be stored per trigger. The electronics also included many scalers such as those needed to calculate deadtime and one-per-pulse corrections which are discussed in the next chapter, and coincidence modules for monitoring accidental coincidences between various trigger components.

1.6 GeV Electronics

The raw PA and PB were first sent to amplifiers. The amplifier outputs were sent to ADC's, and then in groups of four, the signals were sent to fan in/out modules. The output of the fan in/out were sent to a discriminator, which produced logic inputs for the TDC's and scalers, and to another fan in/out module where all the signals in a given layer were combined. The PA combined signal was sent to two discriminators with high and low discriminator thresholds giving PA_HI and PA_LO. The PA and the PB signal were fanned in together and sent to a discriminator to form the SH signal, and the PB was sent to a discriminator to form the PB signal.

The drift chamber wire signals were processed separately for each individual wire. Each signal was first fed into a discriminator to widen the pulse and then to a gate and delay circuit designed to reduce spurious noise in the chambers. The signals were delayed about 400 ns. and then gated with a trigger induced 400 ns. gate to produce the wire chamber TDC starts. The trigger forms the TDC stop.

The scintillator signals were sent directly to discriminators which produced TDC inputs and inputs to logical OR units for combining the signals in a given layer of scintillators. These signals are called XDOR, YDOR, XUOR, and YUOR. XDOR and YDOR formed the SD signal, and XUOR and YUOR formed the SU signal through logical AND modules. Also, the SC signal was formed by requiring three out of the XDOR, YDOR, XUOR, and YDOR signals. The discriminator threshold settings for important trigger components are shown in Table 2.3.

Table 2.3: Discriminator threshold settings.					
Signal	Č	PALO	PAHI	PB	SH
Disc (mV)	100	280	550	150	750

A simplified trigger electronics diagram is shown in Figure 2.13. Like the 8 GeV trigger, the 1.6 GeV trigger was designed for high electron detection efficiency and good pion rejection while allowing a controlled sample of pions to generate a trigger. The trigger components were similar to those in the 8 GeV electronics. El_Hi required PA, SH, and SC to all be true. El-Lo required ČK, and two out of three of the PA, SU, and SD signals. PION required SC and NO_ČK and was
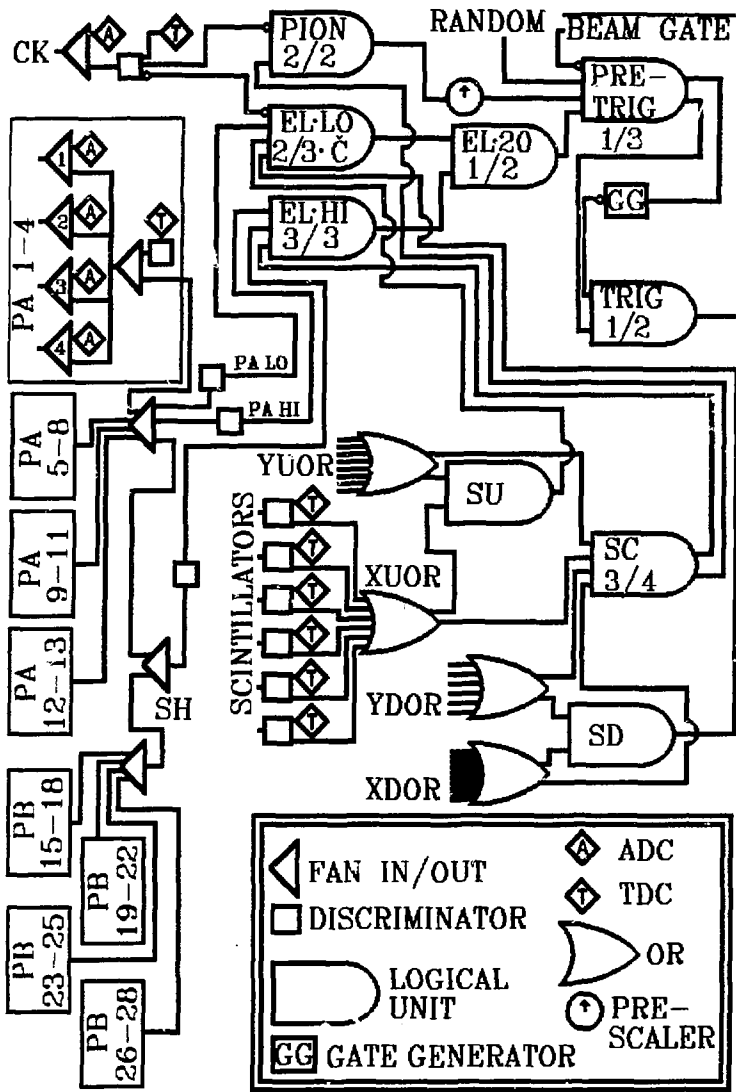
Figure 2.13: 1.6 GeV spectrometer trigger electronics

prescaled by a factor ranging from 2^8 to 2^{11} forming the *PION_PRESC signal*. *EL-20 was formed from an OR of El-Hi and El-1* and PRETRIG required the beam gate and one out of El-20, PION_PRESC, and RANDOM which was the same random trigger used for the 8 GeV electronics. TRIG was formed from the PRETRIG output using a gate generator to restrict the triggers to one per beam pulse similarly to the 8 GeV electronics. TRIG signaled the computer to read the electronics and generated TDC start signals, ADC gates and latch gates, and the common stop for the drift wire chamber TDC's.

Additional electronics not shown in Figure 2.13 included many scalers such as those needed to calculate important corrections like deadtime and one-per-pulse corrections which are discussed in detail in the next chapter. Also, there were several coincidence modules used to monitor random coincidences between key trigger components.

Data Acquisition

Electronics data were interfaced to a PDP-11 computer for each event via CAMAC electronics and were read every time a trigger interrupt was sent. The PDP transferred the information to a VAX 11/780 computer for magnetic tape logging and for an online sampling analysis of the events. The online analysis was very important for diagnostic testing of most aspects of the experiment. The VAX was also responsible for monitoring at a sampling rate of every ten seconds such quantities as target temperature measurements, magnet currents and high voltages. A link between the VAX and MCC
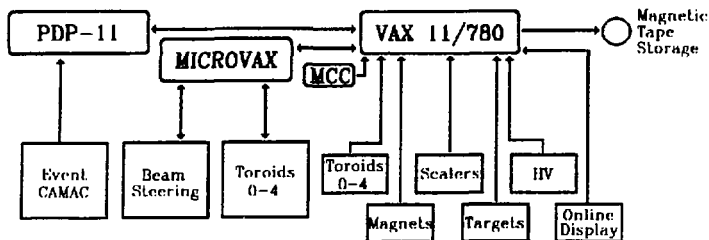
Figure 2.14: Data acquisition system

provided important information on the beam energy and the slit
setting. The microvax computer controlled beam steering,
toroids, and monitored the cavities and wire arrays. It
transferred this information to the VAX for tape logging. A
schematic diagram of the data acquisition system is shown in
Figure 2.14.

3. DATA ANALYSIS

Introduction

The experimental data, as stored on magnetic tape, were divided into many "runs" which differed in kinematic settings and the target type. Generally, several runs made up a kinematic point and targets were routinely rotated. The data analysis, from the raw data stored on magnetic tapes to the final results, consisted of several distinct stages as shown in Figure 3.1. The purpose of the first stage, PASS 0, was to rewrite the magnetic tapes so as to exclude bad or aborted runs and to remove any useless data. During this condensing process, a large data file was created to store important checkpoint information for each run. A checkpoint was a subdivision of a data run defined to be three minutes of real running time. If a problem occurred within a checkpoint, the checkpoint could be eliminated rather than the entire run. Also, a checkpoint could be eliminated for one spectrometer's data and not the other's. A careful study of possible checkpoint problems was made taking into consideration such things as magnet stability, beam steering, scaler counting rates, etc... When a bad checkpoint was found a flag in the data file was set accordingly so that the checkpoint was not included in the subsequent analysis.

The second stage (PASS 1) included event selection, tracking, detector performance studies and spectrometer optics studies. During this stage a new data file was created containing events histogrammed in reconstructed δ and θ at the target for each run. As discussed earlier, δ is defined to be
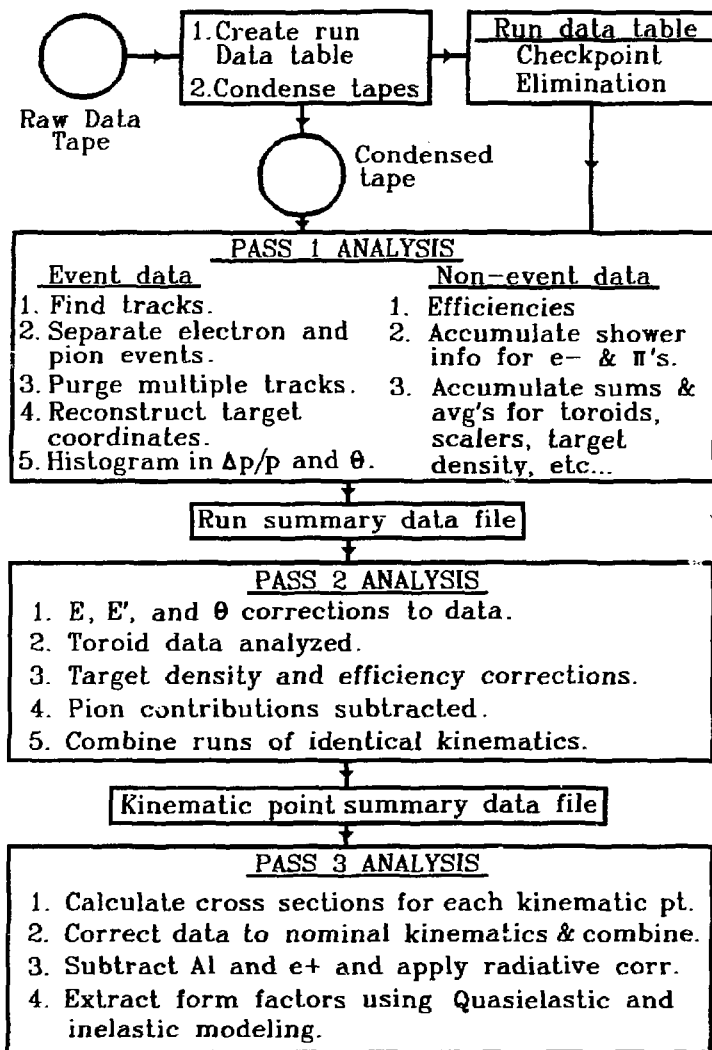
Figure 3.1: Flow chart showing the stages of the data analysis.

the percent deviation of the particle's momentum from the spectrometer central momentum, and θ is the horizontal scattering angle at the target. Histograms were saved for both electrons and pions and for several different cuts on the vertical scattering angle. Also stored in this data file were shower counter energy spectra corresponding to each of the saved δ-θ histograms, Čerenkov ADC spectra, efficiency information, scalers, and toroid and beam steering information. At this point all data were stored on the computer hard disk and magnetic tapes were no longer necessary.

In the third stage, PASS 2, runs of identical kinematics and target were combined. Pion contributions to the electron spectra were calculated and subtracted, incident charge on the target was calculated with all the necessary corrections, all energy, momentum, and scattering angle corrections were made, and target density corrections were made. A new data file was saved for each spectrometer. The data files contained, for each kinematic point, the summed δ-θ histograms still saved for several vertical angle cuts, kinematic information, and the necessary corrections for conversion to cross section.

The final stage of the analysis, PASS 3, converted the data into cross sections, $d\sigma/d\Omega dW^2$, using the spectrometer acceptance function and the corrections saved in PASS 2. W^2 is the missing final mass state of the hit nucleon which, after correcting for the slight θ dependence is equivalent to E', the scattered electron energy. Kinematic points which slightly overlapped were corrected to the same kinematics and were

combined. Aluminum and positron contributions were subtracted and radiative corrections were applied. The analysis then split into the inelastic and the quasielastic analysis. The goal of the inelastic analysis was to study and fit the hydrogen inelastic data and to determine the contribution of the inelastic tail at the deuteron quasielastic peak by smearing the hydrogen fits with models. The quasielastic analysis involved understanding the shape of the peak due to smearing effects, making relativistic corrections and extracting the form factors.

8 GeV Event Analysis

Tracking

The track finding procedure [15] was similar for both the P-type and T-type chambers which were discussed earlier. Tracks in the vertical direction were found with the P-type chambers and those in the horizontal direction were found with the T-type chambers. Adjacent wires which fired in a chamber were treated as a group. The "hit" position in a given chamber was defined as the centroid of the group randomized by one wire spacing, ±0.5 mm. The tracking algorithm looped over pairs of chambers. If both chambers in the pair contained hits a line was defined and the remaining chambers were checked for hits passing through the same track. Final tracks were found by doing a linear least squares fit including all chambers with hits. These tracks required at least three P-type and three T-type chambers and at least seven chambers total. In the event that multiple tracks were found purging was done

based on the shower energy for the tracks, the reconstructed target coordinates, XPLANE cuts, the hodoscope, the number of total chambers in the fit, and the chi-square of the fit. XPLANE was a quantity defined by the X and dX coordinates in the hut, where dX is the name given to dX/dZ or the horizontal angle in the hut. Similarly, the quantity dY is really dY/dZ or the vertical angle in the hut. The XPLANE distribution for many events was very sharply peaked around zero if the particle track rays pointed back to the target. This quantity was closely related to the reconstructed target position along the length of the target.

The tracking efficiency for electrons was measured using a clean sample of electrons which was obtained by requiring a Čerenkov signal above an ADC value of 50, and by requiring the energy deposited in the lead glass shower counter (normalized to the particle momentum as measured by tracking) to be between 1.0 and 1.7. This high cut on the deposited energy helped insure that the calculation was for electrons and not pions. Also, the efficiency calculation required that at least one and no more than three scintillators fired in the vertically segmented hodoscope and also in the horizontally segmented hodoscope. Edge scintillators were not included in this requirement to avoid using tracks which skimmed along the wire chamber edges and generally did not reconstruct to the target well. The measured efficiency was 0.9991. Kinematic quantities at the target were reconstructed from each event measured in the hut using the spectrometer reverse matrix coefficients given in Table 3.1 assuming that X and Y are in

Table 3.1: First and second order reverse TRANSPORT coefficients for the 8 GeV spectrometer giving target coordinates, x,θ,φ, and δ in terms of hut coordinates at the focal plane. OFX and OFDX are momentum dependent offsets given by:
$OFX = -0.6832 + 0.0017|E_c'| + 0.0044|E_c'|^2$,
$OFDX = -0.8019 - 0.0025|E_c'| + 0.0049|E_c'|^2$, where E_c' is the spectrometer central momentum.

	x (cm)	θ (mr)	φ (mr)	δ (%)
X (cm)+OFX	4.88079	0.20871		
dX (mr)+OFDX	-4.57703	0.00916		
Y (cm)			-0.03381	-0.33793
dY (mr)			-0.92823	0.00028
X·X			0.00297	0.00011
X·dX			-0.00572	-0.00025
X·Y	0.00924	0.01547		
X·dY	0.00062	0.00015		
dX·dX			0.00269	0.00014
dX·Y	-0.00436	-0.01471		
dX·dY	-0.00071	-0.00017		
Y·Y			-0.00516	0.00017
Y·dY			-0.00050	0.00136
dY·dY			-0.00002	

cm and dX and dY are in mr. Target coordinates are obtained by multiplying the hut coordinates by the coefficients in Table 3.1 and summing over the nonzero contributions where a blank spot in the table means the coefficient is zero. These coefficients were obtained from a TRANSPORT [34] model which was tuned to agree with measurements of the forward matrix elements made using a floating wire technique [30]. Since only four quantities were measured by the wire chambers and there are five target coordinates $(x,y,\theta,\varphi,\delta)$, it was necessary to assume that the particle originated from the central beam axis in the vertical direction in order to obtain a one-to-one correspondence. That is, no distribution in reconstructed y was allowed. This is a reasonable assumption given that the beam spot size in the vertical direction was

only on the order of three millimeters.

Electron and pion identification

Once a single good track was found in the wire chambers, the event was required to satisfy several criteria as listed here to be called an "electron":

1. The track must have been inside the good fiducial region defined by the active area of the hut detectors which was limited by the size of the lead glass shower counter.

2. The Čerenkov ADC signal must have been higher than 50 channels.

3. The track shower energy normalized to the momentum of the particle track must have been greater than 0.7.

4. The reconstructed kinematic quantities must have been within the acceptance of the spectrometer defined as:

   $|\Delta p/p| \leq 3.6\%$, $|\Delta\theta| \leq 6.4$ mr, and $|\Delta\varphi| \leq 28$ mr.

"Pion" events were also defined and were required to satisfy the following criteria:

1. The event was required to satisfy both criteria 1 and 4 of the electron definition.

2. There must not have been a Čerenkov ADC signal above the pedestal.

3. The normalized track shower energy must have been less than 0.6.

4. The normalized track shower energy seen in the first layer of blocks, PR, must have been less than 0.2.

5. The pion latch in the electronics must have been set.

This latch should have been set for any particle which passed through the spectrometer since it depended on scintillator signals only. It was needed to discriminate against random events, and to get the correct pion prescaling factor.

The electron and pion events were histogrammed separately in reconstructed θ and $\delta = \Delta p/p$ where the θ bins were 0.8 mr. wide and the δ bins were 0.2% wide.

Shower Energy

Electron and pion events can be distinguished from each other by looking at the normalized energy deposited in the shower counter. Raw ADC signals with pedestals subtracted were converted into energy for each block using the shower block calibration data as discussed in detail in Appendix B. The energy for each track was then calculated by summing over the energy of the blocks through which the track passed as well as adjacent blocks. Adjacent blocks were included to capture *possible light leakage due to the transverse spread of the* shower in the lead glass blocks. The layer of TC blocks was only included in this sum for spectrometer momenta greater than 4.0 GeV/c. The energy was then normalized by dividing by the measured particle momentum as defined by the measured hut coordinate, Y, and the leading order reconstruction coefficient (See Table 3.1).

A typical shower spectrum for a deuterium target is shown in Figure 3.2 indicating the same shower energy spectrum for those events which did not fire the Čerenkov counter and for

(a)   (b)
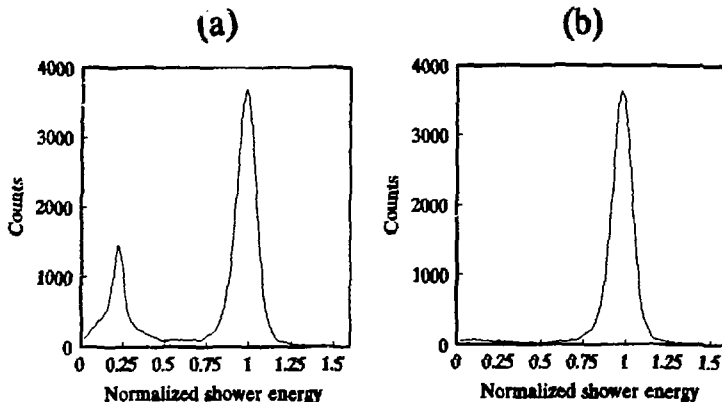
Figure 3.2: (a): Typical shower spectrum for the 8 GeV
spectrometer shower counter requiring a track found in the
wire chambers. (b): Same shower spectrum as in (a) except
with the additional requirement of getting a Čerenkov ADC
signal above 50.

those events which had a Čerenkov ADC cut above 50. Both
spectra required that a track was found. The first spectrum
contains a large pion contribution and thus shows the shower
counter response to pions. The second shows that requiring the
Čerenkov signal greatly reduces the pions in the spectrum, but
leaves the large electron peak at a normalized shower energy
of 1.0 intact. The average FWHM energy resolution of the
shower counter was $\approx$ 17.5%/$\sqrt{E'}$, and its efficiency for
detecting electrons above the shower cut of 0.7 was 99.4%.
This efficiency was measured on a run-by-run basis by
calculating the percentage of shower events above the cut of
0.7 for a clean electron sample. This electron sample was
obtained by requiring "electron" criteria 1, 2, and 4 defined
earlier with the additional restrictions that only one track
must have been found from the wire chambers (no track

purging), at least nine of the ten chambers must have fired, and the quantity XPLANE defined in the tracking section was required to be within cuts of ± 15.0 cm. A plot of the points used in the efficiency calculation are shown in Figure 3.3. These data are for hydrogen target runs with the ratio of pion to electron rates less than 1.0. This cut on π/e ratio was necessary because a large background of pions can skew the measurement of the electron efficiency. The efficiency from

8 GeV Shower Counter Efficiency
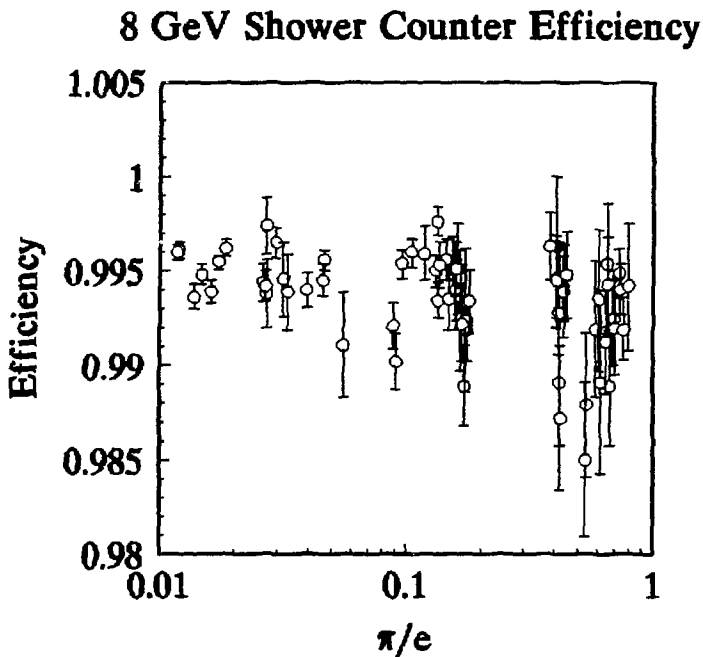
Figure 3.3: Calculated electron detection efficiencies for the 8 GeV spectrometer shower counter using hydrogen target runs where the ratio of pion to electron counting rates was less than 1.0.

the data in Figure 3.3 was calculated using an error weighted average.

Čerenkov Counter

Typical Čerenkov ADC spectra for electrons and pions are shown in Figure 3.4 for scattering from a hydrogen target. A Poisson curve was calculated for the electron spectrum using an average of 6.8 photoelectrons. The pion spectrum clearly shows a single photoelectron peak just to the right of the pedestal peak (which was truncated to emphasize the pion events). The position of the pion peak motivated using an ADC cut of 50 channels for improved electron identification.

A calculation of the efficiency was done using the Poisson fit and computing the fractional area above the ADC cut of 50. This calculation yielded an efficiency of 98.9%. The measured efficiency for detecting electrons above this ADC cut of 50 was found to be 99.0% which is in very good agreement with the calculated efficiency. The measured efficiency was calculated using an electron sample which required "electron" criteria 1 and 4 (see P. 50), the quantity XPLANE was required to be within cuts of ± 15.0 cm, and the normalized track shower energy was required to be greater than 1.0. This high shower cut was made to eliminate background pions from the pion tail and thus, to ensure a good electron sample. Figure 3.5 shows the measured efficiencies versus the ratio of pion to electron rates. These data points include hydrogen and deuterium target runs. The line shown is an error weighted fit to the data which yields the measured efficiency

8 GeV Cerenkov spectra
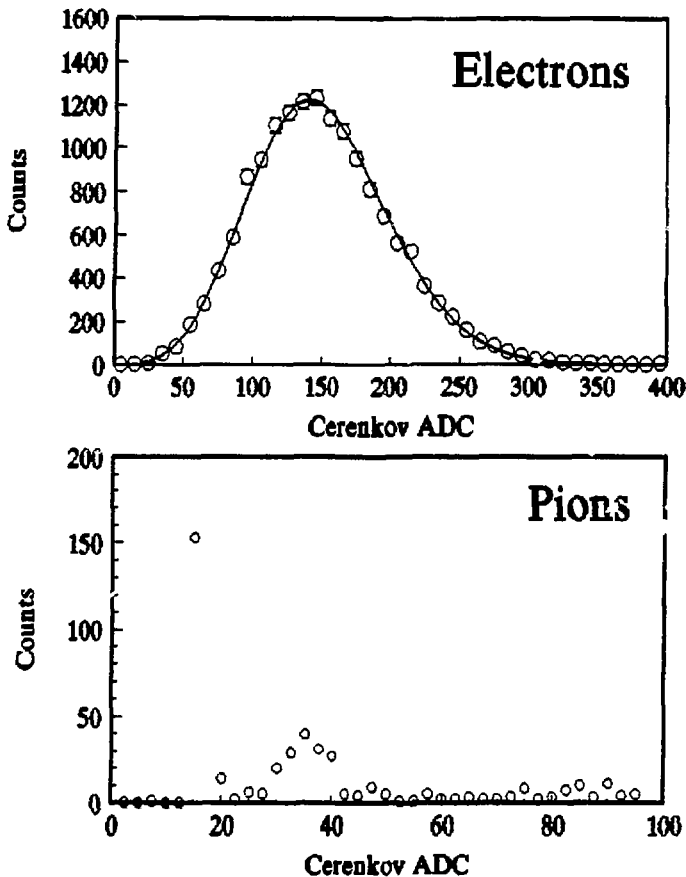
Figure 3.4: 8 GeV spectrometer Čerenkov counter ADC spectra for electrons and pions. A Poisson curve was calculated for the electron spectrum using an average of 6.8 photoelectrons. The small pion peak corresponds to one photoelectron.

8 GeV Cerenkov efficiency
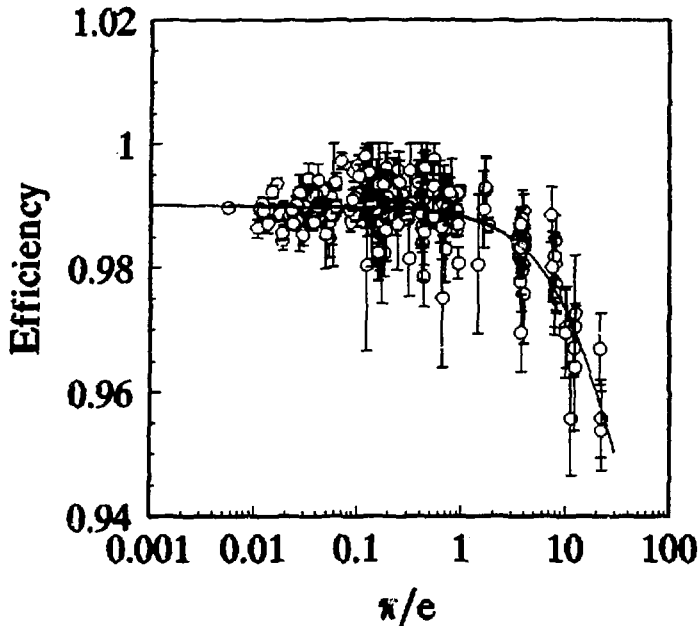
Figure 3.5: Run-by-run electron detection efficiencies versus π/e ratio for hydrogen and deuterium targets. A fit to the data is also shown which yields the measured overall efficiency at $\pi/e = 0.0$.

when extrapolated to a π/e ratio of zero. A study was made of the X and Y hut position dependence of the efficiency. No significant position dependence was found.

Pion subtraction

Pion subtraction was necessary to account for the small, but non-negligible probability of a pion event which fired the

Čerenkov counter and gave a normalized shower energy signal above the cut of 0.7. It was necessary to save shower spectra corresponding to the electron and pion definitions given earlier excluding the cuts on the shower energies. The pion peak in the pion spectrum was scaled down to the pion peak in the electron spectrum to obtain a scale factor using the sum of all the pion counts in the vicinity of the pion peak. The fraction of pion events above the cut was calculated from the pion spectrum.   By multiplying this fraction by the scale factor we obtained the fraction of pion events above the cut in the electron spectrum. Since it was not known which of the electron $\delta-\theta$ bins contained pions, the subtraction was done evenly on a bin by bin basis. Each bin of the pion $\delta-\theta$ histogram was multiplied by the fraction of pions above the electron cut and was subtracted bin by bin from the electron histogram. This produced a non-integer number of counts in each bin. This correction was calculated for each kinematic point, first summing the pion spectra for all the runs contained in the point. The largest corrections found were 0.075% for the hydrogen targets and 0.15% for the deuterium targets.

Efficiency, Electronic, and Computer corrections

A summary of the detector efficiencies discussed in the previous sections is given in Table 3.2. The total efficiency for detecting electrons was found by multiplying these individual efficiencies together since they were uncorrelated.

The electronic dead time correction was calculated using

Table 3.2: Summary of important efficiencies for analysis of the 8 GeV spectrometer data.				
	tracking	shower	Čerenkov	electron
efficiency	0.9991	0.9941	0.9904	0.9837

the scaler rates of a coincidence of PR, TAD and Č (PTC) where the scaler inputs differed in their gate width. Gate widths of 40, 60 and 80 ns were used, while the 20 ns gate width scaler was discarded due to double pulsing. The EL-20, EL-40, EL-60, and EL-80 scalers which were also meant for calculating the deadtime were not used because both EL-20 and EL-40 were double pulsing. A linear extrapolation to a gate width of 0 ns was done to give the scaler rate corresponding to no dead time. This scaler rate was divided by the 40 ns scaler rate to obtain the dead time correction. This correction ranged from 1.000 to 1.009 for this experiment.

The sample fraction was needed for a few runs where the computer failed to save all the events which should have been recorded. It was calculated from the ratio of the trigger scaler to the software event counter. For most runs these counters were the same. In the worst case the sample fraction correction reached 1.0058.

The one per pulse correction accounted for the inability of the computer to save more than one event per beam pulse. After each computer trigger occurred, a trigger veto pulse was created lasting the length of the beam pulse. This pulse was put in coincidence with the PTC-40 pulse and summed by the PTC-40V scaler. The one per pulse correction was defined to be

the ratio of the PTC-40 scaler to the PTC-40V scaler. For a few runs where the PTC-40 scaler counts were low, a similar calculation was used with the less restrictive EL-40 and the EL-40V scalers. EL-40 was formed from an OR of EL-HI and EL-LO triggers and had a pulse width of 40 ns. This correction was small for the majority of runs, but for some very high rate runs became as large as 1.2. A Poisson calculation was also done to obtain the expected correction using the average number of triggers (PRETRIG) per beam spill. The agreement with the measured correction was good. The two quantities typically agreed to 0.2%.

8 GeV Acceptance Function

The acceptance function of a magnetic spectrometer describes the momentum dependence of the solid angle for the cross sections being measured. It is a function of the horizontal and vertical scattering angles, θ and φ, and of the momentum deviation from the spectrometer central momentum, δ. Generally, the acceptance function is also a function of target length, but the data presented here was all taken with the long 15 cm targets so the target length dependence was not an issue.

Monte Carlo model

The purpose of the Monte Carlo program was to produce an acceptance function by simulating the physical properties of the spectrometer. Scattered electron events were generated at the target and transported to the hut area to determine which

particles made it all the way through. The interaction point inside the target was chosen randomly in x and y assuming the beam falls off as a Gaussian distribution and randomly along the length of the target, z. The scattering parameters δ, θ, and φ are also randomly generated within the desired limits.

Assuming the spectrometer momentum was set to 8.0 GeV, the particles were transported through the spectrometer using several sets of forward TRANSPORT coefficients. Each set of coefficients transported the particles to a certain point along the spectrometer such that an aperture check could be done. The choice of spectrometer momentum of 8.0 GeV was made because multiple scattering effects are small. A correction for the momentum dependence of multiple scattering was applied separately and will be discussed. Any particle hitting an aperture anywhere along the way was assumed lost. Particles which reached the spectrometer hut were transported through the detectors, taking into account multiple scattering effects due to passing through materials along the way, such as the Čerenkov counter windows and gas. Particle positions found at each wire chamber were randomly adjusted within the expected resolution of the wire chambers, $\sigma_x = 2.3$ mm and $\sigma_y = 1.0$ mm, and a line was fit to these coordinates to simulate the data tracking algorithm and produce coordinates at the focal plane. The fiducial cut used in the data analysis was checked and the events were reconstructed at the target using the same reverse TRANSPORT coefficients used in the data analysis. These events were then histogrammed in δ, θ, and φ bins.

The acceptance function was calculated in each bin by

taking the ratio of the number of particles in the reconstructed event histogram to the original number of generated particles and normalizing to the size of each bin. The acceptance function was then integrated over φ using four different φ cuts corresponding to those used in the data analysis. This gave four reduced acceptance functions. A 3-D surface plot of the reduced acceptance function with the largest φ cut, $-28.0 < \varphi < +28.0$ mr, is shown in Figure 3.6. Projections of these acceptance functions on the δ and θ axes are shown in Figure 3.7 for all four φ cuts. As the φ cut
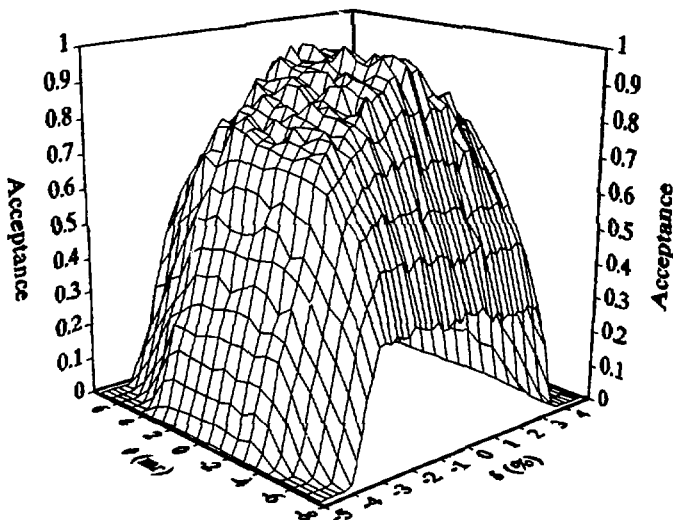
Figure 3.6: 8 GeV spectrometer acceptance vs. δ and θ for $\varphi < |28.0|$ mr and for a target length of 15 cm. Acceptance was normalized to 1.0 where 1.0 in a given δ-θ bin means all particles originating from this bin made it to the hut.
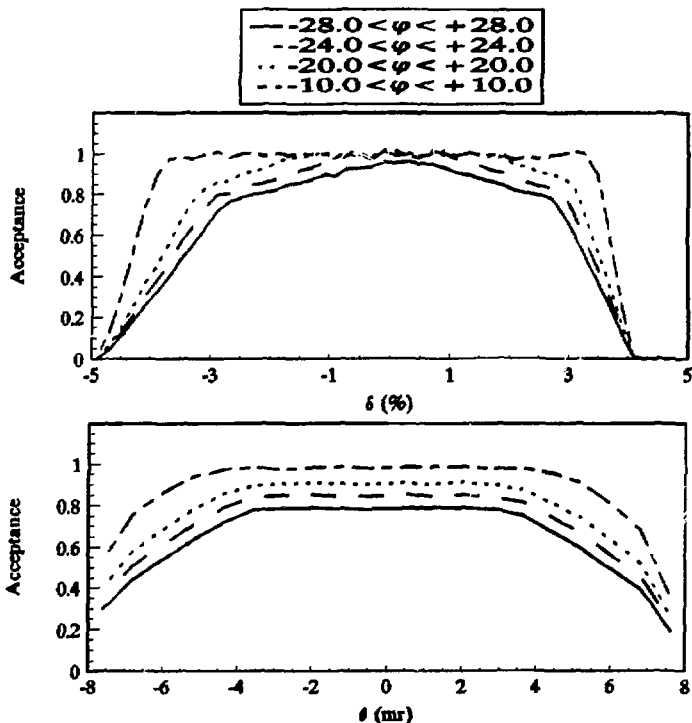
Figure 3.7: 8 GeV spectrometer acceptance function projected against the δ and θ axes. The acceptance is normalized in each bin to 1.0, and four curves are shown, one for each φ cut.

becomes more narrow the function approaches that of "perfect" or flat acceptance.

In addition to calculating the acceptance function, the Monte Carlo also calculated several corrections. During the integration over φ process, the root mean square value for φ was calculated for each δ-θ bin and for each φ range. This quantity was used to correct the horizontal scattering angle,

θ, for each bin to the nominal scattering angle. This correction was small, and never exceeded 0.25%. The Monte Carlo also calculates two corrections to the acceptance function. One correction is for the momentum dependence of the multiple scattering effect and one is for the change in effective target length as the spectrometer rotates about the pivot. At high momenta the effect on the acceptance function due to multiple scattering of the particles is small compared to that at low momenta. This is a bin by bin correction which basically widens the distribution in θ, φ, and δ, and for low momenta averages around 2.0%. The target length correction is necessary because at forward angles the target length as seen by the spectrometer is smaller than the true target length. This is also a bin by bin correction. The average correction can be approximated by the expression $1.0 - 10^{-5}(Tsin\theta)^2$ which at 90° and at a full target length, T, of 15 cm is equal to 0.25%.

Acceptance vs. data studies

It is very important to test for compatibility between the acceptance function and the measured data. One way to do this is to make sure the calculated cross sections agree for each of the φ cut ranges. The cross section calculation will be discussed in greater detail later in this chapter. Figure 3.8 shows three plots of cross section ratios, φcut1/φcut2, φcut1/φcut3, and φcut1/φcut4, where φcut1 < |28.0|, φcut2 < |24.0|, φcut3 < |20.0|, and φcut4 < |10.0|. Each φcut is in mr. The points on these plots are cross sections summed over

8 GeV cross section ratios
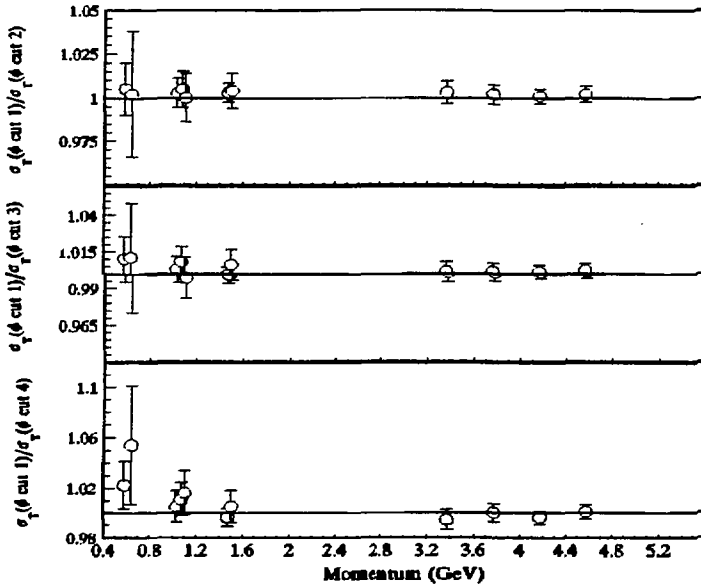
Figure 3.8: Ratio plots of summed cross sections. From top to bottom: φcut1/φcut2, φcut1/φcut3, and φcut1/φcut4, where φcut1 is the largest cut, and φcut4 is the smallest cut.

the kinematic point which is denoted by momentum and the error bars shown are statistical. The points were observed to lie along the line where the ratio is equal to 1.0 within the total expected errors on the cross sections. A similar check with similar results was also done with the proton elastic cross section data.

Another way to check the acceptance function is to take small spectrometer momentum steps within the same kinematic point and verify that the cross section spectra agree in the

overlapping regions. Figure 3.9 is a sample overlap spectrum for the point: E = 5.507 GeV and Q^2 = 2.50 $(GeV/c)^2$ where E' was set as 4.001, 4.167, and 4.334 GeV. It can be seen that the overlap is quite good.

Finally, a check on the acceptance was also made with the proton elastic cross section data to make sure that the acceptance function had no significant θ dependence relative to the model cross section. A study was made of the elastic

8 GeV Overlapping cross sections
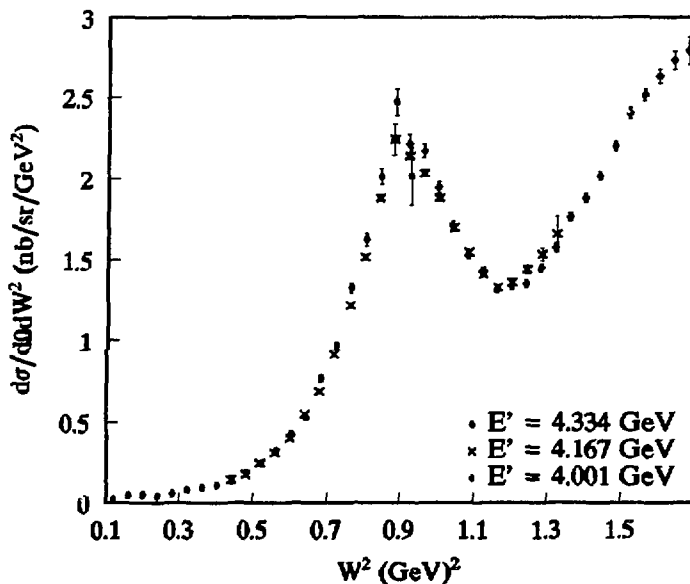
Figure 3.9: Cross section overlap spectrum for the 8 GeV spectrometer with E = 5.507 GeV and Q^2 = 2.50 $(GeV/c)^2$. Data was measured at spectrometer momenta which differed by several percent.

cross section versus theta. This cross section was normalized to the total cross section summed over all θ. Since all the appropriate θ corrections were applied to these cross section, there should be no theta significant dependence unless there is a problem with the acceptance function. The results of this study showed that there was no significant theta dependence.

1.6 GeV Event Analysis

Tracking

In order to analyze the tracking event data, it was necessary to calibrate the drift chamber TDC's, line up the drift time spectra for each TDC channel using drift time offsets, and line up the sum time spectra for adjacent wires using sum time offsets. Each TDC channel was carefully calibrated at the end of this experiment using a pulser-generated random trigger to generate both the start and the stop pulses of the TDC's with known delays for the stop signal using various length cables. All cable time delays were double checked using a pulser and an oscilloscope. The TDC signals were read by the computer for each delay and a fit was done to convert the TDC signal to real time from start to stop for each TDC channel.

The next step was to align the drift time spectra for each wire. Drift chamber TDC data was read, converted to time, and histogrammed for each wire. The start signal for the TDC's during the experiment was formed from the wire signals while the stops were formed from the trigger. Sample drift time spectra for a single run are shown for each chamber in Figure
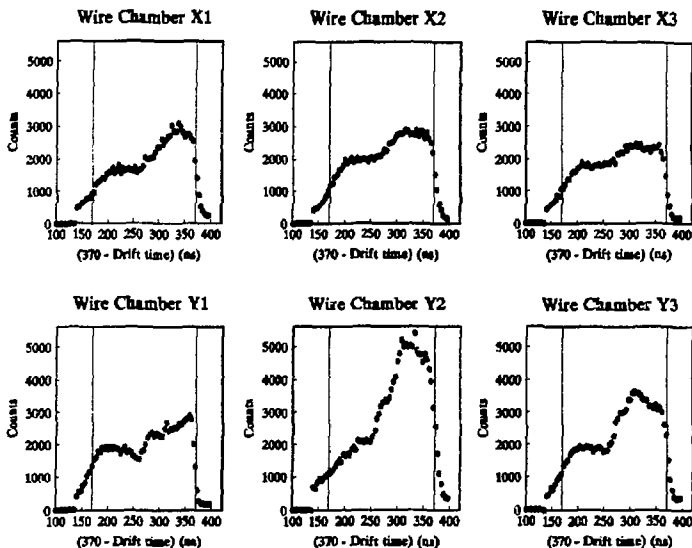
Figure 3.10: Sample drift time spectra summed over all wires in each chamber. Vertical lines indicate drift distances of 1.0 cm (left side) and 0.0 cm (right side).

3.10 using deuterium target data. Each spectrum was summed over all wires where the individual wire spectra had already been aligned at the arbitrarily chosen point of 370.0 ns. Ideally, these spectra should have a square wave distribution, but distortions of the field near and far from the wires can produce nonlinearities. The "two-step" distribution indicates that the drift velocities were somewhat greater for hits occurring within the nearest 0.5 cm of an anode wire. The edges of this spectrum are indicated by vertical lines and correspond to distances from the wire of 0.0 and 1.0 cm. The line on the right is the 0.0 cm line, and this was the point

used to align the individual wire drift spectra.

The 0.0 cm edge for the individual wire drift time spectrum was found by looking at data points in the vicinity of the edge and finding an edge point such that the slope of the line going through the points was maximized. An offset was defined such that the edges lined up at 370.0 ns. A drift velocity of 0.005 cm/ns corresponded to a typical drift spectrum width of 200 ns and a wire spacing of 1.0 cm. Figure 3.11 shows a plot of drift time offsets versus wire number for wire chamber X1. The change in offsets from the odd/even wire planes is evident as well as a shift corresponding to a change in TDC modules at wire number 33. It was necessary to find four such sets of offsets to cover the entire experiment due

X1 chamber drift time offsets
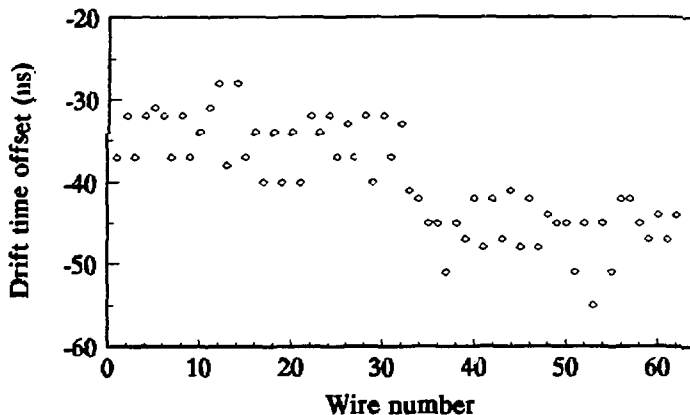
Figure 3.11: One set of drift time offsets for wire chamber X1.

to various changes in running conditions. Due to the field nonlinearities mentioned above there was some uncertainty as to the true time width of these spectra. To help account for this it was necessary to define offsets for the sum time peaks of adjacent wires.

Once the drift times had been corrected for offsets the sum time spectra were accumulated for pairs of adjacent wires which fired. A peak was formed near the desired sum time of 200.0 ns. Sample sum time peaks for a single run are shown in Figure 3.12 for each chamber. These spectra include sum times for all pairs where the sum time offsets had already been
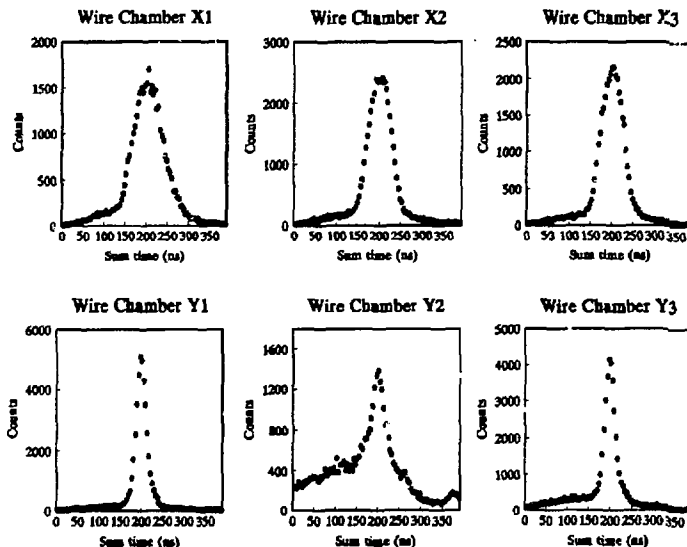
Figure 3.12: Sample sum time spectra for each chamber and for all pairs of wires in the 1.6 GeV spectrometer drift chambers.

applied, and a cut was applied to exclude the sum if the difference in drift times was less than 16.0 ns (See Figure 3.13 and associated discussion). It should be noted that chamber Y2 looks particularly bad compared to the other chambers for this run because for this run the wires in chamber Y2 were exhibiting a large amount of cross talk. The cross talk problem varied in severity from chamber-to-chamber and from run-to-run and will be discussed in detail shortly. Sum time offset corrections were found so that the peaks for individual pairs were all aligned at 200.0 ns. The width of this peak is indicative of the chamber tracking resolution when a pair of wires fired. Clearly, the X chamber resolution is worse than the Y chamber resolution. The measured resolution can be improved for the X chambers by correcting for the change in expected sum time for large angle tracks because of the 0.9 cm separation between the even and odd wire planes. Figure 3.13 shows the same sum time spectra given in Figure 3.12 for the X chambers with these corrections applied. Table 3.3 shows the resolutions of the chambers calculated from these spectra. The X1 chamber resolution was worse than the others because the field shaping wires were not able to hold the proper high voltage and it had to be lowered. The overall chamber resolutions were somewhat larger than these numbers because these do not account for the resolution degradation when only a single wire was used to define a hit position.

The peak positions for the sum time spectra were calculated using just the data greater than half the peak
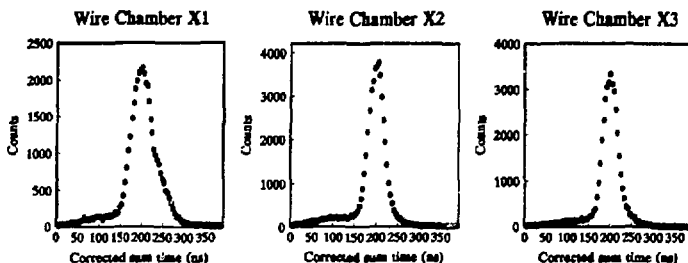
Figure 3.13: X chamber sum time spectra corrected for track angle dependence of sum times. Compare to figure 3.12.

Table 3.3: Drift chamber resolutions for good pairs						
	X1	X2	X3	Y1	Y2	Y3
σ (mm)	1.9	1.4	1.5	0.7	1.2	0.7
σ_corr (mm)	1.4	1.0	1.0			

height in order to stay away from the large tails. Typical sum time offsets are shown in figure 3.14 for wire chamber X1 with different symbols used to designate whether an even or an odd numbered wire was on the left side of the pair. The two sets of symbols balance around an offset of 10.0 ns. A set of sum time offsets was calculated for each set of drift time offsets needed.

After applying the drift time offsets and the sum time offsets for each event, cuts on allowed drift and sum times were used to reduce noise and random signals in the chambers. The drift time cuts used were 140.0 < drift time < 400.0 ns. The cuts on the sum times varied with each chamber due to differences in tracking resolution and are given in Table 3.4.

X1 chamber sum time offsets
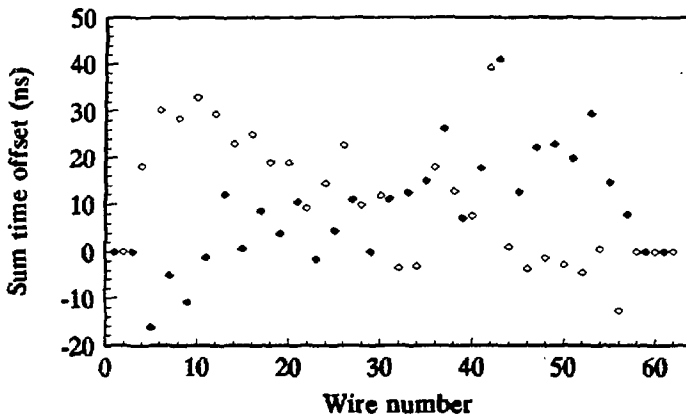
Figure 3.14: One set of sum time offsets for wire chamber X1. Open diamonds correspond to left even wire + right odd wire. Filled diamonds correspond to left odd wire + right even wire assuming wires are ordered from left to right.

Table 3.4: Drift chamber sum time cuts used in tracking algorithm						
	X1	X2	X3	Y1	Y2	Y3
Lo cut (ns)	120.0	120.0	120.0	140.0	140.0	150.0
Hi cut (ns)	300.0	280.0	280.0	250.0	280.0	250.0

The behavior of these drift chambers during the experiment was less than satisfactory. There were many noisy wires, and there was cross talk between wires. This made for a very difficult analysis. Apparently the cross talk problem was because the wires were coated with a layer of residue which was possibly due to using a bad gas mixture in the chambers. The cross talk problem varied in its severity over

the chamber itself and over time. Typically, a real hit would occur within ~ 1 to 2 mm of an anode wire, causing that wire to fire. Adjacent wires which were susceptible to cross talk would produce a similar signal often masking the real signal from being recorded for the wire which should have formed a good pair. Figure 3.15 indicates the severity of this problem. This figure shows a plot of drift time differences between adjacent wires for the same run used to obtain the sum time spectra in Figure 3.12. It was summed over all pairs of wires which fired in each wire plane. Ideally, these distributions should be uniform, but the large peaks near 0.0 are due to
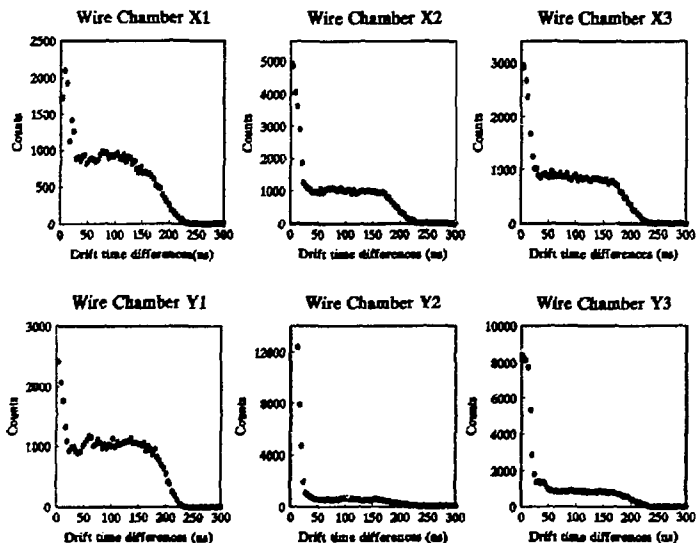
Figure 3.15: Drift time difference plots for each chamber and for all pairs of wires in the 1.6 GeV spectrometer drift chambers.

cross talk. Note that chamber Y2 did not behave this poorly for all runs, and that these plots include all pairs of wires which fired in the chambers. The tracking algorithm was designed to not use possible cross talk events if an event could be found that did not exhibit the cross talk behavior.

One very important feature used in the tracking program was that of hodoscope masking. "Hodoscope" refers to the collection of scintillators contained within the 1.6 GeV spectrometer detector package. The goal of the hodoscope masking was to block from tracking consideration any wires
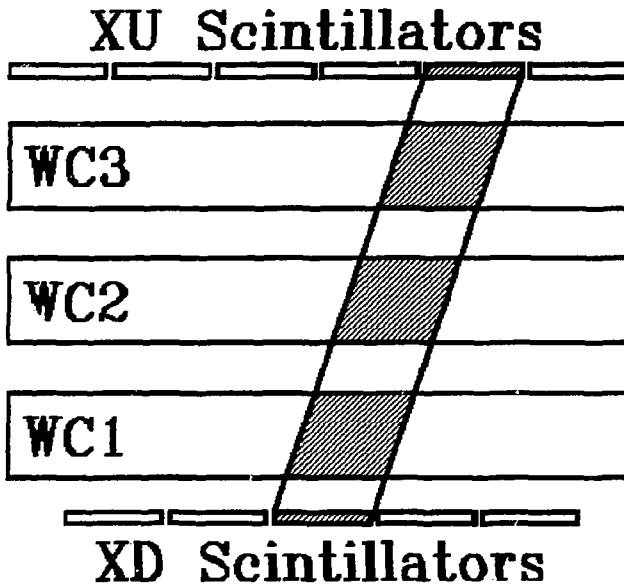
Figure 3.16: Schematic showing hodoscope masking for the 1.6 GeV spectrometer detectors. The shaded scintillators are the ones which "fired" and the shaded regions of the wire chambers indicate the "allowed" wire regions.

which did not intersect the "allowed" range defined by the
scintillators which fired. A schematic of this concept is
shown in Figure 3.16 where the shaded scintillators indicate
which scintillators fired and the shaded regions shown on the
drift chambers are the "allowed" wire regions. Note that the
actual "allowed" regions were slightly larger than those
indicated in figure 3.16 to allow for particle posi ion
deviations due to multiple scattering. Also, if multiple
scintillators fired, the "allowed" regions were widened
accordingly. Hodoscope masking was extremely successful in
rejecting useless wire chamber information and in decreasing
the amount of computer time needed to analyze the data.
However, in the unlikely event that no scintillator fired,
the hodoscope masking was not used. Also, if not enough wires
were found to form a track in the first pass of the tracking
algorithm, a second pass was made with the hodoscope masking
turned off.

The next step was to calculate all the "hit" positions in
each chamber. A "good" pair was defined to be a pair of
adjacent wires firing which had a good sum time within the sum
time cuts (see Table 3.4). The drift times were converted into
drift distances which were combined to calculate a hit
position between the two wires. The error on the position for
track fitting purposes was defined to be 0.1 cm. An "OK" pair
was invented to smooth out bumpy tracking coordinate
distributions due to wire cross talk. An "OK" pair was
defined if a "good" pair could not be found, and if two
adjacent wires had si lar and small drift distances. The hit

position used by the tracking fits was found by randomizing between the two wire positions, and the error was defined to be 0.5 cm. If neither a "good" or "ok" pair could be defined then the wire position was used as the hit position, and the error was defined to be that wire's measured drift distance since the hit could have occurred on either side of the wire.

Once all the possible hit positions were defined, the tracking algorithm calculated the likely track candidates. For X and Y coordinates separately, the two chambers with the least number of hit positions were considered. Tracks formed by hit positions in these chambers were extrapolated to the third chamber, and only hit positions within 4.0 cm of these positions were considered. This cut down on unnecessary calculations for unlikely track candidates. If the third chamber contained no hits in the desired range then a two-chamber track was defined. Otherwise three-chamber tracks were found by doing an error weighted linear fit to the hit positions. A track was also required to have at least one pair of hits, where "good" pairs took precedence over "OK" pairs. If a track was found with two or three pairs then all subsequent tracks found were required to contain at least as many pairs. Also, tracks found must have been within the detector fiducial region of the spectrometer and must have originated within the vacuum tank exit aperture at the top of the magnet.

Track purging was performed if multiple tracks had been found based on several criteria. If some of the tracks passed a given criterion then they were kept. If no tracks passed the

criterion then no purging was done. These criteria included
(in the order of purging):

1. Tracks below a normalized shower track energy of 0.6
   were purged.

2. Tracks pointing more than 2.0 cm away from a
   scintillator hit position were purged. The
   scintillator hit positions were calculated for the
   scintillators with tubes at both ends using the
   phototube timing information. The resolution for the
   scintillator hit positions was ~ 2-4 cm.

3. Tracks giving reconstructed target coordinates outside
   the spectrometer acceptance were purged.

4. Tracks defined by less than the total number of
   chambers were purged.

5. Tracks were purged based on the total number of wire
   pairs used in the fits.

6. Tracks having a corrected large angle sum time for the
   X chambers outside cuts were purged (see Figure 3.13).
   The cuts were 20.0 to 30.0 ns tighter than those given
   in Table 3.4.

7. Tracks were purged based on the chi-square of the fit.
If more than one track still remained at this point then one
was chosen at random.

The tracking efficiency for electrons was measured using
a clean sample of electrons. This sample was obtained by
requiring the Čerenkov ADC signal to be above 25, the total
normalized shower energy in the lead glass shower counter to
be above 0.6, the normalized shower energy in the first layer

of the lead glass counter to be above 0.5, and exactly one scintillator per scintillator plane firing. Also, these scintillators were required to be aligned spatially such that a track originating from the target could have passed through all of them. This measured efficiency was 0.9932.

Kinematic quantities at the target were reconstructed from each event measured in the hut using the spectrometer reverse matrix coefficients given in Table 3.5. These coefficients were obtained by fitting Monte Carlo generated rays which passed through the spectrometer, where X and Y in the hut were in cm and dX and dY were in mr. The quantities dX and dY are really dX/dZ and dY/dZ where Z is the direction of the central ray through the spectrometer. The Monte Carlo program will be discussed in greater detail later. The reconstruction coefficients included second and third order coefficients. The input rays for the reconstruction fit constrained $|y| < 7.2$ cm, $|\delta| < 5.0$ %, $|\theta| < 40.0$ mr, and $|\varphi| < 90.0$ mr. Also, these rays could originate anywhere within a beam height $|x| < 0.25$ cm. The average deviations between the original rays and the fit were calculated to be 0.05 cm in y, 0.02 % in δ, 0.48 mr in θ, and 0.34 mr in φ. Similarly to the 8 GeV spectrometer reconstruction coefficients, for fitting purposes it was assumed that the particle originated from the central beam axis in the vertical direction.

Electron and pion identification

Once an event was indicated by the trigger and a track had been found, the event had to be identified. An "electron"

Table 3.5: First, second and third order reverse transport coefficients for the 1.6 GeV spectrometer giving target coordinates y, θ, φ, and δ in terms of hut coordinates. For example, y at the target is obtained by:
y = 0.804 + 0.247E-2*X - 0.782E-3*dX + 0.381*Y.....

	y (cm)	θ (mr)	φ (mr)	δ (%)
1	0.804E+0	-0.829E+1	0.527E+1	-0.467E-1
X	0.247E-2	0.271E-2	0.189E+1	0.226E+0
dX	-0.782E-3	0.287E-2	-0.119E+1	0.450E-2
Y	0.381E+0	0.208E+1	0.147E-3	-0.631E-3
dY	-0.375E+0	0.577E+0	0.154E-2	0.156E-3
X·X	-0.180E-4	0.113E-3	-0.257E-1	0.853E-3
X·dX	0.425E-5	-0.232E-4	0.126E-1	0.615E-4
X·Y	0.103E-1	-0.492E-1	0.544E-3	-0.638E-5
X·dY	-0.301E-2	0.166E-1	-0.316E-3	0.184E-5
dX·dX	0.703E-6	-0.775E-5	-0.792E-3	-0.201E-4
dX·Y	0.712E-3	-0.470E-2	-0.129E-3	0.239E-5
dX·dY	-0.366E-3	0.147E-2	0.795E-4	-0.260E-6
Y·Y	0.130E-3	-0.126E-2	-0.283E-2	0.113E-2
Y·dY	-0.145E-3	0.141E-2	0.527E-2	-0.116E-2
dY·dY	0.458E-4	-0.495E-3	-0.161E-2	0.331E-3
X·X·X	-0.921E-5	0.300E-4	-0.140E-3	0.312E-4
X·X·dX	0.560E-5	-0.210E-4	0.160E-3	-0.224E-4
X·X·Y	0.176E-3	-0.379E-3	0.248E-5	0.338E-5
X·X·dY	-0.248E-4	-0.702E-4	0.329E-5	-0.150E-5
X·dX·dX	-0.149E-5	0.514E-5	-0.498E-4	0.552E-5
X·dX·Y	-0.306E-4	-0.177E-3	0.129E-5	-0.178E-8
X·dX·dY	-0.940E-5	0.169E-3	0.526E-5	0.638E-6
X·Y·Y	-0.955E-5	0.669E-5	0.103E-3	0.236E-4
X·Y·dY	-0.320E-5	0.316E-4	-0.246E-3	-0.164E-4
X·dY·dY	-0.514E-6	-0.262E-6	0.875E-4	0.199E-5
dX·dX·dX	0.145E-6	-0.499E-6	0.335E-5	-0.434E-6
dX·dX·Y	-0.637E-5	0.857E-4	-0.108E-5	0.272E-6
dX·dX·dY	0.498E-5	-0.436E-4	-0.122E-6	-0.700E-7
dX·Y·Y	0.312E-5	-0.241E-4	-0.211E-3	-0.466E-5
dX·Y·dY	-0.229E-6	0.949E-5	0.272E-3	0.364E-5
dX·dY·dY	0.138E-6	-0.217E-5	-0.815E-4	-0.654E-6
Y·Y·Y	0.385E-5	-0.166E-5	-0.329E-4	0.943E-6

event was required to satisfy the following criteria:

1. The Čerenkov ADC signal must have been above the cut of 25 channels.

2. The normalized track shower energy must have been above the cut of 0.6.

3. The reconstructed kinematic quantities must have been within the defined acceptance of the spectrometer: $\delta = |\Delta p/p| \leq 4.0\%$, $|\Delta\theta| \leq 40$ mr, and $|\Delta\varphi| \leq 120$ mr.

A "pion" event was required to satisfy the following criteria:

1. Requirement 3 of the electron definition.
2. The pion prescaler latch in the electronics must have been set.
3. The normalized track shower energy must have been below the cut of 0.6.
4. The Čerenkov ADC signal must have been below the cut of 25 channels.

The electron and pion events were separately histogrammed in reconstructed θ and ς where the θ bins were 4.0 mr wide and the δ bins were 0.4% wide. For both electrons and pions, four different histograms were saved corresponding to four different φ cut ranges: $\varphi CUT1 = |\varphi| \leq 120.0$ mr, $\varphi CUT2 = |\varphi| \leq 100.0$ mr, $\varphi CUT3 = |\varphi| \leq 80.0$ mr, and $\varphi CUT4 = |\varphi| \leq 60.0$ mr. Corrections for pions mis-identified as electrons were carried out in the same manner as they were for the 8 GeV data discussed earlier.

Shower energy

Pedestal subtracted ADC signals from the shower counter phototubes were converted into energy for each block using the shower block calibration data. The total normalized energy

deposited in the block could then be calculated from

$$
\begin{aligned}
E_{tot}^{sh} &= \sum_{iA=1}^{14} \frac{(ADC_{iA} - PED_{iA})\, C_{iA}}{P_c} + \sum_{iB=1}^{14} \frac{(ADC_{iB} - PED_{iB})\, C_{iB}}{P_c}, \\
&= \sum_{iA=1}^{14} E_{iA} C_{iA} + \sum_{iB=1}^{14} E_{iB} C_{iB}
\end{aligned} \tag{3.1}
$$

where P_c was the central momentum of the spectrometer, A refers to the lower (PA) layer, B refers to the upper (PB) layer, C_{iA} and C_{iB} are the calibration coefficients, E_{iA} and E_{iB} are the individual normalized block energies, and the sums extend over the fourteen blocks in each layer.

The blocks were calibrated using data taken with the deuterium target. The energy of each block was normalized to the spectrometer momentum, and the block coefficients were preset to reasonable values for the first iteration of the coefficient calculation. The block in the PA layer containing more than half of the total PA energy was called the primary block. If the track found in the tracking routine pointed to this block and to the block immediately above it in the PB layer then both were included in the shower coefficient calculations. For tracks pointing to block j, the multiplicative corrections to the coefficients for the blocks were calculated by minimizing, for many events, the chi-square quantity:

$$
\chi_j^2 = \sum_{events} (1 - X_{jA} C_{jA} E_{jA} - X_{jB} C_{jB} E_{jB})^2, \tag{3.2}
$$

where X_{jA} and X_{jB} are corrections to the calibration coefficients, and j ranges from 1 to 14. This calibration

process works because the total normalized energy deposited in the shower counter is 1.0. The coefficient calculation was an iterative process. When the block energies were being calculated correctly then the least-square corrections to the coefficients were consistent with 1.0 within errors. Coefficient calculations were done at several spectrometer momenta, but because of the small momentum range in the spectrometer, no significant momentum dependence to the coefficients was found.

Once the coefficients were found, the energy for each track was calculated by summing over block energies found for blocks through which the track shower passed as well as for blocks which were within 3.0 cm of the track path. A typical shower spectrum for a deuterium target is shown in Figure 3.17 where the shower energy has been normalized to the momentum of the spectrometer. The first plot shows a shower spectrum which required only that a track must have been found. The second spectrum also required a Čerenkov ADC signal above a channel cut of 25. The ability to discriminate against pions with the Čerenkov ADC signal is apparent. The bump which appears in the low energy tail region of the electron peak in the first spectrum is due to pions which lost enough energy in the PA layer of the lead glass shower counter to produce an EL-LO trigger in the electronics. The other pions in the spectrum have been suppressed by the prescaling of the pion triggers, and so the pion tail due to the EL-LO trigger appears enhanced.

The average FWHM energy resolution of the shower counter
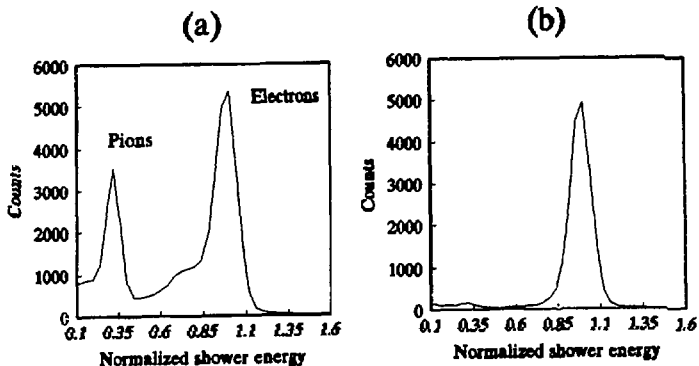
Figure 3.17: (a): Typical spectrum for the 1.6 GeV spectrometer shower counter requiring a track found in the wire chambers. (b): Same shower spectrum as in (a) with the additional requirement of having a Čerenkov ADC signal above 25.

was $\approx 12.9\%/\sqrt{E'}$ where E' is in GeV. The shower counter efficiency for detecting electrons above the shower cut of 0.6 was 98.0%. This efficiency was measured by calculating the percentage of electron events detected which produced a shower energy above the cut of 0.6 for a clean electron sample. This sample was obtained by requiring "electron" criteria 1 and 3 defined earlier with the additional restrictions that the reconstructed target length, y, be within the limits $-11.0 <$ $y < 9.0$, and the scintillators which fired were required to be aligned spatially such that a track could have passed through them. The asymmetric cuts on y were consistent with the observed measured distribution. A plot of the points used to calculate the efficiency versus the electron to pion rate are shown in Figure 3.18. The line shown is an error weighted fit to the data which yields the measured efficiency when

1.6 GeV Shower Counter Efficiency
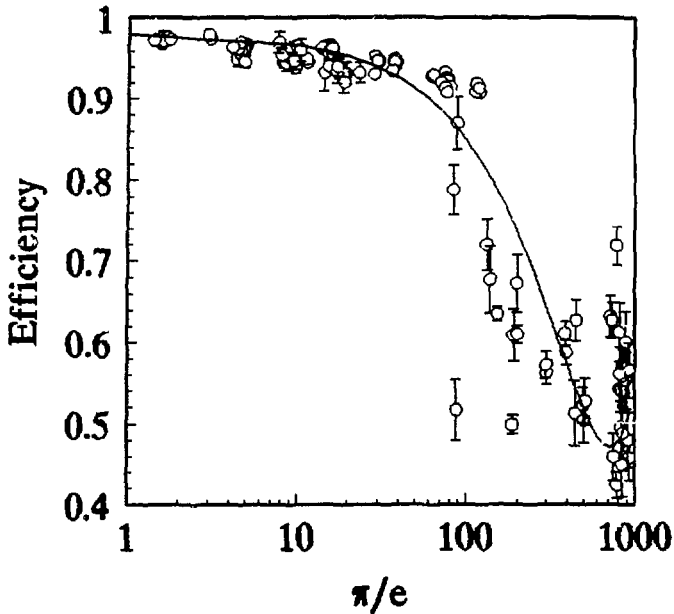
Figure 3.18: Measured electron detection efficiencies for the 1.6 GeV spectrometer shower counter using hydrogen and deuterium target runs. A fit to the data yields the measured overall efficiency at $\pi/e = 0.0$.

extrapolated to a π/e ratio of zero. The efficiency was also calculated from a Gaussian distribution centered at 1.0 using the above resolution and cut of 0.6. The result was consistent with 100%. This large difference from the measured efficiency indicates that the inefficiency of the detector is mostly due to electrons slipping through cracks between the lead glass blocks and to leakage out the back, and is not due to the shower energy cut.

Čerenkov Counter

Figure 3.19 shows a typical Čerenkov ADC spectrum from data taken with a hydrogen target. A Poisson fit to the data indicates an average of 7.8 photoelectrons detected for a typical event. The pion ADC spectra shows no significant counts above the pedestal of the ADC. The measured efficiency for detecting electrons above an ADC cut of 25 was 99.9%. The

1.6 GeV Cerenkov spectrum
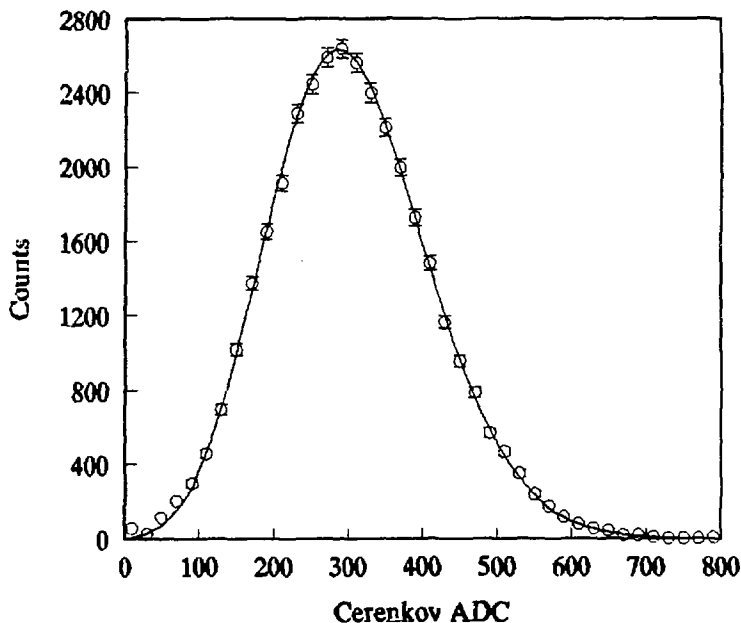
Figure 3.19: 1.6 GeV spectrometer Čerenkov counter spectrum with a Poisson curve calculated using an average of 7.8 photoelectrons.

electron sample used to determine this efficiency was obtained by requiring "electron" criteria 1 and 2 as well as requiring that the reconstructed target length, y, and the scintillators satisfy the same conditions given above for the shower efficiency calculation. Also, the normalized track energy deposited in the PA layer was required to be above 0.35. A plot of the points used in the efficiency calculation are

1.6 GeV Cerenkov Efficiency
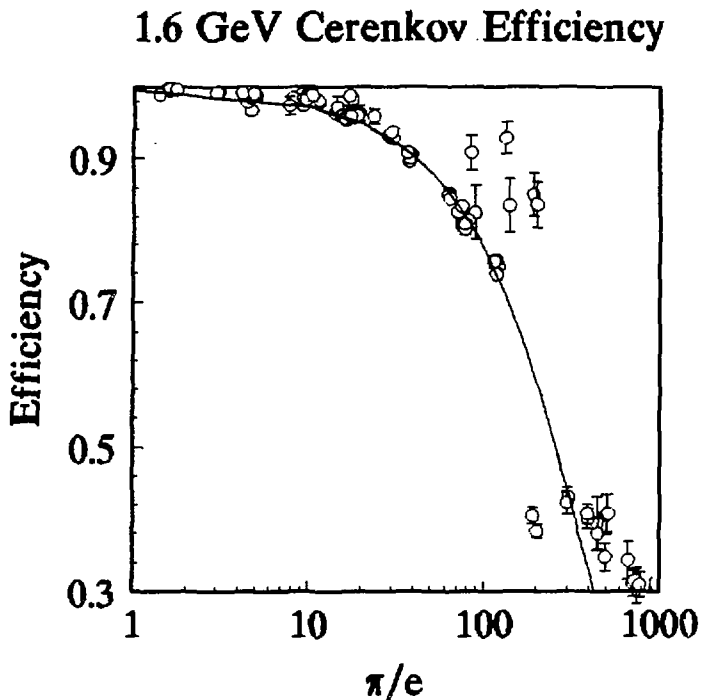
Figure 3.20: Run-by-run electron detection efficiencies versus π/e ratio for hydrogen and deuterium targets. A fit to the data is also shown which yields the measured overall efficiency at π/e equal to zero.

shown in Figure 3.20 versus the ratio of pion to electron rates. These data are for both hydrogen and deuterium target runs. The line shown is an error weighted fit to the data which yields the measured efficiency when extrapolated to a π/e ratio of zero. The efficiency was also calculated using the Poisson fit to the data and the ADC cut of 25. This calculation yielded an efficiency of 99.96% which is in very good agreement with the measured value.

Efficiency, Electronic, and Computer Correction

A summary of the detector efficiencies discussed in the previous sections is given in Table 3.6. The total efficiency for detecting electrons was found by multiplying these individual efficiencies together since they are uncorrelated.

The electronic dead time correction was calculated using scaler rates CAB40, CAB60, and CAB80 where CAB refers to a

Table 3.6: Summary of important efficiencies for analysis of the 1.6 GeV spectrometer data.

	tracking	shower	Čerenkov	electron
efficiency	0.9932	0.9803	0.9992	0.9729

coincidence output of the Čerenkov signal, PA1o and PB signals, and the number refers to the coincidence circuit output width in nanoseconds. PA1o and PB were discriminator signals produced after first summing over the lead glass block signals in the first layer (PA) and the second layer (PB). The CAB20 scaler was not used to calculate this correction because of double pulsing. CAB20 double pulsed because the Čerenkov

signal was double pulsing, and the PAlo and PB signals were long enough such that CAB20 also double pulsed. A linear extrapolation to a gate width of 0.0 ns was done to give the scaler rate corresponding to no deadtime. This scaler rate was divided by the CAB40 scaler to obtain the dead time correction. This was a small correction ranging from 1.000 to 1.003 for this experiment.

The sample fraction correction was needed to correct a few runs where the computer failed to record all of the events on tape. It was calculated from the ratio of the trigger scaler to the software event counter. With the exception of one run, this correction ranged from 1.000 to 1.004. The worst run, which was bad for the data in both spectrometers, had a sample fraction correction of 1.043.

The one per pulse correction was needed because the computer was unable to save more than one event per beam pulse, but more than one event could actually occur. Similarly to the 8 GeV electronics, when a trigger occurred a veto pulse was created which lasted the length of the beam pulse. This pulse was put into coincidence with the CAB40 pulse and counted by the CAB40V scaler. Thus, this scaler counted the number of beam pulses where a CAB coincidence occurred. The CAB40 scaler counted the number of times a CAB coincidence occurred regardless of the number of beam pulses. The one per pulse correction was given by the scaler ratio of CAB40/CAB40V. For a few runs where the CAB40 scaler counts were low, the less restrictive EL40 and EL40V scalers were used in a similar calculation where EL was the electron

trigger formed by an OR of ELLO and ELHI (See electronics diagram, Figure 2.13). This correction was as high as 1.113 for some of the high rate runs.

1.6 GeV Acceptance Function

Monte Carlo model

The purpose of the Monte Carlo program for the 1.6 GeV spectrometer was three-fold. Firstly, it simulated the elastic scattering process at the target and the physical properties of the spectrometer in order to compare with real elastic measurements made from hydrogen targets. This feature enabled us to ascertain that the spectrometer was being modelled properly. Secondly, it produced an acceptance function for use in the data analysis programs. Thirdly, it produced reconstruction coefficients used for reconstructing target coordinates from hut coordinates.

The elastic scattering portion of the Monte Carlo program was given the four-momentum transfer, Q^2, the central scattering angle, θ, and the desired number of successful events, defined as generated events making it through the spectrometer without hitting any apertures. The central incident energy was calculated from these inputs. Electron events were randomly generated about the central energy, the target length, the beam height and width, and the vertical and horizontal scattering angles using input information on the allowed ranges for each of these quantities. The generated particle in the beam was transported to the interaction point taking into account multiple scattering, ionization energy

losses, and radiative energy losses in all materials traversed along the way. The generated particle's scattering energy was calculated for an elastic interaction, and the particle was transported to the hut by ray tracing through the optical system. Again, multiple scattering, ionization energy losses, and radiative energy losses were taken into account for all materials traversed by the scattered particle. Any particles which failed to pass through all apertures along the way were thrown out.

Events which made it through to the hut were saved and could be directly compared to measured data. A comparison of Monte Carlo data and real data was done at three different kinematic points. This comparison failed to agree until important improvements were made to the Monte Carlo model. One such improvement was the development of an elaborate ray trace model through the quadrupole and dipole magnets. This replaced an old transport model which did not allow for many aperture checks and did not take into account field distortions of the *dipole magnet at its entrance* due to the presence of the quadrupole mirror plate, and at its exit due to the presence of an iron plate used to hold shielding and to protect the detector stack from the fringe fields. A ray trace model through the quadrupoles was developed from fits made to field gradient measurements which were taken for a previous experiment. A ray trace model for the dipole was developed from old wire float data [35] and from fringe field calculations using TOSCA code [36] for the entrance and POISSON code [37] for the exit region. These field

calculations were checked against a limited set of fringe field measurements taken before this experiment.

Another important improvement was a recalibration of the quadrupole power supplies after the experiment. It turned out that the true currents of the quadrupoles were lower than the setpoint currents. Q1 was set 1.07% low and Q2 was set 1.75% low. The fact that these currents were set improperly caused the vertical focal plane of the spectrometer to shift by 2 and 1/2 meters. This is evident in figure 2.9 where it can be seen that the vertical focal plane occurs at Z = 9 m. and the horizontal focal plane occurs at Z = 11.5 m.

Another important improvement was the result of recent survey measurements made in an attempt to reconcile problems we were having with the Monte Carlo program. These survey measurements indicated a misalignment between the quadrupole and dipole central axes of ~ 3.2 mr. Once this problem was fixed the elastic Monte Carlo data agreed reasonably well with the real measured data. A sample plot will be shown in the next section.

The acceptance function for the 1.6 GeV spectrometer was also calculated in the Monte Carlo program. Bins for δ, θ, and φ were defined in the input file as well as the number of events to generate per bin. The δ and θ bins corresponded to the same binning used for data storage. In addition, there were twelve φ bins of width 20 mr for a total phi range of -120 mr $< \varphi < 120$ mr. Events were randomly generated within each bin and randomly along the target length and beam height. Each event was transported through the spectrometer using the

ray trace model.

There were many aperture checks along the way, especially inside the quadrupoles. During the installation of the quadrupoles the vacuum pipe was compressed in one direction to make the pipe compatible with the dipole magnet's rectangular vacuum pipe. This made the round pipe become more and more ellipsoidal as it neared the dipole. Careful survey measurements were made and ellipsoidal fits done at many steps along the pipe. These fits defined the apertures inside the pipe. Events were thrown out that did not pass entirely through all apertures.

Events reaching the hut area were transported through the detectors. The coordinates were corrected for multiple scattering effects in each detector layer traversed, and detector apertures were checked. The particle positions found at each drift chamber were randomly adjusted within the average wire chamber resolution, and a track was found by fitting these coordinates to simulate the data tracking algorithm. The final hut coordinates were defined by intersecting the track at the focal plane. The events were reconstructed at the target using reconstruction coefficients and were rebinned in δ, θ, and φ.

The acceptance function was calculated by taking the ratio of the number of particles in each reconstructed δ, θ, and φ bin to the original number of generated particles and normalizing to the size of each bin. The acceptance function was integrated over φ using four different φ cuts corresponding to the same ones used in the data analysis. This

resulted in four reduced acceptance functions. These were not the final acceptance functions, however. Similarly to the 8 GeV spectrometer acceptance functions test, the elastic cross section data was used to study the θ dependence of the acceptance function. The idea is to study the cross section as a function of θ normalized to the total cross section. All θ dependent corrections are made beforehand so this distribution should be flat as a function of θ. If it is not flat then the θ dependence of the acceptance function must be wrong. This was the case with the 1.6 GeV spectrometer acceptance functions. Attempts were made to solve this problem in the Monte Carlo program, but they were unsuccessful.

It was decided to create a new corrected acceptance function using the old acceptance function described above, the measured data, and model cross sections. For each set of deuterium data taken in the 1.6 GeV spectrometer, ratios of measured to expected counts were calculated on a δ-θ bin-by-bin basis. Expected counts were calculated using model cross sections, the old acceptance function, radiative corrections, resolution corrections, and the factor C_{kin} which is defined later (Eq. 3.4) in this chapter. See the discussion in the raw cross section calculation section and the resolution correction to see how this was done. Note that for this calculation, however, that a model cross section is converted to expected counts whereas the cross section calculation converts measured counts into measured cross sections. This ratio was calculated for each δ-θ bin.

The next step was to combine sets of data within each Q^2

point. There were generally three to four sets of data taken
for each Q^2 point which differed in the spectrometer central
momentum setting (See Figure 3.28 in the next section for an
example of the data sets combined). These sets of data were
combined in each $\delta-\theta$ bin using an error weighted average
Next, the ratio functions were normalized at each Q^2 such that
the error weighted average over all $\delta-\theta$ bins yielded 1.0.
Finally, the four normalized ratio functions were then
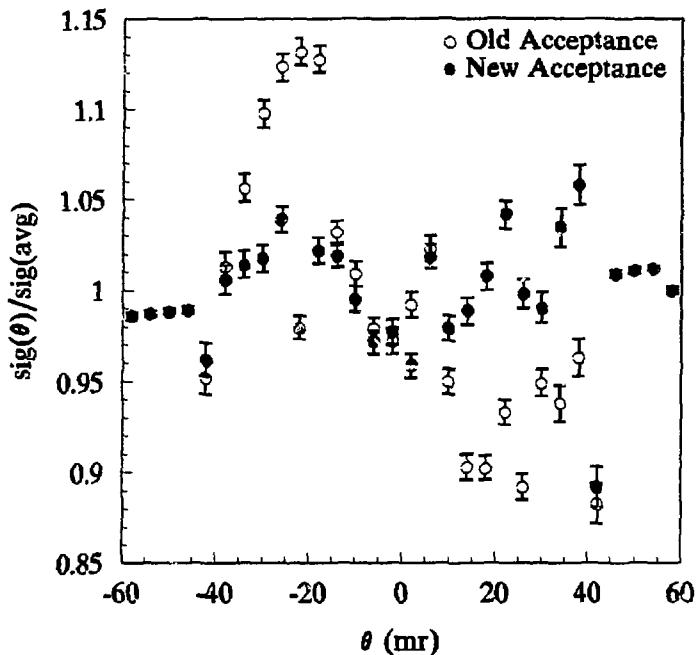
Figure 3.21: Elastic normalized cross section plots showing
the θ dependence for the old and the new, corrected
acceptance function. There should be no dependence since all
the θ corrections have been applied to the cross sections.

combined in quadrature by an error weighted average in each bin to produce one final function used for correcting the old acceptance function. The correction was applied multiplicatively on a bin-by-bin basis. Figure 3.21 shows a plot of the elastic normalized cross sections as a function of θ for before and after applying this new correction. The old acceptance clearly shows an unacceptable θ dependence, while most of this dependence has been removed, as desired, for the corrected acceptance.

Figure 3.22 shows a 3-D surface plot of the reduced acceptance function with the largest φ cut, $\varphi < |120.0|$ mr.
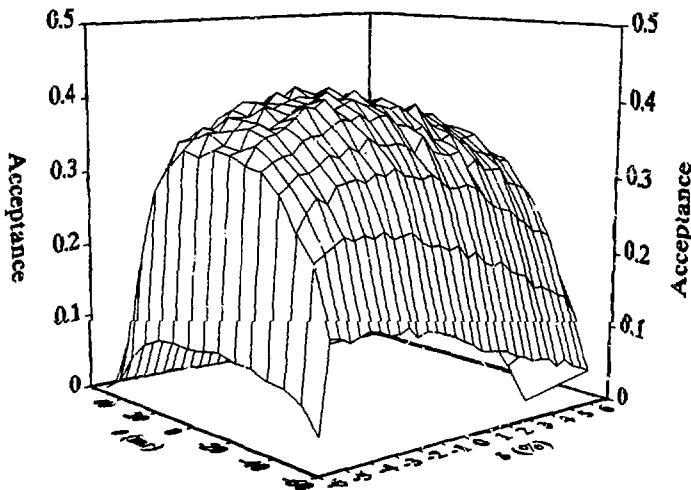
Figure 3.22: 1.6 GeV spectrometer acceptance vs. δ and θ for ~120<φ<120 mr and for a shielded 15 cm target. Acceptance in each bin is normalized to be 1.0 if all generated particles originating from the bin make it all the way through to the hut.

This plot has been normalized so that perfect acceptance in a given bin is 1.0. Projections of these acceptance functions on the δ and θ axes are shown in figure 3.23 for all four φ cuts. The plot versus δ used θ cuts of ± 48 mr, and the plot versus θ used δ cuts of $\pm 4.0\%$. It is interesting to note that the normalized acceptances in Figures 3.22 and 3.23 are at their maximum around 0.4 to 0.5 instead of 1.0. This is due to the very strong correlation between scattering angle and hit target position. For a given scattering angle only hits from a limited region of the target can make it through the spectrometer. This Y-θ correlation is shown in Figure 3.24 along with the δ-φ correlation. These are scatter plots showing the correlation in particle coordinates for particles which made it all the way through the spectrometer.
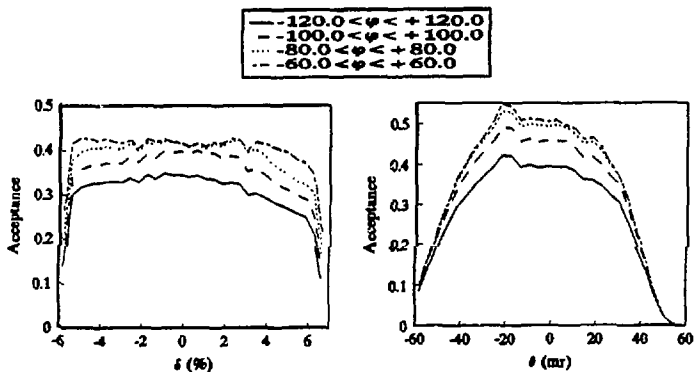
Figure 3.23: 1.6 GeV spectrometer acceptance function for all φ cuts projected against the δ and θ axes. The acceptance is normalized in each δ or θ bin to be 1.0 for perfect acceptance.
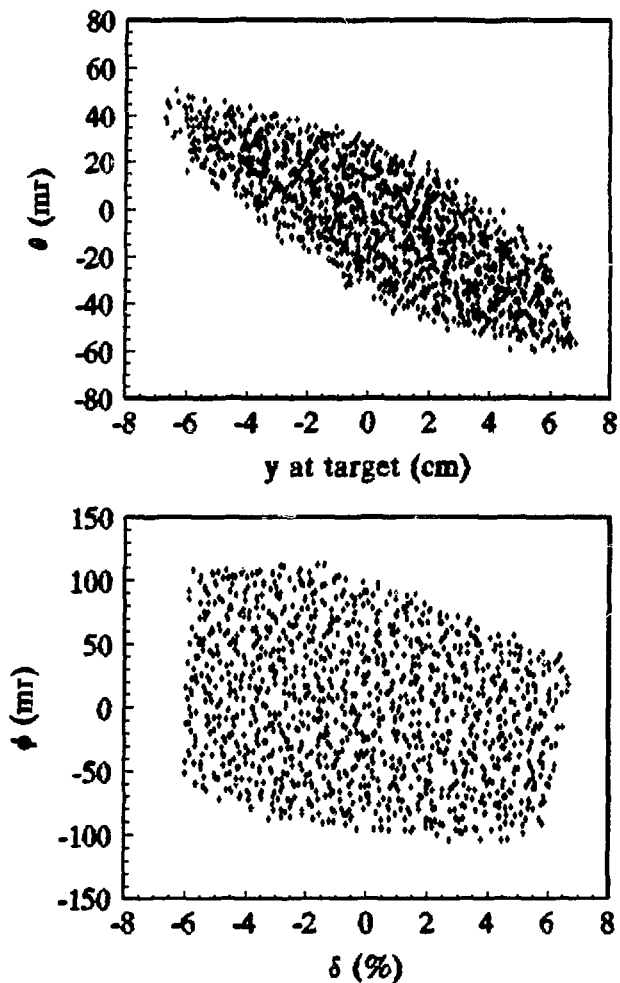
Figure 3.24: Scatter plots showing the correlations in y-θ and in δ-φ for particles which made it all the way through the spectrometer in the 1.6 GeV Monte Carlo code.

Another important job that the Monte Carlo performed was to produce a set of reconstruction coefficients which reconstructed the target coordinates of the event from the measured coordinates in the hut. A data set was generated using two events in each δ, θ, and φ bin. The events which made it through the spectrometer had corresponding coordinates in the hut. A fit was done to this data to produce offsets, first, second, and third order coefficients as shown in Table 3.5. Only data which is within specified limits on the reconstructed coordinates was included in the fit. These limits were given in the discussion accompanying Table 3.5. A few third order coefficients were left out because the coefficients found from the fit were large and compensating. That is, they had a tendency to cancel each other out, but any errors in the measured hut coordinates did not cancel and were magnified since the coefficients were large.

Acceptance vs. data studies

Several tests were done to insure compatibility between the Monte Carlo output and the measured data. As mentioned earlier comparisons were done between elastic data taken with the hydrogen target and the Monte Carlo data. Plots for the kinematic point $E = 1.511$ GeV are shown in Figure 3.24. This figure shows two surface plots showing the elastic stripe in the hut coordinates x and y. The top plot is measured data and the bottom plot is Monte Carlo generated data. The two data sets agree well for the most part. The real data is slightly more peaked in the central region, but the Monte Carlo data
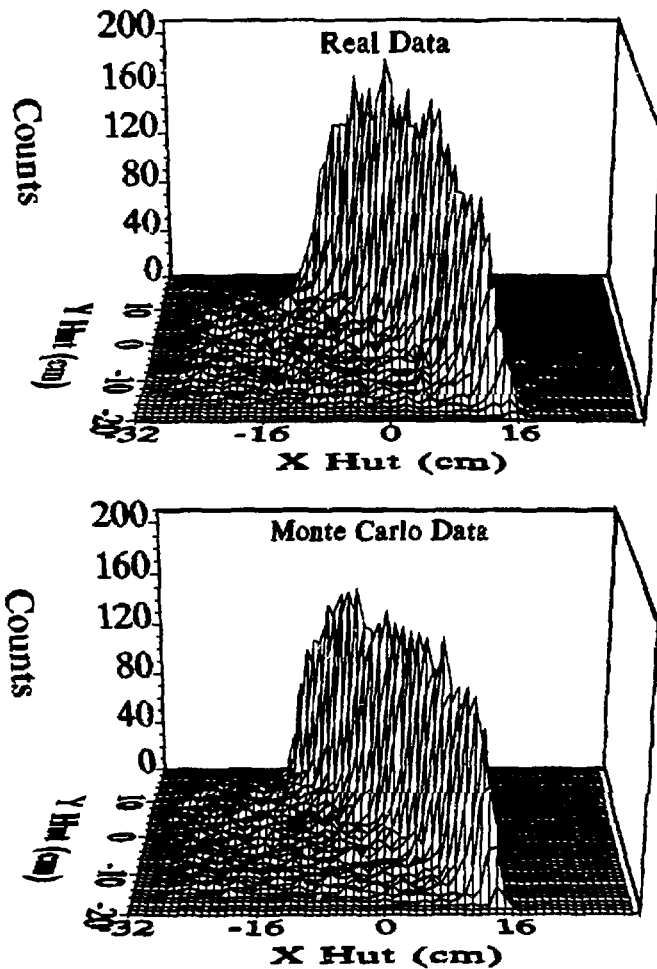
Figure 3.25: Surface plots showing the elastic stripe in the hut for electron scattering off of protons. The top plot is measured data. The bottom plot is Monte Carlo data. Both sets of data are for the kinematic point, E=1.511 GeV.

has a somewhat wider distribution. The number of events in the two plots is the same.

Another test is to make sure that the measured deuterium cross sections are in agreement for each of the φ cut ranges. Figure 3.26 shows cross section ratio plots for the largest φ cut data divided by the three smaller φ cut sets of data. These comparisons are independent of any model cross sections. The cross sections for each φ cut are integrated over the same

1.6 GeV cross section ratios
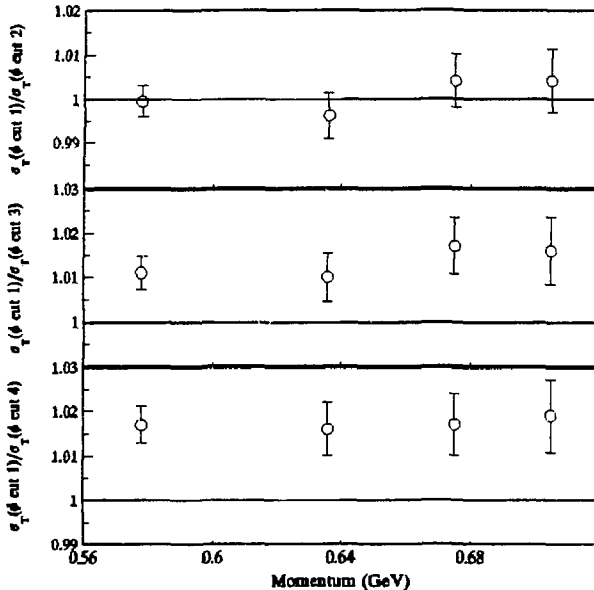
Figure 3.26: Ratio plots of summed cross sections. From top to bottom: φcut1/φcut2, φcut1/φcut3, and φcut1/φcut4, where φcut1 is the largest cut, and φcut4 is the smallest cut.

range of W². The kinematic points are denoted by momentum and
the error bars shown are statistical. The points should
intersect the ratio = 1.0 line. It can be seen that the ratios
are reasonably close to this line. Figure 3.27 shows a plot of
measured deuterium data and Monte Carlo data versus φ. The
Monte Carlo data were normalized to the measured data so that
both had the same number of total counts. The cuts on ϑ were
± 32 mr, and the cuts on δ were ± 3.6%. The agreement between
the data and the Monte Carlo φ dependence is quite good.
Additional tests were done to verify that the φ dependence of
the data was modelled properly by the Monte Carlo. These tests
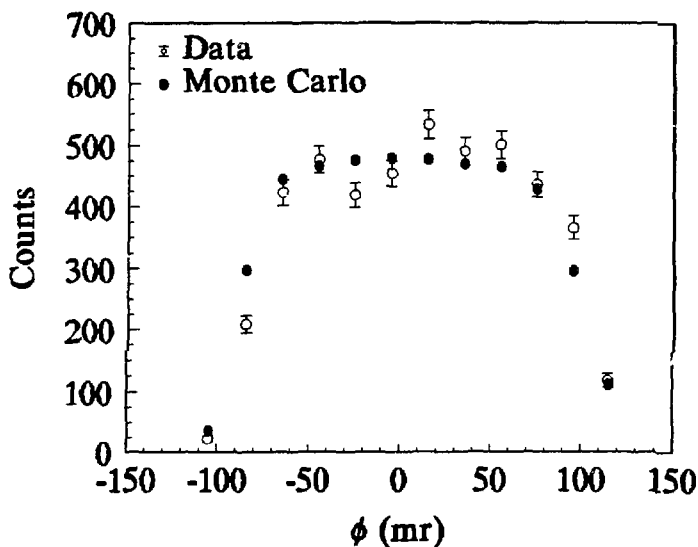
Figure 3.27: Counts versus φ are shown for a deuterium
target data run and for Monte Carlo generated inelastic
data.

include studying ratios of cross sections at different φ cuts versus δ and θ. These tests were particularly useful in spotting problem areas while the Monte Carlo program was in the tuning stage.

Another test for the acceptance function is to compare the cross section spectra for data taken at slightly different momenta. If the acceptance function is good then good overlap

1.6 GeV Overlapping cross sections
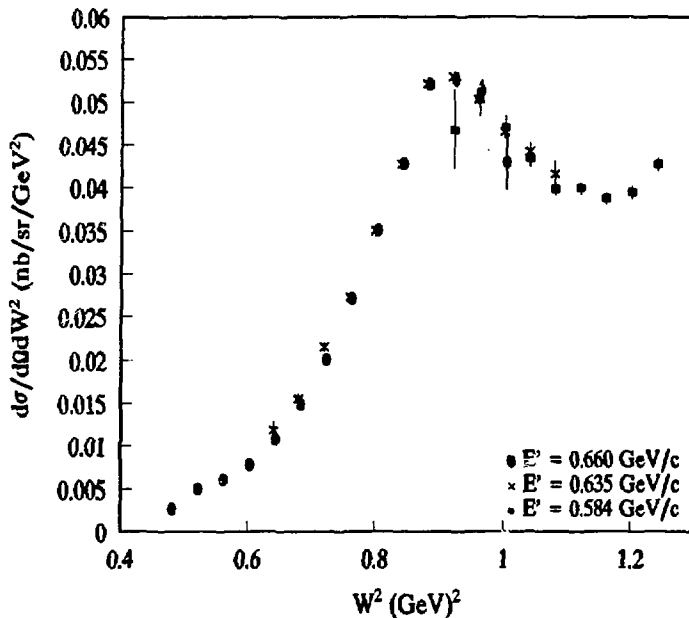
Figure 3.28: Deuterium cross section overlap spectrum for the 1.6 GeV spectrometer with $E = 1.968$ GeV and $Q^2 = 2.50$ $(\text{GeV/c})^2$. Data was measured at spectrometer momenta which differed by several percent.

between the spectra should be observed. A sample overlap plot for deuterium data is shown in Figure 3.28 for the kinematic point: $E = 1.968$ GeV and $Q^2 = 2.50$ $(GeV/c)^2$. The different data sets correspond to central momenta of 0.584, 0.635, and 0.660 GeV/c. The cross sections shown have no radiative corrections applied, nor has there been any subtractions for the aluminum and hydrogen contributions. Overlapping data were taken at most of the kinematic points measured to make sure the acceptance function worked well at all momenta.

For each W^2 bin which had multiple data points contributing, ratios were calculated of the individual cross sections to the total cross section at that point. These ratios were combined using an error weighted average. The ratios were combined in three different regions corresponding to low x, medium x, and high x, where x is the Bjorken scaling variable defined as $Q^2/2M_p\nu$. A value of x equal to 1 corresponds to elastic scattering, and this was assigned to the medium x category. Note that low x corresponds to high W^2. An average over all the kinematic points yielded: ratio(low x)/ratio(med x) = 0.993 ± 0.007 and ratio(high x)/ratio(med x) = 0.997 ± 0.006. The fact that these are consistent with one is a quantitative verification that the overlap between the different momentum data sets is quite good.

Target Density

Energy was deposited in the liquid targets when the electron beam was passing through. This energy caused a temperature increase and a density decrease. The temperature

and pressure were monitored by platinum resistors and vapor pressure bulbs which were place at both the entrance and exit regions of the liquid target material into the target cell. The platinum resistors were calibrated before this experiment and a fit was done to the calibration data in order to determine the temperature from the measured resistance. The best fit found was a second-order polynomial fit to the logarithm of the resistance. The vapor pressure bulbs were converted to temperature using cryogenic data [26]. The densities were then calculated from the temperature also using cryogenic data [27], and then average densities were calculated. A summary of the data used is given in Table 3.7. It should be noted that the hydrogen density point at 23 K is not real because at 2 atm H_2 is a gas. This number was estimated in order to constrain the fits to the data. The temperature fit to the bulb pressure data was a second-order polynomial fit to (Bulb pressure - 6.982), and the density data fit was a second-order polynomial fit to $(T-T_0)$ where

Table 3.7: Summary of cryogenic data used to extract liquid target densities.			
Temperature (K)	Bulb Pressure (psi)	H_2 Density (gm/cm^3)	D_2 Density (gm/cm^3)
18	6.982	0.07339	
19	9.886	0.07234	0.1733
20	13.550	0.07124	0.1712
21	18.120	0.07005	0.1690
22	23.670	0.06878	0.1667
23	30.406	0.06742	0.1644
24			0.1618

reference temperatures, T_o, of 18 and 19 were used for the hydrogen and deuterium fits respectively.

The average densities calculated for individual checkpoints within a run were combined to an average, weighted by the toroid charge measured for each checkpoint. A plot showing the ratio of these checkpoint averaged densities for the vapor pressure bulbs relative to the platinum resistors is shown in Figure 3.29 for the long deuterium target for data taken with and without the beam incident on the target. The
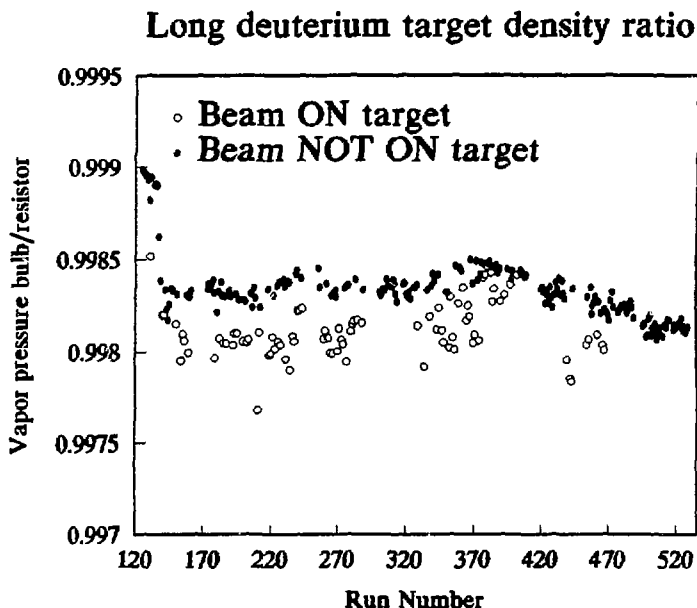
Figure 3.29: Ratio of average densities measured by the vapor pressure bulbs to those from the platinum resistors. Data is for the long deuterium target only, and data with and without beam incident on target are shown.

vapor pressure bulbs were consistently 0.2% lower than the resistor densities. The density used in the cross section calculation was an average of these two numbers.

The average density versus run number for the long deuterium target is shown in Figure 3.30. Different symbols indicate whether the beam was incident on this target for that particular run. The average density for runs with the beam on the targets was 0.16937 gm/cm³ which was 0.26% lower than the average density when the beam was not on the target. Also, the density was observed to vary linearly with beam current.

Long deuterium target average density
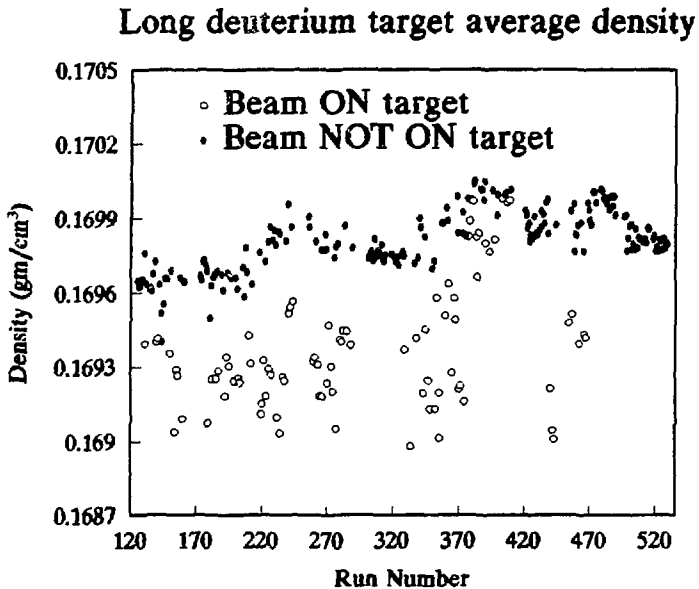
Figure 3.30: Average density for the long deuterium target versus run number. Different symbols are used to designate whether the beam was incident on the target or not.

It is believed that the circulation of liquid target material was fast enough such that the local density (near the beam) was not significantly different from the average measured density. Tests were done during the experiment to study count rate as a function of circulation speed to verify that the chosen circulation speed was sufficiently high. Studies were also made using measured particle counting rates as a function of beam current and beam repetition rate to look for possible local boiling effects in the target. The results were consistent with no boiling.

Energy Calibration

The constraint that the elastic electron-proton cross section peak must sit at $W^2 = M_p^2$, is a useful way to calibrate the incident and final electron energies. If the measured elastic peaks [15] do not sit at M_p^2 then the position can be corrected by changing the incident energy, E, the spectrometer momentum setting, E', the spectrometer angle setting, θ, or any combination of the above. For the 8 GeV spectrometer, survey and wire float [30] measurements indicate that the error on E' was ± 0.05% and on θ was ±0.1 mr. The point-to-point error on the beam energy was ±0.05%. The elastic peak analysis showed that to align the peaks properly, shifts, on the average, would be needed of 0.04% in E', 0.4 mr in θ, or 0.09% in E. The shift necessary in θ was way outside the uncertainty so this was ruled out. Since the necessary shift in E' was well-within the tolerance, it was decided to apply an overall shift of 0.04% to all E'. The W^2 peaks were then

aligned on the average, but there was still some scatter. This scatter was removed, and the individual peaks were aligned by applying the appropriate corrections on a point-by-point basis to E.

For the 1.6 GeV spectrometer the error on θ was ±1.0 mr. The beam energy corrections made for the 8 GeV spectrometer data were also applied for the 1.6 GeV data. An additional average correction of 0.09% was applied to all E' values to align the 1.6 GeV W^2 peaks.

Combining Runs

The data taken for a given target, spectrometer, and φ cut, were combined in two separate steps. First, runs within a kinematic point were combined, and second, kinematic points taken at the same beam energy and scattering angle, but different momentum settings were combined. The latter was not done until after the cross sections had been calculated, and will be discussed in more detail in the next section. For runs within a kinematic point, the δ-θ histograms for electrons were summed bin-by-bin. At this point the pion subtraction was performed. Run quantities which were needed for calculating cross sections (see the discussion in the next section) were combined together in the factor C_{Run} where

$$C_{Run} = \frac{C_{dt} \cdot C_{1pp} \cdot C_{sf} \cdot C_{eff}}{N_{inc} \cdot N_p} . \qquad (3.3)$$

C_{dt} is the dead time correction, C_{1pp} is the one per pulse correction, C_{sf} is the sample fraction correction, C_{eff} is the

electron efficiency correction, N_{inc} is the number of electrons incident on the target, and N_p is the number of target particles per cm^2. N_p is defined as $N_A \rho L/A$ where N_A is Avogadro's number, ρ is the target density in gm/cm^3, L is the target length in cm, and A is the atomic mass of the target in atomic mass units. The C_{Run} quantities were combined for each run to produce the corresponding quantity for the kinematic point, C_{Kin}:

$$C_{Kin} = \frac{1.0}{\sum \frac{1.0}{C_{Run}}} , \qquad (3.4)$$

where the sum was over all runs contained in the kinematic point. C_{Kin} was used to convert counts into cross section for each kinematic point in a later step to be discussed.

Raw Cross Section Calculation

This section discusses the process of converting the $\delta-\theta$ histograms, the reduced acceptance functions, and the quantity C_{Kin} to the deuterium differential cross sections, $d\sigma/d\Omega dW^2$. Note that at a constant value of θ, $d\sigma/d\Omega dE'$ is equivalent to $d\sigma/d\Omega dW^2$. The following steps were followed to calculate these cross sections corrected to a central scattering angle for each kinematic point, θ_k:

1. The relation, $W^2 = M_p^2 + 2M_p(E-E') - 4EE'\sin^2(\theta/2)$ was used to create a mapping between each $\delta-\theta$ bin and each W^2 bin. Note that the W^2 bin edges will cross the $\delta-\theta$ plane diagonally. Assuming a total $\delta-\theta$ plane area of 1.0 the mapping gives the fractional area contributed from

each δ-θ bin to each W^2 bin. Since δ and θ were calculated relative to central values, this mapping had to be calculated for each kinematic point. The mapping function is $F(I_\delta, I_\theta, I_w)$, where I_δ, I_θ, and I_w are the binning indices for the δ, θ, and W^2 bins respectively. The sum of F over all indices yields 1.0. Note that the δ-θ bins were believed to be small enough such that they could be treated as uniform. That is, no weighting was done to take into account the possibility of cross section variation within a given δ-θ bin.

2. Counts for each W^2 bin, $N_w(I_w)$, were accumulated from counts in each δ-θ bin, $N(I_\delta, I_\theta)$ by the formula:

$$N_W(I_W) = \sum_{I_\delta} \sum_{I_\theta} N(I_\delta, I_\theta) \cdot F(I_\delta, I_\theta, I_W) \,. \qquad (3.5)$$

An acceptance function for the N_w spectrum, A_w, was the next quantity to calculate, but various corrections should be discussed first (items 3-6).

3. The units of the acceptance function as calculated by the Monte Carlo programs were in msr·%. This was converted to msr·dW^2 by multiplying by $C_w(I_\theta) = (dE'/d\delta) \cdot (dW^2/dE')$:

$$C_W(I_\theta) = \left(\frac{P_0}{100}\right)(2M_p + 4E_K \sin^2(\theta(I_\theta)/2) \,, \qquad (3.6)$$

where P_0 was the spectrometer central momentum, E_K was the average beam energy for the kinematic point, and $\theta(I_\theta)$ is the value of θ corresponding to each θ bin.

4. The calculated acceptance function had no cross section dependence built into it. However, the cross section

varied enough over the $\delta-\theta$ plane to warrant a bin-by-bin correction of the acceptance so that it varied accordingly with that of the data. This correction was achieved by the function $C_1(I_\delta, I_\theta, I_w)$ which is merely a ratio of deuterium model cross sections. This function is given by:

$$C_1(I_\delta, I_\theta, I_w) = \frac{\left(\dfrac{d^2\sigma}{d\Omega dW^2}(E, E'(I_\delta), \theta(I_\theta))\right)}{\left(\dfrac{d^2\sigma}{d\Omega c'^2}(E, E'(I_w, \theta_K), \theta_K)\right)}, \qquad (3.7)$$

where $E'(I_w, \theta_K)$ is the momentum corresponding to the W^2 bin indexed by I_w and the central scattering angle for the kinematic point, θ_K. This correction also corrects all bins to the central scattering angle. The calculation of the model cross sections will be discussed in greater detail later.

5. Generally, there were several kinematic points which had similar, but not exact, kinematics, and it was desirable to correct all of these points to the same nominal kinematics in order to combine them. This correction was achieved by the function $C_2(I_w)$ which is also a ratio of deuterium model cross sections.

$$C_2(I_w) = \frac{\left(\dfrac{d^2\sigma}{d\Omega dW^2}(E, E'(I_w, \theta_K), \theta_K)\right)}{\left(\dfrac{d^2\sigma}{d\Omega dW^2}(E_{Nom}, E'(I_w, \theta_{Nom}), \theta_{Nom})\right)}, \qquad (3.8)$$

where E_{Nom} was the nominal beam energy, and θ_{Nom} was the nominal scattering angle. Note the cancellation which occurs when C_1 and C_2 are multiplied together.

6. Radiative corrections which will be discussed in greater detail in Appendix C, were calculated as a function of W^2 and θ. The θ dependence of the corrections was taken into account by the function $RC_\theta(I_\theta, I_w)$ which is a ratio of the radiative correction at the nominal scattering angle to the radiative correction corresponding to a given θ bin.

$$RC_\theta(I_\theta, I_w) = \frac{RC(\theta_{Nom}, I_w)}{RC(\theta(I_\theta), I_w)} \,.\tag{3.9}$$

7. The corrected acceptance function versus W^2 can now be expressed:

$$A_w(I_w) = \sum_{I_\delta} \sum_{I_\theta} A(I_\delta, I_\theta) \cdot F(I_\delta, I_\theta, I_w) \cdot C_w(I_\theta) \cdot C_1(I_\delta, I_\theta, I_w) \cdot C_2(I_w) \cdot RC_\theta(I_\theta, I_w),\tag{3.10}$$

where $A(I_\delta, I_\theta)$ is the acceptance function generated from the Monte Carlo.

8. Finally, the cross section and the statistical error on the cross section were calculated:

$$\frac{d^2\sigma}{d\Omega dW^2}(I_w) = \frac{N_w(I_w) \cdot C_{Kin}}{A_w(I_w)}$$

$$\delta\left(\frac{d^2\sigma}{d\Omega dW^2}(I_w)\right) = \frac{\sqrt{N_w(I_w)} \cdot C_{Kin}}{A_w(I_w)} \,.\tag{3.11}$$

It should be noted that similar calculations were done for the data measured with the long hydrogen target and the long aluminum target. However, since it was not as important to keep the errors on these quantities small as it was for the deuterium cross sections, not as much care was taken in applying the corrections during the conversion process. No θ dependence to the radiative corrections was applied, and the

cross section dependence correction, C_1, only corrected for the θ and not the momentum dependence since it was more important. It should also be noted that this calculation was done separately for data at each of the four φ cuts.

The next step was to combine the data with different central momentum settings which had been corrected to the same nominal kinematics. Figure 3.9 and Figure 3.27 are sample plots from each spectrometer showing the overlap of these data sets before they had been combined together. The data points contributing to a single W^2 bin were combined using an error weighted average. This averaging process was performed for each W^2 bin, thus producing a single spectrum of raw cross sections at each kinematic point.

Aluminum Background subtraction

For the 8 GeV spectrometer measured data it was necessary to subtract the contribution to the cross section due to scattering from the aluminum incap and endcap. The aluminum background for the cross sections measured in the 1.6 GeV spectrometer was negligible due to the presence of the tungsten shields. The measured aluminum cross section was scaled by the amount of aluminum seen in the aluminum targets divided by the amount of aluminum seen in the liquid targets, and was corrected for the difference in densities used to calculate the liquid target cross sections and the aluminum cross sections. In other words, the liquid target cross sections (with aluminum contributions) were calculated using the liquid target density while the aluminum cross sections

wer: calculated using the aluminum density. It was necessary to account for this in the subtraction. The resulting quantity was then subtracted from the liquid target cross sections on a bin-by-bin basis.

$$\sigma_{LIQ} = \frac{d^2\sigma}{d\Omega dW^2} = \sigma_{LIQ}(\text{measured}) - \sigma_{AL} \cdot (\frac{\rho_{AL}}{\rho_{liq}}) \cdot (\frac{t_{AL}}{t_{liq}}), \quad (3.12)$$

where ρ_{AL} is the density of aluminum in gm/cm^3, ρ_{liq} was the density of the liquid target in gm/cm^3, t_{AL} was the thickness of aluminum seen by the beam in the liquid targets in cm, and t_{liq} was the thickness of the liquid target in cm. The average aluminum contribution to the deuterium cross sections was 2.0% and to the inelastic hydrogen cross sections was 6.0%.

Pair Production Background subtraction

There was a contribution to the measured cross sections due to electron-positron pair production taking place at the target. The photons producing the pair production originated primarily from π^o decay. The magnitude of this contribution was measured by reversing the polarities of the magnets and measuring the positron cross sections. The largest pair production contributions to the deuterium cross section occurred at a beam energy of 2.837 GeV for both spectrometers. The contribution was 0.5% for the 8 GeV spectrometer data and was 2.3% for the 1.6 GeV spectrometer data where the average was done over W^2. Note that this is the largest measured contribution and that most of the data had a small or negligible contribution from pair production.

Hydrogen Contamination of Target Su. .raction

It was clear from the measured cross sections that there was some amount of hydrogen contamination in the deuterium target because of the presence of an obvious bump at the quasielastic peak due to elastic electron-proton scattering. The target material was analyzed in its gaseous state and a contamination of 2.5% was measured. This, however, was too large to properly account for the bump observed in the data. This discrepancy was not resolved, but it is believed that the contamination percentage could be different when the target is in the liquid state because of the difference in the condensation temperatures of hydrogen and deuterium. The amount of contamination was calculated by varying the contamination factor and minimizing the χ^2 of the ratio of the cross section data to the model as compared to the average ratio. The best fit occurred for a contamination factor of 0.85% by weight. The calculated factor was used for the subsequent subtraction of the hydrogen contamination in the deuterium target. It should be noted that the central angle radiative corrections were applied after all the target contamination subtractions took place.

Resolution Unfolding

Ionization energy losses, multiple scattering, spectrometer optics, the spread in the beam energy, and data binning limitations are all determining factors in the electron momentum resolution. The smearing of the cross sections due to this resolution was corrected using a Gaussian

shaped resolution function. A correction factor was calculated for each kinematic point as a function of W^2 by taking the ratio of the model deuterium cross sections (no resolution effects) to the same model cross section which had been convoluted with the resolution function. This correction factor was applied to the measured cross section. The resolutions (σ) used in the resolution function were measured by fitting a Gaussian peak to the de-radiated elastic e-p cross section peaks which were also measured in this experiment [15]. The measured resolutions ranged from 0.014 to 0.023 GeV^2 for the 8 GeV data and from 0.019 to 0.031 GeV^2 for the 1.6 GeV data (measured in W^2 units). The resolutions can also be estimated by summing in quadrature the expected contributions from each of the factors listed above. However, since elastic e-p data were measured at each of the desired quasielastic e-d points, this calculation was only used as a check that the measured values were reasonable.

1.6 GeV Spectrometer Normalization

Since the 1.6 GeV spectrometer's solid angle was much less well known than that of the 8 GeV spectrometer [30], a si⁻ ;le overall normalization factor was applied to all the 1.6 GeV cross section measurements. A study was made on a W^2 bin-by-bin basis to determine whether the normalization varied over the momentum acceptance range of the 1.6 GeV spectrometer. For three Q^2 points and at all W^2 where there were at least two 8 GeV data points, the reduced cross sections, for the 8 GeV data only, were fit versus epsilon.

These fits were extrapolated to the epsilon of the 1.6 GeV data and a normalization factor was calculated by taking the ratio of the fit cross sections to the 1.6 measured cross sections. No W^2 dependence to the normalization was found within errors. The average normalization was calculated for each of the three Q^2 points. There was not enough 8 GeV data

1.6 GeV Normalization
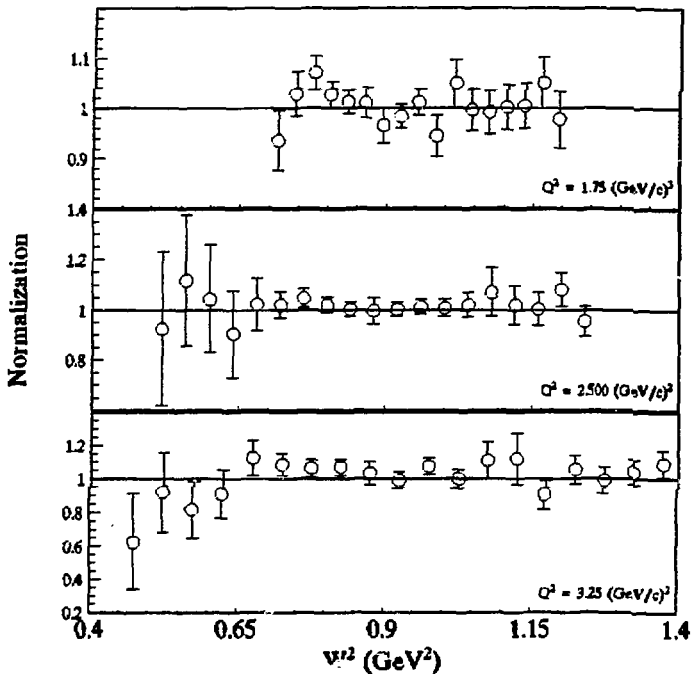
Figure 3.31: 1.6 Gev normalization plotted versus W^2 for three Q^2 points. No significant variation over W^2 is seen so the applied normalization was found using an error weighted average.

to normalize at the $Q^2 = 4.0$ (GeV/c)^2 point. Within errors the normalization did not vary with Q^2, so an overall normalization factor was found by doing a weighted average. The result for the overall normalization was 1.012 ± 0.010. Figure 3.31 shows plots of the normalizations versus W^2 at each Q^2 point where the normalization was studied.

Proton Inelastic Data

There are two important reasons for measuring the proton inelastic cross section in the region of the Δ resonance. First, these measurements are necessary in order to help develop a good model of the inelastic contribution to the quasielastic deuterium cross section. This is crucial to a precision measurement of the neutron form factors at large Q^2 where the tail contribution is significant. Second, there is a need for data on baryon excitation cross sections and transition form factors, especially at large Q^2, in order to test existing theories and models. The following tables summarize the measured inelastic electron-proton cross sections and their errors. A discussion on the errors is given in Chapter 4.

Table 3.8: Proton inelastic cross sections at $E = 5.507$ and $\theta = 15.146°$. Cross section and error units are in $(nb/(sr \cdot GeV^2))$.

W^2 (GeV^2)	Rad. Corr.	$d\sigma/d\Omega dW^2$	±Stat. error	±Total error
1.165	2.097	1.41E+00	0.40E+00	0.40E+00
1.195	1.794	1.82E+00	0.36E+00	0.37E+00
1.225	1.690	2.37E+00	0.37E+00	0.37E+00
1.255	1.636	3.84E+00	0.41E+00	0.41E+00
1.285	1.602	6.00E+00	0.44E+00	0.45E+00
1.315	1.580	7.78E+00	0.46E+00	0.49E+00
1.345	1.565	1.06E+01	0.51E+00	0.55E+00
1.375	1.552	1.42E+01	0.57E+00	0.63E+00
1.405	1.539	1.86E+01	0.62E+00	0.72E+00
1.435	1.519	2.45E+01	0.70E+00	0.84E+00
1.465	1.487	2.79E+01	0.73E+00	0.91E+00
1.495	1.443	2.97E+01	0.75E+00	0.94E+00
1.525	1.391	2.88E+01	0.74E+00	0.93E+00
1.555	1.338	2.61E+01	0.73E+00	0.88E+00
1.585	1.291	2.46E+01	0.74E+00	0.87E+00
1.615	1.253	2.24E+01	0.75E+00	0.87E+00
1.645	1.225	2.23E+01	0.83E+00	0.94E+00
1.675	1.204	2.17E+01	0.98E+00	0.11E+01
1.705	1.190	2.04E+01	0.12E+01	0.13E+01
1.735	1.181	2.33E+01	0.21E+01	0.22E+01

Table 3.9: Proton inelastic cross sections at $E = 5.507$ and $\theta = 15.981°$. Cross section and error units are in $(nb/(sr \cdot GeV^2))$.

W^2 (GeV^2)	Rad. Corr.	$d\sigma/d\Omega dW^2$	±Stat. error	±Total error
1.160	1.956	1.51E-01	0.46E-01	0.46E-01
1.200	1.781	3.30E-01	0.44E-01	0.45E-01
1.240	1.668	5.83E-01	0.47E-01	0.48E-01
1.280	1.613	8.02E-01	0.50E-01	0.53E-01
1.320	1.582	1.20E+00	0.57E-01	0.62E-01
1.360	1.563	1.91E+00	0.70E-01	0.79E-01
1.400	1.545	2.88E+00	0.82E-01	0.99E-01
1.440	1.519	3.71E+00	0.91E-01	0.12E+00
1.480	1.473	4.42E+00	0.98E-01	0.13E+00
1.520	1.409	4.55E+00	0.10E+00	0.13E+00
1.560	1.434	4.37E+00	0.10E+00	0.13E+00
1.600	1.290	3.92E+00	0.10E+00	0.13E+00
1.640	1.253	3.81E+00	0.12E+00	0.14E+00
1.680	1.230	3.68E+00	0.15E+00	0.16E+00
1.720	1.217	3.59E+00	0.21E+00	0.23E+00

Table 3.10: Proton inelastic cross sections at
E = 5.507 and θ = 22.805°. Cross section and
error units are in (nb/(sr·GeV²)).

W² (GeV²)	Rad. Corr.	dσ/dΩdW²	±Stat. error	±Total error
1.175	1.971	3.66E-02	0.87E-02	0.87E-02
1.225	1.696	9.61E-02	0.85E-02	0.87E-02
1.275	1.614	1.68E-01	0.98E-02	0.10E-01
1.325	1.574	2.70E-01	0.12E-01	0.13E-01
1.375	1.550	4.88E-01	0.17E-01	0.19E-01
1.425	1.525	7.30E-01	0.20E-01	0.24E-01
1.475	1.477	9.43E-01	0.22E-01	0.28E-01
1.525	1.402	9.76E-01	0.23E-01	0.29E-01
1.575	1.329	9.73E-01	0.24E-01	0.30E-01
1.625	1.279	8.82E-01	0.25E-01	0.31E-01
1.675	1.251	9.64E-01	0.34E-01	0.39E-01
1.725	1.237	9.00E-01	0.51E-01	0.54E-01
1.775	1.233	9.96E-01	0.23E+00	0.23E+00

Table 3.11: Proton inelastic cross sections at
E = 5.507 and θ = 26.823°. Cross section and
error units are in (nb/(sr·GeV²)).

W² (GeV²)	Rad. Corr.	dσ/dΩdW²	±Stat. error	±Total error
1.175	1.961	1.10E-02	0.28E-02	0.28E-02
1.225	1.689	2.66E-02	0.26E-02	0.27E-02
1.275	1.606	4.13E-02	0.28E-02	0.29E-02
1.325	1.565	7.43E-02	0.34E-02	0.37E-02
1.375	1.540	1.23E-01	0.39E-02	0.46E-02
1.425	1.516	1.80E-01	0.46E-02	0.57E-02
1.475	1.470	2.41E-01	0.52E-02	0.69E-02
1.525	1.400	2.57E-01	0.54E-02	0.73E-02
1.575	1.333	2.63E-01	0.57E-02	0.76E-02
1.625	1.289	2.61E-01	0.64E-02	0.81E-02
1.675	1.264	2.68E-01	0.82E-02	0.97E-02
1.725	1.252	2.67E-01	0.12E-01	0.13E-01
1.775	1.246	2.45E-01	0.41E-01	0.41E-01

Table 3.12: Proton inelastic cross sections at E = 9.300 and θ = 13.248°. Cross section and error units are in $(nb/(sr \cdot GeV^2))$.

W^2 (GeV²)	Rad. Corr.	$d\sigma/d\Omega dW^2$	±Stat. error	±Total error
1.175	2.102	8.58E-02	0.25E-01	0.25E-01
1.225	1.804	1.76E-01	0.24E-01	0.24E-01
1.275	1.716	2.95E-01	0.25E-01	0.26E-01
1.325	1.671	4.67E-01	0.28E-01	0.29E-01
1.375	1.645	7.82E-01	0.36E-01	0.39E-01
1.425	1.619	1.15E+00	0.42E-01	0.47E-01
1.475	1.570	1.46E+00	0.49E-01	0.57E-01
1.525	1.497	1.47E+00	0.54E-01	0.61E-01
1.575	1.427	1.42E+00	0.60E-01	0.66E-01
1.625	1.382	1.37E+00	0.69E-01	0.74E-01
1.675	1.357	1.49E+00	0.91E-01	0.95E-01
1.725	1.345	1.34E+00	0.14E+00	0.14E+00

Table 3.13: Proton inelastic cross sections at E = 9.800 and θ = 15.367°. Cross section and error units are in $(nb/(sr \cdot GeV^2))$.

W^2 (GeV²)	Rad. Corr.	$d\sigma/d\Omega dW^2$	±Stat. error	±Total error
1.188	1.986	3.05E-02	0.73E-02	0.73E-02
1.262	1.741	6.85E-02	0.74E-02	0.75E-02
1.337	1.668	1.35E-01	0.89E-02	0.93E-02
1.412	1.630	2.23E-01	0.11E-01	0.12E-01
1.488	1.561	3.36E-01	0.14E-01	0.16E-01
1.563	1.459	3.92E-01	0.17E-01	0.19E-01
1.637	1.399	3.90E-01	0.22E-01	0.23E-01
1.713	1.375	3.82E-01	0.33E-01	0.33E-01
1.787	1.364	4.77E-01	0.16E+00	0.16E+00

Table 3.14: Proton inelastic cross sections at E = 9.800 and θ = 17.516°. Cross section and error units are in $(nb/(sr \cdot GeV^2))$.

W^2 (GeV²)	Rad. Corr.	$d\sigma/d\Omega dW^2$	±Stat. error	±Total error
1.188	1.993	6.85E-03	0.25E-02	0.25E-02
1.262	1.743	2.85E-02	0.28E-02	0.28E-02
1.337	1.666	4.18E-02	0.32E-02	0.33E-02
1.412	1.626	7.74E-02	0.41E-02	0.44E-02
1.488	1.561	1.00E-01	0.50E-02	0.54E-02
1.563	1.470	1.15E-01	0.61E-02	0.65E-02
1.637	1.414	1.25E-01	0.80E-02	0.83E-02
1.713	1.394	1.21E-01	0.12E-01	0.12E-01
1.787	1.382	1.25E-01	0.39E-01	0.39E-01

Table 3.15: Proton inelastic cross sections at
$E = 9.800$ and $\theta = 19.753°$. Cross section and
error units are in $(nb/(sr \cdot GeV^2))$.

W^2 (GeV²)	Rad. Corr.	$d\sigma/d\Omega dW^2$	±Stat. error	±Total error
1.262	1.992	1.09E-02	0.18E-02	0.18E-02
1.337	1.739	1.28E-02	0.19E-02	0.19E-02
1.412	1.660	2.01E-02	0.24E-02	0.24E-02
1.487	1.617	3.57E-02	0.33E-02	0.33E-02
1.563	1.557	3.37E-02	0.35E-02	0.36E-02
1.637	1.476	4.20E-02	0.49E-02	0.49E-02
1.713	1.429	4.77E-02	0.73E-02	0.73E-02
1.787	1.407	5.39E-02	0.16E-01	0.16E-01

Proton Inelastic Model

The inelastic model was actually a fit to the measured hydrogen cross section data, where the fit coefficients had a polynomial Q^2 dependence. In order to constrain and improve the fits to the measured data, additional data were also considered. All inclusive electron scattering resonance region data measured up until the mid 1970's were evaluated and parameterized by Brasse, et al. [38] This parameterization was used to generate cross sections which were used in the fit at two low values of Q^2, 1.0 and 1.3 GeV/c. Higher Q^2 data were included from SLAC experiment E133 [39]. These data were in the range $2.4 \leq Q^2 \leq 9.8$ $(GeV/c)^2$. The components of the fit included a nonresonant background contribution as well as resonant contributions from the three lowest lying nucleon resonances. Details on this fit will be given after a background discussion on helicity amplitudes for $\Delta(1232)$ electroproduction.

The term helicity refers to the projection of a particle's spin along its direction of motion. It can be shown [40] that helicity is conserved in a vector interaction. Since photon and gluon exchange are both vector interactions helicity is conserved in the limit that the quark masses can be neglected. Perturbative QCD [41] asserts that at very high Q^2 this translates into hadron helicity conservation as well. Thus, it is convenient to use helicity amplitudes when studying nucleon resonance production in order to test PQCD. There are three independent helicity amplitudes (sometimes called helicity form factors) for electromagnetic N-Δ transitions. Using the same notation as Carlson [42], $G_+(Q^2)$ is the helicity conserving amplitude, $G_o(Q^2)$ corresponds to one unit of helicity change, and $G_-(Q^2)$ corresponds to two units of helicity change. G_+ is the dominant amplitude since each unit of helicity change results in a damping of the amplitude by a factor $O(m/Q)$ [42], where m is some mass scale. These damping factors can be established by analyzing the lowest order Feynman diagrams contributing to the N→Δ transition. Vainshtein and Zakharov [43] have given rules for simply analyzing these diagrams within the quark model, assuming that the quark helicities are conserved.

It is very common to see the helicity amplitudes in terms of $A_{1/2}(Q^2)$ and $A_{3/2}(Q^2)$ which contribute to only the transverse virtual photoabsorption cross section. Thus, they are called the transverse helicity amplitudes. The total inelastic electron-proton inclusive scattering cross section can be written as a sum over transverse and longitudinal components

as shown earlier in Eq. 1.16. For the $\Delta(1232)$ resonance:

$$A_{\frac{1}{2}}(Q^2) = e\sqrt{\frac{M_p}{M_\Delta^2 - M_p^2}}\, G_+(Q^2)\, , \quad A_{\frac{3}{2}}(Q^2) = e\sqrt{\frac{M_p}{M_\Delta^2 - M_p^2}} G_-(Q^2)\, , \quad (3.13)$$

where e is electron charge. The other helicity amplitude, $G_o(Q^2)$, only contributes to the longitudinal cross section. Existing resonance cross section measurements (including these data) are consistent with the longitudinal contribution being zero. This is in contrast to the nonresonant cross section which has a non-negligible longitudinal contribution. To simplify the following formulae, the quantity $A_\pi(Q^2)$ is defined to be

$$|A_H(Q^2)|^2 = \left(\left|A_{\frac{1}{2}}(Q^2)\right|^2 + \left|A_{\frac{3}{2}}(Q^2)\right|^2\right). \quad (3.14)$$

Transition form factors are defined in terms of the helicity amplitudes. Stoler [44] defines a dimensionless transition form factor, $F_\Delta(Q^2)$:

$$|F_\Delta(Q^2)|^2 = \frac{1}{4\pi\alpha}\frac{2M_p}{Q^2}(M_\Delta^2 - M_p^2)\,|A_H(Q^2)|^2. \quad (3.15)$$

Another common representation of the transition form factor is $G_M^*(Q^2)$ [45] which is the magnetic dipole transition form factor for $\Delta(1232)$ excitation. $G_M^*(Q^2)$ is related to the transverse helicity amplitudes by the formula:

$$|G_M^*(Q^2)|^2 = \frac{1}{4\pi\alpha}\frac{M_\Delta^2 - M_p^2}{\nu^2 + Q^2}\,|A_H(Q^2)|^2, \quad (3.16)$$

where ν is fixed at the Δ resonance peak for a given Q^2.

The differential scattering cross section was defined in Eq. 1.16 in terms of the transverse and longitudinal virtual photoabsorption cross sections. The transverse virtual photoabsorption cross section of the $\Delta(1232)$ resonance can be related to the transverse helicity amplitudes using a relativistic Breit-Wigner formula, as in the work by Stoler [46],

$$\sigma_{T\Delta} = \frac{\beta M_{\Delta}^2 \Gamma_{\gamma} \Gamma_{\pi}}{(W^2 - M_{\Delta}^2)^2 + (M_{\Delta}\Gamma)^2} |A_H(Q^2)|^2, \qquad (3.17)$$

where the kinematic factor, β, has been corrected from the formula given in the Stoler paper. The correct expression for the Δ resonance is given by:

$$\beta = \frac{2WM_p}{M_{\Delta}^2 \Gamma_{\Delta}} \left(\frac{K_{\Delta} K_{\Delta}^*}{K K^*} \right), \qquad (3.18)$$

The partial widths are defined:

$$\Gamma_{\pi} = \Gamma_{\Delta} \left[\frac{P_{\pi}^*}{P_{\pi\Delta}^*} \right]^3 \left[\frac{P_{\pi\Delta}^{*2} + X^2}{P_{\pi}^{*2} + X^2} \right], \quad \Gamma_{\gamma} = \Gamma_{\Delta} \left[\frac{K^*}{K_{\Delta}^*} \right]^2 \left[\frac{K_{\Delta}^{*2} + X^2}{K^{*2} + X^2} \right], \qquad (3.19)$$

where a value of 120 MeV was used for Γ_{Δ}, and the total width, Γ was set equal to Γ_{π} since the only decay channel for the $\Delta(1232)$ resonance is single pion emission. The photon width contribution to Γ was neglected. The quantities K and K^* are given by the expressions:

$$K = \frac{W^2 - M_p^2}{2M_p}, \quad K^* = \frac{W^2 - M_p^2}{2W}. \qquad (3.20)$$

K and K^* are the equivalent energies of a real photon which,

when absorbed by a proton, produce a final mass state, W, in the laboratory and in the center of mass frames respectively. K and K* evaluated at $W = M_\Delta$ are denoted by K_Δ and K_Δ^* respectively. The pion momentum in the center of mass system of the proton-pion decay state is given by

$$P_\pi^*(W) = \frac{W^2 + M_\pi^2 - M_p^2}{2W}, \quad P_{\pi\Delta}^* = P_\pi^*(M_\Delta) .$$ (3.21)

The quantity, X, is a fit parameter which determines the mass variation of the resonance widths [47]. Photoproduction data fits [48] yield a value for X of 0.160 GeV for the $\Delta(1232)$ resonance. The results are fairly insensitive to this parameter, but a χ^2 best-fit to all the data yielded a value of 0.148 GeV. Equations 3.17 to 3.21 were used in the cross section fitting procedure to account for the $\Delta(1232)$ resonance contribution. The transition form factors were then extracted from the fit.

The new NE11 data only extended just past the $\Delta(1232)$ resonance, while the Brasse and E133 cross sections clearly had contributions from at least two higher mass state resonances. In order to do a global fit to the entire set of data, two higher mass state resonances were modeled using the simpler nonrelativistic Breit-Wigner formula:

$$\sigma_i = A_i(Q^2) \frac{\Gamma_i}{(W - M_i)^2 + \frac{1}{4}\Gamma_i^2} .$$ (3.22)

The index, $i = 2$ or 3 denotes the second or third resonance and Γ_i and M_i are the widths and masses of the resonance. The coefficients, A_i, are fitting parameters. The more complicated

relativistic Breit-Wigner formula was not used because tne transition form factors from these data and for these resonances have been studied previously [46]. Also, the analysis is considerably more complicated due to multiple decay channels, and we were only interested in fitting the total cross section in this region in order to develop a model cross section. The nonrelativistic Breit-Wigner formula was sufficient for this purpose. The first of the two included higher resonances was the $S_{11}(1535)$ which is the prominent resonance in this region for the Q^2 range of the data. The second resonance was the $F_{15}(1680)$ which is known to be dominant at lower Q^2. The masses were allowed to vary to obtain the best χ^2 agreement with the data. The mass found for the $S_{11}(1535)$ was 1.504 GeV. The best mass for the $F_{15}(1680)$ resonance varied with Q^2, however, indicating that perhaps other resonances are contributing in this region at high Q^2. A Q^2-dependent mass was allowed, therefore, of the form $M = 1.680(1 + a \cdot Q^2/1000)$ where the parameter a was varied to find the best fit value of 2.28. Resonance widths of 71 and 95 MeV were used for the $S_{11}(1535)$ and the $F_{15}(1680)$ respectively.

The large nonresonant background contribution to the transverse cross section was included using a fit with the following polynomial-like form [49]:

$$\sigma_b = \sum_{n=1}^{3} C_n (W - W_{th})^{n - \frac{1}{2}} \qquad (3.23)$$

where $C_n(Q^2)$ are fit parameters and $W_{th} = M_p + M_\pi$ is the pion production threshold. This form gives the correct behavior at

pion production threshold. The nonresonant background contribution to the longitudinal cross section was assumed to be proportional to the transverse portion with the usual parameter $R = \sigma_L/\sigma_T$. A value of $R = 0.15$ was assumed. Figure 3.32 shows a sample of some of the data used in the fits and the relative contributions from each of the components discussed above. Note that the error bars on the generated Brasse data have been artificially inflated so that these data do not overwhelm the fitting.

The global fit to the data was found by allowing the coefficients from each of the contributions to have a Q^2 dependence. These fit coefficients were $|F_A|^2$ from Eqs. 3.15 and 3.17, A_1 and A_2 from Eq. 3.22, and C_1, C_2, and C_3 from Eq. 3.23. A third-order polynomial Q^2 dependence was used for all the coefficients except for $|F_A|^2$ which used a fourth-order polynomial. The results of the fit are given in Table 3.16 and are expected to be valid over the Q^2 range 1-10 $(GeV/c)^2$. Using these coefficients and the formulae given above, the proton transverse virtual photoabsorption cross section is obtained in units of μb and normalized to the dipole form factor

Table 3.16: Results from global fit to the proton inelastic cross section data. Each coefficient has a polynomial dependence in Q^2.

	1.0	Q^2	Q^4	Q^6	Q^8
$|F_A|^2$	1.44E+1	-3.52E+0	3.84E-1	-2.31E-2	5.92E-4
A_1	9.97E+0	1.05E+1	6.72E+0	-4.61E-1	
A_2	5.15E+1	-7.05E+1	4.11E+1	-2.72E+0	
C_1	3.57E+2	2.29E+3	2.22E+2	-1.86E+1	
C_2	-7.30E+3	9.74E+2	2.91E+3	-2.42E+2	
C_3	4.44E+3	5.89E+3	-7.34E+3	5.98E+2	
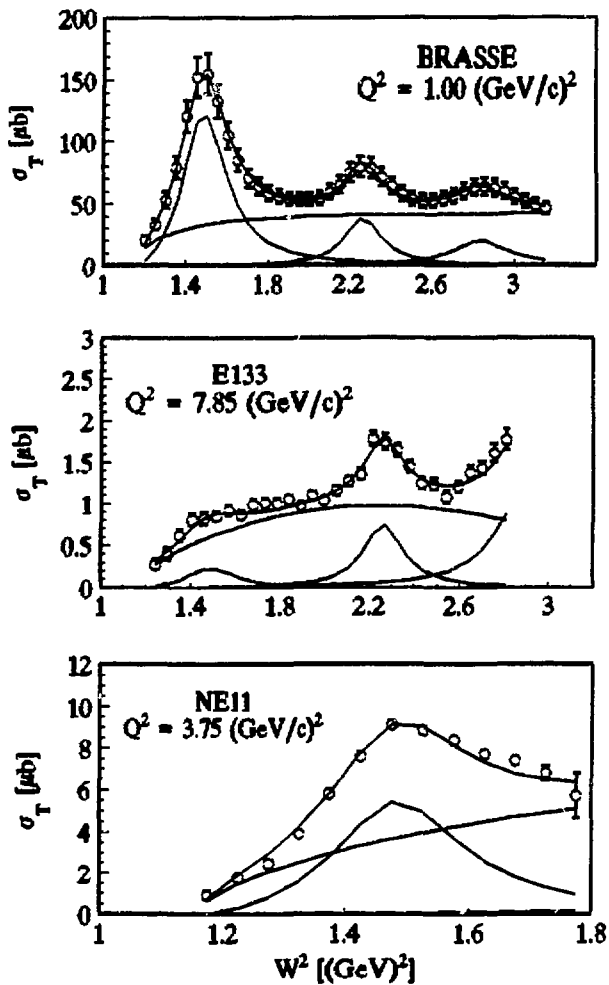
Figure 3.32: Sample transverse virtual photon cross sections, one from each data set. Curves indicate nonresonant, resonant and total cross sections from the global data fit.

squared, $(G_D(Q^2))^2 = 1.0/(1.0 + Q^2/0.71)^4$. The longitudinal resonant component is obtained using $R = \sigma_L/\sigma_T = 0$, while the longitudinal nonresonant component is obtained using $R = \sigma_L/\sigma_T = 0.15$. The model proton inelastic cross sections is then obtained by multiplying the components by $(G_D(Q^2))^2$ and by using Eq. 1.16.

$\Delta(1232)$ Resonance Transition Form Factors

The $\Delta(1232)$ resonance transition form factors were extracted from fits to the cross section data using the formulae given in the last section for each individual Q^2 data point. The NE11 data did not include contributions from the higher mass state resonances. The results are shown in Figure 3.33 and in Table 3.17. The form factors have been normalized to F_{Dipole} which is equal to $3.0*G_D$ where G_D is the dipole form factor defined earlier. The factor of 3.0 is the effective magnetic moment of the Δ resonance. Also included on this plot is the global Q^2 fit to the form factors as given in Table 3.16, a prediction from a diquark model [50] developed by *Kroll, Schürmann, and Schweiger, and asymptotic predictions*

Table 3.17: NE11 $\Delta(1232)$ transition form factor results normalized to $F_{Dipole} = 3.0/(1.0 + Q^2/0.71)^2$.

Q^2 (GeV/c)^2	$F_\Delta(Q^2)/F_{Dipole}$	$\pm$(Stat. error)	$\pm$(Total error)
1.640	1.13	0.036	0.042
2.343	0.99	0.035	0.040
3.046	0.90	0.039	0.043
3.749	0.75	0.040	0.044
3.859	0.89	0.064	0.066
4.824	0.60	0.114	0.115
5.789	0.45	0.158	0.160
6.754	0.66	0.192	0.192

Δ(1232) Transition Form Factor
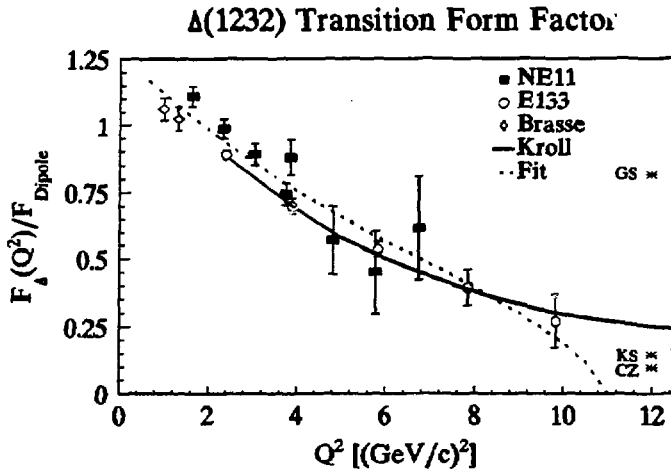
Figure 3.33: Δ(1232) transition form factors extracted from data fits at each Q² point. Comparison to the diquark model of Kroll, *et al* [51], is shown, as well as the global Q² fit.

due to Carlson and Poor [42][51] using different nucleon distribution amplitudes (GS, KS, CZ, see below) for the N→Δ transition calculation.

A distribution amplitude is the momentum-space wave function which has been integrated over the transverse momenta. The helicity amplitude predictions of Carlson and Poor were found using nucleon distribution amplitudes from Chernyak and Zhitnitsky (CZ) [52], King and Sachrajda (KS) [53], and Gari and Stefanis (GS) [54], and QCD sum rule constraints on the moments of the distribution amplitude for the Δ(1232) resonance.

The asymptotic predictions from Carlson and Poor are actually only for the dominant transverse helicity amplitude,

$A_{1/2}(Q^2)$, and are given by:

$$Q^3|A_{1/2}(Q^2)| = \begin{cases} 0.02 \text{ GeV}^{5/2} & (\text{CZ}[52]) \\ 0.03 \text{ GeV}^{5/2} & (\text{KS}[53]) \\ 0.17 \text{ GeV}^{5/2} & (\text{GS}[54]) \end{cases} \tag{3.24}$$

In order to compare with $F_{\Delta}(Q^2)$, some assumption must be made about the contribution from $A_{3/2}(Q^2)$. Perturbative QCD predicts that $A_{1/2}(Q^2)$ falls as $1/Q^3$ and $A_{3/2}(Q^2)$ falls as $1/Q^5$, but this has not been established experimentally. The points shown in Figure 3.33 were calculated at the Q^2 shown assuming that the contribution from $A_{3/2}(Q^2)$ could be neglected.

The diquark model was originally developed to study the elastic electromagnetic nucleon form factors, but has recently been extended to study the $\Delta(1232)$ transition form factors as well [55]. The formula for the virtual photon transverse cross section in this model is given by:

$$\sigma_T = \frac{2m_p}{\Gamma_\Delta m_\Delta}\left(\left|A_{\frac{1}{2}}(Q^2)\right|^2 + \left|A_{\frac{3}{2}}(Q^2)\right|^2 \right)$$
$$= \frac{2m_p}{\Gamma_\Delta m_\Delta}\left(\pi\alpha \frac{Q^2 + (m_\Delta - m_p)^2}{2m_p(m_\Delta^2 - m_p^2)} \right)\left(\frac{h_-^2(Q^2)}{9} + \frac{h_-^2(Q^2)}{3} \right), \tag{3.25}$$

$$h_-(Q^2) = C_P\sqrt{6}\,\frac{16\pi}{9m_V^2}\,f_V^P f^\Delta \int_0^1 dx_1 dy_1 \phi^\Delta(y_1)\phi_V^P(x_1)$$
$$\{-\alpha_s(\tilde{Q}^2)\kappa_V F_V^{(3)}(\tilde{Q}^2) + \frac{\alpha_s(\hat{Q}^2)}{x_1 y_1} F_V^{(4)}(Q^2)$$
$$\left[\kappa_V^2(x_1 + y_1) - \kappa_V(1 - x_1)(1 - y_1)\right]\},$$

$$h_-(Q^2) = C_P\sqrt{6}\,\frac{4\pi}{9m_V^2}\,f_V^P f^\Delta \int_0^1 dx_1 dy_1 \phi^\Delta(y_1)\phi_V^P(x_1)$$
$$\{\frac{8m_V^2}{Q^2}\,\frac{\alpha_s(\tilde{Q}^2)F_V^{(3)}(\tilde{Q}^2)}{(1 - x_1)(1 - y_1)} - \frac{\alpha_s(\hat{Q}^2)}{x_1 y_1} F_V^{(4)}(Q^2)$$
$$\left[\kappa_V^2(1 + x_1)(1 + y_1) + 2\kappa_V(x_1 - y_1) - (1 - x_1)(1 - y_1)\right]\}, \tag{3.26}$$

The diquark model is discussed in more detail in Chapter 4 in the discussion on nucleon form factor models. All of the above variables are defined in this discussion with the exception of

$$f^\Delta = \sqrt{2} f_V^P, \quad \phi^\Delta(x) = B\phi_V^P(x)[1.0 - 5.15x + 5.45x^2]. \quad (3.27)$$

where B is just the normalization for the distribution amplitude function used in the model.

It can be concluded that the $\Delta(1232)$ transition form factor falls off more rapidly with increasing Q^2 than the nucleon form factor and also more rapidly than the transition form factors for the $S_{11}(1535)$ and the $F_{15}(1680)$ resonances as analyzed by Stoler [46]. Plots showing the proton form factors as measured in this experiment will be given later this chapter. The implications of the observed fall-off are not entirely clear, but this is not the prediction of leading-order pQCD which is that $F_\Delta/F_{Dipole} \rightarrow$ constant at large Q^2. A multipole analysis for photoproduction cross section data in the $\Delta(1232)$ region at Q^2 below 0.45 $(GeV/c)^2$ has been done [56]. In this region, pQCD is not expected to be valid. The results show that $\Delta(1232)$ production is primarily a spin-flip transition, and that the $A_{3/2}(Q^2)$ helicity amplitude is dominant. It is possible that at the higher Q^2 of this experiment, the $A_{3/2}(Q^2)$ amplitude is still dominating over the $A_{1/2}$ amplitude, which would explain the fall-off of F_Δ/F_{Dipole} with increasing Q^2.

Quasielastic Cross Section Model

The neutron form factor extraction procedure is model dependent. In order to correctly extract these quantities the quasielastic cross section model should be able to adequately model the shape of the quasielastic peak. The deuterium quasielastic cross section model used in this analysis was based on a simplified version of the theoretical nonrelativistic *PWIA* model due to *McGee* [17][57] and *Durand* [16][58]. Starting with this model as given by *Bartel, et al.* [59], only the terms which were proportional to $u^2(k)$ and $w^2(k)$ were kept. The quantities u and w are the s-state and d-state momentum-space amplitudes of the deuteron wave function, and k is the laboratory momentum of the spectator nucleon in the impulse approximation. The result is given by

$$\frac{d^2\sigma}{d\Omega dE'} = \frac{M_p^2}{2q}\frac{E}{E'}(\sigma_p + \sigma_n)\int_{k_{min}}^{k_{max}}\frac{[u^2(k) + w^2(k)]k dk}{\sqrt{k^2 + M_p^2}}, \qquad (3.28)$$

where q is the magnitude of the vector three-momentum carried by the interacting photon, E' corresponds to elastic scattering given the incident energy, E, and the scattering angle, θ, and $\sigma_p(E,\theta)$ and $\sigma_n(E,\theta)$ are the nucleon elastic cross sections as given by the Rosenbluth formula, Eq. 1.6. The quantities k_{min} and k_{max} are the minimum and maximum allowed values for the longitudinal Fermi momentum carried by the struck nucleon relative to the photon direction as determined

by the energy conservation formula:

$$E + M_d = E' + \sqrt{M_p^2 + k^2} + \sqrt{W^2 + (k+q)^2}, \qquad (3.29)$$

where W is the final mass state of the hit nucleon. A reduced cross section can now be defined by:

$$\sigma_R = \frac{\epsilon(1+\tau') \dfrac{d^2\sigma}{d\Omega dE'}}{\tau' \sigma_{Mott}} = \left[R_T + \frac{\epsilon}{\tau'} R_L\right], \qquad (3.30)$$

where $\tau' = v^2/Q^2$, ϵ was defined in Eq. 1.17 and σ_{Mott} was defined in Eq. 1.5. The transverse and longitudinal components, R_T and R_L, can be calculated using Eqs. 1.6, 3.27, and 3.29 yielding the expressions:

$$R_T(E', Q^2) = \frac{M_p^2}{2q} \frac{E}{E'} \left(G_{Mp}^2(Q^2) + G_{Mn}^2(Q^2)\right) \int_{k_{min}}^{k_{max}} \frac{\psi^2(k)\, k\, dk}{\sqrt{k^2 + M_p^2}},$$

$$R_L(E', Q^2) = \frac{M_p^2}{2q} \frac{E}{E'} \left(G_{Ep}^2(Q^2) + G_{En}^2(Q^2)\right) \int_{k_{min}}^{k_{max}} \frac{\psi^2(k)\, k\, dk}{\sqrt{k^2 + M_p^2}}. \qquad (3.31)$$

Note that a study comparing the full McGee PWIA model to the simplified model described above show < 2 % differences in the peak region [66]. The wave function, $\psi^2(k) = u^2(k) + w^2(k)$, in this study was parameterized using three different nonrelativistic nucleon-nucleon potentials, Paris [60], Bonn [61], and the Reid soft core [62] potentials. These wave functions are similar and only start to significantly disagree for the less probable high momentum components which correspond to the short range part of the nucleon-nucleon interaction [63]. These high momentum components only contribute to the tail regions of the

quasielastic cross section, and thus do not have a big effect on this model calculation. However, the inelastic tail which contributes in the quasielastic peak region can be sensitive to these high momentum components. Results from a study on this possibility will be discussed in the next section.

Also included in this model was a relativistic correction using calculations by Keister [64] based on a light-cone dynamics formulation [65]. The effect of this correction on the final extracted form factors was well within the calculated errors. Another relativistic correction due to Gross is currently under investigation, but preliminary tests indicate that this correction also has a small effect on the final form factors.

Corrections were not made for final state interactions (FSI) and meson exchange currents (MEC) because the necessary theoretical calculations have not been done for the kinematics of this experiment. A careful study of these contributions to the form factors should become available as the calculations are finished [66]. Calculations by Laget [67][68] and Arenhovel [69][70] were presented by Petratos [71] for backward angle electron-deuterium cross sections in the range $0.75 < Q^2 < 2.57$ $(GeV/c)^2$. These calculations include FSI and MEC effects and clearly indicate that these effects are minimal at the quasielastic peak, but can be large in the tail regions. The effects due to FSI are expected to decrease with increasing Q^2 [17], and they should affect the longitudinal and transverse components of the cross section by about the same amount (See Eq. 3.30). To first order the

effects due to MEC only contribute to the transverse component of the cross section [67] and thus only affect the measured value of $G_{Mn}(Q^2)$. The magnitude of this correction is not well known, but the effect increases as W^2 increases from the quasielastic peak region into the "dip" region which is located between the quasielastic peak and the $\Delta(1232)$ resonance.

Fermi Smearing Models

The term "smearing" refers to the effect on measured cross sections due to the Fermi motion of nucleons within a nucleus compared to the cross sections measured off of free nucleons. There are several different formalisms available on how this smearing process should be carried out. Several different approaches will be presented here and compared with one another. The formulae presented will be in terms of the inelastic structure functions, W_1 and W_2, which were defined in Chapter 1. These formulae give the smeared model structure functions for the proton only (denoted by superscript p). After all the smearing methods are presented a discussion will be given on how the deuteron inelastic cross section is found from these smeared proton structure functions. The unsmeared proton inelastic structure functions for all methods were obtained from the proton inelastic model which was discussed earlier in this chapter.

The first smearing model is a simple and quick smearing method based on the simple McGee-Durand representation of the quasielastic cross section and was developed by P. Bosted

[72]. Any good smearing model should be able to adequately reproduce the quasielastic cross section by assuming a delta function elastic peak at $W = M_p$ as the input to the smearing formula. This model goes one step further. If the cross section formula given in Eq. 3.28 represents the Fermi smearing of a delta function proton elastic peak at $W = M_p$, then the inelastic smeared cross section at a given kinematic point can be obtained by replacing the elastic cross section portion of Eq. 3.28 with an integration over the inelastic proton cross section (a sum over the smeared contributions from many delta functions at the desired kinematic point). The formula for this smearing method in terms of the structure function, W_1, is given by the expression:

$$W_{1SM}^p(\nu,Q^2) = \int_{W_{min}}^{W_{max}} W_1^p(W,Q^2) \frac{M_p^2}{2q} dW \int_{k_{min}}^{k_{max}} \psi^2(k) \frac{k\,dk}{\sqrt{k^2 + M_p^2}}. \qquad (3.32)$$

The lower limit of the W integration was defined by the pion production threshold, $W_{min} = M_p + M_\pi$. The upper integration limit was chosen to be sufficiently large such that the smeared contributions from that cutoff point were negligible for the largest W bin where the smeared cross section was needed. This smearing formula assumes a normalization:

$$\int \psi^2(k)\,k^2 dk = 1. \qquad (3.33)$$

This smearing method is quick because the integrand from the integral over k is independent of kinematics (the limits of integration are not). The integral from $k_{min} = 0.0$ to $k_{max} = k_f$ can be evaluated at many values of k_f giving a function,

$I(k_f)$. The smearing formula is then effectively reduced to a single integration where the integral over k is reduced to the factor $I(k_{max}) - I(k_{min})$. Note that this smearing method only involves one smearing formula whereas the following models all have two smearing formulae. The assumption was made for this first model that the ratio σ_L/σ_T for the smeared cross sections was constant, just as this ratio was assumed constant for the proton model cross sections.

The second smearing model uses the formalism of Atwood-West [73] as given by Bodek, et al. [74], and includes off-mass-shell effect modifications. This approach is based on an incoherent impulse approximation which assumes that only one of the two nucleons participates in the interaction and the two nucleons have no additional interactions between them. The other nucleon, referred to as the spectator, is on the mass shell and is unaffected by the interaction. The interacting nucleon is initially off mass shell, but is brought back on to the mass shell with the absorption of the virtual photon. The kinematics of the smearing formulae are given in the laboratory frame where,

$$q = (0, 0, q_3, \nu) \quad = \text{virtual photon 4-momentum,}$$
$$p_d = (0, 0, 0, M_d) \quad = \text{deuteron 4-momentum,}$$
$$p_s = (p_1, p_2, p_3, E_s) = \text{spectator nucleon 4-momentum,}$$
$$p = (-\vec{p}_s, M_d - E_s) \quad = \text{interacting nucleon 4-momentum,} \qquad (3.34)$$
$$p_t = \sqrt{p_1^2 + p_2^2} \quad = \text{transverse nucleon momentum,}$$
$$E_s = \sqrt{\vec{p}_s^2 + M_p^2} \quad = \text{spectator nucleon total energy.}$$

The smearing formulae are given in terms of the inelastic structure functions W_1 and W_2:

$$W_{1SM}^p(\nu, Q^2) = \int \psi^2(\vec{p}) \left[W_1^p(\tilde{\nu}, Q^2) + W_2^p(\tilde{\nu}, Q^2) \frac{p_t^2}{2M_p^2} \right] d^3p,$$

$$W_{2SM}^p(\nu, Q^2) = \int \psi^2(\vec{p}) \left[\left(1 - \frac{p_3 Q^2}{m\nu' q_3}\right)^2 \left(\frac{\nu'}{\nu}\right)^2 + \frac{p_t^2 Q^2}{2M_p^2 q_3^2} \right] W_2^p(\tilde{\nu}, Q^2) d^3p,$$

(3.35)

where W_1 and W_2 in the integrands are the proton off-mass-shell structure functions. These will be discussed in more detail shortly. The remaining kinematic factors are defined:

$$\nu' = \frac{p \cdot q}{M_p} = \frac{1}{M_p}((M_d - E_s)\nu + p_3 q_3),$$

$$W^2 = (p+q)^2 = (M_d - E_s)^2 - p_s^2 + 2M_p \nu' - Q^2,$$

(3.36)

$$\tilde{\nu} = \frac{W^2 - M_p^2 + Q^2}{2M_p}.$$

The wave functions considered are the same as those used for the quasielastic modelling. The normalization assumed is:

$$\int \psi^2(\vec{p}) d^3p = 1$$

(3.37)

The third, fourth, and fifth smearing models are all due to Sargsyan, Frankfurt, and Strikman [75][76]. The third method calculates the smearing formulae using the impulse approximation in terms of light-cone quantum mechanics and its associated light-cone variables. Note that the structure function, F_2 in the original formula of the Sargsyan, Frankfurt, and Strikman paper [75] has been converted to W_2 using the relation $F_2(\nu, Q^2) = \nu W_2(\nu, Q^2)$, and a typographical error in this same formula has been corrected.

The formulae are given by:

$$W_{1SM}^{p}(\nu, Q^2) = \int \psi^2(\vec{k}) \frac{2M_p}{\alpha M_d} \left[W_1^p(\tilde{\nu}, Q^2) + W_2^p(\tilde{\nu}, Q^2) \frac{k_t^2}{2M_p^2} \right] d^3k,$$

$$W_{2SM}^{p}(\nu, Q^2) = \int \psi^2(\vec{k}) \left[(1+\cos\delta)^2 \left(\alpha + \frac{m\nu'\alpha_q}{Q^2} \right)^2 + \frac{(\sin^2\delta) k_t^2}{2M_p^2} \right]$$
$$\cdot \frac{M_d}{2M_p\alpha} W_2^p(\tilde{\nu}, Q^2) d^3k, \qquad (3.38)$$

where it is important to note that the integration variable, k, is not the same integration variable, p, given in smear model 2. The variables k and α are light cone variables, and the spectator four-momentum is defined in terms of them:

$$\alpha = 1 + \frac{k_3}{\sqrt{M_p^2 + k^2}},$$

$$E_s = \sqrt{\vec{p}_s^2 + M_p^2} \qquad (3.39)$$

$$\vec{p}_s = \left(-k_1, -k_2, E_s - M_d \left(\frac{2-\alpha}{2} \right) \right),$$

where the vector $k = (k_1, k_2, k_3)$, $k_t^2 = k_1^2 + k_2^2$, and $(2 - \alpha)/2$ is defined to be the fraction of the deuteron momentum carried by the spectator nucleon in the frame where the deuteron momentum is infinite. The remaining kinematic factors are defined:

$$\sin^2\delta = \frac{Q^2}{q_3^2}, \qquad \alpha_q = \frac{\nu - q_3}{M_p},$$

$$\nu' = \frac{q \cdot (p_d - p_s)}{M_p} = \frac{1}{M_p} \left[(\nu + q_3) \frac{\alpha M_d}{4} + \frac{(\nu - q_3)}{M_d} \left(\frac{M_d^2}{2} - \frac{k_t^2 + M_p^2}{2 - \alpha} \right) \right],$$

$$W^2 = (q + p_d - p_s)^2 = \frac{\alpha}{2} M_d^2 - \left(\frac{2}{2-\alpha} \right) (k_t^2 + M_p^2) + 2M_p\nu' + M_p^2 - Q^2,$$

$$\tilde{\nu} = \frac{W^2 - M_p^2 + Q^2}{2M_p}.$$

The variables q and p_d are defined the same as in Eq. 3.34, and the wave function normalization is given by Eq. 3.37.

The fourth smearing model involves a slight modification of smearing model 3 to account for a possible "EMC effect" in the deuteron at large x, where x, the Bjorken variable, is defined to be $Q^2/(2M_p\nu)$. The "EMC effect" is basically a measured observation that the properties of loosely bound and tightly bound nucleons differ [77][78][79]. This smearing model uses an EMC correction found using a quark color charge screening model [80]. This is not the only model which can explain the EMC effect. The EMC correction factor is given by $\eta(x,k)$. This correction multiplies the free nucleon structure functions which appear in Eq. 3.38 to convert them to bound nucleon structure functions. The form of the correction is given by:

$$\eta(x,k) = \begin{cases} 1 & x < 0.3 \\ 1 + (\delta(k) - 1)\left(\dfrac{x - 0.3}{x_0 - 0.3}\right) & 0.3 \le x \le x_0 \\ \delta(k) & x > x_0 \sim 0.6 - 0.7 \end{cases} \quad (3.41)$$

where:

$$\delta(k) = \left[1 + \frac{2\left(\dfrac{k^2}{2M_p} + \dfrac{1}{2}\epsilon_d\right)}{\Delta E_d}\right]^{-2}, \quad (3.42)$$

ϵ_d is the binding energy of the deuteron, and ΔE_d is the characteristic excitation energy of a nucleon inside the nucleus. Since isospin is conserved and the isospin of the deuteron is zero, this quantity is expected [80] to be on the order of $2(M_\Lambda - M_p) \sim (M_{N^*}(1440) - M_p) \approx 0.6-0.8$ GeV. The

results are fairly insensitive to the choice of ΔE_d. A value of 0.6 was used.

The fifth and last smearing model [75] is the same as model 2, discussed above, except that a correction has been made on the normalization of the deuteron wave function based on baryon charge conservation [81]. This correction factor multiplies the integrands in Eq. 3.35, and is given by $N(p)$:

$$N(p) = \frac{2\left(M_d - \sqrt{M_p^2 + p^2}\right)}{M_d}. \qquad (3.43)$$

In smearing models 2-5, the input structure functions in the integrands, W_1 and W_2, should be the proton off-mass shell structure functions. However, it is not clear how the on-shell and the off-shell structure functions are related, and different prescriptions have been suggested. The use of different off-shell structure functions may help in estimating systematic uncertainties in the smeared model cross sections. The simplest representation is to naively set the off-shell and on-shell structure functions equal to each other:

$$W_1^P(\tilde{\nu}, Q^2)\big|_{\text{off-shell}} = W_1^P(\tilde{\nu}, Q^2)\big|_{\text{on-shell}},$$
$$W_2^P(\tilde{\nu}, Q^2)\big|_{\text{off-shell}} = W_2^P(\tilde{\nu}, Q^2)\big|_{\text{on-shell}}, \qquad (3.44)$$

where Q^2 is not affected by the Fermi motion since it is completely determined by the electron kinematics, and $\tilde{\nu}$ is the energy as dictated by conservation of energy such that the nucleon is brought back on-mass-shell upon absorption of the photon. The approximation of no off-shell correction implies that the interacting nucleon is not far off the mass shell

which is presumably true for the weakly bound deuteron system.

A possible off-shell correction is discussed in the reference, Bodek, *et al.* [74]. The longitudinal virtual photoabsorption cross section for the deuteron, σ_{Ld}, is expressed in terms of the smeared proton and neutron structure functions, and the limit is taken as $Q^2 \rightarrow 0$. According to gauge invariance σ_{Ld} must vanish in this limit. This is equivalent to requiring that the photoabsorption cross sections for real and virtual photons are the same at $Q^2 = 0$. The smeared neutron structure functions can be obtained from the smeared proton structure function formulae by replacing W_1^p and W_2^p by W_1^n and W_2^n respectively, and the deuteron structure function is taken to be the sum of the smeared proton and neutron structure functions. The relationship between the structure functions and the transverse and longitudinal virtual photoabsorption cross sections is given by:

$$W_1(\nu,Q^2) = \frac{K}{4\pi^2\alpha}\sigma_T(\nu,Q^2),$$

$$W_2(\nu,Q^2) = \frac{K}{4\pi^2\alpha}\left(\frac{Q^2}{Q^2+\nu^2}\right)\left[\sigma_T(\nu,Q^2)+\sigma_L(\nu,Q^2)\right].$$

3.45

where K is the same as that given earlier in Eq. 3.20. It can be shown [74][82] that in the limit as $Q^2 \rightarrow 0$ a physical result can only be achieved if an off-shell correction is applied such as:

$$W_1^p(\bar{\nu},Q^2)\Big|_{off-shell} = W_1^p(\bar{\nu},Q^2)\Big|_{on-shell},$$

$$W_2^p(\bar{\nu},Q^2)\Big|_{off-shell} = \left(\frac{\bar{\nu}}{\nu'}\right)^2 W_2^p(\bar{\nu},Q^2)\Big|_{on-shell},$$

(3.45)

or:

$$W_1^P(\tilde{v}, Q^2)\big|_{off-shell} = \left(\frac{v'}{\tilde{v}}\right)^2 W_1^P(\tilde{v}, Q^2)\big|_{on-shell},$$

$$W_2^P(\tilde{v}, Q^2)\big|_{off-shell} = W_2^P(\tilde{v}, Q^2)\big|_{on-shell}, \tag{3.46}$$

or some linear combination of these two corrections. The kinematic variables used in the above equations were defined in Eq. 3.36.

There is some ambiguity in the above off-shell corrections, and there is no reason why the off-shell correction should not have a Q^2 dependence. Kusno and Moravczik [83] have identified a possible set of off-shell structure functions as:

$$W_1^P(\tilde{v}, Q^2)\big|_{off-shell} = W_1^P(\tilde{v}, Q^2)\big|_{on-shell},$$

$$W_2^P(\tilde{v}, Q^2)\big|_{off-shell} = \left(\frac{\tilde{v}^2 + Q^2}{v'^2 + Q^2}\right) W_2^P(\tilde{v}, Q^2)\big|_{on-shell}, \tag{3.47}$$

This off-shell correction to the W_2 structure function is equivalent to assuming that there is no off-shell correction applied to the transverse and longitudinal photoabsorption cross sections, σ_T and σ_L. This is generally assumed to be true for hadronic scattering and has been carried over to electron scattering. This off-shell correction is also completely consistent with the constraint mentioned above that $\sigma_{Ld} \to 0$ as $Q^2 \to 0$, and there are no ambiguities. The effect on the smeared model cross sections and to the extracted neutron form factors due to these various off-shell corrections will be investigated and discussed later.

Deuterium Inelastic Cross Section Model

The inelastic deuterium cross section model was formed using the above smearing models and the proton inelastic cross section model discussed earlier. For fitting purposes the resonant and nonresonant contributions to the structure functions in the smearing formulae were treated separately. The resonant component consisted of the sum over the contributing resonance cross sections which was dominated by the $\Delta(1232)$ in the region of interest, and the nonresonant background component was modeled using Eq. 3.23. W_1 and W_2 used in the integrands of the smearing formulae were calculated using Eq. 3.45 where the ratio σ_L/σ_T for the nonresonant component was parameterized by $R_{nr} = 0.15$, and for the resonant component was parameterized by $R_r = 0.0$. After the smearing process was performed the smeared proton longitudinal and transverse cross sections for the resonant and nonresonant components were extracted, again using Eq. 3.45.

The single most important assumption made in the fitting procedure was that the shape of the smeared neutron cross sections is the same as that of the smeared proton cross sections for each of the cross section components. Thus, the deuterium cross section data was fit using only the smeared proton cross sections components as input, and the coefficients found give information on the neutron contribution to the deuterium cross section, or equivalently information on the ratio of σ_n/σ_p for each of the cross section components. The quantity R_r was assumed to be zero for the smeared structure functions in all of the smearing models.

Smearing models 2-4 were capable of calculating this quantity, but testing indicated that it was negligible for this experiment's kinematics. For smearing model 1, since only one smearing formula was used, R_{nr} for the smeared structure functions was assumed to remain constant, and the same value of $R_{nr} = 0.15$ that was used for the proton nonresonant inelastic cross sections was also used for the smeared proton cross sections. The other smearing models, however, predicted non-constant values for R_{nr} in the vicinity of the quasielastic

σ_L/σ_T Model Cross Section Ratios
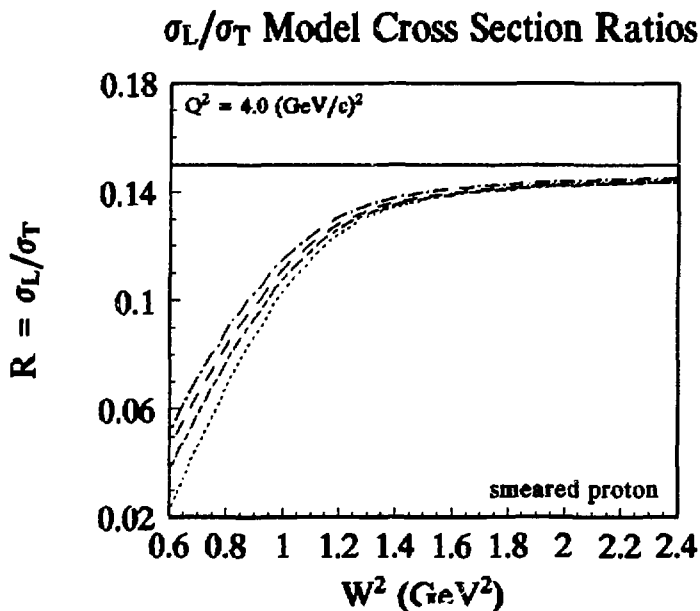
Figure 3.34: Predicted values for $R = \sigma_L/\sigma_T$ (nonresonant) for each of the five smearing models for the smeared proton cross sections. The models predict some shape dependence to R at low W^2.

peak. Figure 3.34 shows a sample plot of $R = R_{nr}$ for each of the five smearing models, with the Paris deuteron wave function and with the off-shell correction given in Eq.3.47 for the smeared proton structure functions. It is clear that the R curves approach a constant at large W^2 for a fixed Q^2 which is consistent with deep-inelastic electron scattering cross section measurements [84]. It is also clear that the smearing models predicts a suppression of the inelastic longitudinal cross section in the vicinity of the quasielastic peak.

A global Q^2 fit to all of the inelastic deuterium data was done in conjunction with the form factor fits which will be discussed in the next section, assuming that the total deuterium cross section is just the sum of the quasielastic and inelastic contributions, $\sigma_d = \sigma_{quasi} + \sigma_{inel}$. The fit to σ_{inel} was done with two parameters:

$$\sigma_{inel} = C_{nr}\left(\sigma_T^{nr} + \varepsilon\,\sigma_L^{nr}\right) + C_r\sigma_T^r, \qquad (3.48)$$

where σ_T^{nr} and σ_L^{nr} are the transverse and longitudinal nonresonant contributions to the smeared proton cross section, and σ_T^r is the resonant contributions to the smeared proton transverse cross section. The fit coefficients are C_{nr} and C_r. Figures 3.35 and 3.36 show sample deuterium reduced cross section plots from each spectrometer (See Eq. 3.30 for the reduced cross section definition). These plots also show the contributions resulting from fits to the data for the quasielastic cross section, the inelastic cross section, and the total deuterium cross section. The fitting method

8 GeV Reduced Cross Sections
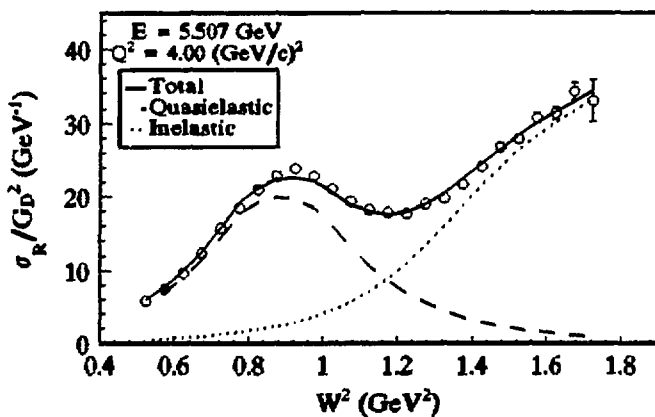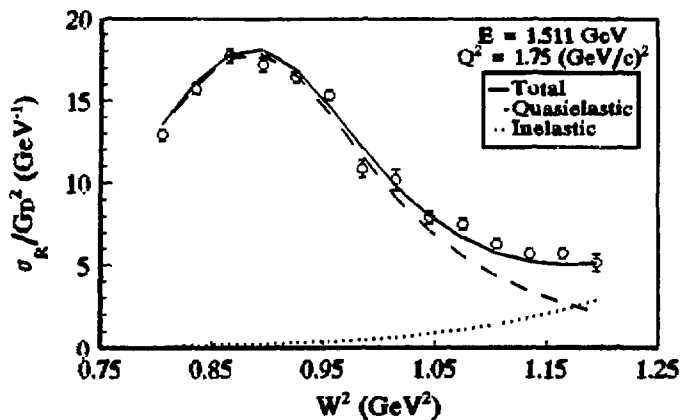
Figure 3.35: Sample 8 GeV spectrometer deuterium reduced cross section data with cross section fits broken up into the quasielastic and inelastic contributions. The data is normalized to the dipole form factor squared.

1.6 GeV Reduced Cross Sections
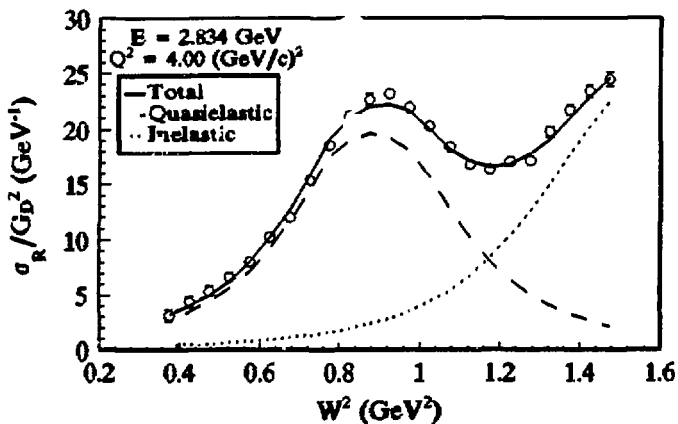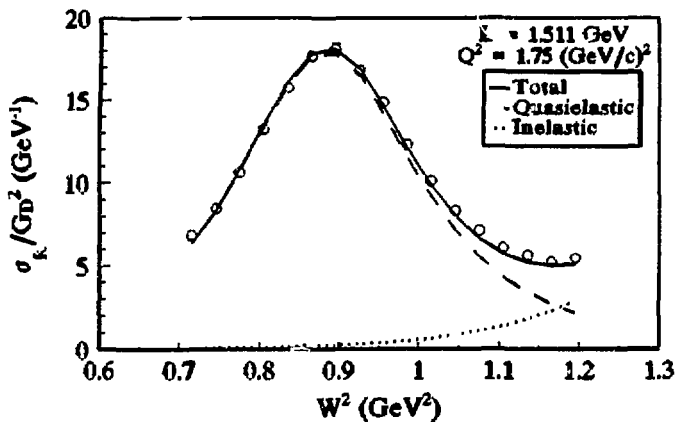
Figure 3.36: Sample 1.6 GeV spectrometer deuterium reduced cross section data with cross sections fits broken up into the quasielastic and inelastic contributions. The data is normalized to the dipole form factor squared.

corresponds to area method I which is described in the next chapter. The inelastic model used for these fits used smearing model 3 with the off-mass-shell correction given by Eq. 3.47 and the Paris deuteron wave function.

σ_n/σ_p ratios in the $\Delta(1232)$ region

It was mentioned earlier that the neutron and proton cross sections were assumed to have the same shape in W^2. If is also assumed that $\sigma_{inel} = \sigma_p + \sigma_n$, where σ_p and σ_n are the proton and neutron smeared cross sections, then the ratio of neutron to proton cross sections, σ_n/σ_p can be estimated for each of the inelastic contributions from the fit coefficients. For example, $(\sigma_n/\sigma_p)^{nr}$, the ratio for the nonresonant cross sections, is estimated from $C_{nr} - 1$ (compare Eq.3.48 with the

Table 3.18: Estimated ratios of σ_n/σ_p for the inelastic resonant and nonresonant cross section components from fits to measured deuterium cross sections using various smearing models, off-mass-shell corrections in the smearing models, and deuteron wave function parameterizations. $I_{sm} = 1,5$ indicates the smearing model used, $I_{off} = 3.44$, 3.45, 3.47 refers to the equation number where the off-mass-shell corrections were defined. $I_{wf} = P$, B, or R refers to the Paris, Bonn, and Reid deuteron wave functions. Errors are statistical.

I_{sm}	I_{off}	I_{wf}	$(\sigma_n/\sigma_p)^{nr}$	$(\sigma_n/\sigma_p)^r$
1	none	P	0.54 ± 0.04	1.34 ± 0.03
2	3.47	P	0.39 ± 0.04	1.11 ± 0.03
3	3.47	P	0.34 ± 0.04	1.10 ± 0.03
4	3.47	P	0.44 ± 0.04	1.15 ± 0.03
5	3.47	P	0.37 ± 0.04	1.10 ± 0.03
3	3.44	P	0.33 ± 0.04	1.07 ± 0.03
3	3.45	P	0.33 ± 0.04	1.13 ± 0.03
3	3.47	B	0.34 ± 0.04	1.07 ± 0.03
3	3.47	R	0.33 ± 0.04	1.12 ± 0.03

expression for σ_{inel} given above). Table 3.18 summarizes these quantities as calculated from the fit coefficients under a variety of model assumptions. Figure 3.37 shows previous measurements made of the ratio σ_n/σ_p for the resonance contribution to the inelastic cross section at the $\Delta(1232)$ resonance [49]. Note that the new measurements shown in Table 3.18 are the result to fitting the data at all Q^2, assuming that the Q^2 dependence is small. These new results are slightly higher than the previous measurements shown in Figure 3.37. This could be due to combining all the Q^2 data for the new results into a single fit parameter, or it could be do
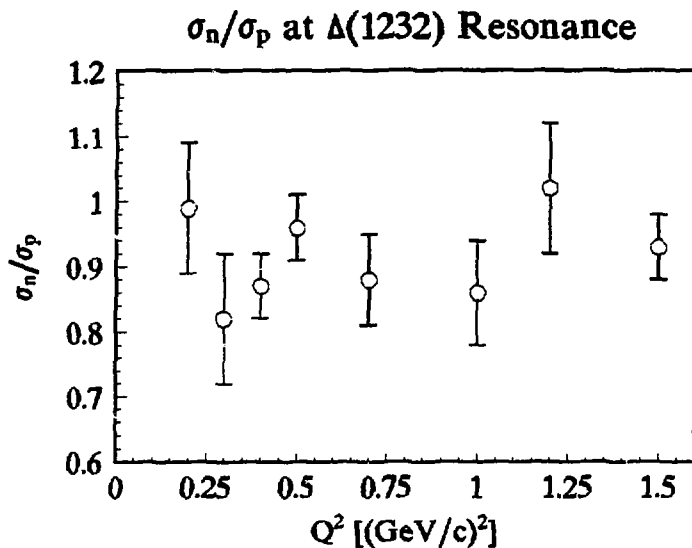
Figure 3.37: Previous data [49] showing σ_n/σ_p for the resonance component of the inelastic cross sections at the $\Delta(1232)$ resonance.

to differences in the models used to extract the two sets of results, or the ratio might really have a Q^2 dependence. Also, the result using smear model 1 is far off from the other models which could be because this method is only a crude approximation to the other smearing methods. A study of the possible Q^2 dependence to these ratios is currently under investigation.

Deuterium model cross section ratios
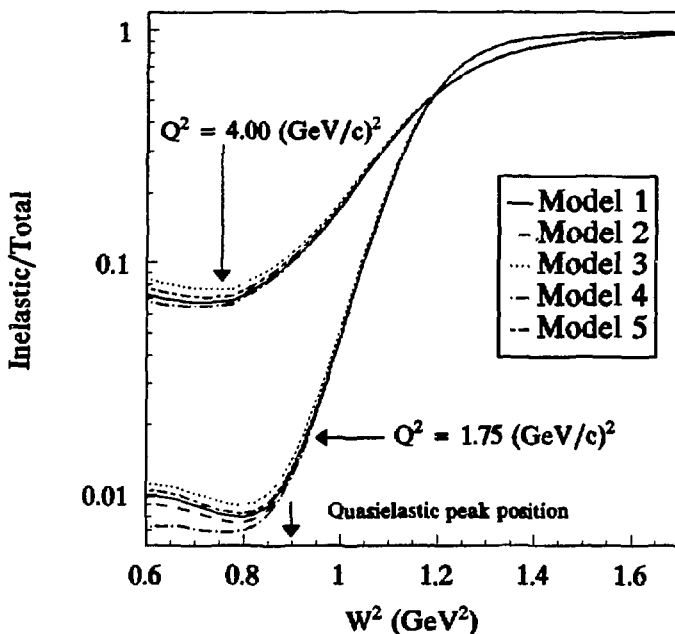
Figure 3.38: Ratio of inelastic to total deuterium model cross sections at the two extreme kinematic points of this experiment for all five smearing models. θ was set to 20.0° for both sets of calculations.

Inelastic model comparisons

Figures 3.38, 3.39, and 3.40 show plots of the model deuterium inelastic cross sections divided by the total model cross sections for each of the model assumptions given in Table 3.18. Figure 3.38 shows the cross section ratios for each smearing model, using the off-shell correction given in Eq. 3.47 and the Paris deuteron wave function, for two kinematic spectra, both of which were calculated at $\theta = 20.0°$. Figure 3.39 shows the cross section ratios for three different

**Deuterium Cross Section Ratios
For Different Off-Shell Corrections**
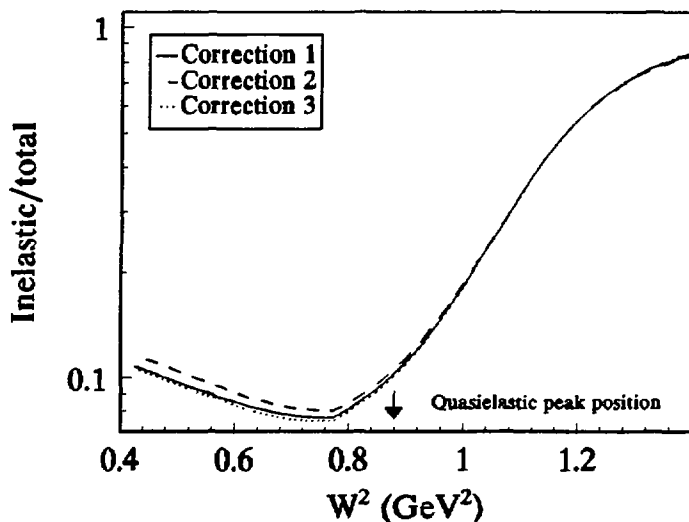
Figure 3.39: Ratio of inelastic to total deuterium model cross sections at $Q^2 = 4.0$ $(GeV/c)^2$ for three possible off-shell corrections. Corrections 1, 2, and 3 correspond to definitions given by Eqs. 3.47, 3.44 and 3.45.

Deuterium Cross Section Ratios
For Different Deuterium Wavefunctions
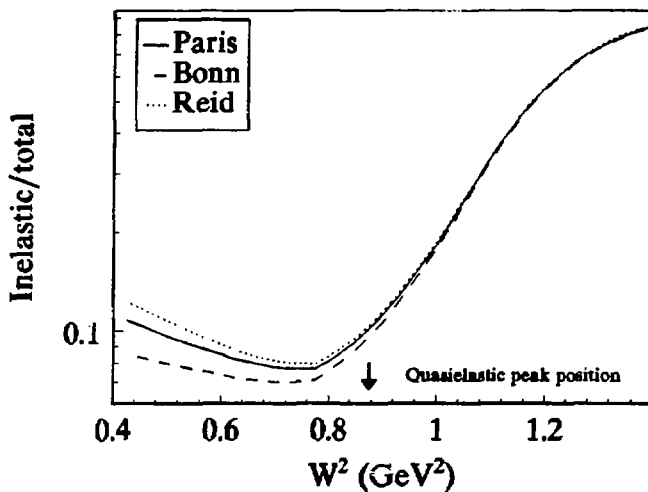
Figure 3.40: Ratio of inelastic to total deuterium model cross sections evaluated at $Q^2 = 4.0$ $(GeV/c)^2$ using three different deuterium wave function parameterizations.

off-mass-shell corrections using smearing model 3 and the Paris deuteron wave function evaluated at $Q^2 = 4.0$ $(GeV/c)^2$ and $\theta = 20.0°$. Figure 3.40 shows the cross section ratios for the Paris, Bonn, and Reid deuteron wave functions, using smear model 3 and the off-shell correction given in Eq. 3.47 and also evaluated at $Q^2 = 4.0$ $(GeV/c)^2$ and $\theta = 20.0°$.

It can be seen from Figures 3.38-3.40 that once the fits to the deuterium cross sections have been done, the resultant model deuterium cross sections are very similar and only start to significantly diverge at low W^2 where the inelastic cross section is very small compared to the quasielastic cross

section. This indicates that the different inelastic modeling should not give appreciably different results for the measurement of the neutron charge and magnetic form factors.

4: FORM FACTORS

Form Factor Models

There are several formalisms which have been used and developed over the years which attempt to understand the nucleon form factors using physical principles. Some of these "models" involve free parameters which are fit to existing data. The types of models can be broken up into six categories. These categories involve calculations based on:

1. Vector Meson Dominance (VMD).

2. Perturbative Quantum ChromoDynamics (pQCD).

3. Hybrid combinations of the above two categories.

4. Dimensional scaling and QCD sum rules.

5. Constituent quark and diquark models.

6. Lattice gauge QCD (low Q^2)

There are several different sets of form factor definitions. The isoscalar and isovector nucleon form factors, F^{IS} and F^{IV}, are combined to form the Dirac, (F_1), and Pauli, (F_2), nucleon form factors:

$$
\begin{aligned}
F_{1p}(Q^2) &= \frac{1}{2}(F_1^{IS}(Q^2) + F_1^{IV}(Q^2)), \\
F_{1n}(Q^2) &= \frac{1}{2}(F_1^{IS}(Q^2) - F_1^{IV}(Q^2)), \\
F_{2p}(Q^2) &= \frac{1}{2}(\kappa_S F_2^{IS}(Q^2) + \kappa_V F_2^{IV}(Q^2)), \\
F_{2n}(Q^2) &= \frac{1}{2}(\kappa_S F_2^{IS}(Q^2) - \kappa_V F_2^{IV}(Q^2)),
\end{aligned}
\tag{4.1}
$$

where κ_s and κ_v are linear combinations of the proton and neutron anomalous magnetic moments (defined in chapter 1). They are given by $\kappa_s = \mu_p - \mu_n - 1 = 3.706$ and $\kappa_v = \mu_p + \mu_n - 1 = -0.120$. The Dirac and Pauli form factors can then be combined to form

the familiar Sachs proton and neutron form factors:

$$
\begin{aligned}
G_{Mp}(Q^2) &= F_{1p}(Q^2) + F_{2p}(Q^2), \\
G_{Ep}(Q^2) &= F_{1p}(Q^2) - \frac{Q^2}{4M^2} F_{2p}(Q^2), \\
G_{Mn}(Q^2) &= F_{1n}(Q^2) + F_{2n}(Q^2), \\
G_{En}(Q^2) &= F_{1n}(Q^2) - \frac{Q^2}{4M^2} F_{2n}(Q^2).
\end{aligned}
\tag{4.2}
$$

Vector Meson Dominance Models

The VMD models/fits have generally been used at low Q^2 and involve a superposition of photon couplings to various vector mesons $(J^P = 1^-)$. The vector mesons can be divided into two categories depending on their isospin. The isoscalar, or isospin singlet, vector mesons and their observed higher mass states (masses in parentheses are in MeV) [85] are the $\omega(782)$, $\omega'(1390)$, $\omega''(1600)$, $\varphi(1020)$ and the not-well-established $\varphi'(1680)$ state. The isovector, or isospin triplet, vector mesons and the higher mass states are the $\rho(768)$, $\rho'(1450)$, and $\rho''(1700)$.

The form factor describing the photon-nucleon interaction via vector meson coupling is written as the product of a meson propagator term and a meson-nucleon form factor:

$$
F(Q^2) = \frac{F_{VNN}(Q^2)}{M_V^2 + Q^2},
\tag{4.3}
$$

where M_V is the vector meson mass. The $1.0/(M^2 + Q^2)$ factor is commonly called a "pole" term whereas this factor squared is called a "dipole", such as in the dipole representation of the neutron and proton form factors. The VMD models which will be discussed were developed in the 1970's before many of the

higher mass meson states were observed experimentally. Thus, expected higher mass state contributions to the form factors were often included using best-fit parameterization. Some of the most successful and popular VMD models are discussed here and are used for comparisons with the measured data. In general, the fits are done simultaneously to all four nucleon form factors using all data available at the time the fit was done. Figure 4.1 shows a schematic of the direct photon-nucleon interaction and the photon-nucleon interaction via an intermediary vector meson.

The VMD model by Iachello, Jackson, and Lande [86] (IJL) is a five-parameter fit which allows both vector and tensor coupling of the vector mesons. The functional form of the fit is given by:

$$F_1^{IS}(Q^2) = g(Q^2)\left[(1-\beta_\omega-\beta_\phi) + \beta_\omega\frac{M_\omega^2}{M_\omega^2+Q^2} + \beta_\phi\frac{M_\phi^2}{M_\phi^2+Q^2}\right],$$

$$F_1^{IV}(Q^2) = g(Q^2)\left[(1-\beta_\rho) + \beta_\rho\frac{M_\rho^2 + 8\Gamma_\rho M_\pi/\pi}{(M_\rho^2+Q^2) + (4M_\pi^2+Q^2)\Gamma_\rho\alpha(Q^2)/M_\pi}\right],$$

$$F_2^{IS}(Q^2) = g(Q^2)\left[(\kappa_V-\alpha_\phi)\frac{M_\omega^2}{M_\omega^2+Q^2} + \alpha_\phi\frac{M_\phi^2}{M_\phi^2+Q^2}\right],$$

$$(4.4)$$

$$F_2^{IV}(Q^2) = g(Q^2)\left[\kappa_S\frac{M_\rho^2 + 8\Gamma_\rho M_\pi/\pi}{(M_\rho^2+Q^2) + (4M_\pi^2+Q^2)\Gamma_\rho\alpha(Q^2)/M_\pi}\right],$$

where M represents various meson masses. The function $g(Q^2)$ is an intrinsic nucleon form factor,

$$g(Q^2) = \frac{1}{[1+\gamma Q^2]^2}.$$ $$(4.5)$$
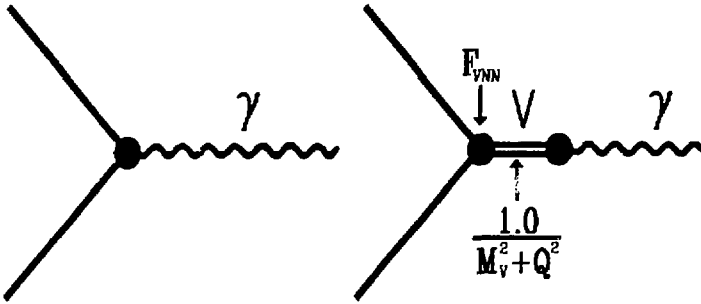
Figure 4.1: Diagram of the nucleon-photon interaction via a direct interaction and by a vector meson coupling.

The function $\alpha(Q^2)$ is used to account for the finite width of the ρ meson, $\Gamma_\rho = 112$ MeV, and is given by:

$$\alpha(Q^2) = \frac{2}{\pi} \sqrt{\frac{4M_\pi^2 + Q^2}{Q^2}} \ln\left[\frac{\sqrt{4M_\pi^2 + Q^2} + \sqrt{Q^2}}{2M_\pi}\right]. \tag{4.6}$$

A fit to the available data in 1973 yielded the following parameter values:

$$\gamma = 0.25\,(\text{GeV/c})^{-2},$$
$$\beta_\rho = 0.672, \quad \beta_\omega = 1.102, \tag{4.7}$$
$$\beta_\phi = 0.112, \quad \alpha_\phi = -0.052,$$

where the β and α parameters represent a product of the coupling constants at the γV vertex and at the VNN vertex. Note that the factors κ_s and κ_v have been absorbed into the isoscalar and isovector form factors as shown in Eq. 4.1.

The VMD model by Blatnik and Zovko [87] (BZ) includes

photon couplings with the three ground state vector mesons and with three higher mass states ρ', ρ'', and ω'. There are four free parameters which are related to the coupling constants. This model uses the asymptotic form factor constraint that $Q^2 G(Q^2) \to 0.0$ as $Q^2 \to \infty$, where $G(Q^2)$ is any one of the Sachs form factors. The functional form for the form factors is given by:

$$
\begin{aligned}
G_E(Q^2) &= \left[\frac{1}{2} - \frac{Q^2}{4M^2} (\mu^s + 2M^2 b^s) \right] R^s(Q^2) \\
&\quad \pm \left[\frac{1}{2} - \frac{Q^2}{4M^2} (\mu^v + 2M^2 b^v) \right] R^v(Q^2) , \\
G_M(Q^2) &= \left[\frac{1}{2} + \mu^s - \frac{1}{2} b^s Q^2 \right] R^s(Q^2) \\
&\quad \pm \left[\frac{1}{2} + \mu^v - \frac{1}{2} b^v Q^2 \right] R^v(Q^2) , \\
R^s(Q^2) &= \left(\frac{m_\omega^2}{m_\omega^2 + Q^2} \right) \left(\frac{m_\phi^2}{m_\phi^2 + Q^2} \right) \left(\frac{m_{\omega'}^2}{m_{\omega'}^2 + Q^2} \right) , \\
R^v(Q^2) &= \left(\frac{m_\rho^2}{m_\rho^2 + Q^2} \right) \left(\frac{m_{\rho'}^2}{m_{\rho'}^2 + Q^2} \right) \left(\frac{m_{\rho''}^2}{m_{\rho''}^2 + Q^2} \right) ,
\end{aligned}
\tag{4.8}
$$

where M is the nucleon mass and the + and − signs correspond to proton and neutron form factors respectively. The quantities μ^s and μ^v were fixed at −0.060 and 1.853 respectively in order to give the correct values for the form factors in the limit as $Q^2 \to 0$. The mass of the ρ'' was assumed to be 1.5 GeV. The best fit parameters were determined to be:

$$
\begin{aligned}
&m_{\rho'} = 1.14 \text{ GeV}, \quad m_{\omega'} = 1.18 \text{ GeV}, \\
&b^s = -0.91 \text{ GeV}^{-2}, \quad b^v = -1.10 \text{ GeV}^{-2}.
\end{aligned}
\tag{4.9}
$$

The VMD model by Höhler et al. [88] is from their fit, 8.2, one of the many fits attempted. This VMD model gives the expected asymptotic large Q^2 dependence for the Pauli form factor (Q^{-4}), but not for the Dirac form factor (Q^{-6}) indicating that it may only be moderately successful at describing the form factors at an intermediate Q^2. This asymptotic dependence is discussed in greater detail in the next section. The functional form for the form factors is basically a sum over a product of pole-terms for each vector meson included. This form factor function is given by:

$$F_1^{IS}(Q^2) = \sum_V \frac{a_i(V)}{m_V^2 + Q^2}, \quad F_1^{IV}(Q^2) = F_1^{IV=\rho}(Q^2) + \sum_{V'} \frac{a_i(V')}{m_{V'}^2 + Q^2}, \qquad (4.10)$$

where the ρ meson terms are given by:

$$2F_1^{IV=\rho}(Q^2) = \frac{0.955 + 0.090\left(1 + \dfrac{Q^2}{0.355}\right)^{-2}}{1 + \dfrac{Q^2}{0.536}}$$

$$2F_2^{IV=\rho}(Q^2) = \frac{5.335 + 0.962\left(1 + \dfrac{Q^2}{0.268}\right)^{-1}}{1 + \dfrac{Q^2}{0.603}}. \qquad (4.11)$$

A discussion on why the typical pole-term formula was not used for the ρ meson is also given by this reference. This fit was chosen over the other fits in the paper because it had the best overall χ^2/n agreement with the data. There were a total of four isovector and three isoscalar vector mesons. These mesons included ρ, ω, and φ as well as a higher mass state isoscalar meson which is arbitrarily labeled as $V=3$, and three higher mass state isovector mesons which are labeled $V'=1,2$

and 3. There are a total of 16 different free parameters for this fit :

$$
\begin{aligned}
&a_1(V=\omega) = 0.71, \quad a_1(V=\phi) = -0.64, \quad a_1(V=3) = -0.13 \\
&a_2(V=\omega) = -0.11, \quad a_2(V=\phi) = 0.13, \quad a_2(V=3) = -0.02 \\
&a_1(V'=1) = 0.05, \quad a_1(V'=2) = -0.52, \quad a_1(V'=3) = 0.28 \\
&a_2(V'=1) = -1.99, \quad a_2(V'=2) = 0.20, \quad a_2(V'=3) = 0.19 \\
&m(V=3) = 1.80 \text{ GeV}, \quad m(V'=1) \approx 1.21 \text{ GeV}, \\
&m(V'=2) = 2.45 \text{ GeV}, \quad m(V'=3) = 2.95 \text{ GeV}.
\end{aligned}
\tag{4.12}
$$

Perturbative Quantum Chromodynamics

Calculations, at present, using pQCD [89][90] alone, have had only limited success at predicting form factors in the intermediate Q^2 range since only leading order calculations have been made. The problem is complicated by the fact that the results are sensitive to the form chosen for the distribution amplitude (DA) for the quark momenta in the nucleons. These calculations do, however, predict the form factor asymptotic behavior at large Q^2 where difficult-to-calculate second order terms can be neglected. These predictions serve as useful constraints on other types of models which have been formulated. The calculations predict that G_M for both nucleons should behave as:

$$
\begin{aligned}
&\underset{q \to \infty}{\text{LIM}}\, G_M(q^2) = \text{Const} \cdot \frac{\alpha_s(Q^2)}{Q^4} (\ln(Q^2/\Lambda^2))^{-4\beta/3}, \\
&\alpha_s = \frac{4\pi}{\beta \ln(Q^2/\Lambda^2)}, \quad \beta = 11 - \frac{2}{3} n_{flavor},
\end{aligned}
\tag{4.13}
$$

where $\alpha_s(Q^2)$ is the strong running coupling constant, $\Lambda \sim 200$ MeV is the QCD scale parameter, and n_{flavor} is the number of contributing quark flavors. The kinematics of this experiment are below heavy quark production thresholds so $n \sim 3$. Assuming

isospin symmetry the calculations also predict that the ratio $G_{Mn}(Q^2)/G_{Mp}(Q^2) \rightarrow -2/3$, and that the helicity-nonconserving term, F_2, should be suppressed by a factor of Q^2 compared to the helicity-conserving term, F_1. Thus, the ratio $Q^2 F_2/F_1 \rightarrow$ constant at large Q^2.

Hybrid VMD-pQCD model

The VMD models are generally used to fit the form factor data in the low Q^2 region. The hybrid form factor model of Gari and Krümpelmann [91] (GK) attempts to describe the intermediate Q^2 region by choosing a functional form for the form factors which gives the expected Q^2 behavior at both high and low Q^2. The chosen form for the model is given by:

$$
\begin{aligned}
F_1^{IS}(Q^2) &= \left[\frac{m_\omega^2}{m_\omega^2+Q^2} \frac{g_\omega}{f_\omega} + \left(1 - \frac{g_\omega}{f_\omega}\right)\right] F_1^{QCD}(Q^2) , \\
F_1^{IV}(Q^2) &= \left[\frac{m_\rho^2}{m_\rho^2+Q^2} \frac{g_\rho}{f_\rho} + \left(1 - \frac{g_\rho}{f_\rho}\right)\right] F_1^{QCD}(Q^2) , \\
\kappa_s F_2^{IS}(Q^2) &= \left[\frac{m_\omega^2}{m_\omega^2+Q^2} \frac{k_\omega g_\omega}{f_\omega} + \left(\kappa_s - \frac{k_\omega g_\omega}{f_\omega}\right)\right] F_2^{QCD}(Q^2) , \\
\kappa_v F_2^{IV}(Q^2) &= \left[\frac{m_\rho^2}{m_\rho^2+Q^2} \frac{k_\rho g_\rho}{f_\rho} + \left(\kappa_v - \frac{k_\rho g_\rho}{f_\rho}\right)\right] F_2^{QCD}(Q^2) ,
\end{aligned}
\tag{4.14}
$$

where the QCD form factor are parameterized by:

$$
F_1^{QCD}(Q^2) = \frac{\Lambda_1^2}{\Lambda_1^2+\hat{Q}^2}\left[\frac{\Lambda_2^2}{\Lambda_2^2+\hat{Q}^2}\right] , \quad F_2^{QCD}(Q^2) = F_1(Q^2)\left[\frac{\Lambda_2^2}{\Lambda_3^2+\hat{Q}^2}\right] ,
\tag{4.15}
$$

and the logarithmic dependence of the strong coupling constant

is reflected in the variable:

$$\hat{Q}^2 = \frac{Q^2 \log\left[\dfrac{\Lambda_2^2 + Q^2}{\Lambda_{QCD}^2}\right]}{\log\left[\dfrac{\Lambda_2^2}{\Lambda_{QCD}^2}\right]}. \tag{4.16}$$

Λ_1 is the approximate scale of the nucleon wavefunction, Λ_2 is the scale where the meson dynamics dominate, and Λ_{QCD} is the scale where the quark dynamics dominate. The seven parameters used for the fit in this model are given by

$$\frac{g_\rho}{f_\rho} = 0.377, \quad \frac{g_\omega}{f_\omega} = 0.411, \quad k_\rho = 6.62, \quad k_\omega = 0.163,$$
$$\Lambda_1 = 0.795 \text{ GeV}, \quad \Lambda_2 = 2.27 \text{ GeV}, \quad \Lambda_{QCD} = 0.29 \text{ GeV}. \tag{4.17}$$

Dimensional scaling and QCD Sum rules

Dimensional scaling is a simple, yet seemingly effective, method for predicting the asymptotic Q^2 behavior for two-body scattering processes, by merely counting the number of bound constituent point-like particles in the hadrons [92]. The basic dimensional scaling prediction is that for an exclusive scattering process

$$\left(\frac{d\sigma}{dQ^2}\right)_{AB \sim CD} \sim s^{2-n} f\left(\frac{Q^2}{s}\right), \tag{4.18}$$

where s is the square of the center of mass energy, and n is the total number of leptons, photons, or quarks carrying part of the momentum in the initial and final states, and f is a

function of the ratio Q^2/s. For elastic and quasielastic electron-nucleon scattering, the initial and final states consist of an electron and a nucleon composed of three valence quarks. Thus, for this scattering process, $n = 8$, and for a fixed value of Q^2/s

$$\left(\frac{d\sigma}{dQ^2}\right)_{eN-eN} \sim s^{-6} \sim (Q^2)^{-6} \sim Q^{-12}. \qquad (4.19)$$

It can also be shown, using the Rosenbluth formula, that for large Q^2 where F_1 dominates

$$\left(\frac{d\sigma}{dQ^2}\right)_{eN-eN} \sim \frac{F_1^2(Q^2)}{Q^4}. \qquad (4.20)$$

Thus, dimensional scaling predicts that $F_1(Q^2) \rightarrow Q^{-4}$ which is very similar to the pQCD prediction aside from the logarithmic term due to the running of the strong coupling constant.

QCD sum rule techniques as developed by Shifman, Vainshtein, and Zakharov [93] have proven to be effective tools for studying nonperturbative properties of hadrons such as masses, coupling constants, resonance widths, etc. This method is employed by Radyushkin [94] (RAD) as another approach to calculating the nucleon form factors. This model uses QCD sum rules in order to fix the parameters of the nucleon soft wavefunctions, and only considers the simplest nonperturbative Feynman diagram contribution to the form factor (i.e. no hard gluon exchange diagrams). A justification for the assumption that this diagram is dominant at moderate

values of Q^2 is discussed in this reference.

The neutron form factor formulas are:

$$F_{1n}(Q^2) = \frac{1}{(2\pi)^4 \lambda_n^2} \int_0^{s_0} ds_1 \int_0^{s_0} ds_2 Q^2 \left(1 - \frac{\sigma}{z}\right)^2$$

$$\cdot \left(\frac{2e_d - e_u}{16} \frac{Q^2}{z}\left(1 + \frac{\sigma}{z}\right)^2 + \frac{e_u + e_d}{12}\left(2 + \frac{\sigma}{z}\right)\right) \qquad (4.21)$$

$$G_{Mn}(Q^2) = \frac{e_d}{(2\pi)^4 \lambda_N^2} \int_0^{s_0} ds_1 \int_0^{s_0} ds_2 \frac{Q^2}{4}\left(1 - \frac{\sigma}{z}\right)^2\left(2 + \frac{\sigma}{z}\right),$$

where the corresponding proton form factors can be obtained by interchanging e_u and e_d. The functions σ, z, and λ_N are:

$$\sigma = s_1 + s_2 + Q^2,$$

$$z = \sqrt{\sigma^2 - 4s_1 s_2},$$

$$\lambda_N^2 = \frac{s_0^3}{12(2\pi)^4}, \qquad (4.22)$$

and $e_u = 2/3$, and $e_d = -1/3$. The quantity s_0 was fixed at 2.3 $(GeV/c)^2$.

Constituent Quark and Diquark Models

Constituent quarks differ from the point-like small mass quarks in pQCD in that they have mass which is ~ $M_p/3$, and they have an extended spatial structure due to the presence of a pionic cloud. This spatial structure translates into the need for quark form factors in the constituent quark models at high Q^2. The relativistic constituent-quark model of Chung and Coester [95] is expected to be valid for Q^2 up to 3 to 6 $(GeV/c)^2$ in calculating nucleon form factors. The main parameters used were the confinement scale, $1/\alpha$, and the

constituent quark mass, m_q, and a Gaussian wave function shape. This preliminary, simplified model, achieved reasonably good results in the Q^2 range of interest provided that the constituent quark mass was chosen around 0.24 GeV which is smaller than the conventionally used value of $M_p/3$. The curves used to compare with this experiment's data were obtained directly from the creators of this model. They correspond to using an m_q of 0.24 GeV and a value for α of 0.635 GeV. The wave function used in this calculation was a spatially symmetric function given by

$$\phi(M_0) = \frac{N(m_q/\alpha)}{\alpha^2} e^{-\left(\frac{M_0^2}{2\alpha^2}\right)}, \qquad (4.23)$$

where $N(m_q/\alpha)$ is a dimensionless factor resulting from the normalization condition and

$$M_0 = \sum_i \sqrt{m_i^2 + \vec{q}_i^2} . \qquad (4.24)$$

The sum extends over the three constituent quarks and m and q represent the constituent quark masses and three-momenta respectively.

A fairly recent model due to Kroll et al [50]. investigates the electromagnetic nucleon form factors within the framework of the diquark model. This model attempts to describe the form factors at moderate values of Q^2, assuming that the diquarks can be treated as quasi-elementary nucleon constituents. In the limit of large Q^2 this model approaches that of a pure quark hard scattering model such as the schemes suggested by Brodsky and Lepage [90] or Chernyak and

Zhitnitsky [96]. This model incorporates the distribution amplitudes (DA) of baryons in terms of quarks and diquarks, with the diquark form factors chosen to ensure the proper asymptotic limit, and a perturbative approach to treating the gluon and photon coupling to the quarks. The formulae in the *original publication were later corrected* [97]. These corrected neutron form factor formulae are given by

$$G_{Mn}(Q^2) = C_F \frac{8\pi}{Q^2} f_S^2 \cdot$$

$$\int_0^1 dx_1 dy_1 \phi_S(y_1) \left[e_d \frac{\alpha_s(\tilde{Q}^2)}{x_2 y_2} F_S^{(3)}(\tilde{Q}^2) + e_{ud} \frac{\alpha_s(\hat{Q}^2)}{x_1 y_1} F_S^{(4)}(Q^2) \right] \phi_S(x_1)$$

$$+ C_F \frac{4\pi}{9} \frac{f_V^2}{m_V^2} \int_0^1 dx_1 dy_1 \phi_V(y_1) \left(-(e_d + 2e_u) \alpha_s(\hat{Q}^2) \kappa_V F_V^{(3)}(\tilde{Q}^2) + (2e_{dd} + e_{ud}) \right)$$

$$\cdot \frac{\alpha_s(\hat{Q}^2)}{x_1 y_1} F_V^{(4)}(Q^2) \left[\kappa_V^2 (1 + x_1)(1 + y_1) + \frac{1}{2} x_2 y_2 ((1 + \kappa_V)^2 - 4) \right] \right) \phi_V(x_1) ,$$

$$F_{2n}(Q^2) =$$

$$C_F \frac{8\pi}{9} f_V^2 \frac{m}{\kappa_n m_V} \int_0^1 dx_1 dy_1 \phi_V(y_1) (4(e_d + 2e_u) \frac{\alpha_s(\tilde{Q}^2)}{Q^2} (1 + \kappa_V) F_V^{(3)}(\tilde{Q}^2)$$

$$+ (2e_{dd} + e_{ud}) \frac{\alpha_s(\hat{Q}^2)}{x_1 y_1} F_V^{(4)}(Q^2) \frac{\kappa_V}{m_V^2} (\kappa_V(1 - x_1 y_1) - x_2 y_2)) \phi_V(x_1) ,$$

$$(4.25)$$

where the corresponding proton form factors are obtained by interchanging the quark charges, e_u and e_d and by replacing κ_n by κ_p. The diquark total charge (for an up-down pair) is denoted by e_{ud}, and m_V and κ_V are the mass and anomalous magnetic moment of the vector (spin 1) diquark. The momentum carried by the quark is denoted by x_1 and y_1, while the momentum fraction carried by the diquark is denoted by

$x_2 = 1 - x_1$ and $y_2 = 1 - y_1$. $C_F = 4/3$ is the color factor and

$$\tilde{Q}^2 = x_2 y_2 Q^2; \qquad \hat{Q}^2 = x_1 y_1 Q^2. \qquad (4.26)$$

The isoscalar (S) and isovector (V) three and four-point diquark form factors are parameterized by the equations:

$$F_S^{(3)}(\tilde{Q}^2) = \delta_S(\tilde{Q}^2) \frac{Q_S^2}{Q_S^2 + \tilde{Q}^2}, \qquad F_V^{(3)}(\tilde{Q}^2) = \delta_V(\tilde{Q}^2) \left(\frac{Q_V^2}{Q_V^2 + \tilde{Q}^2} \right)^2,$$

$$\qquad\qquad\qquad\qquad\qquad\qquad\qquad\qquad\qquad\qquad (4.27)$$

$$F_S^{(4)}(Q^2) = a_S \delta_S(Q^2) \frac{Q_S^2}{Q_S^2 + Q^2}, \qquad F_V^{(4)}(Q^2) = a_V \delta_V(Q^2) \left(\frac{Q_V^2}{Q_V^2 + Q^2} \right)^3,$$

where

$$\delta_{S(V)}(Q^2) = \begin{cases} \dfrac{\alpha_s(Q^2)}{\alpha_s(Q_{S(V)}^2)} & Q^2 \geq Q_{S(V)}^2 \\[2mm] 1 & Q^2 < Q_{S(V)}^2 \end{cases}. \qquad (4.28)$$

Using the distribution amplitude given by

$$\phi_S(x_1) = \phi_V(x_1) = A x_1 x_2^3 \exp\left[-b^2 \left(\frac{m_q^2}{x_1} + \frac{M_D^2}{x_2} \right) \right]$$

$$\qquad\qquad\qquad\qquad\qquad\qquad\qquad\qquad (4.29)$$

$$\int_0^1 \phi_{S(V)}(x)\,dx = 1,$$

with constituent quark and diquark masses $m_q = 0.330$ GeV, and $m_D = 0.580$ GeV yields the following "best-fit" parameters:

$$Q_S^2 = 3.22 \text{ GeV}^2, \quad Q_V^2 = 1.58 \text{ GeV}^2,$$

$$f_S \approx 66.1 \text{ MeV}, \quad f_V = 120.2 \text{ MeV}, \qquad (4.30)$$

$$\kappa_V = 1.16, \qquad\quad a_S = a_V = 0.286.$$

This particular fit corresponds to the solid curves given in the original paper [50]. Another fit using a different distribution amplitude was also studied.

Form Factor Extraction

Peak Method

A "peak" method of form factor extraction is so-named because only a small region in the vicinity of the quasielastic peak is included in the analysis. This method has the advantage of being much less sensitive to the quasielastic model shape. It has the disadvantage of being s tistics limited since much of the measured cross section is excluded.

To use this method we first subtracted off the inelastic contribution as calculated by the inelastic cross section model from the measured deuterium cross sections. This left the quasielastic cross section which was converted to the reduced form, $\sigma_x(\text{data})$ (Eq. 3.30). The model reduced quasielastic cross section, $\sigma_x(\text{model})$, was calculated using model form factors. $G_{Mp}(Q^2)$ was obtained using the form factor model of Gari and Krümpelmann [98] which was discussed earlier in this chapter. $G_{Ep}(Q^2)$ and $G_{Mn}(Q^2)$ were modeled using the dipole formula, and $G_{En}(Q^2)$ was set to zero. It will be shown that these model form factors represent those that were measured in this experiment fairly well. Starting with model *form factors close to the final results reduces possible* second-order corrections to the fitting procedure. Both $\sigma_x(\text{data})$ and $\sigma_x(\text{model})$ were functions of Q^2 and W^2. The ratio of $\sigma_x(\text{data})$ to $\sigma_x(\text{model})$ was averaged using error weighted averaging to give R_{peak} using data within a defined range in W^2 about the quasielastic peak region. R_{peak} was then corrected for the model form factor dependence (see Eq. 3.30) to yield

the measured form factors:

$$
\left[G_{Mp}^2(Q^2) + G_{Mn}^2(Q^2) + \frac{\epsilon}{\tau'}\left(G_{Ep}^2(Q^2) + G_{En}^2(Q^2)\right)\right]\Big|_{\text{measured}}
$$
$$
= R_{\text{peak}}\left[G_{Mp}^2(Q^2) + G_{Mn}^2(Q^2) + \frac{\epsilon}{\tau'}\left(G_{Ep}^2(Q^2) + G_{En}^2(Q^2)\right)\right]\Big|_{\text{model}}
$$

(4.31)

The next step was to do a linear fit in ϵ to the remaining data and then to subtract the measured proton form factors [15] in order to extract $G_{Mn}(Q^2)$ and $G_{En}(Q^2)$. This extraction method was done for several different choices of W^2 ranges about the quasielastic peak to check for consistency. Results will be presented for the largest range investigated which had the smallest statistical error. This range was $0.70 < W^2 < 1.8$ (GeV)^2. Results for the these fits versus ϵ are shown in Figure 4.2 for all four Q^2 points. The data shown is normalized to the dipole form factor squared, G_D^2. The χ^2 per degree of freedom for the fits at $Q^2 = 1.75$, 2.50, and 3.25 (GeV/c)^2 was 0.99, 0.32 and 2.8 respectively. The fourth Q^2 point only had two data points in the linear fit so no χ^2 per degree of freedom was calculated.

Area Method I

An "area" method of extraction is so-named because all of the quasielastic cross section data is used to extract the form factors as opposed to just a region of the measured data. This particular area method is a least-squares simultaneous fit to all spectra at a given Q^2. There were four parameters in this fit. Two of the parameters were the desired form factors summed in quadrature, $(G_{Mp}^2 + G_{Mn}^2)$ and $(G_{Ep}^2 + G_{En}^2)$, and
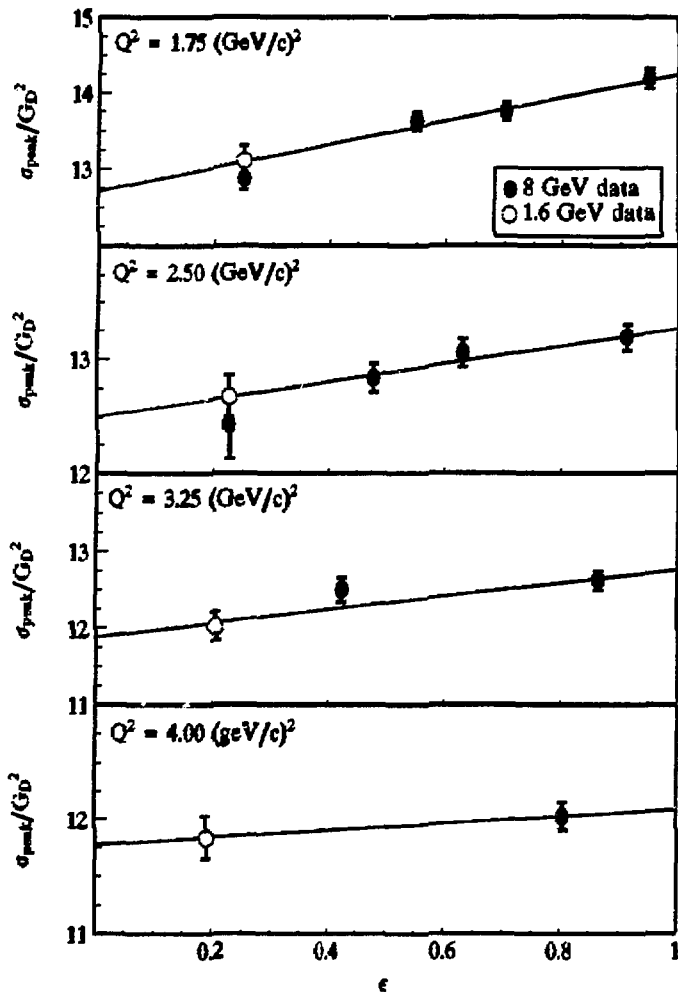
Figure 4.2: The linear fits to these data yielded $(G_{Ep}^2(Q^2) + G_{En}^2(Q^2))/\tau'$ (slope) and $(G_{Mp}^2(Q^2) + G_{Mn}^2(Q^2))$ (intercept).

the other two parameters corresponded to the fitting parameters described earlier for the deuterium inelastic cross section. The reduced cross section, σ_x, had contributions from the neutron and proton quasielastic and the proton and neutron smeared inelastic cross sections. A least squares fit was done for all data points at a given Q^2 using the expression:

$$\chi^2 = \left[\sigma_R' = -\left(C_T F(E',Q^2) + C_L \frac{e}{\tau'} F(E',Q^2) + C_{nr}(\sigma_T^{nr} + \epsilon\sigma_L^{nr}) + C_r\sigma_T^r\right)\right]^2 \quad (4.32)$$

where $F(E',Q^2)$ is the remainders of Eq. 3.31 after the form factors have been divided out so that they can be determined by the fit coefficients. The term F was also multiplied by the square of the dipole form factor, $G_D^2(Q^2) = 1.0/(1.0 + Q^2/0.71)^4$ so that the form factors obtained from the fit coefficients were normalized to the dipole form factor:

$$F(E',Q^2) = G_D^2(Q^2)\left[\frac{M_p^2}{2q}\frac{E}{E'}\int_{k_{min}}^{k_{max}}\frac{\psi^2(k)\,k\,dk}{\sqrt{k^2+M_p^2}}\right]. \quad (4.33)$$

The terms σ_T^{nr}, σ_L^{nr}, σ_T^r are the components of the model inelastic cross sections given in Eq. 3.48 and in the accompanying discussion. The coefficients found from the fit to the data then yielded the sum of the square of the form factors:

$$C_T = \frac{(G_{Mp}^2(Q^2) + G_{Mn}^2(Q^2))}{G_D^2(Q^2)}, \quad C_L = \frac{(G_{Ep}^2(Q^2) + G_{En}^2(Q^2))}{G_D^2(Q^2)}. \quad (4.34)$$

The coefficients for the inelastic contribution were discussed earlier. The proton form factors were subtracted off using the measured proton form factors from this experiment [15]. Sample

plots of reduced cross sections were shown in the last chapter
in Figures 3.35 and 3.36 showing the results of these fits for
some of the kinematic spectra. Smearing model 3 was used for
the inelastic modeling. The χ per degree of freedom for these
fits were not good. For the four Q^2 points, 1.75, 2.50, 3.25,
and 4.00 $(GeV/c)^2$ the calculated χ per degree of freedom for
the fits was 4.2, 2.6, 2.0, 2.1 . The poor quality of the fits
is due to not having the models produce the correct cross
section shape. Most of the problem is believed to be due to
not including effects in the modeling due to meson exchange
currents which can be significant away from the quasielastic
peak region.

Area Method II

This first step in this method was to extract the
longitudinal and transverse components of the reduced cross
section spectra as defined by Eq. 3.30, R_L and R_T, for each set
of Q^2 data. Then, separate fits were done to each spectrum in
order to obtain the form factors. The separation of R_L and R_T
was done on a bin-by-bin basis in W^2. For a given W^2 bin and
a given Q^2 there were from two to four data points with
differing incident energy and scattering angle (see summary
table of kinematic points given in Table 1.1).

Since $\Delta Q^2/Q^2 \sim \Delta W^2/E$, the values for Q^2 varied over the W^2
range with the variation being the largest at the large angle
kinematic points where the incident energy, E, is small for a
given Q^2. Note that the nominal value of Q^2 was only true at
$W^2 = M_p^2$. In order to separate the longitudinal and transverse

cross sections it was necessary to correct each contributing data point in the W^2 bin to the same Q^2 value. To do this it was decided to correct each data point such that the Q^2 variation over W^2 for a given spectra corresponded to that of the arbitrarily chosen kinematic point of $20.0°$. Note that if $0.0°$ had been chosen then Q^2 would not vary at all over W^2.

To clarify this correction the steps involved will be discussed briefly. First, a suming elastic scattering from a nucleon, an incident energy, $E_{nom}(Q^2_{nom}, \theta_{20}=20.0°)$, was calculated. Second, the scattering energy, $E'(W^2, E_{nom}, \theta_{20})$ was calculated. Third, a new Q^2 value was calculated, $Q^2_{new}(E_{nom}, E', \theta_{20})$. It was this factor, Q^2_{new}, to which the data points at a given W^2 bin were corrected. The correction to the data was achieved by multiplying the data point by the ratio of two model cross sections. The numerator was the deuterium model reduced cross section defined by the kinematics W^2, Q^2_{new}, and θ_{nom}. The denominator was the model cross section defined by the kinematics W^2, E, and θ_{nom}, where E was the true incident beam energy, and θ_{ro} was the true scattering angle. The correction factors were always 1.0 at the quasielastic peak and ranged from 0.0 to 1.1 at the highest and lowest W^2 bins for the large angle data where these corrections were the largest.

After all the data points in a W^2 bin were corrected, a linear, error weighted, fit was done versus ϵ/τ' (see Eq. 3.30). The intercept of the fit gave $R_T(W^2, Q^2)$ while the slope gave $R_L(W^2, Q^2)$. The results of these separations are given in Tables 4.1–4.4 and in Figures 4.3–4.4.

Once $R_L(W^2,Q^2)$ and $R_T(W^2,Q^2)$ were extracted, the form factors were found by performing two least square fits to the data in a similar manner as was done in the last extraction method discussed. The quantities minimized were:

$$\chi_T^2 = \left[R_T - \left(C_T F(E',Q^2) + C_T^{inel}(\sigma_T^{nr} + \sigma_T^{r})\right)\right]^2,$$
$$\chi_L^2 = \left[R_L - \left(C_L F(E',Q^2) + C_L^{inel}\sigma_L^{nr}\right)\right]^2, \tag{4.35}$$

These quantities were minimized for all the data points within a given Q^2. The fit coefficients, C_T and C_L, for the quasielastic components yielded the form factors as shown in Eq. 4.34 for the previous method. Similarly, the proton form factors were then subtracted to yield the neutron results.

Table 4.1: Extracted transverse and longitudinal deuterium reduced cross section components for $Q^2 = 1.75$ (GeV/c)^2 at the quasielastic peak and $\theta = 20.0°$. ERR1 and ERR2 are the statistical and the statistical plus systematic errors respectively. W^2 is in GeV^2 and R_T, R_L and the errors are in units 1/GeV. Overall χ^2 per degree of freedom = 1.58.

W^2	R_T	ERR1$_T$	ERR2$_T$	R_L	ERR1$_L$	ERR2$_L$
0.715	6.19	0.24	0.28	0.12	0.33	0.35
0.745	8.17	0.19	0.27	0.38	0.28	0.33
0.775	10.44	0.16	0.29	0.42	0.25	0.34
0.805	12.75	0.15	0.33	1.50	0.26	0.38
0.835	15.27	0.14	0.38	1.81	0.26	0.43
0.865	17.11	0.23	0.45	2.20	0.41	0.55
0.895	17.29	0.30	0.48	2.39	0.49	0.59
0.925	16.31	0.14	0.40	2.28	0.27	0.45
0.955	14.61	0.13	0.37	1.87	0.24	0.40
0.985	11.90	0.17	0.34	1.82	0.26	0.38
1.015	9.89	0.23	0.33	1.51	0.32	0.38
1.045	8.55	0.12	0.24	0.94	0.21	0.28
1.075	7.48	0.13	0.22	0.63	0.21	0.26
1.105	6.39	0.13	0.20	0.85	0.21	0.25
1.135	6.18	0.12	0.18	0.27	0.19	0.23
1.165	5.72	0.14	0.19	0.62	0.22	0.25
1.195	6.16	0.15	0.21	0.01	0.24	0.27

Table 4.2: Same as Table 4.1 except that $Q^2 = 2.50$ (GeV/c)2 at the quasielastic peak and $\theta = 20.0°$. Overall χ^2 per degree of freedom = 0.96.

W²	R_T	ERR1_T	ERR2_T	R_L	ERR1_L	ERR2_L
0.520	2.40	0.28	0.29	0.16	0.33	0.34
0.560	3.00	0.21	0.22	0.32	0.26	0.27
0.600	3.83	0.19	0.21	0.51	0.24	0.25
0.640	5.14	0.18	0.22	0.71	0.24	0.27
0.680	7.32	0.17	0.25	0.21	0.24	0.29
0.720	9.72	0.19	0.30	0.09	0.27	0.34
0.760	12.82	0.19	0.35	0.35	0.28	0.40
0.800	15.97	0.19	0.42	0.23	0.30	0.46
0.840	18.10	0.21	0.47	1.36	0.34	0.52
0.880	19.41	0.43	0.62	1.58	0.71	0.83
0.920	19.71	0.25	0.51	0.72	0.40	0.58
0.960	17.29	0.23	0.46	1.68	0.35	0.51
1.000	14.62	0.24	0.41	1.90	0.34	0.47
1.040	12.84	0.24	0.39	1.13	0.32	0.43
1.080	11.01	0.25	0.37	1.09	0.31	0.40
1.120	10.10	0.27	0.36	0.64	0.34	0.40
1.160	9.46	0.23	0.32	0.47	0.29	0.36
1.200	9.44	0.23	0.32	0.81	0.30	0.37
1.240	10.13	0.26	0.35	0.52	0.35	0.41

Table 4.3: Same as Table 4.1 except that $Q^2 = 3.25$ (GeV/c)2 at the quasielastic peak and $\theta = 20.0°$. Overall χ^2 per degree of freedom = 1.22.

W²	R_T	ERR1_T	ERR2_T	R_L	ERR1_L	ERR2_L
0.475	3.21	0.62	0.62	-0.11	0.80	0.81
0.525	4.26	0.55	0.56	-0.30	0.70	0.70
0.575	5.54	0.51	0.52	0.00	0.65	0.66
0.625	7.18	0.38	0.42	0.27	0.51	0.54
0.675	9.59	0.32	0.40	0.59	0.47	0.52
0.725	12.36	0.29	0.42	1.16	0.47	0.56
0.775	16.14	0.28	0.48	0.60	0.49	0.62
0.825	19.28	0.31	0.55	0.74	0.53	0.69
0.875	20.60	0.47	0.69	2.37	0.86	1.00
0.925	20.38	0.32	0.59	2.20	0.54	0.73
0.975	18.95	0.32	0.55	1.79	0.51	0.68
1.025	17.20	0.28	0.50	1.62	0.44	0.60
1.075	14.52	0.31	0.48	1.77	0.45	0.58
1.125	13.10	0.34	0.47	1.97	0.47	0.57
1.175	13.11	0.37	0.49	1.30	0.56	0.60
1.225	13.47	0.40	0.51	0.84	0.51	0.64
1.275	14.41	0.40	0.52	0.86	0.56	0.68
1.325	15.66	0.42	0.56	0.91	0.60	0.78
1.375	16.84	0.51	0.64	2.18	0.79	0.89

W^2	R_T	$ERR1_T$	$ERR2_T$	R_L	$ERR1_L$	$ERR2_L$
Table 4.4: Same as Table 4.1 except that $Q^2 = 4.00$ $(GeV/c)2$ at the quasielastic peak and $\theta = 20.0°$.

Table 4.4: Same as Table 4.1 except that $Q^2 = 4.00$ $(GeV/c)2$ at the quasielastic peak and $\theta= 20.0°$.

W^2	R_T	$ERR1_T$	$ERR2_T$	R_L	$ERR1_L$	$ERR2_L$
0.475	5.32	0.55	0.57	-1.89	0.82	0.83
0.525	6.39	0.50	0.53	-0.81	0.73	0.74
0.575	7.76	0.44	0.48	-0.47	0.65	0.68
0.625	10.06	0.41	0.49	-0.66	0.62	0.67
0.675	11.35	0.44	0.53	1.27	0.66	0.73
0.725	14.73	0.45	0.59	1.17	0.70	0.80
0.775	18.25	0.44	0.64	0.27	0.70	0.85
0.825	20.75	0.45	0.70	0.31	0.73	0.91
0.875	22.17	0.59	0.82	0.86	1.07	1.22
0.925	22.52	0.49	0.76	1.70	0.80	1.00
0.975	21.23	0.46	0.71	2.03	0.72	0.92
1.025	19.69	0.48	0.69	1.80	0.72	0.89
1.075	17.98	0.47	0.65	1.90	0.69	0.84
1.125	16.12	0.49	0.64	2.78	0.72	0.84
1.175	16.49	0.49	0.64	1.90	0.72	0.85
1.225	17.02	0.62	0.75	1.07	0.89	0.99
1.275	16.88	0.64	0.78	2.97	0.96	1.07
1.325	20.14	0.68	0.85	-0.18	1.07	1.19
1.375	22.35	0.70	0.90	-0.52	1.15	1.29
1.425	23.54	0.80	1.00	1.08	1.29	1.43
1.475	24.04	0.92	1.11	3.89	1.45	1.60

As can been seen in Figures 4.3 and 4.4, the fits to R^T are quite good while the fits to R_L are not nearly as good because of the scatter in the data points. It is believed that the problems seen in the R_L plots (Negative data points and non-smooth behavior) is due to uncertainty in the 1.6 GeV optics (and thus acceptance function and reconstruction coefficients). A great deal of time and effort went into solving these problems with only limited success. The large errors in the peak region are due to errors on the hydrogen contamination subtraction. The inelastic contribution to the R_L plot for Q^2 of 1.75 $(GeV/c)^2$ is so small that it is not visible on the plot.

Extracted R_T Cross Sections
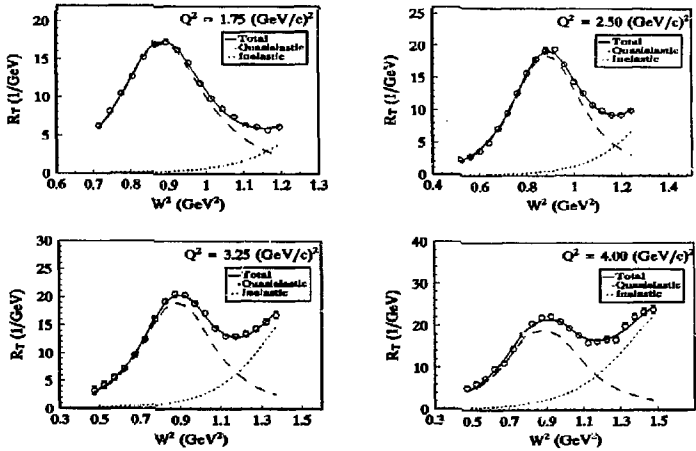
Figure 4.3: Extracted R_T deuterium cross section at all four Q^2 points. Fits found during the form factor extraction process are also shown. Errors are statistical only.

Extracted R_L Cross Sections
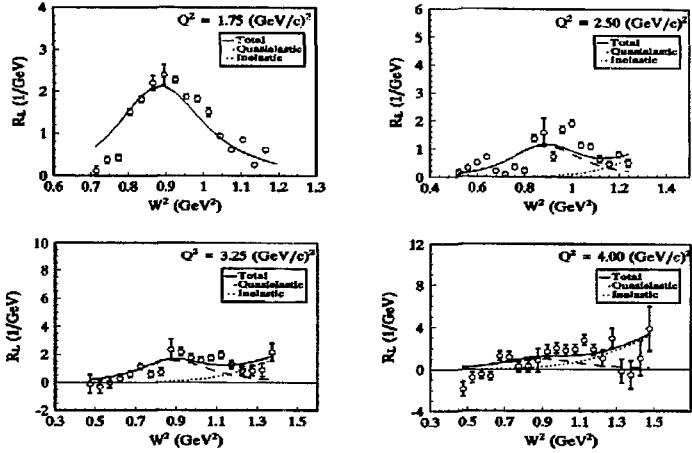
Figure 4.4: Extracted R_L deuterium cross section at all four Q^2 points. Fits found during the form factor extraction process are also shown. Errors are statistical only.

Proton Results

The use of the proton form factors for extracting the neutron form factors from the deuterium cross sections has been mentioned several times. The proton form factors which have been measured in this experiment [14][15] and were used in the deuterium cross section analysis are shown in Figures 4.5 and 4.6. Also shown on these plots are many curves as calculated from various form factor models which were discussed in the previous section. It is clear that for $G_{Mp}(Q^2)$, the best curve which describes the data is that of
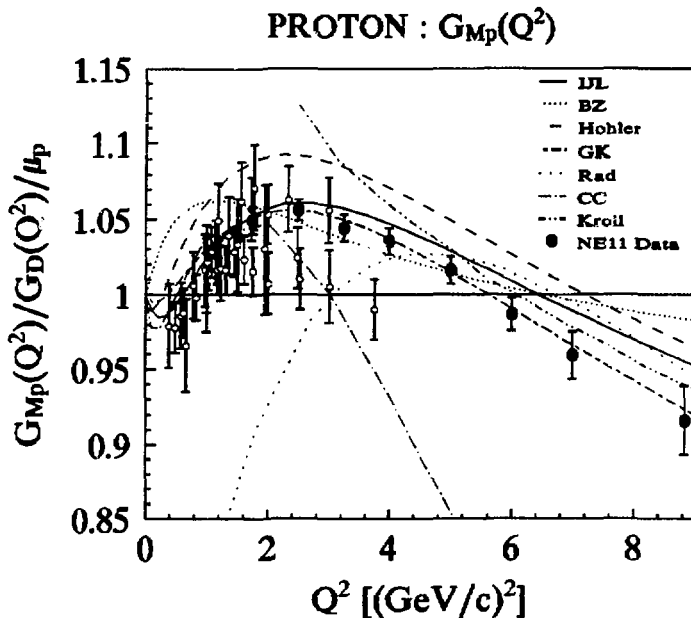
Figure 4.5: Proton magnetic form factors. Old and new data points are shown as well as results from many model/fits.

PROTON : $G_{Ep}(Q^2)$
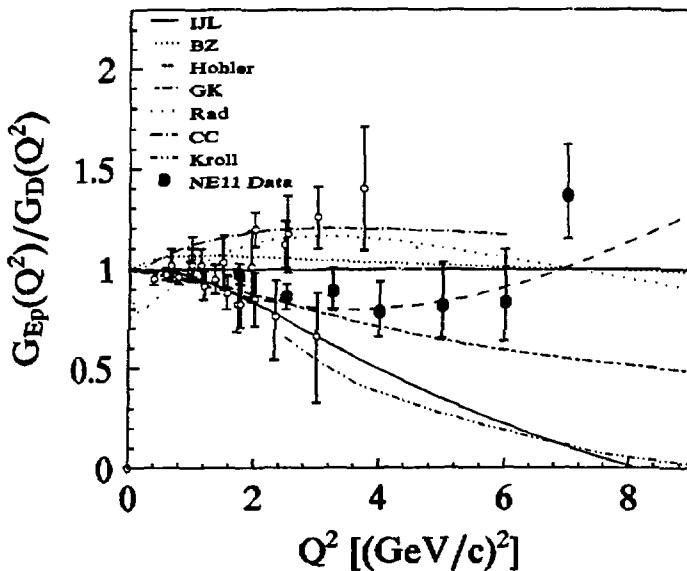
Figure 4.6: Proton electric form factors. Old and new data points are shown as well as results from many model/fits. The form factors are normalized to the dipole form factor.

Gari and Krümpelmann [98] while for $G_{Ep}(Q^2)$ the VMD model by Höhler, et al., [88] works well, and the results are not far off from the dipole form factor representation. However, since many of the models are really fits to the low Q^2 data, it is quite possible that many of the other models could be made to agree with the new results by just refitting the model parameters.

Form Factor Results

Final values for $G_{Mn}(Q^2)/G_D(Q^2)/\mu_n$ and $(G_{En}(Q^2)/G_D(Q^2))^2$ are shown in Figures 4.7 and 4.8. The quantities which were actually measured were the form factor squared. Since G_{En}^2 is small, it is possible to get negative results which are consistent with zero within the errors. This is the reason for not taking the square root of the quantity $(G_{En}(Q^2)/G_D(Q^2))^2$. The inner error bars in Figures 4.7 and 4.8 indicate the total
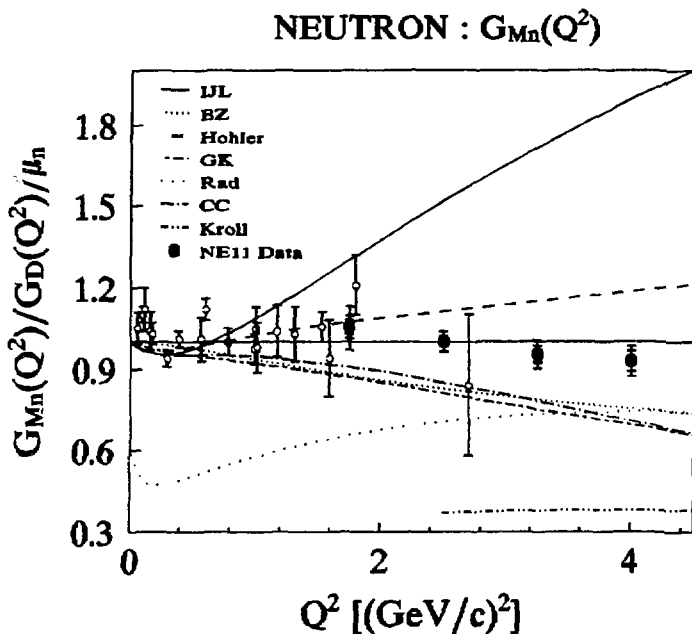
Figure 4.7: Results for the neutron magnetic form factor measurements for one choice of the inelastic model. Also shown are old measurements and model predictions from the various models discussed in the text.

NEUTRON : $G_{En}(Q^2)$
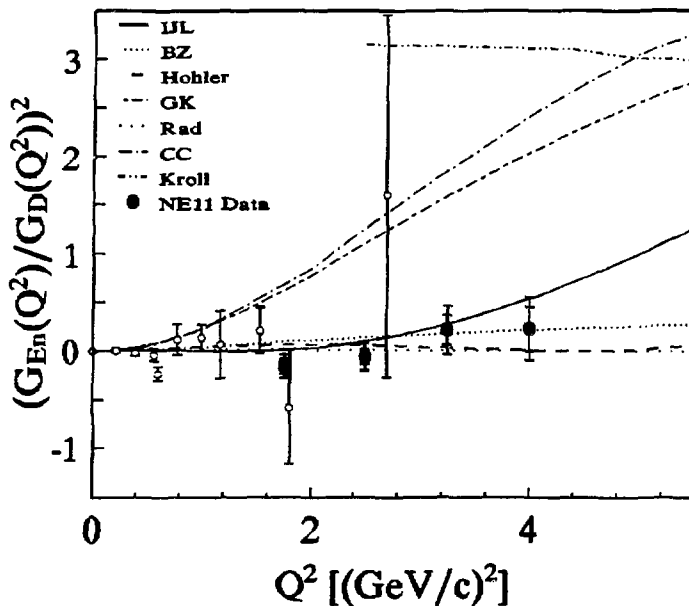
Figure 4.8: Results for the neutron charge form factor measurements for one choice of the inelastic model. Also shown are old measurements and model predictions from the various models discussed in the text.

statistical uncertainty and the outer error bars are the statistical plus systematic errors. No modeling errors were included in these error bars. A discussion of the experimental errors will be given in the next section. The data in Figures 4.7 and 4.8 were extracted using the Paris potential, smearing model 3 and the off-mass-shell correction given by Eq. 3.47. The area method I was used to extract the form factors. Also shown in these figures are many model form factor curves. The

corresponding curves for the proton form factors were given earlier.

Basically, the results for $G_{mn}(Q^2)/G_D(Q^2)/\mu_n$ are consistent with 1.0 which means that the empirical dipole formula is a good representation of the neutron magnetic form factor out to a Q^2 of 4.0 (GeV/c)^2. Previous measurements which are also shown in Figure 4.7 are consistent with the new measurements as well. There are, however, no model form factor curves which can describe these new measurements which indicates that more work is needed on form factor (and nuclear structure) modeling. It is possible that some of the existing models could be made to fit the data by adjusting some of the fit parameters. This remains to be seen. Note the improvement on the errors for the new form factor measurements as compared to the old measurements.

The new results for $(G_{En}(Q^2)/G_D(Q^2))^2$ are consistent with zero within the errors on the measurement as are the previous measurements at lower Q^2. There are several model curves which are consistent with these new measurements, such as the IJL curve [86], BZ [87], Höhler [88], and Rad [94]. Refer back to the first section in this chapter for more information on these models. Note, however, that there are several curves which predict a large G_{En} at large Q^2. This is equivalent to saying that F_{1n} goes to zero at large Q^2 instead of G_{En} (See Eq. 4.2). The new measurements clearly rule out this possibility for the Q^2 range of the measurements. Note again the improvement on the errors for the new form factor measurements as compared to the old measurements.

Figure 4.9 shows a plot of the ratio G_{Mn}/G_{Mp} using the measured form factors from this experiment. The error bars are statistical plus systematic. As mentioned earlier in the discussion on perturbative QCD, pQCD predicts that this ratio should go as $-2/3$ at large Q^2. The new data is in agreement with this prediction which is shown as a straight line over all Q^2. Note, however, that additional points are included which were calculated using $G_{Mn} = \mu_n \cdot G_D$ and G_{Mp} from the
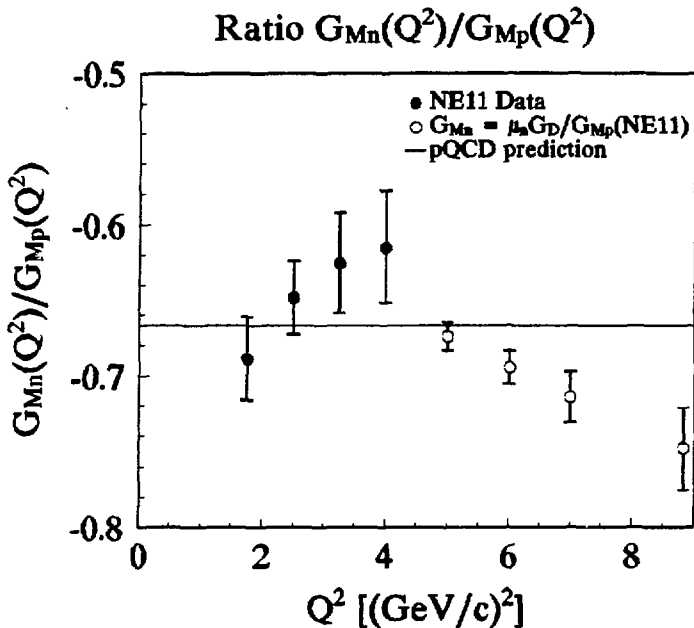
Figure 4.9: Ratio plots of measured G_{Mn}/G_{Mp}. The pQCD prediction is shown as a straight line, and the results at higher Q^2 are shown assuming that G_{mn} continues to agree with the dipole.

measurements in this experiment. It is clear that if the neutron magnetic form factor continues to agree with the dipole form factor at larger Q^2 then the pQCD prediction doesn't work. Otherwise, if the pQCD prediction is correct then G_{Mn} must begin to decrease with increasing Q^2 at roughly the same rate as the proton magnetic form factor fall-off.

Results for $G_{Mn}(Q^2)/G_D(Q^2)/\mu_n$ using the Paris potential, smearing model 3 and the off-mass-shell correction given by Eq. 3.47 for all three extraction methods are given in Table 4.5. The corresponding results for $(G_{Mn}(Q^2)/G_D(Q^2))^2$ are given in Table 4.6. Note that the quasielastic model used was the same for all these results and was discussed in Chapter 3. Tables 4.7-4.10 shows the extracted form factors with different model assumptions and for all three extraction methods. Each table is for a different Q^2 point. The variation in these numbers is indicative of the error in the form factors due to the inelastic modeling. A similar study has been done [66] on the effect on the form factors due to the quasielastic modeling.

Table 4.5: Results for $G = G_{mn}(Q^2)/G_{D}(Q^2)/|\mu_n|$ with statistical error, S1, and total error S2 given. Results are shown for each of the three extraction methods. Q^2 is in $(GeV/c)^2$.

	Peak method			Area method I			Area method II		
Q^2	G	S1	S2	G	S1	S2	G	S1	S2
1.75	1.064	0.013	0.026	1.056	0.027	0.041	1.044	0.025	0.053
2.50	1.024	0.010	0.028	1.002	0.017	0.037	1.007	0.012	0.051
3.25	0.959	0.019	0.037	0.960	0.031	0.050	0.968	0.025	0.059
4.00	0.934	0.031	0.050	0.930	0.047	0.062	0.942	0.032	0.063

Table 4.6: Results for $G = (G_{En}(Q^2)/G_{D}(Q^2))^2$ with statistical error, S1, and total error S2 given. Results are shown for each of the three extraction methods. Q^2 is in $(GeV/c)^2$.

	Peak method			Area method I			Area method II		
Q^2	G	S1	S2	G	S1	S2	G	S1	S2
1.75	-0.167	0.077	0.157	-0.167	0.074	0.117	-0.076	0.065	0.070
2.50	-0.189	0.082	0.222	-0.076	0.074	0.141	-0.167	0.047	0.104
3.25	0.084	0.177	0.352	0.148	0.153	0.251	0.298	0.123	0.185
4.00	0.110	0.322	0.515	0.198	0.268	0.356	0.341	0.308	0.325

Table 4.7: Results for the neutron charge and magnetic form factor for $Q^2 = 1.75$ (GeV/c)^2 using various smearing models, off-mass-shell corrections in the smearing models, deuteron wave function parameterizations, and extraction methods. $I_{sm} = 1,5$ indicates the smearing model used, $I_{off} = 3.44, 3.45, 3.47$ refers to the equation number where the off-mass-shell corrections were defined. $I_{wf} = P$, B, or R refers to the Paris, Bonn, and Reid deuteron wave functions.

			Peak Method		Area Method I		Area Method II	
I_{sm}	I_{off}	I_{wf}	$G_{Mn}/G_D/\mu_n$	$(G_{En}/G_D)^2$	$G_{Mn}/G_D/\mu_n$	$(G_{En}/G_D)^2$	$G_{Mn}/G_D/\mu_n$	$(G_{En}/G_D)^2$
1	3.47	P	1.068	−0.171	1.063	−0.167	1.048	~0.076
2	3.47	P	1.068	−0.168	1.061	−0.165	1.049	~0.076
3	3.47	P	1.064	−0.167	1.056	−0.167	1.044	~0.076
4	3.47	P	1.069	−0.168	1.063	−0.162	1.050	~0.076
5	3.47	P	1.067	−0.168	1.059	−0.167	1.047	~0.076
3	3.44	P	1.061	−0.169	1.055	−0.176	1.042	~0.078
3	3.45	P	1.066	−0.166	1.057	−0.160	1.046	~0.074
3	3.47	B	1.056	−0.176	1.048	−0.181	1.037	~0.083
3	3.47	R	1.067	−0.163	1.058	−0.152	1.046	~0.073
Range of deviation			0.013	0.013	0.015	0.029	0.013	0.010
Statistical + Systematic error			0.026	0.157	0.041	0.117	0.053	0.070

Table 4.8: Results for the neutron charge and magnetic form factor.
This table is the same as Table 4.7 except Q^2 =2.50 (GeV/c)^2.

I_{ae}	I_{off}	I_{wf}	Peak Method		Area Method I		Area Method II	
			$G_{en}/G_n/\mu_n$	$(G_{en}/G_D)^2$	$G_{en}/G_D/\mu_n$	$(G_{en}/G_D)^2$	$G_{en}/G_D/\mu_n$	$|G_{en}/G_D|^2$
1	3.47	P	1.033	−0.195	1.012	−0.057	1.016	−0.195
2	3.47	P	1.032	−0.187	1.010	−0.060	1.016	−0.170
3	3.47	P	1.024	−0.189	1.002	−0.076	1.007	−0.167
4	3.47	P	1.034	−0.187	1.012	−0.052	1.017	−0.171
5	3.47	P	1.029	−0.187	1.007	−0.067	1.013	−0.169
3	3.44	P	1.021	−0.202	1.000	−0.104	1.005	−0.195
3	3.45	P	1.026	−0.183	1.002	−0.062	1.009	−0.152
3	3.47	B	1.017	−0.196	0.995	−0.088	1.001	−0.178
3	3.47	R	1.027	−0.186	1.004	−0.063	1.010	−0.159
Range of deviation			0.017	0.019	0.017	0.052	0.016	0.043
Statistical + Systematic error			0.028	0.222	0.037	0.141	0.051	0.104

			Peak Method		Area Method I		Area Method II	
I_{em}	I_{off}	I_{wf}	$G_{mn}/G_D/\mu_n$	$(G_{en}/G_D)^2$	$G_{mn}/G_D/\mu_n$	$(G_{en}/G_D)^2$	$G_{mn}/G_D/\mu_n$	$(G_{en}/G_D)^2$
1	3.47	P	0.976	0.061	0.981	0.153	0.986	0.256
2	3.47	P	0.972	0.082	0.976	0.162	0.983	0.293
3	3.47	P	0.959	0.084	0.960	0.148	0.968	0.298
4	3.47	P	0.976	0.082	0.979	0.173	0.986	0.293
5	3.47	P	0.968	0.083	0.970	0.154	0.978	0.295
3	3.44	P	0.955	0.059	0.959	0.096	0.965	0.251
3	3.45	P	0.961	0.096	0.961	0.171	0.970	0.324
3	3.47	B	0.956	0.074	0.958	0.135	0.966	0.280
3	3.47	R	0.961	0.089	0.960	0.158	0.969	0.310
Range of deviation			0.021	0.037	0.023	0.077	0.021	0.073
Statistical + Systematic error			0.037	0.352	0.050	0.251	0.059	0.185

Table 4.9: Results for the neutron charge and magnetic form factor. This table is the same as Table 4.7 except $Q^2 = 3.25$ $(GeV/c)^2$.

Table 4.10: Results for the neutron charge and magnetic form factor. This table is the same as Table 4.7 except $Q^2 = 4.00$ (GeV/c)^2.

I_{on}	I_{off}	I_{uf}	Peak Method		Area Method I		Area Method II	
			$G_{Mn}/G_D/\mu_n$	$(G_{En}/G_D)^2$	$G_{Mn}/G_D/\mu_n$	$(G_{En}/G_D)^2$	$G_{Mn}/G_D/\mu_n$	$(G_{En}/G_D)^2$
1	3.47	P	0.959	0.072	0.960	0.186	0.970	0.265
2	3.47	P	0.953	0.107	0.953	0.209	0.964	0.338
3	3.47	P	0.934	0.110	0.930	0.198	0.942	0.341
4	3.47	P	0.959	0.106	0.960	0.221	0.970	0.335
5	3.47	P	0.946	0.108	0.944	0.202	0.956	0.339
3	3.44	P	0.929	0.066	0.929	0.121	0.938	0.252
3	3.45	P	0.936	0.128	0.931	0.231	0.944	0.386
3	3.47	B	0.936	0.098	0.935	0.179	0.946	0.315
3	3.47	R	0.933	0.117	0.926	0.212	0.939	0.364
Range of deviation			0.030	0.051	0.034	0.110	0.032	0.134
Statistical + Systematic error			0.050	0.515	0.062	0.356	0.063	0.325

Errors

The types of errors which contributed to the final experimental results can be broken up into two categories, statistical and systematic uncertainties. This experiment was designed to have as small as possible statistical errors given a reasonable amount of experimental running time. The systematic errors can also be broken up into two sub-categories, namely point-to-point errors and absolute errors. Point-to-point errors are those which can vary from run-to-run or at different kinematics (such as beam energy fluctuations). Absolute errors are those which are the same for all data. A

Table 4.1: Summary of systematic uncertainties and their approximate effect on the cross section error (σ) and the neutron form factor errors at $Q^2 = 4.0$ (GeV/c)^2. The labels 8 and 1.6 refer to either the 8 GeV spectrometer or the 1.6 GeV spectrometer.

Quantity	Error	$\Delta\sigma/\sigma$	$\Delta G_{Mn}/G_D/\mu_n$	$\Delta(G_{En}/G_D)^2$
Incident Energy	0.05%	0.35%	0.010	0.054
$\theta_{1.6}$	0.05°	0.2%	0.005	0.015
θ_8	0.005°	0.15%	0.001	0.011
Incident charge	0.15%	0.15%	0.004	0.023
Target density	0.15%	0.15%	0.004	0.023
Efficiency	0.25%	0.25%	0.007	0.038
Rad. corrections	0.5%	0.5%	0.014	0.076
1.6 Acceptance(E')	0.5%	0.5%	0.011	0.038
1.6 Acceptance(θ)	0.5%	0.5%	0.011	0.038
8 Acceptance (E')	0.2%	0.2%	0.001	0.015
8 Acceptance (θ)	0.2%	0.2%	0.001	0.003
Al. subtraction 8	0.1%	0.1%	0.001	0.008
Total Point-to-point 8		0.77%	0.026	0.122
Total point-to-point 1.6		1.02%		
Incident charge	0.5%	0.5%	0.008	0.001
Target density	0.85%	0.85%	0.014	0.002
Target length	0.2%	0.2%	0.003	0.000
Rad. Corrections	1.0%	1.0%	0.017	0.003
Overall Acceptance	1.0%	1.0%	0.017	0.003
1.6 Normalization	1.0%	1.0%	0.022	0.075
Total Absolute errors		2.0%	0.036	0.075

summary of the major sources of errors is given in Table 4.1 and in the following discussion. In addition to these errors, the errors in the proton subtraction were also propagated through.

Error summary:

1. Incident beam energy: The point-to-point error on the incident beam energy was obtained from the observed scatter in energy needed to align the elastic peak positions at $W^2 = M_p^2$ as determined by the elastic peak analysis [15]. The effect on the cross section was calculated for each data point using a model cross section evaluated with different beam energies but constant W^2.

2. Scattering angle: The uncertainty was based on the accuracy of the measured beam incident angle as given by the wire arrays and cavity monitors, and on the uncertainty in the survey of the spectrometers and the wire chambers. The effect on the cross section was calculated for each data point using a model cross section evaluated with different scattering angles but constant W^2.

3. Incident charge: The absolute error on the toroid charge measurement was obtained from a calibration against measurements made with a Faraday cup [39]. The point-to-point systematic error was obtained from the observed run-by-run fluctuation in the two toroid measurements relative to each other (see appendix A).

4. Target density: The absolute error on the target density was calculated based on several contributing factors. The error on the bulb pressure measurements was ~0.3%, and the resistance measurements were good to ~0.2% [99]. The conversion from pressure to temperature had an error of 0.5% due to uncertainty in the cryogenic data [26][27]. The error in the conversion from resistance to temperature was unknown, but believed to be small, so an estimated error of 0.5% was used. The conversion from temperature to density had an error of 0.6%. Summing these error in quadrature for each measurement and averaging since the bulb pressure and resistance density measurements were averaged gives an absolute error on the density measurement of 0.85%. The point-to-point error was obtained from the observed run-to-run fluctuations in the different measurement methods.

5. Target length: The target length uncertainty due to uncertainty in the amount of shrinkage due to temperature effects was estimated to be 0.2%.

6. Efficiency: The electron detection efficiency was estimated by calculating the various detector efficiencies with slightly different assumptions. The main concerns were efficiency dependence on tracking and the possible variation of efficiency with changing counting rates. Also the efficiency can change with π/e ratios.

7. Radiative corrections: The dominant uncertainty in the absolute radiative corrections was due to neglecting the two-photon exchange contribution which is suppressed by a factor $\alpha = 1/137$. There were additional uncertainties due to higher order processes and using the peaking approximation. An absolute error of 1.0 was assigned, and a point-to-point error of 0.5%.

8. Acceptance: Absolute and point-to-point acceptance errors for the 8 GeV spectrometer were obtained from the wire float measurement of the optics [30] and from studies of the effective target length dependence of the acceptance. Point-to-point errors for the 1.6 GeV spectrometer acceptance was estimated from quadrupole saturation studies.

9. 1.6 Gev normalization: The error on the normalization was calculated along with the normalization factor using statistical error weighted averaging over all W^2 bins where 1.6 data existed along with at least two 8 GeV data points. This procedure was discussed in greater detail earlier.

The point-to-point systematic errors on the form factors were calculated by summing the statistical and point-to-point sytematic errors in quadrature and then refitting the data. The resultant error calculated by the fitting routine was called the statistical plus point-to-point error. The absolute errors were then combined in quadrature to give the total error (excluding modeling errors). Since the 1.6 GeV data was

combined with the 8 GeV data, the 1.6 normalization was treated as a point-to-point error in the error analysis.

Conclusions

Results have been presented for new measurements of the $\Delta(1232)$ transition form factor, measurements for the extracted transverse and longitudinal deuterium cross section components, $R_T(W^2,Q^2)$ and $R_L(W^2,Q^2)$, and measurements of the neutron elastic electromagnetic form factors which were extracted from the data under a variety of model assumptions.

The $\Delta(1232)$ transition form factor measurements verified previous measurements. The fall-off of the form factor with increasing Q^2 was observed to fall faster than that expected from pQCD, although the fall-off of the proton elastic form factor, G_{M_p}, and of the higher resonance, S_{11}, do have the predicted pQCD fall-off with Q^2.

The measurements of the deuterium transverse and longitudinal components were presented for the range $1.75 < Q^2 > 4.0$ $(\text{GeV/c})^2$. These results are independent of deuterium cross section modeling. As better models are developed for the quasielastic cross section and/or the inelastic cross section model the neutron form factors can be re-extracted from the R_T and R_L results.

The form factors were extracted from the deuterium cross section data using three different extraction methods. Three methods were used as a check that the form factors were being calculated properly. The different extraction methods agree very well as expected.

In comparing the form factor results for both the proton and the neutron, one thing is very clear. Namely, there is not a single model shown which can adequately describe all four nucleon form factors. However, since most of these models involve free parameters which were fit to lower Q^2 data, it is quite likely that the parameters could be adjusted to give better fits. It remains to be seen whether one of these models can be adjusted to describe the measurements for all the form factors.

The results for G_{Mn} are consistent with the dipole form factor representation, and in fact, there is no model shown in Figure 4.7 which passes through these data. The results for G_{En} are consistent with zero. This is an important result because some models predict an increasing G_{En} with increasing Q^2. At least at the Q^2 of these measurements this does not seem to be the case, and this result should be used to constrain all existing and future models. If G_{En} continues to be consistent with zero at high Q^2 then existing deuterium cross section measurements out to $Q^2 = 10.0$ $(GeV/c)^2$ [8] can be used to extract information on G_{Mn} at these higher Q^2.

A study has been made of the extracted form factor results under several different assumptions pertaining to the inelastic model. Assuming that these results are indicative of the systematic error due to the inelastic model, one could conclude that the systematic error due to the smearing models is small compared to the "total" systematic error. The term "total" means statistical plus systematic errors (no modeling errors). The systematic error due to different off-shell

corrections is small for G_{Mn}, but for G_{En} at large Q^2 is ~ half of the "total" systematic error. The systematic error due to different deuterium wave functions is larger than that due to smearing models but smaller than that due to off_shell corrections.

In conclusion, these difficult measurements have produced very interesting results and will serve a very useful purpose in the development of nuclear structure theory and in the understanding of the strong interaction. Since no theoretical model was able to reproduce all the nucleon form factors, additional theoretical work is needed to explain these new results. This experiment has nearly pushed to the experimental high Q^2 limit the extraction of the nucleon form factors using a Rosenbluth separation. Now, experimentalists must turn to different techniques if more information is to be learned about the nucleon elastic charge and magnetic form factor.

APPENDIX A: TOROIDS

The toroidal charge monitors, or toroids, in the End
Station A were composed of iron rings which encircled the beam
pipe. They were located a few meters upstream from the target
area. When the beam current passed through a toroid a magnetic
field was induced inside the iron. This field induced a
current in a wire which was looped several times around the
toroid. The toroid winding was placed in parallel with a
capacitor to produce a resonant signal when the charged
electron pulse passed through the core. This resonant signal
passed through a nearby pre-amplifier and was then carried to
the counting house where it was branched to the "old" and the
"new" readout systems. Both of these readout systems were used
for this experiment as a consistency check. However, the old
system performance began to deteriorate and proved unreliable
towards the end of the experiment. The actual data from the
old readout system were only used for a few early runs when
the Microvax was not running, and thus the new readout system
was not working.

The old readout system began with a three stage
amplifier. Each stage could amplify by one, three or ten. The
signal next entered a circuit which sampled the pulse just
beyond the second peak of the resonance and produced a square
wave pulse with the same amplitude as the sampled point. This
square wave was converted to an ADC signal which was
proportional to the charge in the beam pulse. These signals

were continuously accumulated and were read by the Vax and the Microvax computers periodically.

The new readout system began with a solid state amplifier equipped with a divide by three attenuator to produce gains of 1, 1/3, 10, 10/3, 100, 100/3, 1000, and 1000/3. The amplified signal was integrated over one half-period of the signal and then converted to an ADC signal which was proportional to the charge in the beam pulse. The ADC signals were accumulated by the Microvax computer. Figure A.1 shows the toroid readout and calibration systems.

Calibration

Each toroid had its own independent calibration system. The main component of this system was a capacitor of known capacitance. For one of the toroids, the capacitance, $C1$, was given by 21.80 nF, and for the other toroid $C2$ was given by 21.99 nF. Both capacitances were measured to 0.1%. The capacitor was charged to a known voltage, V, set by a digital-to-analog converter, or DAC. The DAC voltage had been calibrated to be correct to 0.1%. The capacitor was then discharged through a single turn winding around the toroid, thus acting like a beam pulse of known charge, $Q = CV$. An attenuator circuit located near the toroids was set by the Microvax computer to attenuate by 1, 10, or 100. This allowed for simulating large and small beam charge pulses. The resultant resonant signal produced in the toroid circuitry was handled in the normal manner for both the old and the new systems. Periodically, a maxi-calibration was done which
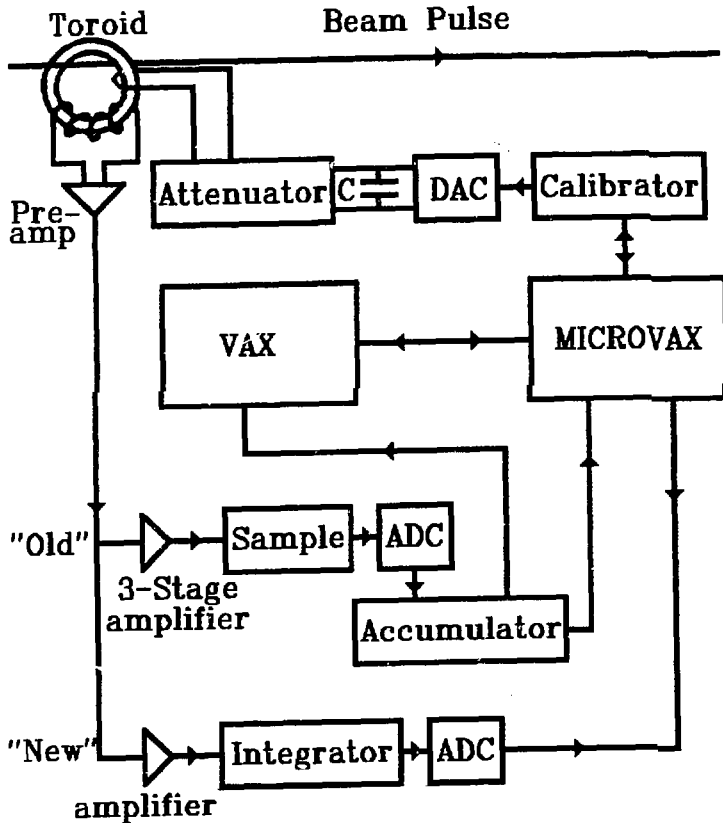
Figure A.1: Toroid data acquisition and calibration system. Each toroid has its own independent and identical system.

consisted of calibrating at several different gains, attenuator values, and DAC voltages. This was done to monitor any changes in the system which might have occurred such as temperature effects, gain drifts, and timing changes. Also, a mini-calibration was done before every run at a single gain,

attenuator, and DAC voltage setting corresponding to what was needed for the beam currents at that time. These calibration data were used to correct the measured beam charge on a run by run basis.

Corrections

Several corrections were needed to the measured toroid real data and calibration data. Corrections for the new toroid readout system were made for attenuation, the nonlinear response of the toroids, and timing. Corrections for the old toroid readout system were made for beam repetition rate dependence, and ADC drifts.

The attenuation correction was done for calibrations which used the divide by ten attenuator because the attenuation was not exactly equal to 10 (the divide by 100 attenuator was never used for normal running conditions). The correction, using the maxi-calibration data, was found by averaging the ratio of calibration data:

$$\bar{K}_A = \frac{(CAL(Attenuator=1, DAC\ voltage=1)}{(CAL(Attenuator=10, DAC\ voltage=10)} . \qquad (A.1)$$

The DAC voltage was changed with the attenuator to produce what should be the same calibration pulse. The corrections for the two toroids were small but on the same order as the error on the toroid measurement, 0.9985 and 0.9994.

The nonlinearity correction accounted for the small nonlinear response of the toroids with changing DAC voltage. Figure A.2 shows a typical plot including the fit for this nonlinearity calculated from the maxi-calibration data.

Linearity correction for gain = 3
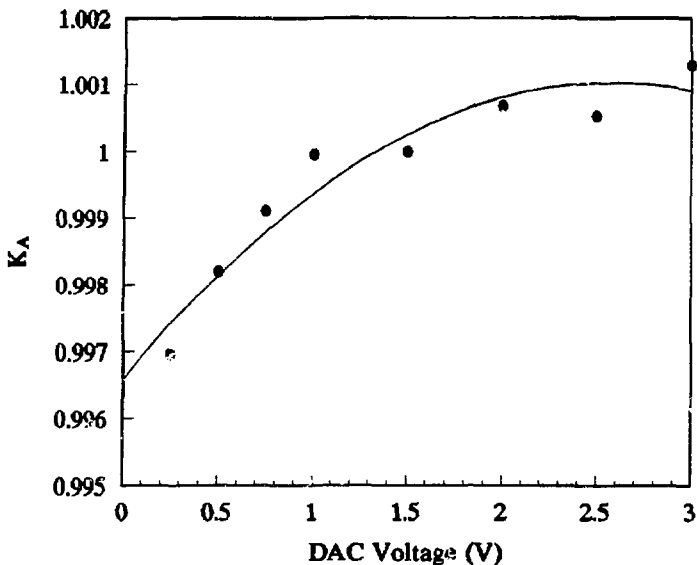
Figure A.2: Sample plot showing the toroid nonlinearity correction as a function of DAC voltage.

The calibration data in this plot were normalized to the mini-calibration data taken at a gain of 3. To calculate the linearity correction, an average equivalent DAC voltage must first be calculated for the measured beam charge data. This equivalent voltage was the DAC voltage needed to reproduce the average beam pulse charge. The linearity correction was calculated from the fit to the data shown in figure A.2. It multiplied the mini-calibratio⁻ data. These corrections never exceed 0.2% for this experiment.

The timing correction was the biggest correction applied

to the toroid data. The new toroid readout system involved integrating over a portion of the toroid resonant signal. The start and stop to the integration were triggered by the beam gate. If the beam pulse position changed in time relative to the beam gate then a different result would be obtained for the signal integration. The timing correction takes this into account. Figure A.3 shows a typical timing correction plot calculated from the ratio of the calibration data at different

Timing correction for gain = 1
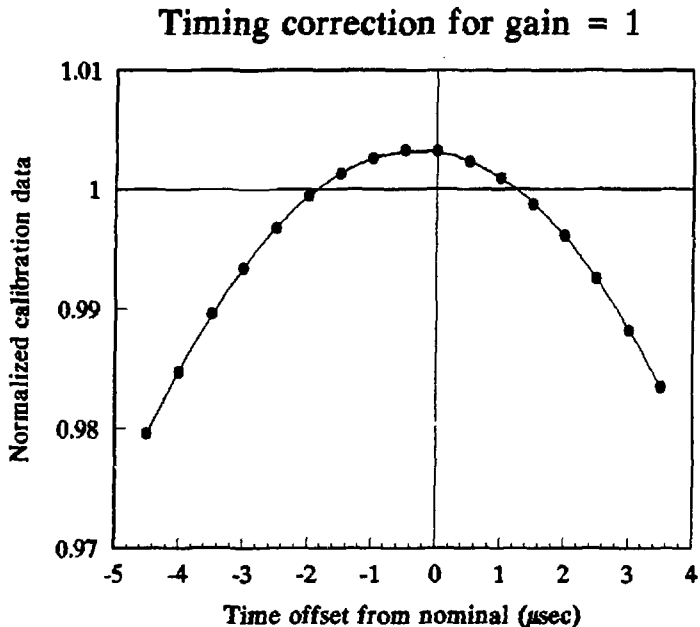
Figure A.3: Typical timing correction plot. Calibration coefficients versus the time shift from the nominal time between the beam gate and the beam pulse is normalized to the calibration coefficient at the nominal time.

time delays to the calibration data at the nominal timing. The timing was calculated from the event scaler histogram which was accumulated during data taking. The event scaler measured the time between the beam gate and the event trigger using a scaler to count pulse generator clock counts between the timing start and stop. A histogram of many events outlined the shape of the beam pulse since the event trigger could occur anywhere in time along the pulse. The timing correction for this experiment was as low as 0.985 for a few runs.

New toroids ratio
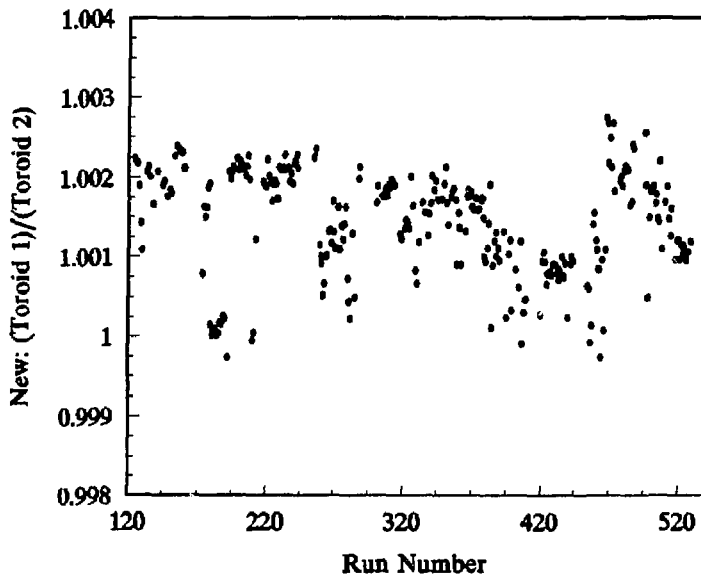
Figure A.4: Ratio of corrected new toroid reading measurements for the two independent toroids versus run number over the entire experiment.

Overall, the performance from the new toroid readout was very good. Figure A.4 shows a plot of ratios of the two toroid measurements with the new toroid readout systems. The measured charge value used was the average between these independent charge measurements, and it had an error ~ ±0.2%.

It was discovered in the middle of this experiment that the old toroid readout was exhibiting a dependence on the beam

Gain = 3
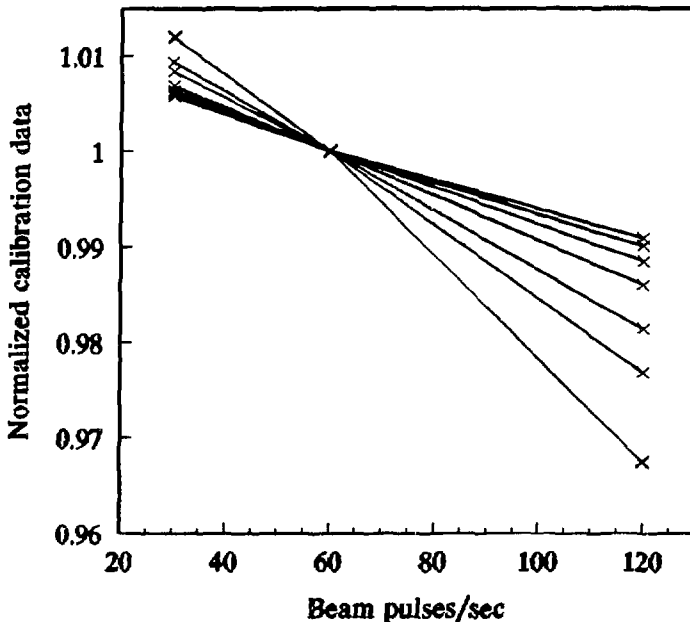
Figure A.5: Calibration data normalized to the 60 pulses-per-second rate calibration data. The different sloped lines correspond to different DAC voltages. The lines become less sloped as the DAC voltage is increased.

repetition rate. Some investigation indicated that the problem was occurring in the module which samples the toroid resonant signal. An increase in repetition rate somehow produced a negative DC offset in the sampling module which lowered the measurement of the toroid charge. The repetition rate correction for the old toroids which was needed to take this effect into account had an ADC readout dependence as well as the repetition rate dependence. Special maxi-calibration data was taken at repetition rates of 30, 60, and 120 pulses-per-second and at several DAC voltages and gain settings. Figure A.5 shows a plot for a gain = 3 of these measurements normalized to the 60 pulses-per-second point. Data at the same DAC voltage are connected by lines. Linear fits to the data at the same DAC voltage were found, and the DAC voltages were converted to their equivalent ADC readings. Fits to the slopes versus ADC were found as shown in Figure A.6. To apply the correction for a given run, the average measured ADC reading was calculated and a slope was calculated from the fit. Using this line which passes through 1.0 at 60 pulses-per-second, the correction was calculated by interpolating to the actual repetition rate for the run. This correction ranged from 2.0% to 2.5% for the few runs where the old toroid readout was necessary.

The last correction to discuss is the ADC linearity correction for the old readout system. This correction was similar to the nonlinearity correction found for the new toroid readout. Figure A.7 shows a plot of the nonlinear response of the calibration with ADC value. The average ADC
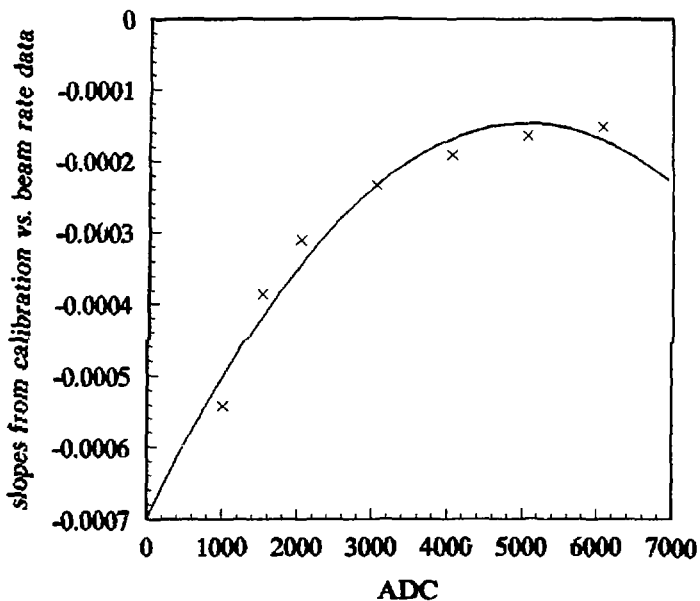
Figure A.6: Plot and fit to slopes found from data in Figure A.5 versus ADC.

value for each run was calculated and the calibration coefficients were corrected using the fit shown in figure A.7. This correction was fairly constant for the few runs of interest, and had a value of ~ 0.7%.

As mentioned earlier, the old toroid readout behavior was only good in the first part of the experiment. Note that the first run of the experiment was run number 125. The old readout system for Toroid 1 completely died after ~ run 200, and the performance of the old readout system for Toroid 2

Gain = 3
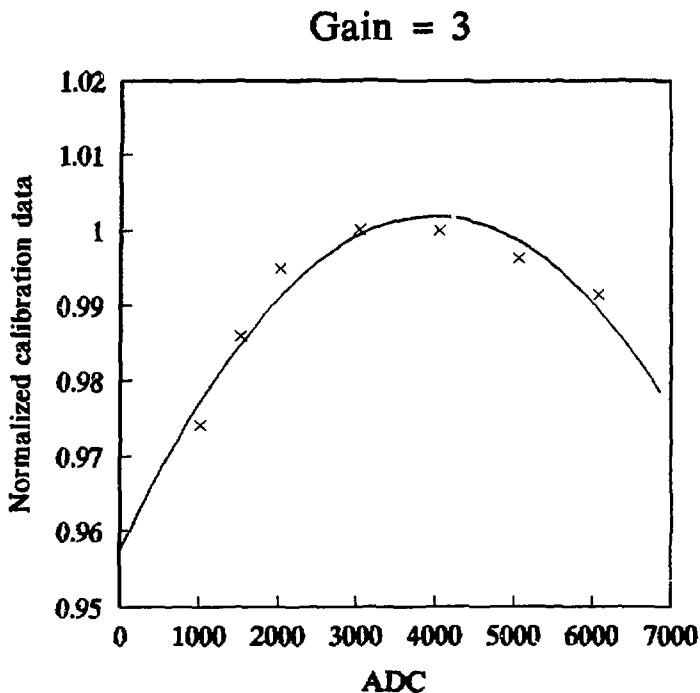
Figure A.7: Sample plot of toroid calibration coefficients normalized to the mini-calibration data versus ADC and the fit used for calculating the correction.

slowly deteriorated over time. Figure A.8 shows two plots which give strong indication that is satisfactory to use the old toroid readings for a few runs. The top plot is a ratio of measurements from the new and the old readout systems for the same toroid, toroid 1. The agreement is reasonably good. The bottom plot shows the ratio of measurements from the old toroid readout for toroids 1 and 2. The open circles are the runs where the new readouts were not available. Again, the
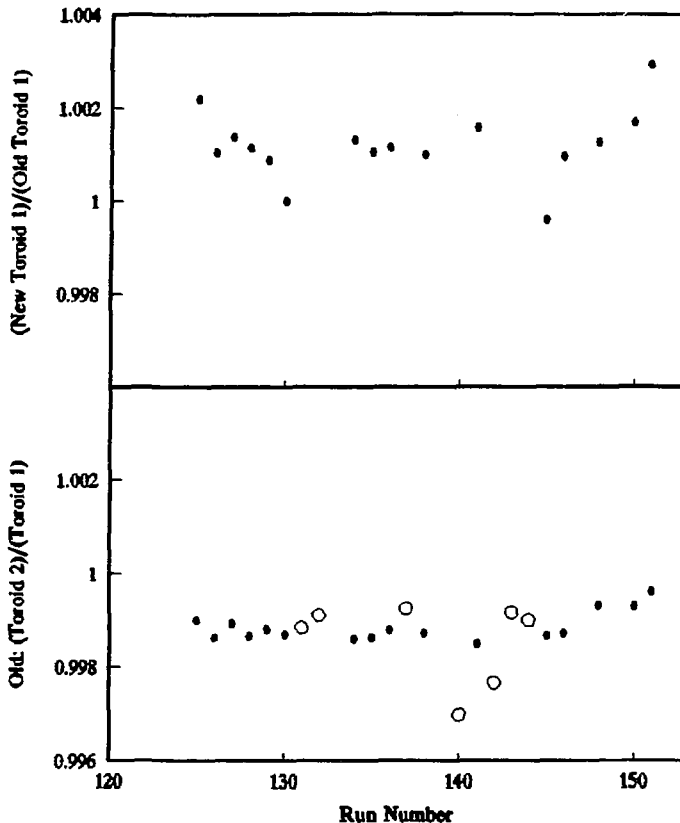
Figure A.8: Top: plot of new toroid over old toroid reading for the same toroid. Bottom: Ratio of old toroid readouts. The open circles are the data for the old toroid when the new toroid data was unavailable.

agreement is good, and the toroid readings look reliable for this range of runs. The absolute error on the toroidal charge measurement was found to 0.5% from a cross calibration measurement made using a Faraday cup [39].

APPENDIX B: 8 GEV SHOWER COUNTER CALIBRATION

The calibration of the shower counter blocks was a very important component of the shower energy calculation process. The desire was to find coefficients for each block which would convert the pedestal-subtracted ADC pulse height to the energy deposited by the particle in that block. Two different shower energies were needed. SHSUM was the sum over all computed energies in all blocks. It was used for calculating the tracking efficiency for electrons since a pion leaves considerably less energy than an electron. SHTRK was the sum over all block energies through which a track passed or passed near. It was used for identifying electrons and pions. It should be noted that in the following discussion the term "track" will be loosely used to describe the avalanche of shower particles created in the lead glass array for a single particle passing through.

Before the calibration coefficients could be calculated it was necessary to correct the measured energy versus Y, the vertical direction. There was a decrease in the measured energy for hits far from the phototube as compared to hits near the phototube. This is indicated in Figure B.1 for a PR block and a TA block. The PR blocks had phototubes only at the top, or at +Y, while the TA blocks had phototubes at both ends whose outputs were summed. For the Y dependence calculation a constant, but approximately correct, block coefficient was used to calculate the energy. The energy data in Figure B.1
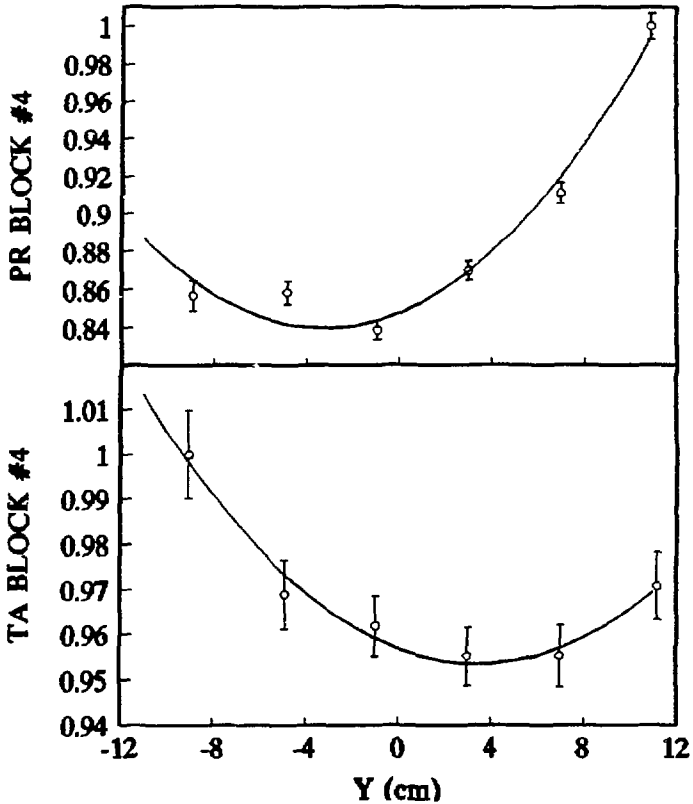
Figure B.1: Sample plots showing the vertical dependence of the measured energy in a block from each of the first two layers in the shower counter.

have been normalized to the highest measured energy. A polynomial fit to the vertical Y position, $FIT = A + BY + CY^2$, was done to these normalized data. The fits were then used in the subsequent data analysis to correct the measured energy to the nominal value depending on the Y position of the particle

track as determined by the tracking code. This was done by multiplying the measured energy by 1.0/FIT(Y). Note that Y corrections were not done for the TC blocks because low statistics did not allow for obtaining good fits.

Now, in order to calculate the block coefficients, blocks were grouped together in six sets corresponding to the six PR blocks. The TA, TB, (and TC for momenta above 4.0 GeV). Blocks included in each group were the ones which could contain some
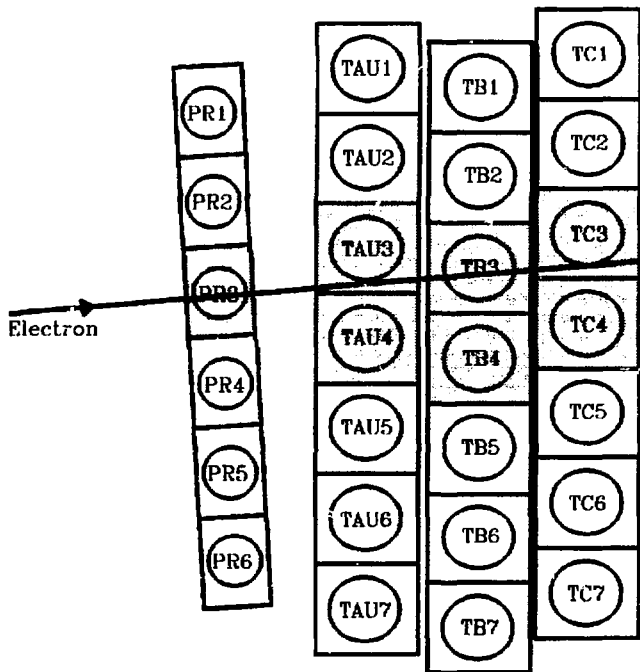
Figure B.2: Shaded blocks indicate those which could contain some shower energy contribution due to a track hitting block PR3 at a point near the center of the block.

of the shower energy for any track which passed near the
center of the corresponding PR block. One such group is shown
in Figure B.2 for PR block #3. Testing was done by looking at
many individual events to verify that the track energy for
tracks hitting within the central limits of the hit PR block
was contained within that block's corresponding group. The
central limits were defined to be the central 70% of the block
or 11.1 cm out of a total width of 15.8 cm. Each group
contained one PR block, two TA blocks, two TB blocks, (and two
TC blocks when these blocks were needed).

    The energy deposited in block i contained in group j for
a single particle track was given by:

$$E_{trk}(i,j) = \frac{(ADC(i,j) - PED(i,j)) \cdot C_{cal}(i,j)}{P_{trk}}, \qquad \text{B.1}$$

where C_{cal} was the calibration coefficient for the block, and
P_{trk} was the particle momentum as determined from the wire
chamber tracking data. The initial values for C_{cal} were
arbitrarily chosen at reasonable values and the final values
were determined by iterating the calibration procedure. Since
a given group completely contained the tracks which hit in the
designated area, the coefficients were found by minimizing,
for many events, the chi_square quantity:

$$\chi^2(j) = (1.0 - \sum_i c(i,j) \cdot E_{trk}(i,j))^2, \qquad \text{B.2}$$

where j is an index of the hit PR blocks, the sum over i loops
over all blocks contained in a group, and the fit
coefficients, c, were the multiplicative corrections to the

block coefficients. It should be noted for the TA layer there were two coefficients for each block because there were two phototubes. The two coefficients found were not the same, and there was evidence that the response of some of the tubes was changing over the course of the experiment. The quantity E_{trk} for a TA block was shared between the two phototube contributions. As mentioned above, the least square fit was an iterative procedure, and when good block coefficients were being used the fit coefficients, c, were found to be consistent with 1.0 within errors.

It should be noted that some blocks, because of the way the block groups were defined, could belong to two different groups. These blocks thus had two different block coefficients found which may or may not have been the same. It is possible for a piece of lead glass to have different responses in different regions due to radiation damage. A block shared by two groups probably only has tracks passing through a certain region of the block for a given group.

The block coefficients as determined for each group were used to define the shower quantity SHTRK depending on which PR block was hit as defined by tracking. If a track passed outside the central region defined earlier, then the PR block energy for the adjacent block was also added in to SHTRK. The contributions from the adjacent blocks in the second, third, and fourth layers for these cases was small, and were not included because it was desirable to discriminate between multiple particle events by including as few blocks as possible in the SHTRK calculation. The quantity SHTRK was

calculated for each track found by the tracking programs.

Average block coefficients were found by averaging the coefficients for the blocks which belonged to two groups. These coefficients were needed to calculate the shower quantity SHSUM which was independent of tracking, and thus the group coefficients were not applicable.

In order to obtain good calibration over the entire experiment, sets of different Y corrections and block coefficients were found at many momenta. Tests were done to eliminate as many of these sets as possible by using the
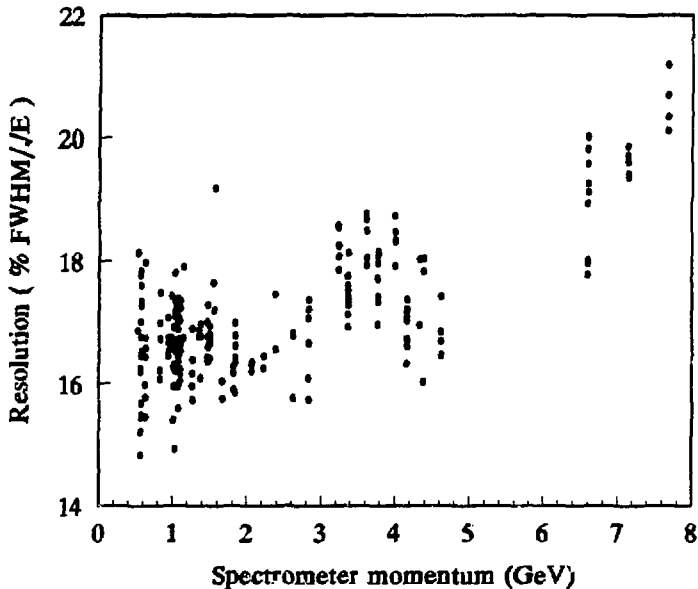
Figure B.3: Measured resolution of the 8 GeV spectrometer shower counter as a function of spectrometer momentum.

calibration from one data set on another data set and checking the degradation of shower resolution. It was found that four sets of coefficients was sufficient to minimize the overall resolution. The momentum ranges which the final sets covered were: $0.578 < E' < 1.095$, $1.095 < E' < 2.395$, $2.395 < E' <$ 3.995, and $3.995 < E' < 7.7$, here E' was the spectrometer momentum in GeV.

The measured SHTRK resolution for this detector was consistent with results achieved in previous experiments. Figure B.3 shows a plot of these resolutions calculated from a Gaussian fit to the SHTRK peak. The resolution as scaled by E' gets worse at high momentum as expected. The average FWHM resolution for the entire experiment was $17.5\%/\sqrt{E'}$.

APPENDIX C: RADIATIVE CORRECTIONS

The cross section formulas used for this experiment's data, such as the Rosenbluth cross section, assume that the only contributing process to the cross section is that of single photon exchange, or the Born approximation. This is the lowest order contributing process in α, the fine structure constant. There are, however, higher order electromagnetic processes in α which also contribute to the measured cross sections. The purpose of the radiative corrections was to correct the measured cross sections for most of these higher order processes. Radiative corrections were necessary for the aluminum cross sections used for the target endcap subtraction, for the proton inelastic cross sections used for formulating the proton inelastic model, and for the deuterium cross sections from which the neutron form factors were extracted. The radiative corrections for the proton inelastic data also included the subtraction of the proton elastic radiative tail.

In order to calculate radiative corrections and the proton radiative tail a good target model was necessary as well as cross section models for deuterium, elastic and inelastic hydrogen, and aluminum. The deuterium and the hydrogen inelastic models are discussed in great detail in the main text since they are also used for the form factor extraction. The remaining models will be discussed here as well as an in-depth summary of the formulas used for the radiative corrections.

Target Model

The purpose of the target model was to calculate the amount of material traversed by the electrons before and after scattering at any interaction point along the target length. A computer program which modeled the target was given the interaction point in the target for an electron scattering event and the desired scattering angle, and for the liquid targets, returned the radiation lengths traversed for the aluminum and the target materials separately. A summary of the target materials is given in Table 2.1 and Figure 2.2 shows the target assembly. The incap, or entrance region, for each liquid target was stamped out of a flat sheet of aluminum. The radius of curvature of the incap was 5.019 cm, and the depth of the curve was 0.528 cm for a central beam particle as indicated in Figure C.1. This figure shows a top view of a long liquid target. The incap dimensions for each of the four liquid targets was assumed to be the same. The endcap shape
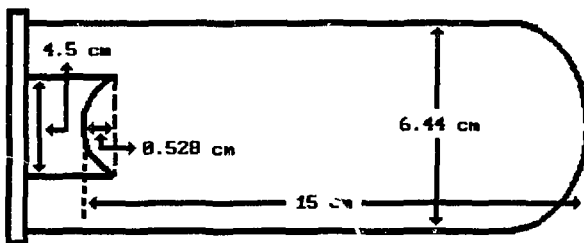
Figure C.1: Bird's eye view of a short target indicating important dimensions.

was measured and fit by an elliptical curve. The curve used for the inner target surface had semi-axes of 1.270 and 3.219 cm. The endcap in the region where the endcap meets the wall varied in thickness. To account for this thickness variation the outer target endcap surface was modeled using thickness measurements with three different elliptical fits depending on the point of exit of the scattered electron. A

Table C.1: Elliptical fits used for modelling outer endcap region.		
Intersection pt. along major axis (cm)	Semi-minor axis (cm)	Semi-major axis (cm)
$r \leq |2.20|$	1.2780	3.2290
$|2.20| < r \leq |2.95|$	1.2766	3.2344
$r > |2.95|$	1.2710	3.2443

summary of these ellipse fits is given in Table C.1. The endcap dimensions for each of the four liquid targets was assumed to be the same. The quantities determined by the target model were TB_{liq} and TB_{al} (B for before scattering) and TA_{liq} and TA_{al} (A for after scattering) in units of radiation length. The total radiation length for before and after scattering is given by $TB = TB_{liq} + TB_{al}$, $TA = TA_{liq} + TA_{al}$, and $T_{tot} = TB + TA$.

Proton Elastic Cross Section Model

The proton elastic cross section model used for the calculation of the elastic radiative tail was a simple Rosenbluth formula which used input form factors. The form factors used were consistent with the values measured in this

experiment. $G_{Ep}(Q^2)$ followed the dipole form and $G_{Mp}(Q^2)$ followed the fit of Gari and Krümpelmann [84].

Aluminum Cross Section Model

Aluminum cross section calculations due to Liuti [99] were used for creating the model aluminum cross section. These model cross sections were in good agreement with the measured data in this experiment [66]. The calculations [100] included a quasielastic contribution calculated using a plane wave impulse approximation with light cone dynamics, and an inelastic contribution calculated by convoluting the spectral function for aluminum with the nucleon structure functions. These calculations also include two-nucleon correlations. The cross section model used merely interpolated between the calculated cross sections points.

Radiative Corrections

The higher order radiative processes in α can be broken up into two main categories. These categories are listed below along with their contributing processes.

1. Internal effects are those which occur during the scattering process.

   A. Internal bremsstrahlung refers to the emission of photons in the field of the nucleus during the scattering process. Only electron bremsstrahlung effects were taken into account for these calculations.

   B. Vacuum polarization refers to the production and annihilation of a particle-antiparticle pair from

the photon propagator. Loops considered include electron, muon, tau, and quark pairs where five types of quarks were included (The top quark was neglected).

C. Vertex processes refer to the emission and absorption of a secondary photon about the vertex at which the exchanged photon is emitted or absorbed.

D. Multiple photon exchange refers to processes involving the exchange of more than one photon.

E. Soft multiple photon emission refers to the emission of many very low energy photons during the scattering process.

2. External processes are those which occur either before or after the scattering process takes place and involve

Vacuum polarization   Electron vertex   Nucleus vertex
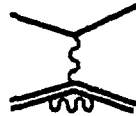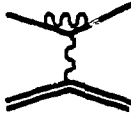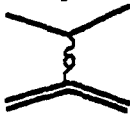
Internal bremsstrahlung
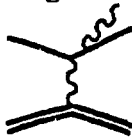
Two-photon exchange
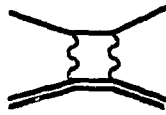
C.2: Feynman diagrams for the lowest order radiative processes contributing to the measured cross sections.

interactions with other nuclei.

A. External bremsstrahlung refers to the emission of photons from the incident or scattered electron in the target material.

B. Ionization energy losses refer to the electron energy lost due to ion producing interactions in the medium traversed.

Figure C.2 gives a schematic of the most important of the internal processes. The formalism used for the calculation of radiative corrections was that of Mo and Tsai [101] [102] with several improvements and corrections as noted by Walker [103]. Walker's corrections were for elastic radiative corrections, but much of this was carried over to the quasielastic and inelastic radiative corrections presented here. The process of calculating the radiative corrections is an iterative procedure. After each iteration, the data were fit and the input models were adjusted accordingly. The iterations continued until the radiative corrections converged. All radiative corrections were lumped together in a single correction, RC, defined:

$$RC = \frac{\sigma(E, E')}{\sigma_R(E, E')},$$ (C.1)

where $\sigma(E, E')$ is the calculated unradiated differential cross section (model cross section) and $\sigma_R(E, E')$ is the calculated radiated cross section. RC multiplied the data which were basically the measured radiated cross sections in order to obtain the measured unradiated cross section. RC was

calculated for each kinematic point as a function of W^2 (which is equivalent to E') and for several values of θ within each spectrometer's acceptance.

The internal bremsstrahlung effect was modeled using the method of equivalent radiators. One radiator was effectively placed before the scattering vertex and one after, and each of the equivalent radiators was assigned a thickness

$$T_{EQ} = \left(\frac{\alpha}{b\pi}\right)\left[\ln\left(\frac{Q^2}{M_e^2} - 1\right)\right], \qquad (\text{C}.2)$$

which is in units of radiation lengths and where

$$b = \frac{4}{3}\left[1 + \frac{1}{9}\left(\frac{Z+1}{Z+\eta}\right)(\ln(184.15Z^{-1/3}))^{-1}\right], \quad \eta = \frac{\ln(1194Z^{-2/3})}{\ln(184.15Z^{-1/3})}. \qquad (\text{C}.3)$$

Z is the atomic number of the target material and M_e is the electron mass. The amounts of radiator material before and after scattering are now defined to be $TB_{EQ} = TB + T_{EQ}$ and $TA_{EQ} = TA + T_{EQ}$.

The complete formula used to calculated the radiated cross section in the peaking approximation is given by

$$\sigma_R(E, E') = \left(\frac{R\Delta}{E}\right)^{bTB_{EQ}}\left(\frac{\Delta}{E'}\right)^{bTA_{EQ}}\left(1 - \frac{\xi}{(1-bT_{tot})\Delta}\right)\sigma(E, E')F(Q^2, T_{tot})$$

$$+ \int_{E_{min}}^{E-R\Delta} (r^{bTA_{EQ}}S^{bTB_{EQ}})\left(\frac{bTB_{EQ}\phi(s)}{sE} + \frac{\xi}{2(sE)^2}\right)\sigma(\epsilon, E')F(Q^2, T_{tot})d\epsilon \quad (\text{C}.4)$$

$$+ \int_{E'+\Delta}^{E'_{max}} (u^{bTB_{EQ}}V^{bTA_{EQ}})\left(\frac{bTA_{EQ}\phi(v)}{vE'} + \frac{\xi}{2(vE')^2}\right)\sigma(E, \epsilon')F(Q^2, T_{tot})d\epsilon'$$

where

$$r = \frac{(E-\epsilon)}{E'R}, \quad s = \frac{(E-\epsilon)}{E}, \quad u = \frac{(\epsilon'-E')}{E}, \quad v = \frac{(\epsilon'-E')}{E'},$$

$$R = \frac{(M_p + 2E\sin^2(\frac{\theta}{2}))}{(M_p - 2E'\sin^2(\frac{\theta}{2}))}, \quad \xi = 154\frac{Z}{A}T_{tot}X_0 \quad (GeV),$$

(C.5)

and M_p is the proton mass, A is the atomic mass, X_0 is the unit radiation length of the target material, and ξ is the Landau straggling parameter for the ionization energy loss contributions. Δ is an integration parameter needed because the integrals are improper. If Δ is chosen according to the directions given by Tsai then the calculation should be independent of Δ. The terms containing the function φ in the $\sigma_R(E,E')$ calculation represent the effects due to bremsstrahlung. The shape of the bremsstrahlung distribution is given by [104]

$$\dot{\phi}(y) = 4\alpha r_0^2 \left\{ \left(\frac{4}{3} - \frac{4}{3}y + y^2\right)\left[Z^2(L_{rad} - f(\alpha Z)) + ZL'_{rad}\right] + \frac{1}{9}(1-y)(Z^2+Z) \right\},$$

(C.6)

where f is the Coulomb correction,

$$f(\alpha Z) = 1.202(\alpha Z)^2 - 1.0369(\alpha Z)^4 + \frac{1.008(\alpha Z)^6}{1+(\alpha Z)^2},$$

(C.7)

and r_0 was defined such that $\varphi(0)$ was normalized to 1.0. For Z = 1, the parameter L_{rad} was 5.310 and L'_{rad} was 6.144, while for Z = 13, L_{rad} was 4.361 and L'_{rad} was 5.375. The quantities E_{min} and E'_{max} in the integration limits are the kinematically allowed extremes for the interaction to take place due to

energy conservation:

$$E_{min} = \frac{M_p E'}{M_p - 2E' \sin^2(\frac{\theta}{2})} \ , \quad E'_{max} = \frac{M_p E}{M_p + 2E \sin^2(\frac{\theta}{2})} \ . \quad (C.8)$$

Finally, the function $F(Q^2, T_{tot})$ is expressed as

$$F(Q^2, T_{tot}) = 1.0 + 0.5772bT_{tot} - 0.66(bT_{tot})^2 - \frac{\alpha}{2\pi}\left[\ln(\frac{E}{E'})\right]^2 -$$
$$\frac{\alpha}{\pi}\left[\frac{\pi^2}{6} - \Phi(\cos^2(\frac{\theta}{2}))\right] + \delta_{vac} + \delta_{vertex}, \quad (C.9)$$

where the Spence function, $\Phi(x)$, is defined as

$$\Phi(x) = \int_0^x \frac{-\ln|1-y|}{y} dy \ . \quad (C.10)$$

The contribution from vacuum polarization for producing a particle and anti-particle of mass M is given by

$$\delta_{vac}(M) = \frac{2\alpha}{\pi}\left[-\frac{5}{9} + \frac{M^2}{Q^2} + \left(\frac{1}{3} - \frac{2}{3}\frac{M^2}{Q^2}\right)\sqrt{1 + \frac{4M^2}{Q^2}}\ln\left(\frac{Q^2}{4M^2}\left(1 + \sqrt{1 + \frac{4M^2}{Q^2}}\right)^2\right)\right].$$

Vacuum polarization contributions were calculated for electron, muon, and tau loops,

$$\delta_{vac}^{lepton} = \delta_{vac}(M_e) + \delta_{vac}(M_\mu) + \delta_{vac}(M_\tau) \ . \quad (C.12)$$

The vacuum polarization contributions due to quarks was obtained using the parameterization given by the TASSO collaboration [105] which is valid for $1.0 \leq Q^2 \leq 64.0$ $(GeV/c)^2$:

$$\delta_{vac}^{quark} = 2(0.001512 + 0.002822\ln(1 + 1.218Q^2)) \quad (C.13)$$

The non-divergent contribution from the electron vertex diagram is given by

$$\delta_{VERTEX} = \frac{2\alpha}{\pi}\left[-1 + \frac{3}{4}\ln\left(\frac{Q^2}{M_{e}^2}\right)\right]. \tag{C.14}$$

The divergent, infrared terms (terms which are evaluated in the limit as the photon 4-momentum approaches 0 and exhibit a logarithmic divergence) from this process and others can be shown to cancel [102]. The observable contribution from the nucleus vertex diagram was assumed to be negligible. It should be noted that contributions due to two-photon exchange were not included in the radiative corrections. This is probably the biggest source of error in the corrections.

The θ-dependence of the radiative corrections for each spectrometer is shown in figure C.3. These sample plots show the radiative corrections plotted against the θ acceptance of each of the spectrometers and are normalized to the central scattering angle. The θ dependence was quite significant for the 1.6 GeV spectrometer because of the large θ acceptance. The sudden change in the correction at large θ for the 1.6 GeV spectrometer is due to the presence of the tungsten shields and the strong correlation between detected particle's scattering angle and the position of its interaction point within the target.

Proton Radiative Tail

The proton elastic radiative tail extends from the elastic peak region into the inelastic, or pion production

Radiative correction θ dependence
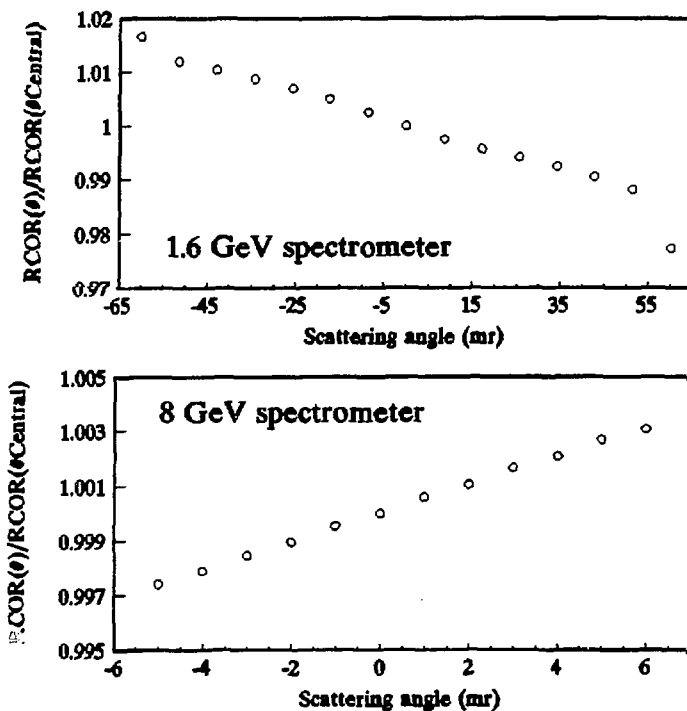
Figure C.3: The θ dependence of the radiative corrections for each spectrometer plotted against each spectrometer's θ acceptance.

region. This contribution must be calculated and subtracted in order to study the inelastic data. A study was also made of the radiative tail from the elastic deuterium peak. This tail tends to rise again after its initial descent from the elastic peak and can become significant in the deep inelastic region. However, this tail was found to be completely negligible for

the kinematic region corresponding to the data measured in this experiment.

The proton elastic radiative tail was calculated using the formula, which is exact to lowest order in α, due to Tsai [102]. The quantities s, p and k refer to the four-momenta of the incident and scattered electron and the photon respectively. The quantities t and p_r are the four momenta of the initial and final target particle states. This formula was calculated in the coordinate system where $u = s+t-p = k+p_r$ is along the z-axis and s and p are in the x-z plane. This choice was made to simplify the azimuthal angle integration. θ_k is the angle between u and k. The cross section formula for the tail is:

$$\frac{d^2\sigma}{d\Omega dE'} = \sigma_{soft} + \frac{\alpha^3}{2\pi}\frac{E'}{E}\int_{-1}^{1}\frac{2M_p\omega \ d(\cos\theta_k)}{Q^4(u_0 - |\vec{u}|\cos\theta_k)}\cdot F(Q^2, T_{tot})$$

$$(W_2(Q^2)\cdot T1(\cos\theta_k) + W_1(Q^2)\cdot T2(\cos\theta_k)),$$

$$T1(\cos\theta_k) = \frac{-am_e^2}{x^3}\left[2E(E'+\omega) + \frac{Q^2}{2}\right] - \frac{a'}{y^3}\left[2E'(E-\omega) + \frac{Q^2}{2}\right] - 2 +$$

$$2\nu\left(\frac{1}{x} - \frac{1}{y}\right)\left[m_e^2(s\cdot p - \omega^2) + (s\cdot p)(2EE' - (s\cdot p) + \omega(E-E'))\right] +$$

$$\left(\frac{1}{x} - \frac{1}{y}\right)\left[2EE' + \frac{Q^2}{2} - (s\cdot p) - m_e^2\right] + \left[\frac{E\omega + E'^2}{x} - \frac{E' + E^2}{y}\right],$$

$$T2(\cos\theta_k) = \left(\frac{a}{x^3} - \frac{a'}{y^3}\right)m_e^2(2m_e^2 + Q^2) + 4 +$$

$$\left(\frac{1}{x} - \frac{1}{y}\right)(4\nu(s\cdot p)(s\cdot p - 2m_e^2) + 2s\cdot p + 2m_e^2 - Q^2).$$

where σ_{soft} is the first term appearing in Eq. C.4, and the remaining kinematic variables are defined by:

$$u = s + t - p = p_f + k, \quad u_0 = E + M_p - E', \quad |\vec{u}| = \sqrt{u_0^2 - u^2},$$

$$\omega = \frac{1}{2}\left(\frac{u^2 - M_p^2}{u_0 - |\vec{u}|\cos\theta_k}\right), \quad u^2 = 2m_e^2 + M_p^2 - 2(s \cdot p) + 2M_p(E - E'),$$

$$Q^2 = 2m_e^2 - 2(s \cdot p) - 2\omega(E - E') + 2\omega|\vec{u}|\cos\theta_k,$$

$$a = \omega(E' - |\vec{p}|\cos\theta_p\cos\theta_k), \quad a' = \omega(E - |\vec{s}|\cos\theta_s\cos\theta_k),$$

$$\cos\theta_p = \frac{|\vec{s}|\cos\theta - |\vec{p}|}{|\vec{u}|}, \quad \cos\theta_s = \frac{|\vec{s}| - |\vec{p}|\cos\theta}{|\vec{u}|},$$

$$\nu = \left(\frac{1}{a'} - \frac{1}{a}\right), \quad x = \sqrt{a^2 - b^2}, \quad y = \sqrt{a'^2 - b^2}.$$

$$\cos\theta_k = \frac{1}{\sin\theta}\left[\frac{E}{|\vec{s}|}\sin\theta_p - \frac{E'}{|\vec{p}|}\sin\theta_s\right]$$

The quantities $W_1(Q^2)$ and $W_2(Q^2)$ are the structure functions
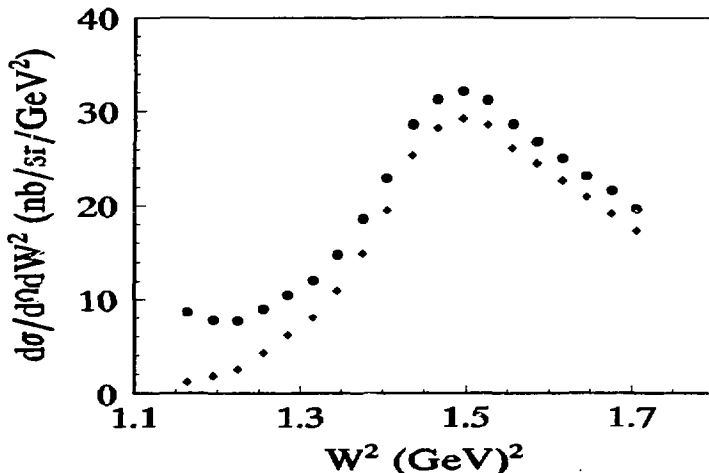
Figure C.4: Sample inelastic hydrogen plot showing the effect of the radiative tail subtraction. These data were taken at E = 5.507 GeV and Q^2 = 1.75 (geV/c)^2.

for the proton in the elastic limit (equivalent to form factors). The radiative tail from the deuteron elastic peak is calculated with the same formula using $W_1(Q^2)$ and $W_2(Q^2)$ for the deuteron. Figure C.4 shows a sample inelastic hydrogen cross spectrum before and after the subtraction of the elastic radiative tail. It is clear that the cross sections which have had the tail subtracted clearly fall to zero, as expected, at the pion threshold of $W^2 = 1.15$ GeV².

APPENDIX D: DEUTERIUM CROSS SECTIONS

All of the following tables contain results for the meas red deuterium cross sections as a function of W^2. Cross section and errors are in $nb/sr/GeV^2$. ERR1 is the statistical error, ERR2 is the total error, and R_c is the applied radiative correction.

Table D.1: 8 GeV spectrometer data
$Q^2 = 1.750$ $(GeV/c)^2$, $E = 1.511$ GeV, TH $= 90.067°$.

W^2	$d\sigma/d\Omega dW^2$	ERR1	ERR2	R_c
0.775	1.65E-01	0.80E-02	0.86E-02	1.280
0.805	2.06E-01	0.54E-02	0.66E-02	1.270
0.835	2.58E-01	0.56E-02	0.74E-02	1.251
0.865	2.99E-01	0.64E-02	0.86E-02	1.219
0.895	2.99E-01	0.67E-02	0.87E-02	1.176
0.925	2.94E-01	0.57E-02	0.80E-02	1.122
0.955	2.82E-01	0.60E-02	0.80E-02	1.056
0.985	2.02E-01	0.10E-01	0.11E-01	0.988
1.015	1.96E-01	0.12E-01	0.12E-01	0.922
1.045	1.59E-01	0.77E-02	0.82E-02	0.861
1.075	1.55E-01	0.70E-02	0.76E-02	0.810
1.105	1.34E-01	0.63E-02	0.67E-02	0.773
1.135	1.25E-01	0.62E-02	0.66E-02	0.753
1.165	1.29E-01	0.68E-02	0.72E-02	0.752
1.195	1.19E-01	0.12E-01	0.12E-01	0.768

Table D.2: 8 GeV spectrometer data
Q² = 1.750 (GeV/c)², E = 1.968 GeV, TH = 55.209°.

W²	dσ/dΩdW²	ERR1	ERR2	R_c
0.565	1.06E-01	0.23E-01	0.23E-01	1.334
0.595	1.03E-01	0.52E-02	0.56E-02	1.337
0.625	1.38E-01	0.42E-02	0.49E-02	1.339
0.655	1.79E-01	0.44E-02	0.56E-02	1.341
0.685	2.41E-01	0.50E-02	0.67E-02	1.342
0.715	3.09E-01	0.52E-02	0.77E-02	1.343
0.745	4.24E-01	0.58E-02	0.98E-02	1.341
0.775	5.59E-01	0.67E-02	0.12E-01	1.337
0.805	7.17E-01	0.77E-02	0.16E-01	1.327
0.835	8.66E-01	0.89E-02	0.19E-01	1.307
0.865	9.79E-01	0.15E-01	0.24E-01	1.274
0.895	1.01E+00	0.22E-01	0.29E-01	1.229
0.925	9.83E-01	0.18E-01	0.26E-01	1.174
0.955	8.67E-01	0.21E-01	0.27E-01	1.107
0.985	6.49E-01	0.41E-01	0.43E-01	1.039
1.015	6.41E-01	0.17E-01	0.21E-01	0.973
1.045	5.33E-01	0.11E-01	0.15E-01	0.914
1.075	4.39E-01	0.96E-02	0.13E-01	0.865
1.105	3.89E-01	0.87E-02	0.11E-01	0.831
1.135	3.68E-01	0.83E-02	0.11E-01	0.814
1.165	3.63E-01	0.85E-02	0.11E-01	0.817
1.195	3.80E-01	0.91E-02	0.12E-01	0.838
1.225	3.98E-01	0.11E-01	0.13E-01	0.872
1.255	4.57E-01	0.27E-01	0.28E-01	0.914

Table D.3: 8 GeV spectrometer data
$Q^2 = 1.750$ (GeV/c)^2, E = 2.407 GeV, TH = 41.111°.

W^2	$d\sigma/d\Omega dW^2$	ERR1	ERR2	R_c
0.475	9.03E-02	0.13E-01	0.13E-01	1.370
0.505	1.17E-01	0.10E-01	0.10E-01	1.373
0.535	1.30E-01	0.93E-02	0.96E-02	1.377
0.565	1.79E-01	0.10E-01	0.11E-01	1.380
0.595	2.22E-01	0.11E-01	0.12E-01	1.382
0.625	3.09E-01	0.13E-01	0.14E-01	1.384
0.655	3.80E-01	0.14E-01	0.16E-01	1.386
0.685	5.07E-01	0.16E-01	0.18E-01	1.387
0.715	6.73E-01	0.13E-01	0.18E-01	1.388
0.745	9.10E-01	0.12E-01	0.21E-01	1.386
0.775	1.17E+00	0.13E-01	0.25E-01	1.381
0.805	1.50E+00	0.14E-01	0.32E-01	1.370
0.835	1.78E+00	0.16E-01	0.37E-01	1.350
0.865	2.05E+00	0.25E-01	0.46E-01	1.315
0.895	2.10E+00	0.31E-01	0.51E-01	1.269
0.925	1.99E+00	0.17E-01	0.41E-01	1.213
0.955	1.79E+00	0.16E-01	0.37E-01	1.146
0.985	1.51E+00	0.15E-01	0.32E-01	1.078
1.015	1.26E+00	0.15E-01	0.28E-01	1.013
1.045	1.05E+00	0.24E-01	0.31E-01	0.955
1.075	9.41E-01	0.43E-01	0.47E-01	0.908
1.105	8.57E-01	0.22E-01	0.27E-01	0.875
1.135	7.69E-01	0.17E-01	0.23E-01	0.859
1.165	7.31E-01	0.16E-01	0.21E-01	0.863
1.195	7.17E-01	0.16E-01	0.21E-01	0.883
1.225	7.68E-01	0.16E-01	0.22E-01	0.918
1.255	8.89E-01	0.18E-01	0.25E-01	0.959
1.285	9.92E-01	0.20E-01	0.27E-01	1.002
1.315	1.12E+00	0.22E-01	0.31E-01	1.041
1.345	1.30E+00	0.26E-01	0.36E-01	1.074
1.375	1.55E+00	0.40E-01	0.49E-01	1.098
1.405	1.66E+00	0.12E+00	0.13E+00	1.114

```
Table D.4:   8 GeV spectrometer data
Q² = 1.750 (GeV/c)², E = 5.507 GeV, TH = 15.146°.
```

W²	dσ/dΩdW²	ERR1	ERR2	R_c
0.355	4.62E-01	0.10E+00	0.11E+00	1.520
0.385	4.74E-01	0.78E-01	0.79E-01	1.525
0.415	5.65E-01	0.64E-01	0.65E-01	1.531
0.445	8.65E-01	0.68E-01	0.70E-01	1.536
0.475	9.39E-01	0.65E-01	0.68E-01	1.541
0.505	1.20E+00	0.64E-01	0.68E-01	1.546
0.535	1.59E+00	0.71E-01	0.77E-01	1.550
0.565	2.12E+00	0.78E-01	0.88E-01	1.553
0.595	2.61E+00	0.88E-01	0.10E+00	1.556
0.625	3.32E+00	0.97E-01	0.12E+00	1.559
0.655	4.42E+00	0.11E+00	0.14E+00	1.561
0.685	5.62E+00	0.12E+00	0.16E+00	1.562
0.715	7.62E+00	0.14E+00	0.20E+00	1.562
0.745	1.02E+01	0.16E+00	0.25E+00	1.560
0.775	1.27E+01	0.18E+00	0.30E+00	1.554
0.805	1.68E+01	0.21E+00	0.38E+00	1.541
0.835	2.06E+01	0.23E+00	0.46E+00	1.516
0.865	2.32E+01	0.35E+00	0.55E+00	1.475
0.895	2.36E+01	0.36E+00	0.58E+00	1.422
0.925	2.25E+01	0.25E+00	0.50E+00	1.358
0.955	1.99E+01	0.21E+00	0.43E+00	1.283
0.985	1.64E+01	0.18E+00	0.36E+00	1.207
1.015	1.35E+01	0.16E+00	0.30E+00	1.135
1.045	1.13E+01	0.14E+00	0.26E+00	1.072
1.075	9.70E+00	0.13E+00	0.22E+00	1.021
1.105	8.61E+00	0.13E+00	0.21E+00	0.987
1.135	7.67E+00	0.13E+00	0.20E+00	0.972
1.165	7.54E+00	0.14E+00	0.20E+00	0.977
1.195	7.48E+00	0.16E+00	0.21E+00	1.001
1.225	7.57E+00	0.19E+00	0.23E+00	1.039
1.255	8.61E+00	0.20E+00	0.26E+00	1.084
1.285	9.45E+00	0.21E+00	0.28E+00	1.130
1.315	1.06E+01	0.23E+00	0.31E+00	1.173
1.345	1.17E+01	0.25E+00	0.33E+00	1.208
1.375	1.26E+01	0.26E+00	0.36E+00	1.235
1.405	1.45E+01	0.29E+00	0.40E+00	1.253
1.435	1.54E+01	0.30E+00	0.42E+00	1.262
1.465	1.69E+01	0.32E+00	0.46E+00	1.263
1.495	1.77E+01	0.33E+00	0.47E+00	1.257
1.525	1.79E+01	0.34E+00	0.48E+00	1.246
1.555	1.82E+01	0.36E+00	0.50E+00	1.232
1.585	1.89E+01	0.38E+00	0.53E+00	1.215
1.615	1.81E+01	0.42E+00	0.55E+00	1.197
1.645	1.87E+01	0.52E+00	0.63E+00	1.179
1.675	1.84E+01	0.68E+00	0.76E+00	1.163
1.705	1.65E+01	0.11E+01	0.11E+01	1.148
1.735	1.49E+01	0.47E+01	0.47E+01	1.135

```
┌─────────────────────────────────────────────────────────────┐
│ Table D.5:   8 GeV spectrometer data                        │
│ Q² = 2.500 (GeV/c)², E = 1.968 GeV, TH = 89.949°.           │
├─────────────────────────────────────────────────────────────┤
```

W²	dσ/dΩdW²	ERR1	ERR2	R_c
0.720	3.00E-02	0.51E-02	0.51E-02	1.268
0.760	3.72E-02	0.26E-02	0.27E-02	1.262
0.800	4.29F-02	0.25E-02	0.27E-02	1.249
0.840	4.65E-02	0.25E-02	0.27E-02	1.220
0.880	5.67E-02	0.30E-02	0.32E-02	1.180
0.920	5.64E-02	0.28E-02	0.30E-02	1.129
0.960	5.89E-02	0.31E-02	0.33E-02	1.071
1.000	3.45E-02	0.43E-02	0.43E-02	0.997

```
┌─────────────────────────────────────────────────────────────┐
│ Table D.6:   8 GeV spectrometer data                        │
│ Q² = 2.500 (GeV/c)², E = 2.407 GeV, TH = 58.883°.           │
├─────────────────────────────────────────────────────────────┤
```

W²	dσ/dΩdW²	ERR1	ERR2	R_c
0.680	4.25E-02	0.60E-02	0.60E-02	1.320
0.720	7.17E-02	0.22E-02	0.26E-02	1.318
0.760	1.00E-01	0.19E-02	0.27E-02	1.312
0.800	1.25E-01	0.20E-02	0.31E-02	1.298
0.840	1.49E-01	0.21E-02	0.35E-02	1.269
0.880	1.59E-01	0.38E-02	0.49E-02	1.229
0.920	1.64E-01	0.22E-02	0.38E-02	1.180
0.960	1.51E-01	0.21E-02	0.35E-02	1.125
1.000	1.35E-01	0.22E-02	0.33E-02	1.056
1.040	1.15E-01	0.34E-02	0.41E-02	0.995
1.080	1.09E-01	0.65E-02	0.68E-02	0.946
1.120	9.20E-02	0.34E-02	0.38E-02	0.916
1.160	8.59E-02	0.30E-02	0.34E-02	0.906
1.200	9.33E-02	0.30E-02	0.35E-02	0.916
1.240	9.41E-02	0.30E-02	0.35E-02	0.942
1.280	1.05E-01	0.33E-02	0.39E-02	0.974
1.320	1.25E-01	0.39E-02	0.45E-02	1.007
1.360	1.46E-01	0.51E-02	0.58E-02	1.034
1.400	1.85E-01	0.15E-01	0.16E-01	1.053

Table D.7:   8 GeV spectrometer data
$Q^2 = 2.500$ $(GeV/c)^2$, $E = 2.837$ GeV, TH = 44.994°.

W^2	$d\sigma/d\Omega dW^2$	ERR1	ERR2	R_c
0.440	2.19E-02	0.76E-02	0.76E-02	1.347
0.480	2.34E-02	0.31E-02	0.31E-02	1.350
0.520	3.61E-02	0.29E-02	0.30E-02	1.353
0.560	4.94E-02	0.32E-02	0.33E-02	1.356
0.600	6.28E-02	0.35E-02	0.37E-02	1.359
0.640	8.10E-02	0.39E-02	0.42E-02	1.361
0.680	1.16E-01	0.34E-02	0.41E-02	1.361
0.720	1.52E-01	0.31E-02	0.42E-02	1.359
0.760	2.04E-01	0.33E-02	0.50E-02	1.353
0.800	2.54E-01	0.36E-02	0.60E-02	1.339
0.840	3.02E-01	0.39E-02	0.69E-02	1.308
0.880	3.32E-01	0.72E-02	0.95E-02	1.267
0.920	3.32E-01	0.45E-02	0.77E-02	1.217
0.960	3.05E-01	0.42E-02	0.71E-02	1.161
1.000	2.62E-01	0.42E-02	0.65E-02	1.091
1.040	2.32E-01	0.44E-02	0.62E-02	1.031
1.080	2.01E-01	0.75E-02	0.84E-02	0.983
1.120	1.98E-01	0.12E-01	0.12E-01	0.953
1.160	1.76E-01	0.70E-02	0.78E-02	0.945
1.200	1.82E-01	0.64E-02	0.73E-02	0.957
1.240	1.88E-01	0.64E-02	0.73E-02	0.984
1.280	2.08E-01	0.67E-02	0.78E-02	1.017
1.320	2.41E-01	0.74E-02	0.87E-02	1.050
1.360	2.65E-01	0.80E-02	0.95E-02	1.078
1.400	3.27E-01	0.94E-02	0.11E-01	1.097
1.440	3.57E-01	0.11E-01	0.13E-01	1.106
1.480	4.09E-01	0.21E-01	0.22E-01	1.107

Table D.8: 8 GeV spectrometer data
$Q^2 = 2.500$ $(GeV/c)^2$, E = 5.507 GeV, TH = 18.981°.

W^2	$d\sigma/d\Omega dW^2$	ERR1	ERR2	R_c
0.080	1.68E-02	0.67E-02	0.67E-02	1.451
0.120	2.57E-02	0.62E-02	0.62E-02	1.456
0.160	5.47E-02	0.74E-02	0.75E-02	1.462
0.200	6.71E-02	0.75E-02	0.76E-02	1.468
0.240	5.30E-02	0.67E-02	0.68E-02	1.474
0.280	7.36E-02	0.78E-02	0.80E-02	1.480
0.320	1.12E-01	0.91E-02	0.93E-02	1.486
0.360	1.30E-01	0.97E-02	0.10E-01	1.491
0.400	1.55E-01	0.10E-01	0.11E-01	1.496
0.440	1.92E-01	0.11E-01	0.11E-01	1.500
0.480	2.53E-01	0.10E-01	0.11E-01	1.504
0.520	3.49E-01	0.11E-01	0.12E-01	1.507
0.560	4.50E-01	0.11E-01	0.14E-01	1.510
0.600	5.88E-01	0.11E-01	0.16E-01	1.513
0.640	8.01E-01	0.12E-01	0.20E-01	1.515
0.680	1.04E+00	0.14E-01	0.24E-01	1.516
0.720	1.35E+00	0.16E-01	0.30E-01	1.513
0.760	1.81E+00	0.18E-01	0.39E-01	1.505
0.800	2.24E+00	0.21E-01	0.48E-01	1.489
0.840	2.69E+00	0.24E-01	0.57E-01	1.452
0.880	2.91E+00	0.52E-01	0.76E-01	1.406
0.920	2.84E+00	0.27E-01	0.61E-01	1.349
0.960	2.63E+00	0.22E-01	0.55E-01	1.284
1.000	2.29E+00	0.19E-01	0.48E-01	1.211
1.040	1.94E+00	0.17E-01	0.41E-01	1.145
1.080	1.68E+00	0.15E-01	0.35E-01	1.095
1.120	1.50E+00	0.15E-01	0.32E-01	1.065
1.160	1.39E+00	0.14E-01	0.30E-01	1.058
1.200	1.43E+00	0.16E-01	0.31E-01	1.073
1.240	1.50E+00	0.19E-01	0.34E-01	1.102
1.280	1.64E+00	0.22E-01	0.38E-01	1.139
1.320	1.80E+00	0.29E-01	0.44E-01	1.175
1.360	2.07E+00	0.31E-01	0.50E-01	1.205
1.400	2.23E+00	0.34E-01	0.54E-01	1.225
1.440	2.41E+00	0.36E-01	0.58E-01	1.236
1.480	2.65E+00	0.38E-01	0.63E-01	1.237
1.520	2.88E+00	0.41E-01	0.69E-01	1.232
1.560	2.99E+00	0.45E-01	0.72E-01	1.221
1.600	3.10E+00	0.52E-01	0.79E-01	1.207
1.640	3.18E+00	0.66E-01	0.89E-01	1.192
1.680	3.21E+00	0.97E-01	0.11E+00	1.179
1.720	2.85E+00	0.22E+00	0.22E+00	1.167

Table D.9: 8 GeV spectrometer data
$Q^2 = 3.250$ $(GeV/c)^2$, $E = 2.837$ GeV, $TH = 61.206°$.

W^2	$d\sigma/d\Omega dW^2$	ERR1	ERR2	R_c
0.475	4.35E-03	0.76E-03	0.77E-03	1.293
0.525	6.66E-03	0.71E-03	0.72E-03	1.297
0.575	8.41E-03	0.73E-03	0.75E-03	1.300
0.625	1.16E-02	0.83E-03	0.86E-03	1.301
0.675	1.79E-02	0.78E-03	0.85E-03	1.301
0.725	2.32E-02	0.66E-03	0.79E-03	1.296
0.775	2.98E-02	0.69E-03	0.89E-03	1.285
0.825	3.65E-02	0.76E-03	0.10E-02	1.254
0.875	4.05E-02	0.11E-02	0.13E-02	1.215
0.925	3.99E-02	0.88E-03	0.12E-02	1.168
0.975	3.95E-02	0.87E-03	0.11E-02	1.117
1.025	3.50E-02	0.90E-03	0.11E-02	1.052
1.075	3.26E-02	0.16E-02	0.17E-02	1.000
1.125	2.99E-02	0.21E-02	0.22E-02	0.967
1.175	2.67E-02	0.12E-02	0.13E-02	0.956
1.225	3.03E-02	0.12E-02	0.13E-02	0.966
1.275	3.20E-02	0.13E-02	0.14E-02	0.987
1.325	3.68E-02	0.13E-02	0.15E-02	1.013
1.375	4.30E-02	0.15E-02	0.17E-02	1.034
1.425	5.00E-02	0.18E-02	0.20E-02	1.048
1.475	5.88E-02	0.33E-02	0.34E-02	1.052

Table D.10: 8 GeV spectrometer data
Q^2 = 3.250 (GeV/c)^2, E = 5.507 GeV, TH = 22.805°.

W^2	$d\sigma/d\Omega dW^2$	ERR1	ERR2	R_c
0.425	6.56E-02	0.11E-01	0.11E-01	1.461
0.475	7.46E-02	0.55E-02	0.56E-02	1.465
0.525	9.51E-02	0.43E-02	0.47E-02	1.468
0.575	1.32E-01	0.41E-02	0.48E-02	1.471
0.625	1.77E-01	0.42E-02	0.54E-02	1.472
0.675	2.41E-01	0.46E-02	0.65E-02	1.471
0.725	3.20E-01	0.52E-02	0.80E-02	1.466
0.775	4.01E-01	0.57E-02	0.95E-02	1.452
0.825	4.81E-01	0.62E-02	0.11E-01	1.416
0.875	5.51E-01	0.11E-01	0.15E-01	1.371
0.925	5.47E-01	0.64E-02	0.12E-01	1.319
0.975	5.03E-01	0.55E-02	0.11E-01	1.264
1.025	4.60E-01	0.50E-02	0.10E-01	1.195
1.075	3.98E-01	0.45E-02	0.88E-02	1.143
1.125	3.69E-01	0.44E-02	0.82E-02	1.111
1.175	3.57E-01	0.45E-02	0.81E-02	1.104
1.225	3.57E-01	0.51E-02	0.84E-02	1.118
1.275	3.83E-01	0.61E-02	0.95E-02	1.144
1.325	4.14E-01	0.75E-02	0.11E-01	1.172
1.375	4.77E-01	0.87E-02	0.13E-01	1.196
1.425	5.27E-01	0.94E-02	0.14E-01	1.211
1.475	5.95E-01	0.10E-01	0.15E-01	1.216
1.525	6.48E-01	0.11E-01	0.17E-01	1.214
1.575	6.73E-01	0.13E-01	0.18E-01	1.207
1.625	7.22E-01	0.16E-01	0.21E-01	1.197
1.675	7.18E-01	0.23E-01	0.27E-01	1.187
1.725	7.55E-01	0.55E-01	0.56E-01	1.179

Table D.11: 8 GeV spectrometer data
$Q^2 = 4.000$ (GeV/c)^2, E = 5.507 GeV, TH = 26.823°.

W^2	dσ/dΩdW^2	ERR1	ERR2	R$_c$
0.425	1.87E-02	0.32E-02	0.32E-02	1.426
0.475	1.98E-02	0.16E-02	0.16E-02	1.429
0.525	3.01E-02	0.13E-02	0.14E-02	1.432
0.575	3.91E-02	0.12E-02	0.14E-02	1.433
0.625	5.06E-02	0.12E-02	0.15E-02	1.434
0.675	6.60E-02	0.13E-02	0.18E-02	1.431
0.725	8.41E-02	0.14E-02	0.21E-02	1.423
0.775	9.97E-02	0.15E-02	0.24E-02	1.412
0.825	1.14E-01	0.16E-02	0.27E-02	1.372
0.875	1.25E-01	0.27E-02	0.36E-02	1.335
0.925	1.32E-01	0.18E-02	0.31E-02	1.296
0.975	1.27E-01	0.15E-02	0.29E-02	1.257
1.025	1.18E-01	0.14E-02	0.26E-02	1.207
1.075	1.10E-01	0.13E-02	0.25E-02	1.165
1.125	1.04E-01	0.13E-02	0.24E-02	1.139
1.175	1.03E-01	0.14E-02	0.24E-02	1.128
1.225	1.03E-01	0.15E-02	0.25E-02	1.134
1.275	1.11E-01	0.19E-02	0.28E-02	1.148
1.325	1.17E-01	0.23E-02	0.32E-02	1.166
1.375	1.29E-01	0.27E-02	0.36E-02	1.182
1.425	1.45E-01	0.29E-02	0.40E-02	1.194
1.475	1.62E-01	0.32E-02	0.44E-02	1.200
1.525	1.70E-01	0.34E-02	0.47E-02	1.200
1.575	1.89E-01	0.40E-02	0.54E-02	1.197
1.625	1.95E-01	0.49E-02	0.62E-02	1.193
1.675	2.14E-01	0.74E-02	0.84E-02	1.187
1.725	2.11E-01	0.16E-01	0.16E-01	1.183

Table D.12:   1.6 GeV spectrometer data
$Q^2 = 1.750$ (GeV/c)^2, E = 1.511 GeV, TH = 90.00°.

W^2	$d\sigma/d\Omega dW^2$	ERR1	ERR2	R_c
0.715	1.01E-01	0.40E-02	0.45E-02	1.254
0.745	1.29E-01	0.23E-02	0.34E-02	1.253
0.775	1.65E-01	0.19E-02	0.38E-02	1.249
0.805	2.11E-01	0.17E-02	0.45E-02	1.240
0.835	2.59E-01	0.16E-02	0.54E-02	1.223
0.865	2.98E-01	0.29E-02	0.66E-02	1.193
0.895	3.15E-01	0.42E-02	0.76E-02	1.152
0.925	3.01E-01	0.17E-02	0.62E-02	1.102
0.955	2.74E-01	0.16E-02	0.57E-02	1.039
0.985	2.30E-01	0.23E-02	0.51E-02	0.974
1.015	1.91E-01	0.36E-02	0.52E-02	0.910
1.045	1.67E-01	0.18E-02	0.38E-02	0.851
1.075	1.48E-01	0.20E-02	0.36E-02	0.802
1.105	1.29E-01	0.21E-02	0.33E-02	0.765
1.135	1.24E-01	0.18E-02	0.30E-02	0.745
1.165	1.17E-01	0.22E-02	0.32E-02	0.743
1.195	1.28E-01	0.23E-02	0.34E-02	0.758

Table D.13:   1.6 GeV spectrometer data
$Q^2 = 2.500$ (GeV/c)^2, E = 1.968 GeV, TH = 90.00°.

W^2	$d\sigma/d\Omega dW^2$	ERR1	ERR2	R_c
0.520	6.11E-03	0.55E-03	0.56E-03	1.228
0.560	7.59E-03	0.40E-03	0.42E-03	1.231
0.600	9.87E-03	0.35E-03	0.40E-03	1.234
0.640	1.35E-02	0.34E-03	0.43E-03	1.236
0.680	1.88E-02	0.33E-03	0.50E-03	1.237
0.720	2.52E-02	0.38E-03	0.63E-03	1.236
0.760	3.39E-02	0.38E-03	0.78E-03	1.231
0.800	4.32E-02	0.39E-03	0.95E-03	1.219
0.840	5.11E-02	0.45E-03	0.11E-02	1.192
0.880	5.66E-02	0.97E-03	0.15E-02	1.155
0.920	5.85E-02	0.59E-03	0.13E-02	1.106
0.960	5.33E-02	0.57E-03	0.12E-02	1.051
1.000	4.65E-02	0.62E-03	0.11E-02	0.981
1.040	4.12E-02	0.60E-03	0.10E-02	0.917
1.080	3.60E-02	0.61E-03	0.94E-03	0.865
1.120	3.34E-02	0.72E-03	0.98E-03	0.830
1.160	3.20E-02	0.61E-03	0.88E-03	0.815
1.200	3.26E-02	0.64E-03	0.91E-03	0.821
1.240	3.66E-02	0.76E-03	0.11E-02	0.843

Table D.14: 1.6 GeV spectrometer data
Q² = 3.250 (GeV/c)², E = 2.407 GeV, TH = 90.00°.

W²	dσ/dΩdW²	ERR1	ERR2	Rc
0.475	2.22E-03	0.34E-03	0.34E-03	1.209
0.525	2.61E-03	0.31E-03	0.31E-03	1.212
0.575	3.58E-03	0.27E-03	0.28E-03	1.215
0.625	4.52E-03	0.18E-03	0.21E-03	1.218
0.675	6.01E-03	0.16E-03	0.20E-03	1.214
0.725	7.97E-03	0.14E-03	0.21E-03	1.218
0.775	1.06E-02	0.14E-03	0.25E-03	1.204
0.825	1.30E-02	0.16E-03	0.31E-03	1.175
0.875	1.46E-02	0.25E-03	0.39E-03	1.138
0.925	1.50E-02	0.18E-03	0.35E-03	1.092
0.975	1.41E-02	0.19E-03	0.34E-03	1.041
1.025	1.33E-02	0.16E-03	0.31E-03	0.975
1.075	1.15E-02	0.19E-03	0.29E-03	0.920
1.125	1.06E-02	0.20E-03	0.29E-03	0.882
1.175	1.10E-02	0.24E-03	0.33E-03	0.870
1.225	1.13E-02	0.28E-03	0.36E-03	0.866
1.275	1.26E-02	0.28E-03	0.38E-03	0.887
1.325	1.42E-02	0.31E-03	0.42E-03	0.909
1.375	1.60E-02	0.39E-03	0.50E-03	0.928

Table D.15: 1.6 GeV spectrometer data
Q² = 4.000 (GeV/c)², E = 2.837 GeV, TH = 90.00°.

W²	dσ/dΩdW²	ERR1	ERR2	Rc
0.375	5.02E-04	0.87E-04	0.87E-04	1.186
0.425	7.30E-04	0.81E-04	0.82E-04	1.190
0.475	9.22E-04	0.76E-04	0.78E-04	1.194
0.525	1.18E-03	0.70E-04	0.74E-04	1.197
0.575	1.46E-03	0.62E-04	0.68E-04	1.201
0.625	1.92E-03	0.60E-04	0.71E-04	1.201
0.675	2.29E-03	0.64E-04	0.79E-04	1.200
0.725	3.01E-03	0.68E-04	0.90E-04	1.194
0.775	3.76E-03	0.68E-04	0.10E-03	1.185
0.825	4.39E-03	0.71E-04	0.11E-03	1.151
0.875	4.84E-03	0.95E-04	0.14E-03	1.119
0.925	5.10E-03	0.82E-04	0.13E-03	1.082
0.975	4.95E-03	0.79E-04	0.13E-03	1.044
1.025	4.70E-03	0.85E-04	0.13E-03	0.994
1.075	4.40E-03	0.85E-04	0.12E-03	0.948
1.125	4.07E-03	0.92E-04	0.12E-03	0.915
1.175	4.22E-03	0.93E-04	0.13E-03	0.897
1.225	4.43E-03	0.12E-03	0.15E-03	0.893
1.275	4.61E-03	0.13E-03	0.16E-03	0.900
1.325	5.51E-03	0.14E-03	0.18E-03	0.912
1.375	6.28E-03	0.15E-03	0.20E-03	0.924
1.425	6.92E-03	0.18E-03	0.23E-03	0.932
1.475	7.45E-03	0.22E-03	0.26E-03	0.935

ENDNOTES

1. R. Hofstadter and . W. McAllister, . ys. Rev., **98**, 217 (1955).

2. M. R. Yearian and R. Hofstadter, Phys. Rev., **110**, 552 (1958).

3. R. Arnold *et al.*, Phys. Rev. Lett. **57**, 174 (1986).

4. T. Janssens, *et al.*, Phys. Rev. **142**, 922 (1966).

5. J. Litt, *et al.*, Phys. Rev. **31B**, 40 (1970).

6. C. Berger, *et al.*, Phys. Lett. **35B**, 87 (1971).

7. R. C. Walker, *et al.*, Phys. Lett. B, **224**, 353, (1989).

8. S. Rock, *et al.*, SLAC-PUB-5239, (1991), also submitted to Phys. Rev. D.

9. Akerlof, *et al.*, Phys. Rev. B, **135**, 810, (1964).

10. C. de Vries, *et al.*, Phys. Rev. B, **134**, B48, (1964).

11. Dunning, *et al*, Phys. Rev. **141**, 1286 (1966).

12. Budnitz, *et al*, Phys. Rev. **173**, 1357, (1968).

13. Bartel, *et al.*, Nucl. Phys. B ! ⌐, 429 (1973).

14. P. Bosted, *et al*, SLAC-PUB-5744, (1992), also submitted to Phys. Lett.

15. L. Clogher, American University Ph.D. thesis (199?).

16. L. Durand III, Phys. Rev. **123**, 1393 (1961).

17. I. J. McGee, Phys. Rev. **161**, 1640 (1967).

18. G. G. Petratos, American University Ph.D. Thesis (1988, unpublished).

19. R. F. Koontz, SLAC-PUB-3329 (1984).

20. R. F. Koontz, *et al*, SLAC-PUB-3615 (1985).

21. R. B. Neal, *The Stanford Two-Mile Accelerator*, (Benjamin, New York, 1968).

22. H. Weidner, *et al*, SLAC-PUB-285 (1967), published in *IEEE Transactions on Nuclear Science*, Vol. NS-14, NO. 3, 918 (1967).

23. NPAS Users Guide, SLAC-PUB-269 (1984).

24. R. S. Larsen and D. Horelick, SLAC-PUB-398 (1968).

25. D. Horelick and R. S. Larsen, SLAC Report, SLAC-100 (1969).

26. Roder, *et al*, National Bureau of Standards Report, Oct. (1972).

27. National Bureau of Standards, Memoranda M4 and M94.

28. L. Mo and C. Peck, SLAC Technical note, SLAC-TN-65-29 (1965).

29. P. N. Kirk, *et al*, Phys. Rev. D8, 63 (1973).

30. L. Clogher, *et al*, Submitted to Nucl. Inst. Meth. (1992).

31. P. Bosted and A. Rahbar, Technical note, SLAC NPAS-TN-85-1 (1985).

32. G. F. Knoll, *Radiation Detection and Measurement*, (John Wiley & Sons, 1979).

33. R. Anderson, *et al*, Nucl. Inst. Meth. 66, 32° (1968).

34. K. L. Brown, *et al*, SLAC Report, SLAC-91, (1977)

35. W. Atwood, Ph.D. Thesis, SLAC-Report no. 185 (1975)

36. A.G.A.M. Armstrong, C.P. Riley, and J. Simkin, User Guide, Rutherford Appleton Laboratory, RL-81-070, (1982).

37. Los Alamos Accelerator Code Group, Reference Manual, Los Alamos National Laboratory, LA-UR-87-126, (1987).

38. F. W. Brasse, *et al*, Nucl. Phys. B110, 413 (1976).

39. S. Rock, *et al*, SLAC-PUB-5239 (1991, Submitted to Phys. Rev. D)

40. D. H. Perkins, *Introduction to High Energy Physics*, Addison-Wesley Publishing Company, Inc. (1987).

41. S. J. Brodsky and G. P. Lepage, Phys. Rev. D 24, 2848 (1981).

42. C. E. Carlson, Phys. Rev. D 34, 2704 (1986).

43. A. I. Vainshtein and A. V. Zakharov, Phys. Lett. 72B, 368 (1978).

44. P. Stoler, Phys. Rev. Lett. 66, 1003 (1991).

45. W. W. Ash, *et al*, Phys. Lett. **24B**, 165 (1967).

46. P. Stoler, Phys. Rev. D **44**, 73 (1991).

47. S. Stein, *et al*, Phys. Rev. D 12, 1884 (1975).

48. R. L. Walker, Phys. Rev. **182**, 1729 (1969).

49. M. Köbberling, *et al*, Nucl. Phys. **B82**, 201 (1974).

50. P. Kroll, M. Schürmann, and W. Schweiger, University of Wuppertal, Fed. Rep. Germany, WU B 90-16 (1990).

51. C. E. Carlson and J. L. Poor, Phys. Rev. D **38**, 2758 (1988).

52. V. L. Chernyak and A. R. Zhitnitsky, Phys. Rep. **112** 173 (1984).

53. I. D. King and C. T. Sachradja, Nucl. Phys. **B279**, 785 (1987).

54. M. Gari and N .G. Stefanis, Phys. Lett. B **175**, 462 (1986).

55. P. Kroll, M. Schürmann, and W. Schweiger, University of Wuppertal, Fed. Rep. Germany, WU B 91-7 (1991).

56. R. M. Davidson, *et al*, Phys. Rev. D **43**, 71 (1991).

57. I. J. McGee, Phys. Rev. **158**, 1500, (1967).

58. L. Durand III, Phys. Rev. **115**, 1020 (1959).

59. W. Bartel, *et al*, Nucl. Phys., **B58**, 429 (1973).

60. M. Lacombe, *et al*, Phys. Lett. **101B**, 139 (1981).

61. R. Machleidt, K. Holinde, and C. Elster, Phys. Rep. **149**, (1987).

62. R. V. Reid, Ann. Phys. **50**, 411 (1968).

63. A. Fukunaga and K. Saito, Z. Phys. A, **334**, 473 (1989).

64. B. D. Keister, Private communication.

65. P. L. Chung, *et al*, Phys. Rev. C, 37, 2000 (1988).

66. A. Lung, American University Ph.D. thesis (1992).

67. J. M. Laget, Can. J. Phys. **62**, 1046 (1984).

68. J. M. Laget, Phys. Lett. B **199**, 493 (1987).

69. H. Arenhovel, Nucl. Phys. A **384**, 287 (1982).

70. H. Arenhovel, Nucl. Phys. A **393**, 385 (1983).

71. G. G. Petratos, American University Ph.D. thesis (1988).

72. P. Bosted, American University, private communication.

73. W. B. Atwood and G. B. West, Phys. Rev. D, **7**, 773 (1973).

74. A. Bodek, *et al*, Phys. Rev. D, **20**, 1471 (1979).

75. M. M. Sargsyan, L. L. Frankfurt, and M. I. Strikman, Z. Phys. A **335**, 431 (1990).

76. M. I. Strikman, formula for W_1 obtained by private communication.

77. J. J. Aubert, *et al*, Phys. Lett. **123B**, 275 (1983).

78. A. Bodek, *et al*, Phys. Rev. Lett. **50**, 1431 (1983); **51**, 534 (1983).

79. R. G. Arnold, *et al*, Phys. Rev. Lett. **52**, 727 (1984).

80. L. L. Frankfurt and M. I. Strikman, Nucl. Phys. B **250**, 143 (1985).

81. L. L. Frankfurt and M. I. Strikman, Phys. Lett. **64b**, 433, (1976).

82. A. Bodek, Ph. D. thesis, Massachusetts Institute of Technology, MIT Report No. LNS-COO-3069-116 (1972).

83. D. Kusno and M. J. Moravczik, Phys. Rev. C **27**, 2173 (1983).

84. S. Dasu, *et al.*, Phys. Rev. Lett. **61**, 1061 (1988).

85. Particle Data book, Phys. Lett. B, 1 (1990).

86. F. Iachello, A. D. Jackson, A. Lande, Phys. Lett. **43B**, 191 (1973).

87. S. Blatnik and N. Zovko, Acta Phys. Aust. **39**, 62, (1974).

88. G. Höhler, *et al*, Nucl. Phys. **B114**, 505 (1976).

89. G. P. Lepage and S. J. Brodsky, Phys. Rev. Lett, **43**, 545, (1979).

90. G. P. Lepage and S. J. Brodsky, Phys. Rev. D **22**, 2157 (1980).

91. M. Gari and W. Krümpelmann, Z. Phys. A **322**, 689 (1985).

92. S. J. Brodsky and G. F. Farrar, Phys. Rev. D 11, 1309 (1975).

93. M. A. Shifman, A. I. Vainshtein, and V. I. Zakharov, Nucl. Phys. B147, 385,448 (1979).

94. A .V. Radyushkin, Acta Phys. Polo. B15, 403 (1984).

95. P. L. Chung and F. Coester, Phys. Rev. D 44,229 (1991).

96. V. L. Chernyak and I. R. Zhitnitsky, Nucl. Phys. B246, 52 (1984).

97. P. Kroll, University of Wuppertal, Fed. Rep. Germany, WU B 91-17 (1991)

98. M. Gari and W. Krümpelmann, Z. Phys. A 322, 689 (1985).

99. J. Mark, Private communication.

100. C. Ciofi degli Atti, D. B. Day, and S. Liuti, accepted by Phys. Rev. C (1992).

101. L. W. Mo and Y. S. Tsai, Rev. Mod. Phys. 41, 205 (1969).

102. Y. S. Tsai, SLAC-PUB-848, (1971).

103. R. W. Walker, California Institute of Technology Ph.D. thesis (1989).

104. Y. S. Tsai, Rev. Mod. Phys. 46, 815 (1974).

105. H. Burkhardt, TASSO Note no. 192 (1981).